



Angular contact ball bearing modelling with flexible cage

Karine Petuya

► To cite this version:

Karine Petuya. Angular contact ball bearing modelling with flexible cage. Mechanics [physics.med-ph]. INSA de Lyon, 2022. English. NNT : 2022ISAL0128 . tel-04121405

HAL Id: tel-04121405

<https://theses.hal.science/tel-04121405>

Submitted on 7 Jun 2023

HAL is a multi-disciplinary open access archive for the deposit and dissemination of scientific research documents, whether they are published or not. The documents may come from teaching and research institutions in France or abroad, or from public or private research centers.

L'archive ouverte pluridisciplinaire **HAL**, est destinée au dépôt et à la diffusion de documents scientifiques de niveau recherche, publiés ou non, émanant des établissements d'enseignement et de recherche français ou étrangers, des laboratoires publics ou privés.



N°d'ordre NNT : 2022ISAL0128

**THESE de DOCTORAT DE L'INSA LYON,
membre de l'Université de Lyon**

**Ecole Doctorale N° ED162 : MEGA
Mécanique, Energétique, Génie Civil et Acoustique**

Spécialité/ discipline de doctorat :

Ingénierie mécanique

Soutenue publiquement le 09/12/2022, par :
Karine PETUYA

**Angular Contact Ball Bearing modelling
with flexible cage**

Devant le jury composé de :

LINARES Jean-Marc
DAIDIE Alain
SADOULET Emeline
DETERRE Geoffray
NELIAS Daniel
LEBLANC Alexandre
LEROUX Julien
DUREISSEIX David

Professeur (Université Aix-Marseille)
Professeur (INSA Toulouse)
Maître de Conférences (Université Bourgogne Franche-Comté)
Expert Roulements (Safran Aircraft Engines)
Professeur (INSA Lyon)
Maître de Conférences HDR (Université d'Artois)
Docteur (Safran Aircraft Engines)
Professeur (INSA Lyon)

Président
Rapporteur 1
Rapporteur 2
Examinateur
Directeur de thèse
Codirecteur de thèse
Invité, encadrant
Invité

Département FEDORA – INSA Lyon - Ecoles Doctorales

SIGLE	ECOLE DOCTORALE	NOM ET COORDONNEES DU RESPONSABLE
CHIMIE	<u>CHIMIE DE LYON</u> https://www.edchimie-lyon.fr Sec. : Renée EL MELHEM Bât. Blaise PASCAL, 3e étage secretariat@edchimie-lyon.fr	M. Stéphane DANIELE C2P2-CPE LYON-UMR 5265 Bâtiment F308, BP 2077 43 Boulevard du 11 novembre 1918 69616 Villeurbanne directeur@edchimie-lyon.fr
E.E.A.	<u>ÉLECTRONIQUE, ÉLECTROTECHNIQUE, AUTOMATIQUE</u> https://edeea.universite-lyon.fr Sec. : Stéphanie CAUVIN Bâtiment Direction INSA Lyon Tél : 04.72.43.71.70 secretariat.edeea@insa-lyon.fr	M. Philippe DELACHARTRE INSA LYON Laboratoire CREATIS Bâtiment Blaise Pascal, 7 avenue Jean Capelle 69621 Villeurbanne CEDEX Tél : 04.72.43.88.63 philippe.delachartre@insa-lyon.fr
E2M2	<u>ÉVOLUTION, ÉCOSYSTÈME, MICROBIOLOGIE, MODÉLISATION</u> http://e2m2.universite-lyon.fr Sec. : Sylvie ROBERJOT Bât. Atrium, UCB Lyon 1 Tél : 04.72.44.83.62 secretariat.e2m2@univ-lyon1.fr	M. Philippe NORMAND Université Claude Bernard Lyon 1 UMR 5557 Lab. d'Ecologie Microbienne Bâtiment Mendel 43, boulevard du 11 Novembre 1918 69 622 Villeurbanne CEDEX philippe.normand@univ-lyon1.fr
EDISS	<u>INTERDISCIPLINAIRE SCIENCES-SANTÉ</u> http://ediss.universite-lyon.fr Sec. : Sylvie ROBERJOT Bât. Atrium, UCB Lyon 1 Tél : 04.72.44.83.62 secretariat.ediss@univ-lyon1.fr	Mme Sylvie RICARD-BLUM Institut de Chimie et Biochimie Moléculaires et Supramoléculaires (ICBMS) - UMR 5246 CNRS - Université Lyon 1 Bâtiment Raulin - 2ème étage Nord 43 Boulevard du 11 novembre 1918 69622 Villeurbanne Cedex Tél : +33(0)4 72 44 82 32 sylvie.ricard-blum@univ-lyon1.fr
INFOMATHS	<u>INFORMATIQUE ET MATHÉMATIQUES</u> http://edinfomaths.universite-lyon.fr Sec. : Renée EL MELHEM Bât. Blaise PASCAL, 3e étage Tél : 04.72.43.80.46 infomaths@univ-lyon1.fr	M. Hamamache KHEDDOUCI Université Claude Bernard Lyon 1 Bât. Nautibus 43, Boulevard du 11 novembre 1918 69 622 Villeurbanne Cedex France Tél : 04.72.44.83.69 hamamache.kheddouci@univ-lyon1.fr
Matériaux	<u>MATÉRIAUX DE LYON</u> http://ed34.universite-lyon.fr Sec. : Yann DE ORDENANA Tél : 04.72.18.62.44 yann.de-ordenana@ec-lyon.fr	M. Stéphane BENAYOUN Ecole Centrale de Lyon Laboratoire LTDS 36 avenue Guy de Collongue 69134 Ecully CEDEX Tél : 04.72.18.64.37 stephane.benayoun@ec-lyon.fr
MEGA	<u>MÉCANIQUE, ÉNERGÉTIQUE, GÉNIE CIVIL, ACOUSTIQUE</u> http://edmega.universite-lyon.fr Sec. : Stéphanie CAUVIN Tél : 04.72.43.71.70 Bâtiment Direction INSA Lyon mega@insa-lyon.fr	M. Jocelyn BONJOUR INSA Lyon Laboratoire CETHIL Bâtiment Sadi-Carnot 9, rue de la Physique 69621 Villeurbanne CEDEX jocelyn.bonjour@insa-lyon.fr
ScSo	<u>ScSo*</u> https://edsciencessociales.universite-lyon.fr Sec. : Mélina FAVETON INSA : J.Y. TOUSSAINT Tél : 04.78.69.77.79 melina.faveton@univ-lyon2.fr	M. Christian MONTES Université Lumière Lyon 2 86 Rue Pasteur 69365 Lyon CEDEX 07 christian.montes@univ-lyon2.fr

*ScSo : Histoire, Géographie, Aménagement, Urbanisme, Archéologie, Science politique, Sociologie, Anthropologie

Acknowledgements

Si la thèse est un projet très solitaire, l'encadrement technique et l'entourage humain sont essentiels et font toute la différence. C'est pourquoi, je souhaite avant tout remercier mon directeur de thèse Daniel Nélias pour m'avoir permis de réaliser cette thèse. Merci pour sa confiance, son optimisme permanent et pour avoir toujours cru en la réussite du projet. Mais surtout, merci d'avoir pris le temps de m'aider, me conseiller et partager ses connaissances. Merci de m'avoir permis de partir en conférence et de m'avoir mis en contact avec certains experts du domaine. En particulier, ces travaux n'auraient jamais été aussi aboutis sans l'intervention d'Alexandre Leblanc, co-directeur de thèse. Je le remercie pour son implication, sa rigueur et ses conseils toujours très pertinents. Je remercie également les professeurs David Dureisseix et Régis Dufour pour s'être penché à plusieurs reprises sur certains de mes problèmes et m'avoir apporté des solutions. Je souhaite aussi remercier Samy Lacroix pour s'être replongé dans le code et avoir répondu à mes questions.

La thèse a commencé et s'est terminée en entreprise, chez Safran Aircraft Engines. Merci à toutes les personnes du bureau des méthodes et des roulements pour leur accueil, leur gentillesse et leur aide. Je remercie tout particulièrement mes encadrants Julien Leroux, Geoffray Deterre et Daniel Bainachi pour m'avoir fait confiance, m'avoir donné tant de liberté dans mes travaux et pour avoir été si compréhensifs sur le fait qu'ils ne puissent pas se dérouler comme prévu. Merci pour le support technique et humain, mon expérience chez Safran a été très enrichissante. C'est notamment grâce à eux et à Daniel Nélias que je pourrais la poursuivre chez Safran Helicopter Engines, je leur en suis très reconnaissante. Merci également de m'avoir apporté le support de MECALAM; start-up dans laquelle je remercie Quentin Thoret-Bauchet et François Besson pour leur aide, leur rigueur et les très bons échanges que nous avons pu avoir.

Je tiens également à remercier tous les membres du laboratoire que j'ai eu la chance de côtoyer. J'adresse tout d'abord mes remerciements à Isabelle et Sophie, pour leur gentillesse, leur réactivité et tous leurs services. Je remercie ensuite les anciens doctorants de la team Algeco: Zi, Médéric, Florian, Efoe, Alexis (x2), Tristan (x2), Noël, Thomas, Raphaël, Yvan, Zhaofeng, Du, Marie, Ethel. Un énorme merci pour leur accueil, leurs conseils et surtout pour les parties de Coinche, apéros, raclettes, soirées jeux, week-end ski, ect. La relève MIMESIS et MULTIMAP est bien là, pleine d'énergie, de bonne humeur et de blagues raffinées ; merci à Julie, Adrien, Victor, Pierre, Nicolas, Zineb, Audrey et Loïc. Je n'oublie pas les personnes des autres équipes avec qui j'ai eu la chance d'échanger en TP ou en conférences notamment Lucas, Jonathan, Éric, Nicolas, Aurore ou Augustin. De façon plus générale, merci à toute l'INSA et au LaMCoS. Ces huit années m'auront énormément apporté tant intellectuellement qu'humainement grâce à des équipes pédagogiques et des étudiants bienveillants et investis.

Pour terminer, je remercie mes parents et mon frère pour m'avoir toujours supportée, guidée et aidée dans mes projets. Enfin, un grand merci à Pauline (x2), Camille (x2), Marine et Elsa, mes copines du Béarn et d'ailleurs, pour leur éternel soutien et tous les bons moments partagés.

Résumé

Les roulements à billes à contact oblique sont particulièrement utilisés dans l'industrie aérospatiale pour leurs capacités de fonctionnement à grandes vitesses et fortes charges. Sous certaines conditions de fonctionnement, le comportement cinématique et la dynamique de billes sont particulièrement complexes et l'optimisation du roulement essentielle. C'est pourquoi cette étude vise à poursuivre le modèle quasi-statique avec billes et bagues, initialement développé par Leblanc et Nélias. Une des principales difficultés réside dans le fait qu'un à quatre points de contact bille-piste soient considérés. Également, tous les degrés de liberté de billes sont calculés sans avoir recours à des hypothèses cinématiques simplificatrices. Ainsi, l'un des objectifs de cette thèse est d'améliorer les méthodes de calcul d'efforts, de lubrification et la cinématique de billes calculée en chaque point de l'ellipse de contact. Ce modèle est aussi uniformisé pour ne considérer qu'un seul système d'équations permettant de limiter les discontinuités numériques liées aux changements de contacts. Des solutions sont proposées pour étendre les conditions de fonctionnement à de plus petites vitesses et de plus grands chargements radiaux et mésalignements.

Par ailleurs, l'industrie aéronautique développe actuellement des roulements à billes avec des matériaux de cage plus légers mais aussi plus souples. De tels roulements sont sujets à d'importantes déformations et concentrations de contraintes dues aux chocs billes-alvéoles. Ceux-ci ont lieu lors des phases d'accélération ou de décélération, voir en régime de croisière lorsque le roulement est soumis à des efforts axiaux et radiaux combinés. Cette thèse a donc également pour objectif d'ajouter la cage au modèle quasi-statique initial. Les interactions billes-alvéoles et cage-piste sont modélisées, tout comme l'élasticité de cage globale et locale en 3 dimensions. In fine, l'ensemble du système est transposé en dynamique pour être résolu temporellement et prendre en compte les accélérations.

Pour différentes conditions de fonctionnement, la cinématique de billes, les interactions billes-pistes, le mouvement du centre de cage et les déformations de cage locales et globales sont étudiés. Le modèle est validé par comparaison à des modèles existants ainsi qu'à des résultats expérimentaux issus de la littérature.

Mots-clés: Roulement à billes à contact oblique, Modélisation, Quasi-statique, Dynamique, Cage, Flexible, Mécanique des contacts, Lubrification.

Abstract

Angular Contact Ball Bearings are widely used in aerospace industry because of their ability to work at high-speed and to support important loads. Depending on operating conditions, kinematic and dynamic behaviours are complex and bearing design optimisation is essential. That is why this study aims at continuing Leblanc and Nelias' quasi-static model with balls and rings. Difficulty of this model lies in the fact that up to four ball-race contact points are considered. As well, all balls degrees of freedom are calculated without making any kinematic assumption. Then, one of the purpose of this thesis is to improve computation of friction forces, EHD lubrication and kinematics at each point of contact ellipse. The model is also harmonized in order to get a single system of equations that better deals with numerical discontinuities due to contact changes. Solutions are proposed to extend operating conditions at lower speeds and higher radial loads or misalignments.

Besides, aeronautical industry is currently developing ball bearings with cages made of lighter but softer materials. Such bearings experience cage deformation and stress concentration due to ball-to-pocket impacts. These are produced during acceleration and deceleration phases or during cruise when operating with combined thrust and radial load. That is why this study aims, in a second time, at adding cage into the quasi-static model. Ball-to-pocket and cage-race interactions are considered as well as global and local cage elasticity in three dimensions. Finally, the whole system is transposed in dynamics in order to be solved over time and to consider acceleration components.

For various operating conditions, ball kinematics, ball-race interactions, cage center motion, cage local and global deformations are analysed. Model validation is done by comparison with existing models or with experimental results found in literature.

Keywords: Angular Contact Ball Bearing, Modelling, Quasi-static, Dynamic, Cage, Flexible, Contact mechanics, Lubrication.

Contents

Contents	i
List of Figures	v
List of Tables	ix
Introduction	5
1 From quasi-static to dynamic, a Review about Angular Contact Ball Bearing modelling	11
1 Time independent models	12
1.1 First reference models	12
1.1.1 Quasi-static	12
1.1.2 Quasi-dynamic	15
1.2 Lubrication modeling	15
1.2.1 Film thickness	15
1.2.2 Traction forces	16
1.2.3 Thermal effects	18
1.3 Skidding issues	19
1.3.1 Skidding criteria	19
1.3.2 Parameters to limit skidding	20
1.4 Models without raceway control hypothesis	21
1.4.1 Geometric assumption	21
1.4.2 Hybrid theory	21
1.4.3 Contact friction minimisation	22
1.4.4 Ball torque equilibrium	22
1.4.5 Rolling contact analysis	23
1.5 Other areas explored	23
2 Time dependent models	25
2.1 Bases on cage dynamical motion	25
2.2 Dynamical reference models	27
2.3 Cage stability evaluation	28
2.4 Skidding issues in dynamics	31
2.5 Improved models for surface defects	33
2.6 Cage elastic behaviour	34
2.7 Squeeze-film damping modeling	38
3 Conclusions	43

2	Quasi-static model with balls and rings	45
1	Markers definition	47
1.1	Global coordinate system \mathcal{R}_G	47
1.2	Inner ring coordinates systems	47
1.2.1	Inner ring position \mathcal{R}_{i1}	47
1.2.2	Inner ring rotation \mathcal{R}_i	48
1.3	Balls coordinates systems	49
1.3.1	Balls positions \mathcal{R}_{b1}^j	49
1.3.2	Balls own rotations $\mathcal{R}_{b2}^j, \mathcal{R}_{b3}^j$	50
1.3.3	Ball-raceway contacts $\bar{\mathcal{R}}_{km}^j$	51
2	Geometric equations	53
2.1	Geometric closure on outer ring	54
2.2	Geometric closure on inner ring	54
2.3	Geometric closure on inner and outer ring	55
2.4	Choice of equations depending on rings truncations	56
3	Ball kinematic	56
3.1	Detailed computation for outer race, side 2	58
3.2	Kinematic synthesis at 4 contacts	59
3.3	Point of pure rolling	60
4	Forces definition	61
4.1	External forces on the inner ring	61
4.2	Forces due to ball motion	61
4.3	Coulomb's friction	62
5	Friction forces computation	65
5.1	Analytic expressions	65
5.1.1	Gupta's method	65
5.1.2	Gauss-Legendre's method	66
5.1.3	Monte-Carlo's method	71
5.2	Validation	72
5.2.1	Friction without spinning or transverse sliding	72
5.2.2	Friction for combined axial and radial loads (rolling, sliding, spinning)	74
6	Quasi-static resolutions	77
6.1	R1 Resolution	77
6.1.1	Inner race equilibrium	77
6.1.2	Balls equilibrium	78
6.1.3	Numerical procedure	79
6.1.4	Stiffness matrix computation	80
6.2	R2 Resolution	80
6.2.1	Inner ring equilibrium	80
6.2.2	Balls equilibrium	82
6.2.3	Numerical procedure	83
6.2.4	Ball-to-inner race detachment	84
6.3	New features of BB20 version 5	86
7	Results analysis	88
7.1	Investigation of existing bearings	88

7.1.1	Pure axial load	88
7.1.2	Combined axial and radial loads	90
7.1.3	Comparison BB20 Version 4 vs 5	90
7.1.4	Power loss	91
7.2	Comparison with literature	94
7.2.1	Reference analytical models	94
7.2.2	Experience measuring pitch angle β^j	99
8	Summary	101
3	Quasi-dynamic model with cage	103
1	Markers definition	104
1.1	Cage coordinate systems	104
1.1.1	Cage center \mathcal{R}_c	104
1.1.2	Pocket initial position \mathcal{R}_p^j	105
1.1.3	Pocket removed position $\mathcal{R}_{p'}^j$	105
1.1.4	Bridge position \mathcal{R}_{br}^j	105
1.2	Relative displacements	106
1.2.1	Balls positions	106
1.2.2	Pockets motions	107
1.2.3	Ball-to-pocket geometric approach	108
2	Ball-to-pocket interactions	108
2.1	Interactions in (G_p^j, y_p^j, z_p^j) plan	109
2.1.1	Barrel-plan HD contact	109
2.1.2	Dry contact	110
2.1.3	Contact forces continuity	111
2.1.4	Forces summary	113
2.2	Interaction in (G_p^j, z_p^j, x_p^j) plan	114
2.2.1	Short journal bearing modeling for HD contact	114
2.2.2	Extension of short journal bearing theory to EHD contact	115
2.2.3	Forces summary	116
2.3	Total interactions	117
3	Cage-ring interactions	117
3.1	General model	117
3.2	Computation for whole cage	119
3.3	Computation for each pocket	121
4	Rigid cage resolution	123
4.1	Inner Ring equilibrium	123
4.2	Balls equilibrium	124
4.3	Cage equilibrium	124
4.4	Numerical procedure	124
5	Flexible cage resolution	126
5.1	Cage elasticity definition	126
5.2	Pocket equilibrium	128
5.3	Numerical procedure	128
5.4	Cage center motions and pocket elastic deformations	128
6	Results analysis	130

6.1	Investigation of existing bearings	130
6.1.1	Pure axial load	130
6.1.2	Combined loads with a rigid cage	133
6.1.3	Combined loads with a flexible cage	138
6.2	Comparison with a 4 contact-points literature model	142
6.2.1	Pure axial load	143
6.2.2	Combined loads	146
7	Summary	148
4	Dynamic model	151
1	Inertia matrices	152
1.1	Inner ring	152
1.2	Balls	152
1.3	Cage	153
2	Dynamic torsors	154
2.1	Inner ring	154
2.2	Balls	154
2.3	Cage	155
3	Dynamic equations	156
3.1	Inner ring	156
3.2	Balls	156
3.3	Cage	157
4	Geometric equations	157
5	System resolution	158
5.1	Adaptive Stepsize Runge-Kutta-Fehlberg algorithm	158
5.2	System of equations and unknowns	159
6	Summary	161
	Conclusion	163
	A Review summarising Tables	167
	B R2 results under pure axial load	175
	C Rheological parameters	177
1	Dynamic viscosity μ	177
2	Reciprocal asymptotic isoviscous pressure α^*	177
3	Friction coefficients	178
4	Thermal reduction factor on film thickness	178
	Bibliography	179

List of Figures

1	LEAP-1A engine designed by CFM International, a joint-venture gathering Safran Aircraft Engines and General Electric Aviation [80]	5
2	Aerodynamic functioning of double flow turbojet engines [268]	6
3	Bearings present at each stage of aircraft engines [63]	6
4	Ball Bearing components [155]	7
5	Different bearing types and load capacity	8
1.1	Geometric constraints on the bearing	13
1.2	Bearing kinematic parameters	14
1.3	Kingsbury's model for cage whirl motion at initial position and at 90°, schematized by Niu [194]	26
1.4	Cage center of mass motion under stable whirl and squeal	26
1.5	Pederson's flexibility modeling [203], [204]	35
1.6	Weinzapfel's flexibility modeling [262]	35
1.7	Houpert's flexibility modeling [129]	36
1.8	Li's flexible cage model [161]	37
1.9	Liu's flexibility modeling [167]	38
1.10	Walford's squeeze-film modeling [252]	38
1.11	Hagiu's squeeze-film modeling [106]	39
1.12	Dietl's squeeze-film modeling [57], [58]	40
1.13	Wijnant's squeeze-film modeling [267]	40
1.14	Sarangi's squeeze-film modeling [225] under pure EHD lubrication	41
1.15	Sarangi's squeeze-film modeling [227] under mixed EHD lubrication	41
2.1	Inner ring motions relative to bearing center	48
2.2	Inner ring self-rotation	48
2.3	Balls orbital positions and precession speeds in the bearing	49
2.4	Balls translations	49
2.5	Ball self-rotations	50
2.6	Contacts orientations	51
2.7	Curvature centres at inner and outer ring	53
2.8	Contact parameters on outer race, side 2	57
2.9	Contact forces acting on each ball	63
2.10	Contact momentums acting on each ball	64
2.11	Coulomb's parameters definition	64
2.12	$\tan \varphi$ functions over contact ellipses	67
2.13	Sliding lines on contact ellipses	67
2.14	$F_{X_{km}}$ integrands over contact ellipses	68

2.15	Sliding speeds $-x\omega_S^j - V_Z^j$ and $z\omega_S^j + V_X^j$ over contact ellipses	68
2.16	Sliding speed V_{Zkm}^j and friction force F_{Zkm}^j without spinning or transverse sliding	73
2.17	Sliding lines on contact ellipses	73
2.18	For each method, friction calculated over iterations	75
2.19	For each method, outer race friction forces obtained for $F_X=15\ 000\text{N}$ and $F_Y=14\ 000\text{N}$	76
2.20	Illustration of ball rotations fall for bearing A	85
2.21	Results for bearing A after ball detachment improvements	87
2.22	Sliding lines for bearing A, under different working conditions	89
2.23	Sliding lines for bearing A under low radial loads	91
2.24	Sliding lines for bearing A under important radial loads	92
2.25	Comparison of BB20V4/V5 for bearing D under $F_X=100\ 000\text{N}$	93
2.26	Evolution of spin-to-roll ratio at inner and outer race with shaft speed	95
2.27	Evolution of pitch angle β with shaft speed	96
2.28	Evolution of cage-to-shaft speed ratio $\frac{\omega_c}{N_i}$ with shaft speed	97
2.29	Evolution of ball-to-shaft speed ratio $\frac{\omega_R}{N_i}$ with shaft speed	97
2.30	Evolution of spin-to-roll ratio at inner and outer race with axial load	98
2.31	Evolution of cage-to-shaft speed ratio $\frac{\omega_c}{N_i}$ with axial load	98
2.32	Influence of drag coefficient C_d on cage speed ω_c	99
2.33	Influence of friction coefficient μ on cage speed ω_c	99
2.34	Evolution of pitch angle β^j with shaft speed	100
2.35	Evolution of ball-to-cage rotational speeds $\frac{\omega_R^j}{\omega_c}$ with shaft speed	100
3.1	Cage center motions	104
3.2	Pocket center motions	104
3.3	Pocket centers and bridge centers positions	106
3.4	Ball tangential displacement	107
3.5	Pocket motion and deformation	108
3.6	Ball-to-pocket geometric interaction	109
3.7	Barrel-plan contact	109
3.8	Contact at each side	111
3.9	Normal load evolution with ball-to-pocket gap $\frac{c_p}{2} - \Delta_{pb}^j$, for different contact models	112
3.10	Short journal bearing interaction	114
3.11	Short journal bearing parameters	118
3.12	Cage-inner races interactions	120
3.13	Races-Pocket interactions	122
3.14	Cage discretisation by finite elements	126
3.15	3D Beam element	126
3.16	Results for different type of cages under pure axial load	131
3.17	Ball-race kinematics for rigid cage centered on IR	132
3.18	Evolution of β' with axial load F_X and shaft speed Ω_i for rigid cage centered on IR	133
3.19	Rigid cage results with an increasing radial load	134
3.20	Positions of ball-to-inner race contact points: $ G_I C_{i1}^j $	135

3.21	Positions of ball-to-outer race contact points: $ \mathbf{GC}_{o2}^j $	136
3.22	Ball-to-pocket displacements in $(G_p^j, \mathbf{z}_p^j, \mathbf{x}_p^j)$ plan, for rigid cage	137
3.23	Ball-to-pocket interactions under increasing radial loads	139
3.24	Comparison between flexible and rigid cage for increasing radial loads . . .	140
3.25	Ball-to-pocket displacements in $(G_p^j, \mathbf{z}_p^j, \mathbf{x}_p^j)$ plan, for flexible cage	141
3.26	Pocket elastic deformations with steel cage	142
3.27	Pocket elastic deformations with PEEK cage	142
3.28	Comparison between BB20 and Ma [174] under pure axial load	145
3.29	Comparison between BB20 and Ma [174] under combined loads	146
3.30	Synthesis of cage modelling and numerical resolution	149

List of Tables

1.1	Traction coefficient expressions	17
1.2	Relations that implies ball skidding	19
1.3	Raceway control hypothesis	21
2.1	Overview of ball-raceway possible contacts	52
2.2	Bearing configurations and corresponding equations	56
2.3	Roots and weights for $n = 5$	66
2.4	Bearing dimensions and working conditions	67
2.5	Comparison of friction forces calculated with different methods	74
2.6	Results obtained with different methods	75
2.7	Parameters used to nondimensionalize related equation or unknown	83
2.8	Bearing data	84
2.9	Operating conditions applied for bearing A under pure axial load	88
2.10	Data of bearing tested	94
2.11	Bearing design data from Harris' first study [120]	95
2.12	Bearing design data from Kawamura's study [150]	99
3.1	Cage parameters used to nondimensionalize related equations or unknowns	125
3.2	Pocket parameters used to nondimensionalize related equation or unknown	128
3.3	Material properties of steel and PEEK	141
3.4	Data of bearing tested	143
4.1	Inner ring and cage unknowns and equations in dynamics	160
4.2	Balls unknowns and equations in dynamics	161
A.1	Quasi-static and quasi-dynamic sophisticated models	169
A.2	Quasi-static and quasi-dynamic developed models	170
A.3	Quasi-static and quasi-dynamic simplified models	171
A.4	Sophisticated dynamical models	172
A.5	Developed dynamical models	173
A.6	Simplified dynamical models	174
B.1	Results obtained for bearing A under pure axial load	176

Nomenclature

Equilibrium parameters

a_{km}^j, b_{km}^j	: Contact ellipse semi-major and semi-minor axis.
α_{km}^j	: Ball-race contact angle.
β^j	: Ball pitch, attitude angle.
β'^j	: Ball yaw angle.
C_b^j, C_p^j	: Ball and pocket friction torques due to short journal bearing effect.
C_d	: Drag coefficient.
C_{1km}, C_{2km}	: Cage and race friction torques due to short journal bearing effect.
C_{km}^j	: Pocket friction torque due to short journal bearing effect of race.
δ	: Translation.
δ_{km}^j	: Ball-race contact deformation (if positive) or gap (if negative).
Δ_{pb}^j	: Projection of δ_{pb}^j in $(P^j, \mathbf{x}_p^j, \mathbf{z}_p^j)$ plan.
δ_{pb}^j	: Ball-to-pocket displacement.
$\delta_x, \delta_y, \delta_z$: Inner ring translations.
e	: Eccentricity.
ϵ	: Relative eccentricity.
F_{BP}^j, M_{BP}^j	: Ball-to-pocket forces and momentums in $(G_p^j, \mathbf{y}_p^j, \mathbf{z}_p^j)$ plan.
F_c^j	: Centrifugal force on ball j .
F_{dr}^j	: Drag force on ball j .
F_{el}^j, M_{el}^j	: Pocket elastic deformation forces and momentums.
F_{τ}^j	: Ball-to-pocket shear force.
F_f^j, F_r^j	: Friction force at front and rear side of ball-to-pocket interaction.
F_{sb}^j, M_{sb}^j	: Ball-to-pocket forces in $(G_p^j, \mathbf{z}_p^j, \mathbf{x}_p^j)$ plan.
F_{Xkm}^j, F_{Zkm}^j	: Ball-race friction forces.
F_X, F_Y, F_Z	: External forces on inner ring.
GE_{km}^j	: Distance $\mathbf{B}^j \mathbf{C}_{km}^j$.
h_f^j, h_r^j	: Ball-to-pocket film thickness at front and rear side.
h_{tr}^j	: Ball-to-pocket transition film thickness from HD to EHD regime.
h_{km}^j	: Ball-race film thickness.
λ	: Mathematical coefficient for projections.
λ_c	: Mathematical coefficient to relax δ_{bz}^j .
$LMCC^j$: Number defining a combination of ball-race contacts.
M_{GY}^j, M_{GZ}^j	: Gyroscopic momentums on ball j .
$M_{Rkm}^j, M_{Skm}^j, M_{Zkm}^j$: Ball-race friction momentums due to rolling, spinning and gyroscopic effects.
M_Y, M_Z	: External momentums on inner ring.

Ω, ω	: Rotational speed.
ω_i^j	: Ball-inner race relative speed.
ω_m^j	: Ball precession, orbital speed.
ω_o^j	: Ball-outer race relative speed.
ω_R^j	: Ball self-rotational speed.
$\omega_{Rkm}^j, \omega_{Skm}^j$: Ball-race rolling and spinning speeds.
ϕ^j	: Orientation of ball-to-pocket contact.
ϕ_{Gk}	: Angle defining cage-race short journal bearing orientation.
ϕ_{km}	: Attitude angle for cage-race short journal bearing interaction.
ϕ_{sb}^j	: Ball-to-pocket short journal bearing attitude angle.
ψ^j	: Ball angular position.
ψ_c	: Angular position of first pocket.
ψ_{br}^j	: Angular position of bridge center.
Q_{km}^j	: Ball-race normal load.
R_k	: Radius of ball-race deformed surface.
\bar{r}_{km}^j	: Distance between ball center and a point on surface ellipse.
r_{km}^j	: Effective rolling radius.
SR	: Spin-to-roll ratio.
θ	: Rotation angle.
θ_m^j	: Ball-to-pocket relative rotation.
θ_y, θ_z	: Inner ring rotations.
U	: Ball-to-pocket relative sliding speed.
V	: Sliding speed.
W_{lub}	: Lubricant flow rate.
W_f^j, W_r^j	: Normal load at front and rear side of ball-to-pocket interaction.
W_{BP}^j	: Ball-to-pocket normal load due to barrel-plan effect.
W_H^j	: Ball-to-pocket normal load due to Hertzian elastic deformation at contact.
W_{km}	: Cage-race normal load.
W_{km}^j	: Pocket-race normal load.
W_{sb}^j	: Ball-to-pocket normal load due to short journal bearing effect.
x_c, y_c, z_c	: Cage center coordinates in global system.
x_G^j, y_G^j, z_G^j	: Ball center coordinates in global system.

Bearing data

α_f	: Free contact angle.
c_{IR}, c_{OR}	: Cage-race clearances.
c_G	: Minimum clearance between c_{IR} and c_{OR} .
c_p	: Pocket clearance.
D	: Ball diameter.
D_{ci}, D_{co}	: Inner and outer diameters of cage.
d_{ekm}	: Race shoulders diameters.
d_m	: Bearing average diameter.
E_c	: Cage Young's modulus.
f_i, f_o	: Races conformity.
g_i, g_o	: Rings truncations.
h_c	: Cage thickness.
$I_b, I_{c**}, I_{IR**}, I_{s**}$: Ball, cage, inner ring and shaft moments of inertia.
J_d	: Bearing diametral clearance.
L_{km}	: Race width.
m_b, m_c, m_{IR}, m_s	: Ball, cage, inner ring and shaft masses.
μ	: Friction coefficient or dynamic viscosity.
N	: Balls number.
N_i	: Shaft rotational speed.
ν_c	: Cage poisson's ratio.
R_b, R_c, R_p	: Ball, cage and pocket radius.
w_{Bk}, w_c	: Ring and cage width.

Points

B^j	: Ball center.
C_{km}^j	: Race curvature center.
G_{i1}	: Inner ring center.
C_b^j, C_p^j	: Closer points on ball and pocket that approaches each other.
G_c	: Cage center.
G	: Bearing center.
G_p^j	: Pocket center initially.
G_{br}^j	: Bridge center.
I_{km}^j	: Ball-race contact point.
P^j	: Removed and deformed pocket center.

Indices, exponents

$b1, b2, b3$: Balls coordinate systems.
br	: Bridge.
c	: Cage.
el	: Pocket elastic deformations.
f	: Ball-to-pocket interaction at front side.
G	: Global coordinate system.
i, IR	: Inner race.
$i1$: Inner ring coordinate system.
j	: Ball index.
o, OR	: Outer race.
p	: Pocket.
r	: Ball-to-pocket interaction at rear side.
RBM	: Rigid Body Motion.
$\overline{\mathcal{R}}_{km}$: Ball-race contact coordinate system.
1	: Side 1.
2	: Side 2.
x, y, z	: Local axis.

Equations

f_{IR}^j	: Geometric closure on inner ring.
f_{OR}^j	: Geometric closure on outer ring.
f_{IROR}^j	: Geometric closure on inner and outer ring.
$F_{QS/IR}$: Quasi-static forces on inner ring.
$M_{QS/IR}$: Quasi-static momentums on inner ring.
$F_{QS/b}^j$: Quasi-static forces on ball j .
$M_{QS/b}^j$: Quasi-static momentums on ball j .
$F_{QD/IR}$: Quasi-dynamic forces on inner ring.
$M_{QD/IR}$: Quasi-dynamic momentums on inner ring.
$F_{QD/b}^j$: Quasi-dynamic forces on ball j .
$M_{QD/b}^j$: Quasi-dynamic momentums on ball j .
$F_{QD/c}$: Quasi-dynamic forces on cage.
$M_{QD/c}$: Quasi-dynamic momentums on cage.
$F_{QD/p}^j$: Quasi-dynamic forces on pocket j .
$M_{QD/p}^j$: Quasi-dynamic momentums on pocket j .

Introduction

Aircraft engines bearings

Bearing is a common mechanism used in many applications like bikes, cars, washing machines, tower cranes or wind turbines. In this thesis, we are interesting in Angular Contact Ball Bearings (ACBB) present on aircraft engines. As illustrated in Figure 1, turbojet engine is a cutting-edge technology with different stages designed to catch and accelerate airflow. This generates a thrust force that propel the airplane according to Newton's law of action-reaction.



Figure 1 : LEAP-1A engine designed by CFM International, a joint-venture gathering Safran Aircraft Engines and General Electric Aviation [80]

During operation, as represented on Figure 2, streamlined blades of the fan continuously aspirate air into the engine. The airflow enters the compressor that increases its pressure in order to get optimum pressure and temperature for combustion. Then, high-pressure airflow is mixed with kerosene before entering combustion chamber where combustion of the mixture generates air acceleration. At the last stage, energy arising from pressure and speed of hot gazes, drives a rotating turbine that drives itself fan and compressor at the entrance. Is this way, a continuous movement of the engine is ensured. Finally, high-speed airflow is ejected at the exit to propel the aircraft.

In simple flow turbojet engines, all the flow takes this path. Such engines are mainly used in military applications because of their high efficiency above Mach 1. For civilian applications, double flow turbojet engines are preferred because of their low fuel consumption and noise reduction. In this technology, 20% of the flow passes by the core with its compression and depression stages, whereas 80% bypasses it and is only accelerated by the fan and directly ejected in outlet [19].

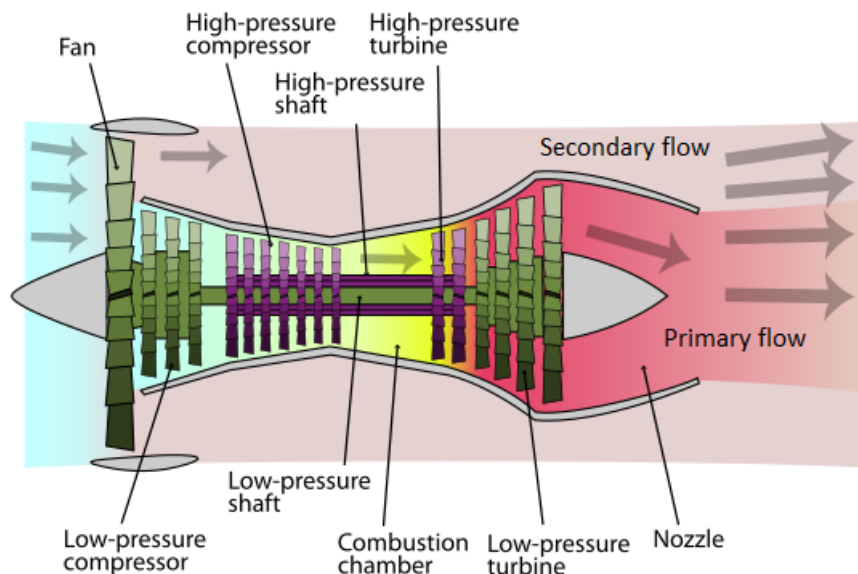


Figure 2 : Aerodynamic functioning of double flow turbojet engines [268]

Regarding bearings, they are mounted between rotors and stator at different levels of the engine. They ensure axial shaft rotation, transfer forces from the shaft to the outside and reduce friction. Ball bearings 1 and 3 and cylindrical bearings 2 and 5 schematized in Figure 3, are always present in engines. In order to gain weight, inter-shaft bearing 4 can be added between high-pressure and low-pressure rotors. However, it can generate vibrational issues since energy is transferred between both shafts [63].



Figure 3 : Bearings present at each stage of aircraft engines [63]

Bearing designs

Angular Contact Ball Bearings are made of an inner ring (IR) that rotates with shaft and that is in contact with balls. These last ones have an orbital motion around shaft and 3D self-rotations. They transfer forces from IR to outer ring (OR). This last one is bound to stator, the fixed part of the engine. Ball-ring contacts occur on races where balls can slide, roll and spin, resulting in complex kinematics. A cage is also present to distribute balls around the bearing and to avoid their collision. Besides, aircraft engines work under high-speeds and high-temperatures that is why lubricant circulates between each element. Purpose is to reduce scuffing, friction, heating and to transfer energy outside. Grease lubricated bearings are limited in speed and fatigue-life because grease tends to heat-up and to leak outside the bearing. That is why, this study focuses on oil-lubricated ACBB, more appropriated to high-speed applications.

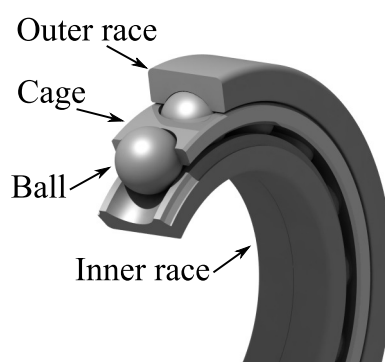


Figure 4 : Ball Bearing components [155]

Currently, major part of ball bearings are Deep Groove Ball Bearings (DGBB). They do not present ring truncations, then they have two contact points (one on IR and another one on OR). They are mainly designed to support radial load but can withstand small axial load or misalignment.

ACBB carries higher thrust load but only in one direction. Mounting two ACBB back-to-back allows to handle thrust load in two directions. Like DGBB, they only support small axial misalignment. Some of them only have one truncation, generally on the inner ring. Then, under combined axial and radial load, 1, 2 or 3 contact points can be present. To be able to support higher radial loads, ACBB can have two truncations (one on each ring), then they can have up to 4 contact points. Some SAE engines are made of these 4 contact points ball bearings, also called FCPBB. Because of operating conditions, in practice, SAE FCPBB mainly works under 2 contact-points. Contrary to ordinary ACBB, they are able to support axial load in two directions. Races are not portions of spheres anymore but arches as shown in Figure 5. These arches give space at the top to better drain lubricant and to set up holes on OR to evacuate it. Advantage of working with further contact points is that centrifugal forces are better distributed, then ball-race normal loads are less concentrated, fatigue life is significantly increased. However, many studies have shown that working under more than two contact points complicates kinematics, increases skidding, scuffing risk or friction [111], [157].

To limit the number of contact points, a solution is to reduce radial load. That is why in turbo-machineries, ACBB are coupled with cylindrical roller bearings (CRB) that take over radial forces. Indeed, CRB supports important radial load but limited axial load and misalignment. As a matter of fact, thrust load induces friction at roller end-to-race flange contact that creates problematic roller skewing.

Other applications like landing systems, use tapered roller bearings (TRB). With their conical rollers, they can handle high radial load, high thrust load in one direction but limited misalignment. Like ACBB, axial load in two directions can be carried by arranging two TRB back-to-back.

Spherical roller bearings (SRB) are designed with a spherical outer race and one or two sets of rollers with barrel shapes. With such design, rollers conform closely to races. Cage, IR and rollers can rotate in an additional direction. Then, high radial load, axial misalignment and some axial load can be handled [210].

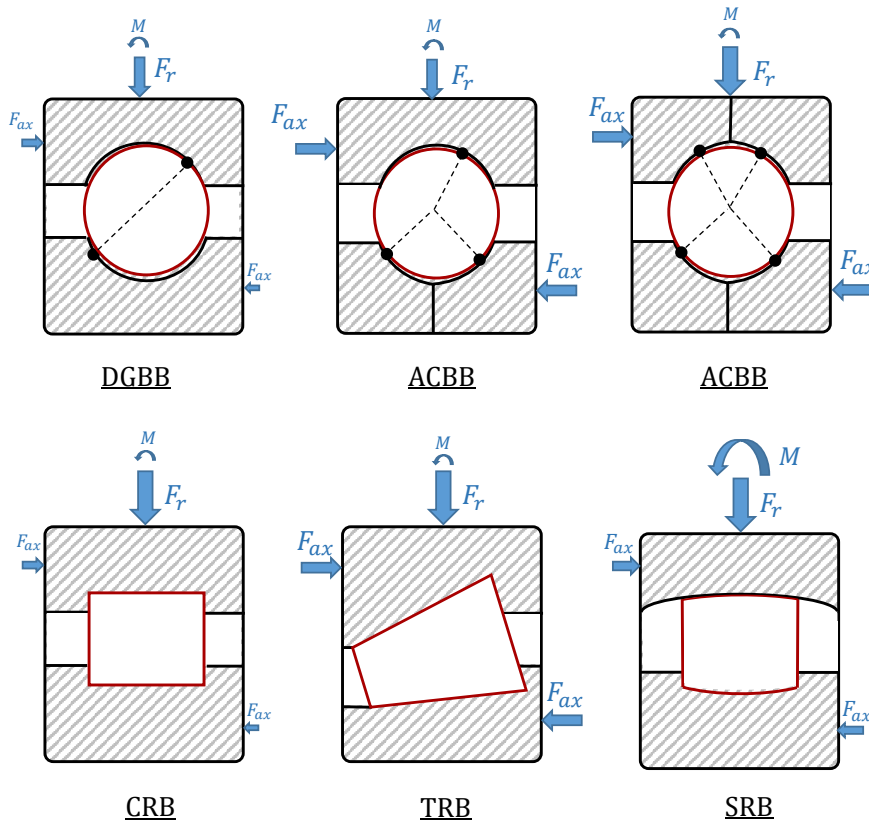


Figure 5 : Different bearing types and load capacity

Motivations and objectives

Initially ball bearings were entirely made of steel. Thereafter, for high-speed applications, hybrid bearings with ceramic balls were developed in order to reduce mass, inertial forces, then contact loads. As well, cages with lighter materials like aluminium, S-Monek, graphite, nylon or cast iron were designed [122]. These recent years, polymeric cages are getting more and more attention because of their low density, manufacturing and assembly assets, good chemical resistance, low friction, low coefficient of thermal expansion and quiet running. Especially, Safran Aircraft Engines (SAE) is interesting in polymeric cages made of PEEK (polyetheretherketone) which has a density six times lower than steel. However, such material is also softer and results in large stresses under ring misalignment or in radial cage deformation, under high-speeds, because of centrifugal forces. Experiences have particularly shown local ball-to-pocket deformations and three-dimensional cage ovalisation during acceleration and deceleration phases or during cruise when the bearing is submitted to combined load, misalignment or unbalanced defects. For these reasons, 3D cage flexibility should be considered while designing bearings. However, before 2019 and the beginning of this thesis, no model considering 3D cage elasticity existed in literature. And, recent models developed are not open access which explains SAE interest in this subject.

Besides, SAE bearing design department is currently using ADORE computer code [91] to develop and improve their bearings. Even if this dynamic model is very achieved, it does not consider cage flexibility or ACBB with rings truncations. User does not have control on the whole model and few modelling details stays unclear. That is why in 2007, SAE in collaboration with LaMCoS laboratory, started to develop BB20: a quasi-static ball bearing code. It considers balls and rings with lubrication, inertial forces, drag forces, external shaft forces, ball-race normal and friction forces for ACBB with 1 to 4 contact points [157], [158]. Rings deformations were also added in 2014 [156]. If this computer code has proven its efficiency for many years, few limitations have been noticed. Indeed, it is mainly adapted to high-speed and high axial-to-radial load ratios. Few results are unexpected and indicates problems like in stiffness matrix computation, in PV product (contact pressure time sliding speeds) or in certain friction forces.

Consequently, in this study, BB20 quasi-static code will first be pursued to understand unexpected results, to fix problems and to extend working conditions. In a second time, cage will be added and its flexibility will be considered both locally and globally in three dimensions. In a third time, reflection on dynamical modelling will be conducted. Developed model should solve bearing equilibrium under low or high speeds and small or important axial, radial loads and misalignment. Cage center motions, cage deformations, ball-to-pocket interactions and cage centering forces should be calculated. With this computer code we should be able, for given working conditions, to estimate optimal geometry and materials that ensure effective bearing behaviour and long lifetime. Before starting this code development, a bibliographic study about ACBB modelling is led in order to better understand possibilities, limits and novelties that can be brought.

Chapter 1

From quasi-static to dynamic, a Review about Angular Contact Ball Bearing modelling

Contents

1	Time independent models	12
1.1	First reference models	12
1.2	Lubrication modeling	15
1.3	Skidding issues	19
1.4	Models without raceway control hypothesis	21
1.5	Other areas explored	23
2	Time dependent models	25
2.1	Bases on cage dynamical motion	25
2.2	Dynamical reference models	27
2.3	Cage stability evaluation	28
2.4	Skidding issues in dynamics	31
2.5	Improved models for surface defects	33
2.6	Cage elastic behaviour	34
2.7	Squeeze-film damping modeling	38
3	Conclusions	43

1 Time independent models

1.1 First reference models

In this section, quasi-static and quasi-dynamic models that are time independents are addressed. Usually, they can be solved by a basic Newton-Raphson algorithm. A quasi-static model consists in solving the static equilibrium of a mechanism but by considering inertial effects (centrifugal forces and gyroscopic moments). Generally, such model only takes into accounts balls, rings and lubricant interactions since the cage mostly contributes in dynamics. A quasi-dynamic model consists in solving the dynamic equilibrium of a mechanism by considering first derivatives of rotational speed vectors and second derivatives of element position vectors as a function of position instead of time. For example, ball rotational accelerations $\dot{\omega}$ are computed from azimuth angle ψ^j and orbital velocity ω_m^j such that $\frac{d\omega^j}{dt} = \omega_m^j \frac{d\omega^j}{d\psi^j}$. Is this way, the system of equations is simplified and computational time is saved compared to the full dynamic resolution. Generally, steady state conditions are applied, cage motion is considered and ball precession velocity ω_m^j is differentiated from cage rotational velocity ω_c . Nevertheless, the distinction between quasi-static and quasi-dynamic models can differ depending on authors since difference is thin.

1.1.1 Quasi-static

In 1959, Jones [144] developed a quasi-static model for high-speed ACBB. This model considers one point of contact between ball and inner ring and one between ball and outer ring. At each contact, the Hertzian pressure resulting from elastic deformations creates slippage. The resulting friction forces are calculated using Coulomb's model and integrating shear stress over the pressure ellipse. Ball centrifugal forces and gyroscopic moments are present and auxiliary relations enable to consider ball-races spinning, slipping and rolling velocities. Then, the problem consists in solving eight equations:

- Two geometrical constraints defining locations of ball center relative to raceway curvature center as schematized on Figure 1.1.
- Two equilibrium equations on forces on each ring.
- Two equilibrium equations on forces and two on momentums on each ball.

The associated unknowns are β^j, β'^j the pitch and yaw angles that defines ball rotation directions, r_i^j, r_o^j the effective rolling radius that locates the position of pure rolling, P_i^j, P_o^j the contact pressures, and α_i^j, α_o^j the contact angles between balls and inner or outer races as represented on Figure 1.2. However, the analytical closed form solution of this system cannot be found directly. So, to avoid the use of iterative methods and high-speed computer, Jones assumed that the ball rolls without spin on one race called the "controlling" one, and rolls and spin on the other race. Then, motional resistance to gyroscopic moment only occurs at the controlling raceway whereas gyroscopic slippage occurs at the other one. As represented on Figure 1.2, coefficients λ_i and λ_o are introduced to model gyroscopic moment distribution. To define the type of control, Jones introduced criterion (1.1) that postulates that outer raceway control (ORC) applies if the inequality is satisfied ($\lambda_o = 2, \lambda_i = 0$) and that inner raceway control (IRC) applies otherwise ($\lambda_o = 0, \lambda_i = 2$). Such hypothesis highly simplifies the problem and enables to obtain explicit formulas on pitch angle β^j such as summarised in two first columns of Table 1.3.

Note that in expression (1.1), Q_i, Q_o are ball-race normal load, a_i, a_o are ellipse major semi-axis, α_i, α_o are contact angles and \bar{E}_i, \bar{E}_o are complete elliptic integral of the second kind.

$$Q_o a_o \bar{E}_o \cos(\alpha_i - \alpha_o) > Q_i a_i \bar{E}_i \quad (1.1)$$

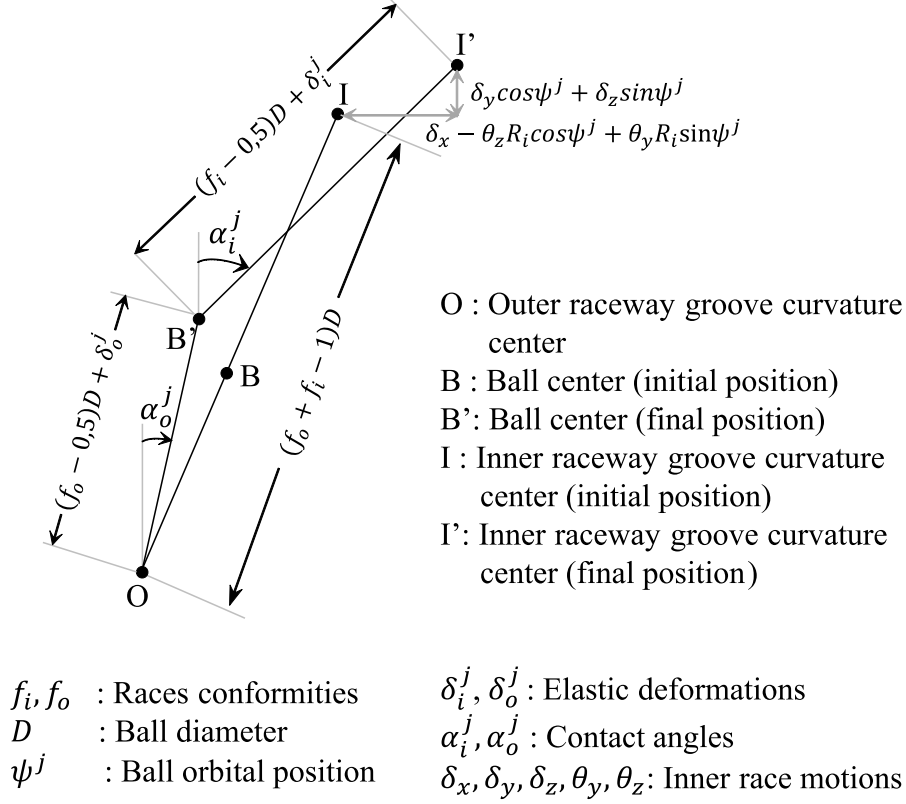


Figure 1.1 : Geometric constraints on the bearing

However, such hypothesis has been rapidly questioned by experimental studies. For example, Shevchenko and Bolan [234] found different results when comparing Jones' analytic model to contact angle measurements. Poplawski and Mauriello [208] restricted ORC to light-loads conditions, because they observed that increasing thrust load decreases skidding and makes slide-to-roll (S/R) ratio at the outer race approaching S/R at the inner race. Kingsbury [151], by investigating experimental slip, pivoting, spin and precession of ACBB, deduced that races control slipping motion at ball-race contact whereas cage controls spinning.

Consequently, Harris [120] further worked on Jones' analytical model and confirmed its accuracy, but also its complexity which explains the use of raceway control hypothesis (RCH). However, he showed that such simplification was not appropriate to predict S/R, friction torque and frictional heat generation. He modified the later system [119] to get rid of this assumption and to consider resistance to gyroscopic slippage at both raceways, simple drag forces, inertia forces and three-dimensional ball motion with precession, pitch and yaw angles. Above all, Harris implemented EHD lubrication by considering the film thickness of an isothermal Newtonian lubricant.

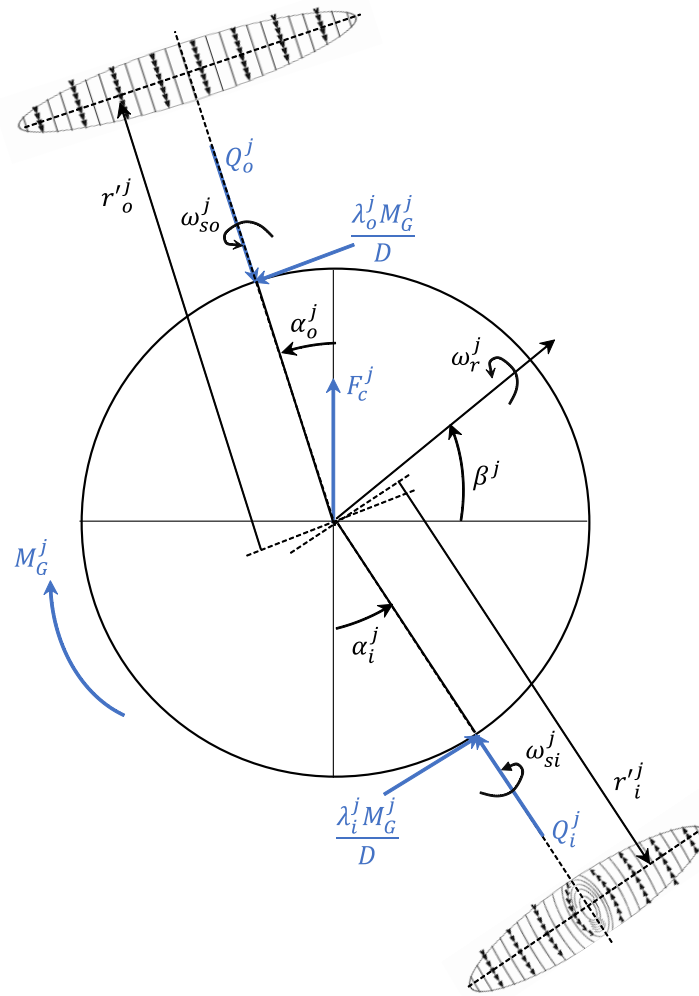


Figure 1.2 : Bearing kinematic parameters

Such study gave results closer to experiments and confirmed that RCH does not hold under certain operating conditions, particularly under EHD lubrication or when traction coefficient is not high enough to prevent gyroscopic slip. Mauriello [178] also developed a general model that only considers 5-DOF on balls in order to avoid the use of raceway control hypothesis. Retainer is also introduced with corresponding normal and traction forces, but without ball-to-retainer impacts since same orbital speed is assumed. With this method, RCH is verified under low axial-loads where skidding occurs, but it appears to be less correct for higher thrust loads.

In 1973, Hamrock and Anderson developed a simplified thrust loaded arched outer-race ball bearing model (ARBB) [111] which was mainly based on geometrical considerations. It was the first model dedicated to an ARBB, here with three contact points. Later, Hamrock [110] improved this model by following Jones' theory [144] and by considering gyroscopic moments and sliding friction. These modifications have shown that the amount of spinning on the outer race of arched bearing is an order of magnitude greater than conventional ones. To get the initial conditions for its dynamic resolution, Gupta [87],

[88], [89], [90] also developed a quasi-static model without cage but particularly complete with consideration of centrifugal forces, EHD lubrication and thermal effects. If gyroscopic momentums were not considered and if Jones RCH [144] was made, these assumptions were abandoned later in dynamics.

1.1.2 Quasi-dynamic

First ACBB quasi-dynamic models date back to the 1970's with Boness [23], Poplawski [206] or Rumbarger [220] for roller bearings that especially focused on lubrication, thermal effects and cage slip. Regarding ball bearings, Harris and Mindel [123] pursued Harris' quasi-static model [119]. They considered cage-to-pocket normal and friction forces and cage-ring normal forces or cage rail-to-raceway HD friction forces, depending on cage riding type and interaction intensity. Crecelius developed SHABERTH code [46] on the same principle but with a different parametrisation of orthoradial ball-to-pocket displacements, and a different method to compute ball-to-pocket and cage-ring interactions depending if dry, HD or EHD contacts are present. A thermal resolution was also introduced. Gentle and Boness [25], [77] set up an EHL traction formulation in a quasi-dynamic DGBB and ACBB model in order to understand more accurately ball bearing kinematics and skidding motion. Dominy [59] also developed a simplified dynamical model that focuses on cage motion, friction forces (drag), traction forces and spinning power to investigate the nature and causes of slip in lightly loaded BB under axial load. As well, to compute ACBB frictional losses and evaluate silicon nitride BB, Aramaki [6] and Shoda [238] reused Harris and Mindel's [123] approach. They added modifications such as different cage interactions formulations or the implementation of centrifugal and thermal expansions. In all of these quasi-dynamic models one of the most important issue was to represent accurately cage motion, traction forces, lubrication with thermal effects and to ensure numerical continuity while contact changes.

1.2 Lubrication modeling

1.2.1 Film thickness

At the beginning, bearing models considered dry contacts by neglecting film thickness. Ertel [67] and Grubin [82] were the first one to introduce a formulation of film thickness for a stationary line contact, as a function of relative speeds, load and lubricant parameters. Later, Dowson and Higginson [62] also proposed an isothermal EHD lubricant film thickness for a line contact. Boness [23] used this theory to model fully lubricated roller bearings and showed that a reduction in oil supply decreases cage slip significantly. Harris [119] also modelled EHD lubricated ACBB under purely axial load, but he assumed that all balls presented same film thickness and rolling speed. Then, Poplawski [206] developed a model for full film lubricated rolling bearings under axial and radial loads. It differentiates each roller parameters (load, speed, film thickness) and considers cage friction and drag forces (pushing, unbalance and churning effects) in order to study their influence on skidding. This work marked the beginning of the bearing code COBRA that has now become a reference among bearing computation codes. In 1967, in order to consider film thickness reduction due to temperature, Cheng [40], [41] introduced a coefficient on Dowson's formulation to include thermal effects and side leakage. Rumbarger [220] con-

sidered this improvement with Poplawski's [206] novelties in its rolling bearing model. He also computed drag torque on rolling elements, thermal and centrifugal expansions and conducted a thermal analysis. Always based on Dowson's study, Allen, Townsend and Zaretsky [2], [3], [4] developed an EHD theory with a new lubricant rheological model to predict spinning friction in non-conforming grooves. They introduced it into a fully lubricated ACBB model [246] that considers friction torque due to spinning, rolling resistance, drag and material hysteresis.

Later, Hamrock and Dowson [112], [113], [114], [115], [116] proposed film thickness expressions for circular and elliptical EHL contact either fully lubricated or starved. This formulation relies on three parameters on material, speed and load. This theory is today the reference for film thickness computation. Other authors proposed similar formulas as Chittenden [42] for punctual contacts or Archard and Cowking [8] for elliptic contacts. Moes and Venner [248] also introduced solutions for line contact and 2D circular contact problems with a set of two parameters that regroups Hamrock and Dowson parameters. Nijenbanning [191] extended this model to elliptic contact by introducing an ellipticity parameter. All of these models present the advantage to propose a single and continuous solution to represent the EHL film thickness under any lubrication regime (rigid isoviscous, elastic isoviscous, rigid piezoviscous or elastic piezoviscous).

To compute correctly these EHD film thicknesses, it is essential to consider lubricant rheology and properties under high pressure and temperature [250]. First rheological parameter to compute is dynamic viscosity μ , the simplest expression was given by Barus' [17] where μ is an exponential function of pressure. Gupta [103] modified it to consider temperature. However, this law is very inaccurate under high pressure. Then, Roelands [219] proposed a law for mineral or synthetic lubricants. Prat [209] also developed a power law, however it does not account for temperature and it is not suitable under very high pressure. Finally, an appropriate model for aeroengine lubricants is the modified W.L.F for William, Landel and Ferry model [250] resulting from Winer's previous work [275]. It is based on free volume dependence on temperature and pressure. Another parameter essential to compute film thickness is α^* , the reciprocal asymptotic isoviscous pressure as explained by Bair [12] and expressed by Blok [21].

1.2.2 Traction forces

Traction forces are computed by integration of shear stress or traction coefficient over the ellipse of contact between two bodies. Different models exist to express traction coefficient as a function of the slip velocity between two bodies. They can be divided into three types such as presented in Table 1.1. The first one, expressed in Eq. (1.2), is simplified and consists in a Newtonian behaviour with linear evolution of traction coefficient with slip at low sliding and a constant traction coefficient otherwise. Another traction model was proposed by Kragelskii [154] to represent more accurately traction variation with slip. In Eq. (1.3), coefficients A , B , C and D are empirical constants derived from experimental traction tests. Gupta [92], [103] with DREB (Dynamics of Roller Element Bearing) or Crecelius [46] with SHABERTH code were among the first to promote such EHL semi-empirical traction model. They implemented them in their computer code and considered lubricant drag forces and churning moments due to ball motion in surrounding lubricant. Then, they underlined the need to consider EHL lubrication, traction and both cage and thermal effects to investigate bearing motion and particularly skidding.

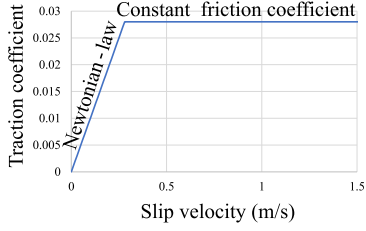
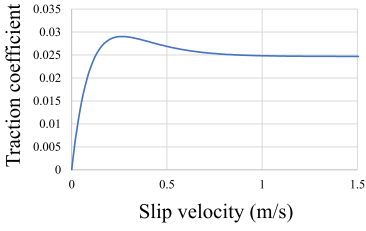
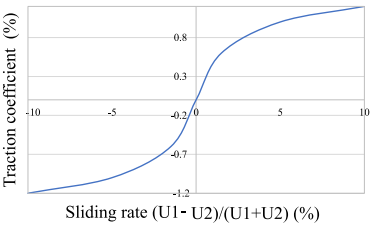
Simple-type	Kragelskii-type	Maxwell-type
		
$\begin{cases} \tau = \frac{\eta \Delta u}{h}, \text{ if } u < u_L \\ \tau = \tau_L \text{ if } u \geq u_L \end{cases} \quad (1.2)$	$\tau = (A + B \Delta u) e^{-C \Delta u} + D \quad (1.3)$	$\begin{aligned} \vec{\gamma} &= \vec{\gamma}_E + \vec{\gamma}_V \\ &= \frac{\vec{\tau}}{G} + \frac{\vec{\tau}}{\ \vec{\tau}\ } \frac{\tau_{ref}}{\mu} F\left(\frac{\ \vec{\tau}\ }{\tau_{ref}}\right) \end{aligned} \quad (1.4)$

Table 1.1 : Traction coefficient expressions

Because of inaccuracy in previous EHD traction lubricant models, Gentle and Boness [25], [77] developed their own model for DGBB and ACBB. They formulated an expression of traction forces as a function of pressure, S/R ratio and lubricant coefficients determined experimentally. They also understood the need to add an elastic force that acts when lubricant is not too viscous and that is proportional to shear modulus and inversely proportional to film thickness. Then, such model anticipated the need of a Maxwell-type one. Results were very close to experiment and showed the importance of EHD traction modelling. This model also enabled to understand better ball bearing kinematics and particularly skidding motion.

Subsequently, a complex Maxwell type traction model [190] was developed, as formulated in (1.4). It express shear rate $\dot{\gamma}$ by summing an elastic part ($\dot{\gamma}_E$) with a viscous component ($\dot{\gamma}_V$) developed by Johnson and Tevaarwerk [143]. For a Newtonian fluid, i.e., for low shear stress, the shear behaviour is linear, only made of the elastic component ($\dot{\gamma}_E$). On the contrary, for a non-Newtonian fluid, or for high shear stress, different non-linear forms F of the viscous term have been proposed by Ree and Eyring [217], [218], Bair and Winer [14], [15], Gecim and Winer [76] or by Elsharkawy and Hamrock [66]. Such shear rates can be defined in two directions according to sliding motion. Note also that, depending on the model, reference shear stress τ_{ref} becomes characteristic stress τ_o or limiting shear stress τ_L . As well, shear stress τ and shear modulus G are pressure and temperature dependant as expressed by Gupta [101]. Thereafter, this Maxwell traction model was widely used. For example, Chittenden [43] employed it with Gecim and Winer shear stress formulation [76] to compute rolling, sliding and spinning power losses in an EHD lubricated ball bearing in dynamics. Nélías [186] also used this Maxwell traction model with Ree-Eyring shear stress formulation [217], [218], to compute quasi-static motion of a ball bearing submitted to axial and radial loads. Features of Nélías' model are the consideration of EHD lubrication and a planar cage with cage-ring interaction represented by HD short journal bearing theory and ball-to-pocket interactions by barrel-plan theory in one direction and short journal bearing in another direction. Such model shows

good correlation with experimental results, it especially appears that ball-ring sliding motion increases by decreasing axial or radial loads [188]. Later, this model was reused to compute and locate power losses due to friction forces and sliding speeds in an ACBB [189]. Such study proves the important role of cage-slip, rotational shaft speed and oil flow in power losses.

We should precise that there does not only exists these three types of traction models, but they are the most frequently used for ACBB modelling. For more details, in Tables A.1 to A.6, for each ACBB model presented in this review, we have associated the corresponding traction model used at ball-race interaction. But in any case, analytical traction models developed are always based on the same principle that is to say that they depend on sliding, temperature and contact pressure. They are always based on experimental results because lubricant coefficients are needed. This is particularly a limit raised by Gupta [99] because traction experiments require specialized test rigs and the amount of lubricant traction data available is few, especially for solid lubricants. Then a limited amount of lubricant can be modelled in traction.

1.2.3 Thermal effects

If film thicknesses presented previously were isothermal, for high rolling or sliding velocities, energy is dissipated by shearing, then lubricant temperature increases which decreases oil viscosity and film thickness. That is why a thermal reduction factor ϕ_T was first introduced by Cheng [40], then modified by Wilson, Sheu and Murch [185], [269] and finally improved by Gupta [101]. Such coefficient is a function of contact pressure and surfaces velocities. Another formulation of thermal reduction factor ϕ_T adapted to linear contact was also introduced by Hsu and Lee [135].

As well, thermal effects can be considered in shear stress computation on the basis of Johnson and Tevaarwerk work [143], [243] improved by Houpert [132], [133], [127], [126]. As for that, Maxwell shear rate equation is coupled with an energy equation integrated along the film thickness and with an equation giving temperature rise along contact surface. To solve this system Houpert [126] proposed fast and accurate procedures for nonlinear viscoelastic sliding traction force in one or two directions. In this model, it is confirmed that elastic effects are needed to compute lateral traction forces when spin occurs in ACBB.

Let's note again that DREB [92], [103] and SHABERTH codes [46] were pioneers in bearings thermal modelling. Especially, Gupta solved three thermal equations on shear rate to compute EHL thermal lubrication and Crecelius solved an entire system of heat transfer equations to map temperatures over the bearing. Later, Poplawski [207] adapted SHABERTH into SHABHYB for hybrid ACBB with grease oil. As for that, ball-race contact model was adapted, thermal and lubrication models were modified after benchmarking and experimental measuring and skidding criteria were improved to include a peak traction coefficient at ball/race contacts. RBL4 code designed by Legrand [159] is another example of quasi-static ACBB model that considers accurately thermal lubricant effects. It considers arched-races with two, three or four contact points, centrifugal forces, gyroscopic moments, normal and tangential forces, spinning, rolling, sliding motions, tangential elastic deformations and thermal effects in EHD film thickness and in lubricant shearing computation but with a procedure a bit different than Houpert's [126].

Authors	Criterion	Parameters
Jones [145] Poplawski and Mauriello [208]	$0.06 > \frac{2M_{GY}}{QD} \quad (1.5)$	M_{GY} : Gyroscopic momentum Q : Ball-race contact load D : Ball diameter
Hirano [124]	$\frac{NF_c}{Q_a} > 0.1 \quad (1.6)$	N : Number of balls F_c : Centrifugal force on a ball Q_a : Thrust load acting on the bearing
Kliman [153]	$\frac{NF_c}{Q_a} > \cos(\alpha_o - \alpha_i) \quad (1.7)$	α_o, α_i : Outer and inner ring contact angles
Boness [24]	$\sigma_{max} = 0.00733(N_i^2 d_m)^{0.22} (d_m N \eta)^{-0.175} GPa \quad (1.8)$	N_i : Shaft speed (rev/min) d_m : Mean diameter (mm) η : Lubricant viscosity (Pa.s)

Table 1.2 : Relations that implies ball skidding

1.3 Skidding issues

High speed ACBB are subjected to skidding which is gross sliding motion at ball-inner race contact that creates important surface shear stresses and unstable cage speed. It also increases lubricant and bearing temperatures, accelerates wear and reduces bearing life and reliability. It occurs when applied load is too low to develop sufficient EHD tractive force to overcome cage drag, then slips occur at the contact. As well, forces are not enough to prevent gyroscopic spin that is to say to keep the ball rotational axis aligned with rolling axis, then spinning motion also contributes to skidding.

1.3.1 Skidding criteria

For thrust loaded bearings, several authors developed criteria to evaluate the threshold over which skidding occurs. The four majors ones are summarised in Table 1.2. Based on raceway control hypothesis, Jones [145] proposed equation (1.5) on gyroscopic momentum at the controlling ball-race contact. Poplawski and Mauriello [208] extended it for distributed gyroscopic effects at inner and outer race contacts. Hirano [124], based on axially loaded ACBB experiences, underlined that skidding occurred when relation (1.6) was satisfied. Kliman proposed the similar expression (1.7), but different in amplitude, that suggests that skidding can be limited by minimizing the difference between inner and outer ring contact angles. From his previous model [25], Boness [24] ran several computations for different bearing characteristics, lubricants and operating conditions to establish the empirical equation (1.8). It relates maximum Hertzian pressure at inner race contact that predicts minimum thrust load over which skidding does not occur. Nevertheless, many parameters are involved in skidding, then these criterion are not sufficient to estimate its occurrence. As a consequence, more refined models were developed in order to investigate qualitatively skidding in details.

1.3.2 Parameters to limit skidding

Harris [119] is considered as a pioneer in investigating skidding in quasi-static models, especially with lubrication and without raceway control hypothesis. However, first ACBB skidding models were only considering thrust external load and constant contact angles over the bearing. Liao and Lin [163] developed a different parametrization than Jones to compute contact forces and angles by assuming that osculation of inner and outer raceways was the same and that inner ring displacements were known. This study proved that contact angle variation is not influenced by axial but only by radial load. Increasing this load increases maximum contact load for balls located near the application point, but decreases those of balls at the opposite side. Bearings submitted to combined load also experiences ball slip at ball-race contact. Subsequently, to differentiate inner and outer ring contact angles, authors added centrifugal forces [164] but assumed the same one for every ball. Results analysis shows that increasing ω_c , increases inner-race contact angles α_i , decreases outer-race contact angles α_o , and that maximal α_i and minimal α_o are located at the opposite of the radial load application point. Above all, this study shows that limiting cage rotational speed ω_c is the first criterion to apply to reduce skidding. Increasing axial load can be another solution. Skidding is inevitable when combining axial and radial deformations. However, for a given cage rotational speed, depending on these deformations, the authors found refined functions defining skidding threshold. Later, they also added misalignment [165] and validated the model by a comparison with Jones' model. They proved its computational time improvement, its efficiency and showed that increasing angular misalignment lowered axial and radial load capacities. They also took over the model without misalignment [164] to add thermal effects. As for that, they implemented Hamrock Dowson film thickness and traction forces due to frictional heat created by shear stress formulated by Kannel and Walowit relation [149]. With this thermal model [166], sliding velocities and friction forces at ball-to-inner race contact are increased. Wang [256] also continued the isothermal model [164] and considered different centrifugal force and gyroscopic moment for each ball for an ACBB under combined radial, axial and moment loads. To improve skidding prediction, Yoshida [278] added in Jones' theory, one equation on cage with cage-race HD interactions. He also represented fluid as non-Newtonian with Eyring theory [217], [218]. He solved energy equations to compute ball-race film thickness, ball, inner and outer ring temperatures in order to estimate the temperature rise induced by ball slip. As well, Xu [271] used Harris' [119] and Jones' theory and Hirano's criterion [124] to estimate the optimum preload to limit skidding and heat generation for given bearing parameters and running speed in a high-speed ACBB.

In 2018, Oktaviana [199] used De Mul's model [56] and Hirano's criterion [124] to evaluate the influence of external loading, rotational speed and angular misalignment on bearing skidding. They observed that under purely axial load, increasing misalignment increases skidding. However, for given bearing conditions, it exists an optimal misalignment angle to avoid skidding. For bearing submitted to axial and radial loads, increasing misalignment will develop two skidding regions instead of one. And, increasing radial load will increase these areas. Besides, the initial contact angle does not influence skidding for axially loaded bearings whereas for bearings under combined loads, increasing this angle will enlarge skidding area.

	Outer Race Control (ORC)	Inner Race Control (IRC)	Equal distribution	Hybrid theory
λ_i	0	2	1	$\tan \beta = \frac{\frac{2C}{1+C} \cdot \frac{2}{1+C} \cdot \frac{C(S+1) \sin \alpha_i + 2 \sin \alpha_o}{C(S+1) \cos \alpha_i + 2(\cos \alpha_o + \gamma) + A}}{C(S+1) \cos \alpha_i + 2(\cos \alpha_o + \gamma) + A}$
λ_o	2	0	1	
β	$\tan \beta = \frac{e \sin \alpha_o}{e \cos \alpha_o + r_o}$	$\tan \beta = \frac{e \sin \alpha_i}{e \cos \alpha_i - r_i'}$	$\beta = \frac{\alpha_o + \alpha_i}{2}$	
				with $\begin{cases} C = \frac{Q_i a_i L_i}{Q_o a_o L_o} \\ A = \gamma C [\cos(\alpha_i - \alpha_o) - S] \\ S = \frac{1 + \gamma \cos \alpha_o}{1 - \cos \alpha_i} \end{cases}$

Table 1.3 : Raceway control hypothesis

1.4 Models without raceway control hypothesis

RCH has been widely used in literature, however under specific operating conditions such assumption does not hold. That is why many recent studies interested in ways to get rid of it.

1.4.1 Geometric assumption

One of the most simplified method is to use the geometric hypothesis that considers equal gyroscopic moment distribution between inner and outer race ($\lambda_i = \lambda_o = 1$), then pitch angle is the mean of contact angles and S/R ratio are equal on both races.

1.4.2 Hybrid theory

Another method based on d'Alembert's principle was established by Changan [35] to compute yaw angle as a function of kinematic parameters and loads. Corresponding formulas are summarized in Table 1.3. Advantage of this hybrid theory is that, contrary to discrete RCH, it considers a continuous gyroscopic moment distribution between races. Like most theories, it assumes an equal coefficient of friction between both races, as expressed in (1.9).

$$\mu^j = \frac{T_i^j}{Q_i^j} = \frac{T_o^j}{Q_o^j} \Leftrightarrow \lambda_i + \lambda_o = 2 \quad (1.9)$$

This hybrid theory has been reemployed by many searchers. For instance, Lei [160] compared Jones' model with a quasi-static planar ACBB model that couples Hybrid theory with an EHD lubrication model based on a semi-empirical friction coefficient. As well, Noel [195] investigated the influence of kinematic hypothesis on gyroscopic moments and stiffness matrix. Like Harris, they observed that ORC applies for high-speed and light loaded bearings. Hybrid theory is suitable under these conditions, but also under higher loads. Geometric hypothesis is less correct than hybrid one, but easier to implement and provide good results for significantly loaded bearings. Wang [257] and Zhang [280],[283] also used hybrid hypothesis for ACBB under combined axial, radial and momentum loads.

It appears that radial load causes contact angles variation over the bearing and uneven load distribution. However, the use of a proper momentum can compensate it and improve load distribution and service characteristics under combined load. On the contrary, misalignment reduces bearing performances under pure axial load. Rabréau [214] also coupled a thermal FE model with a kinematic model with either Hybrid or Jones' model to investigate their influence on internal kinematics and frictional torque. Recently, Liu [167] developed an optimised algorithm that uses Hybrid theory to study the effects of elastic modulus, ball diameter, radial clearance, rotational speed and ring angular misalignment on time-varying stiffness matrix.

1.4.3 Contact friction minimisation

Another approach is to focus on contact friction minimization. For instance, Dusserre and Nélías [64] have shown that bearing components were working such that spinning power losses between inner and outer races were minimal. Then, pitch angle β is equal to IRC pitch angle β_i when operating under low speeds and high loads, it is equal to ORC pitch angle β_o for high speeds and light-loads and it is distributed between those angles otherwise. As well, Foord [71] replaced RCH by a minimisation of the total contact friction power. It enables to compute accurate kinematics for any load or speed condition. The only limit occurs when axial and radial loads are of a similar magnitude. To compute EHD traction model in quasi-static, Gupta proposed first [98] to replace RCH by a constraint that minimises frictional energy due to rolling element-inner and outer races slip with respect to pitch angle. Later, improvements [100] gave realistic rolling and slipping motions at ball-race contacts, with an efficient friction simulation much closer to dynamical results than RCH.

1.4.4 Ball torque equilibrium

For ACBB with tractive lubricant in aircraft gas turbine engines, especially under high speed and temperature operating conditions, Chapman [36] has led an experimental study that proves that RCH is inadequate to compute ball axis attitude angle and ball rotational speed. Then, he proposed to compute β by a moment balance calculation. For rings with same conformity, it appears that β is shared between IRC and ORC for low speed whereas β is a bit smaller than β_{ORC} at high speed. In a similar way, Brecher [28] iterated on ball pitch and yaw angles and ball and cage rotational velocities to access ball torque equilibrium. Contrary to most models, friction coefficient is not based on usual EHL theory but is expressed by an empirical relation that applies locally at each contact and determined from experiments. Likewise, Bozet and Servais [27] developed a quasi-static, axially loaded, dry lubricated, ball bearing model to compute the pitch angle without RCH but by ball equilibrium resolution and by neglecting yaw angle. Significant differences have been observed compared with traditional RCH models, especially in terms of power losses. Later, they considered transverse loads T_i^j and T_o^j due to gyroscopic torques [232]. Contrary to other models, they did not impose prescribed values on T_i^j and T_o^j but they iterated on λ_i^j and λ_o^j through a process that consists in studying in detail ball kinematics (transverse slip speed fields) to equilibrate transverse torque then transverse load and ball spin attitude. Results have shown the strong influence of bearing rotational speed and ball spin attitude angle on the transverse loads. Leblanc and Nélías [157], [158]

interested in ACBB with 2, 3 or 4 contact points and computed pitch and yaw angles without any assumption but by a resolution of ball equilibrium equations. They showed that raceway control hypothesis is less correct when more than two contact-points are present. This model also enables to better understand arched bearing kinematics and particularly the fact that getting two contact points on a race distributes loads but also increases sliding and spinning motions. Then, it enhances friction power losses, surface friction shear stresses, pressure-velocity product, so surface temperatures. However, drain holes can be designed on arched races to improve lubricant flow, to reduce oil churning and to compensate friction power losses.

1.4.5 Rolling contact analysis

Chen [38], [39] used rolling contact theory, a new differential slip model and linked creepage with slip and spin ratio to determine precisely ball and raceway relative motions without making RCH or any assumption on traction forces. Such developed model enables to represent more accurately ball kinematics (friction, traction, sliding and spinning at ball-race contacts).

1.5 Other areas explored

Based on Jones' and Harris' [119] theory, many ACBB quasi-static models could be developed, each one presenting its advantages depending on application field. For example, de Mul [56] developed a highly modular, systematic and complete system to compute equilibrium, loads and bearing stiffness analytically for any kind of bearing. To model a coupled spindle-bearing system made of spindle shaft, ACBB and housing, Jorgensen [146] reused de Mul's theory, whereas Cao [34] or Shin [237] used Jones' analysis directly. Both of them solved ACBB quasi-static problem and computed stiffness matrix to introduce it into a dynamic spindle system. Shin has especially shown the influence of speed variation on the decrease of bearing stiffness and natural frequencies that impacts the prediction of stability lobes. Ignacio Amasorrain [136] proposed a procedure to compute load distribution, ball-race contact parameters and ring motion in a four contact-point slewing bearing under axial, radial and moment load working at low speeds. Jedrzejewski and Kwasny [141] also developed an ACBB model for high-speed spindle bearing with moving sleeves in order to forecast moving sleeve position depending on bearing kinematical operating conditions. Brecher [29] also proposed a very simplified procedure to compute cage friction in spindle bearings. He considers a constant cage-to-outer race contact and a unique ball-to-pocket contact with normal forces and Coulomb's friction forces. Thermal and centrifugal expansion of cage and outer ring are also implemented to estimate the effects of radial clearance on cage friction. For thrust loaded ACBB, Antoine [5] proposed a precise and quick tool to compute explicitly inner and outer ring contact angles depending on preload and rotational speed. Chunjiang [45] investigated the influence of axial load and rotational speed on ball-race contact angles, normal forces, centrifugal forces, gyroscopic torque and coefficient of friction with their own quasi-static model of thrust loaded ACBB. Zeng [279] also proposed a novel calculation method to improve non-linear quasi-static resolution. As for that, recursive relations are found to reduce the number of unknowns, a new initialization method is used and an improved

artificial bee colony algorithm is developed to improve solutions accuracy, computational time and reliability in solving large root difference problems.

Many studies also interested in computing ACBB running torque that is to say the moment required to sustain a constant rotational speed. It is directly related to power losses, heat generation and bearing efficiency. For example, Houpert [128] proposed expressions to compute hydrodynamic rolling forces, elastic rolling moments and friction moments due to curvature effects and pivoting at ball-race contacts. Then, he obtained sliding forces by ball equilibrium. Finally, he derived the running torque on the bearing by summing all forces and moments around rotational axis. Joshi [147] also computed bearing running torque of an ACBB with 2 or 4 contact points under high load and slow speed. As for that, they simplified Leblanc and Nélias' model [157] by neglecting centrifugal forces and gyroscopic moments. Tong and Hong [245] also proposed new formulations for EHL rolling resistance and spinning friction, and considered elastic hysteresis friction, differential sliding losses and lubricant viscous drag. Later, this model was coupled with de Mul's one [56] and gyroscopic effects were added in order to study the effects of angular misalignment on the running torque of ACBBs under different preloads [244]. In all these running torque studies, particular attention has been paid to model friction coefficient. As well, they all concluded that hydrodynamic rolling forces and spinning friction were the main components responsible for running torque.

Regarding quasi-dynamics, Yan [272] developed a model that computes balls, rings, and planar cage motion combined with heat transfers through a heat-flux method. They investigated oil-air flow, lubrication and thermal ball bearing performances depending on pocket shape (spherical or cylindrical), cage guiding type, cage guiding clearance and pocket clearance. Similarly, Yang [273] developed another planar cage quasi-dynamic model coupled with a convective heat transfer system. They studied the influence of cage guiding clearance and pocket hole clearance on high-speed ACBB heating characteristics. On the same principle, Wen [265] developed a quasi-dynamic planar cage model for high-speed micro ball bearing. It appears that angular misalignment significantly modifies ball-race contact load, contact angle, spinning and skidding velocity variations over a cycle. Under axial load, angular misalignment increases bearing power losses, decreases fatigue life, whereas for combined loads, depending on misalignment direction and amplitude it can either improve or alter power losses and fatigue life. We should note that contrary to traditional models, SHABERTH code [46] or these last quasi-dynamic models do not neglect ball-to-pocket orthoradial displacements due to radial load or misalignment. They also usually consider ball rotation velocities (ω_m^j , ω_x^j , ω_y^j , ω_z^j) as unknowns instead of ball self-rotations (pitch β^j and yaw β'^j angles) and effective rolling radius $r_i'^j$, $r_o'^j$.

Wang [255] and Cui [51] also developed READ (Rolling Element Bearing Advanced Dynamics), a 3D quasi-dynamic model for aero-engine ball bearings. For high-speed and heavy-load ACBB, Shi [236] reused Cui's [51] model with consideration of spinning, sliding and rolling motions. At ball-race contact, they solved EHL problem by multi-grid method in parallel with thermal equations. Results show that full film lubrication occurs under normal operating conditions whereas poor lubrication occurs when the bearing slow down, start-up or shut-down. That is why they extended this coupled quasi-dynamic/TEHL model to mixed lubrication regime [235]. As for that, continuous Reynolds equations, film thickness equations and film energy equations are considered whether the contact is under EHL or boundary lubrication. Similarly, Wu [270] coupled mixed lubrication

with Wang's model [255] in order to investigate the effects of rotational velocity, inner raceway curvature coefficient or initial contact angle on bearing behaviour under mixed lubrication. Li [162] also implemented on Wang's model [255], curve fitted relationships of traction coefficient obtained from experimental studies on aviation lubricating oil. Results especially show that ball-race traction force and relative sliding speeds causes a greater increase of outer race temperature than inner race one. Cui [52] recently reused its quasi-dynamic model and coupled it with a thermal model based on moving heat source method. Minimum load to prevent skidding, maximal load to prevent overheating and maximal speed to avoid both of them were evaluated depending on operating conditions such as rotational speed, axial, radial loads, oil or grease lubrication, ceramic or steel balls.

2 Time dependent models

Dynamic models consider time-dependant accelerations of bearing components. Usually, quasi-static or quasi-dynamic solutions are used to initialise such dynamical problems. Systems of equations are solved with a time step numerical scheme, like fourth order Runge Kutta (RK4), which can be time consuming [91]. Consequently, dynamic developments were made possible by constant improvements of computer machines performances. And, with the increasing of high-speeds, loads and temperatures in ball bearings, searchers had to further interest in these time dependant models. But, one of the most important issue in dynamic modelling is the investigation of cage motion and stability. Indeed, the cage is a critical component in bearings and can be subject to defective operation, excessive wear or failure. Difficulties in setting up experimental studies in dynamics due to the requirement of sophisticated instrumentation and measurement systems, also explains the need for analytical models development.

2.1 Bases on cage dynamical motion

Kingsbury [65] conducted an experimental study and brought solid bases to understand cage dynamical motion. He measured cage orbital velocity about its mass center, cage mass center angular velocity, races speeds and bearing torque. Then, as schematized in Figure 1.3, he observed a whirling motion which is a very fast translation of the center of mass of the retainer in a rotational motion around the bearing center. When whirl velocity $\dot{\alpha}$ and whirl radius r_w are constant over time, a pure tone at a particular pitch angle can be heard, this phenomenon is called pure whirl. On the contrary, if whirl velocity and whirl radius vary irregularly in an erratic motion, large changes in bearing torque are observed, a noisy irregular sound can be heard also called squeal. These cage center motions are illustrated in Figure 1.4. Besides, if whirl velocity is equal to bearing angular velocity, bearing torque is unchanged, this is synchronous whirl. When whirl velocity is equal to ball group velocity the mode is stable with a uniform torque, otherwise a ball jump mode is observed with a sinusoidal torque variation. Later, Kingsbury and Walker [152] further investigated bearing instabilities and confirmed that during squeal, a high-frequency retainer motion is superimposed to the retainer ball group rotation rate. As well, whirl is driven by friction and ball-to-pocket geometry, then squeal can be limited by an asymmetric ball distribution, by adding oil lubricant or by reducing applied axial load to limit ball-race traction. He also observed that whirl frequency is approximately

proportional to ball spin rate and that for inner-race guided cage, whirl velocity is in the same direction as retainer rotational speed whereas it is in the opposite direction for outer-race guidance. We should also note that squeal instabilities do not obviously lead to important damages. Thereafter, a stable cage motion will be defined by a constant whirl speed (equal to cage rotational speed), a regular whirl orbit and a constant whirl radius.

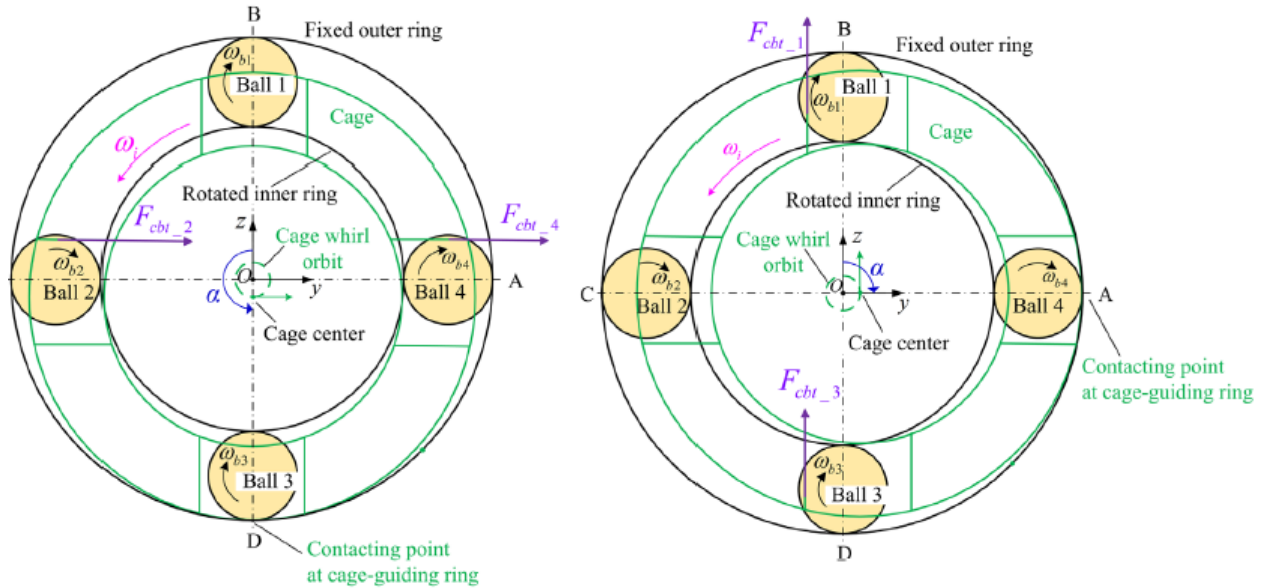


Figure 1.3 : Kingsbury's model for cage whirl motion at initial position and at 90° , schematized by Niu [194]

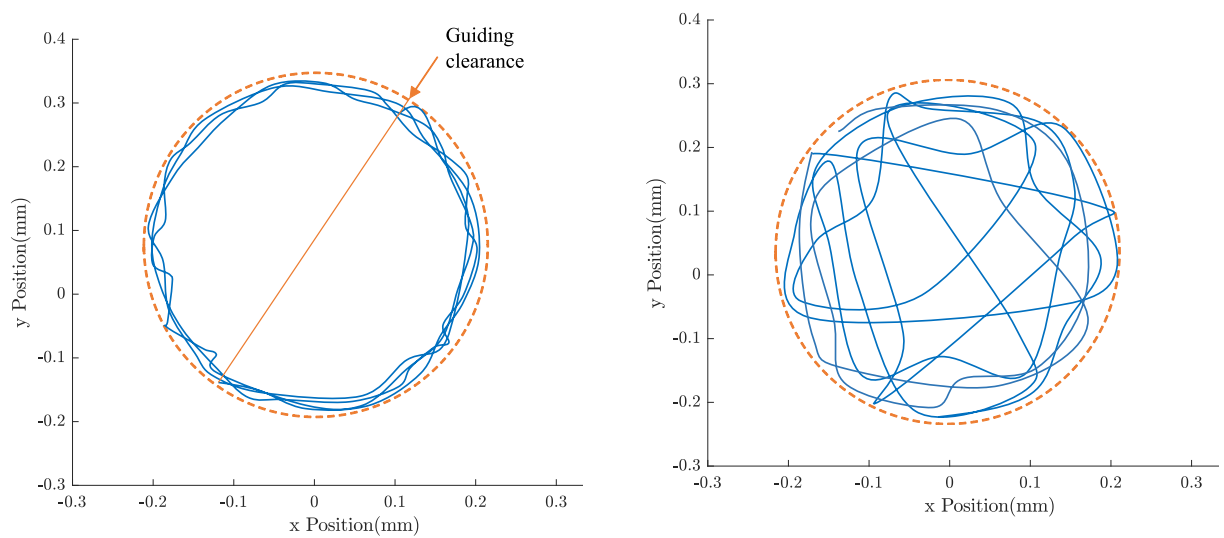


Figure 1.4 : Cage center of mass motion under stable whirl and squeal

2.2 Dynamical reference models

The first analytical dynamic model was designed by Walters [253] with the code BASDAP which is a Ball And Separator Dynamic Analysis for ball bearings. It considers 4-DOF for balls and 6-DOF for separator and solves Jones' ball/race elasticity problem independently to dynamic analysis. Particular attention was also paid to compute ball-to-races, ball-to-separator and separator-to-races normal and traction forces depending on lubrication and component positions. Especially, when a ball contacts the separator, Walters imposed a constraint such that the normal ball and separator velocities are equal at the contact point. Then, separator motion relative to ball motion was observed and especially orbital speeds like whirling. Later, Kannel and Bupara [148] programmed BASDAP II that simplifies cage motion in a plan, but considers ball-to-pocket impacts with traction, normal spring and damping effects depending on EHD lubrication. Ball-cage bouncing and ball sliding over the film results in cage-race energy dissipation. Results align with Kingsbury's observations and showed that stable motion highly depends on lubricant since it is enhanced by low ball-to-pocket friction coefficient, low lubricant viscosity or low film thickness that affect damping.

In the 1970's, Gupta developed BDYN (Bearing DYNamic) and DREB (Dynamics of Rolling Element Bearings) [89], [90] considering all bearing dynamical elements with hydrodynamic or dry interactions. Later, with RAPIDREB and ADORE (Advanced Dynamics of Rolling Element Bearings) [91], Gupta improved lubrication models. Then, thermal effects were added, and today, ADORE still continues to be developed. An animated interface called AGORE (Animated Graphics of Rolling Elements) was also created to visualise bearing motion. While very complete as it considers any kind of bearing, all possible interactions, solid effects or defaults, ADORE limitation is that cage is assumed to be rigid even if it can be considered segmented between pockets. Also, only two contact points between balls and rings are considered, the system is solved in a fixed referential coordinate frame and is particularly time-consuming. This model enabled to observe typical ball bearing phenomenon and instabilities such as skidding or whirling. Extensive investigations on the effect of misalignment, squeeze-film, clearances, radial-to-axial load ratio or lubrication models on accelerations, contact and friction forces or power losses enabled to better understand bearing dynamics and to improve the model over the years. Especially, important achievements have been done on EHD traction, lubrication and thermal models that highly influence bearing behaviour.

In order to lead a parametric and optimisation study with a more cost effective code than ADORE, Meeks [181], [180] developed a SEPARATOR DYNamic program (SEPDYN) for ball bearing under axial load. The analytic problem is simplified with two dynamic equations for balls and six for the separator. To reduce resolution complexity, the system is solved in rotating coordinate frames instead of fixed inertial one. Different cage types are considered (ball or race-guided, with conical or cylindrical pockets). Results showed the influence of high friction and traction coefficients, of high separator-races and separator-pocket clearances on ball-to-pocket collision forces, wear energy dissipated, whirl and squeal frequencies. Later, the system was improved into BABERDYN [182] to consider radial load and misalignment, inertial effects, lubricant film, torque, heating and power dissipation.

Later, Boesiger [22] developed PADRE for Planar Analysis of a Dynamic Retainer that considers thrust loaded ball bearings with 2-DOF for balls without inertial effects.

Retainer interactions are precisely introduced, especially with the consideration of cage flexibility and asymmetric cages. A retainer instability investigation showed the whirl occurrence at a characteristic frequency and its sensitivity with ball-to-retainer friction increasing.

For the company SKF, Stacke [240], [239] designed BEAST, a very complete 3D BEARING Simulation Tool, that models the dynamic of all kind of bearing with any geometry, external load or lubricated conditions. It has proven its efficiency to solve industrial problems and to understand better cage motion and ball-to-pocket interactions around the bearing depending on loads applied.

2.3 Cage stability evaluation

All dynamical models are more or less the same, the only difference is the consideration or not of typical effects like inertia, external load and various interactions between balls, cage, races and lubricant. In these tables, unless stated otherwise, ball-race and ball-to-pocket normal forces are represented by Hertzian theory, ball-race friction forces by shear stress integration over contact surface for given traction and lubrication model. Cage-race interactions are represented by short journal bearing theory [73] if no contact occurs and sometimes usual normal and friction forces are also added if contact is considered. Regarding friction, pure sliding with high velocities occurs at ball-to-pocket and cage-race contact, then frictional behaviour is represented by a constant coefficient.

Gupta developed an important work to characterise factors influencing cage instabilities in solid lubricated ball and cylindrical bearings. First, he investigated the effect of friction [93] on ball and cage stability by studying ball-race sliding velocities, cage whirl orbit motion, velocity and time average wear rates of bearing elements for different Kragelskii-type or simplified traction curves. To minimise instabilities it appears that lubricant should present a limited traction slope at low slip rates for any interaction and a minimum negative slope at high slip velocities for ball-race traction. Then, he investigated the influence of cage unbalance [95], [102] on ACBB motion experimentally and numerically with ADORE. For both inner and outer-race guided cages, stable cage whirl occurs at any rotational speed. On the contrary, if cage unbalance increases under a certain level, cage interactions are more important, whirl radius increases and whirl velocity varies. With excessive unbalance, ball-cage collisions are also extended in time which worsen cage wear. Such behaviours are confirmed by power loss and time-averaged wear rates of cage which increase with unbalance. Besides, for inner race guided bearing, cage-race contact occurs at the opposite location of unbalance which increases cage wear then unbalance itself and instabilities. And, the severity of this interaction increases with rotational speed and unbalance. On the contrary, for outer race guided bearing, the contact occurs at the same location as the unbalance which limits this phenomenon, such bearing is “self-balanced”. In another parametric study, Gupta [97] has also shown that increasing ball-to-pocket clearance triggers instabilities at a certain threshold and that an optimal ratio of cage-race to ball-pocket clearances exists. And, if these conclusions only apply for the solid-lubricated bearing studied with given geometry, it clearly appears that correlations exist between cage clearances and stability. Besides, Gupta [96] investigated the influence of the type of load variation on ball-race contact load variation, whirl motion, ball-to-pocket contact amplitude and duration, then on the steady-state wear rate

of the cage. In terms of stability, contact severity, wear and risk of failure, results show that the stationary radial load is preferable than unbalanced load rotating with the shaft which is itself less critical than a radial load rotating at half the shaft speed.

Based on Discrete Element Method (DEM), Saheta [221] developed an efficient Dynamic Bearing Model (DBM) for ACBB and DGBB. 6-DOF are considered for each element represented with simple geometries and with dry contact interactions in order to save computational time. A parametric study was led and confirmed previous observations from Gupta [91] and Kingsbury [65] about the effects of rotational velocity and ball-race traction models on ball and cage motion. Especially, at high-speed, if increasing the slope of the traction curve reduces ball-race slipping, it increases fluctuations in cage whirl and radial velocities then motion is unstable. However, a symmetric distribution of balls around the bearing can limit such instabilities. This model also proves that cage velocities fluctuations are enhanced by ball-to-pocket friction coefficient increasing, that ball-race maximum stresses increases with race curvature, that reducing ball-race clearance reduces slip and maximum contact load whereas reducing ball-to-pocket clearance increases the region of slip at ball-inner race contact. Later, Ghaisas [79] replaced the simple traction model by a microslip model to consider the curvature of contact ellipse and the different slipping velocities on each slice of the surface. This consideration tends to increase ball angular velocity computed, especially on the loaded zone of the bearing. Lubricant effects are also implemented with drag forces computation and ball-to-pocket normal forces modified to consider the effect of EHD or PVR (piezoviscous rigid) film thickness on elastic deformation computation. DBM was also extended to cylindrical and tapered roller bearing with the consideration of new effects like churning, rolling friction or the computation of roller-race normal forces by slicing method. Based on DBM theory, Prenger [210] also modelled in three-dimension ACBB, DGBB and SRB dynamics on ADAMS software. Every element interaction is defined on subroutines with the possibility, at each contact, to consider dry or lubricated interaction to compute normal forces. Friction forces and momentums are also calculated with Kragelskii's traction coefficient along with spin-resisting moment on the ellipse of contact. Later, Dattawadkar [55] extended DBM to four contact point ACBB and confirmed the effectiveness of such bearings to support large axial and moment load.

Liu [169] also developed an ACBB dynamical model with only 3-DOF in translation for inner ring but with 3D cage. All possible interactions were taken into account with usual bearings theories. In particular, oil damping at ball-race contact is represented by Sarangi's [225] expression, whereas imperfect elastic contact is considered by material damping implementation at each possible contact. Cage motion analysis confirms that improving cage stability requires to increase inner ring rotational speed or applied load to limit skidding, to choose material with an important coefficient of restitution that enhances damping effects and to restrict the ratio of pocket clearance to guiding clearance below a value of 1 in order to avoid ball-to-pocket collisions then cage-race collisions. To investigate the effect of external load on cage stability, Ye [276], [277] developed a 4-DOF cage dynamical model with only normal and dry friction forces at each contact. Under steady state, analysis of whirl track, cage sliding-ratio and deviation ratio of cage whirl speed confirms that stability increases with axial load but decreases with radial load. On the contrary, during starting process, if radial load has little influence, axial load plays an opposite role on cage dynamics and enhances instabilities. Niu [194] has adopted

Gupta's BB dynamical model [89], [91] for an outer-race guided cage in order to deepen previous researches on cage stability. An extensive analyse of stable and unstable motion under skidding conditions shows precisely the involvement of ball-to-pocket normal and friction forces, of cage-race forces, of centrifugal forces and the role of combined load or spacing between balls in ensuring constant whirl radius and velocity. Zhang [281] studied the dynamical behaviour of ACBB for three lubricants presenting different viscosity and temperature resistance. Kragelskii's traction coefficients are determined experimentally and expressed as a function of lubricant temperature, entrainment speed and normal load. Analysis of cage's mass center motion, period of dynamic response and cage's slip ratio, under different temperature, axial or radial load, shows the influence of lubricant traction coefficient on cage dynamical characteristics and stability. Then, depending on working conditions an appropriate lubricant can be chosen. Using the same approach, Liu [172] investigated effects of lubricant type and temperature on skidding behaviour and ball-to-pocket impacts. It appears that increasing lubricant temperature reduces ball-race traction coefficient, especially in the radially loaded zone and under low axial load. As a consequence, sliding and spinning velocities increase, whereas ball-to-pocket contact forces decrease. Under high temperatures, increasing axial load is a solution to limit skidding and ball-to-pocket forces. As well, dynamic behaviour is different depending on lubricant viscosity-temperature coefficient, then on temperature resistance. That is why, according to operating temperature, the appropriate lubricant should be chosen. Later, balls, cage and shaft assembly gravity effects [171] were added in this model in order to compare bearing behaviour under microgravity and gravity. Analysis of skidding, impact forces and cage center orbital motion shows that stability is improved under microgravity whereas under gravity, traditional dynamical bearing problems gets worse with shaft assembly increasing.

Bovet [26] developed a non-planar dynamical model for BB submitted to high moment load, then to important cage-race impacts. That is why these interactions are accurately represented through a hybrid short journal model that considers the transition from hydrodynamic to metal-to-metal contact by boundary layer theory. An equivalent viscoelastic hinge joint is also present on the inner ring to represent shaft dependence, so inertia, damping and rigidity of the rest of the system. Results confirms the importance of these new features for moment load modelling. And, severe cage-race and ball-to-pocket impacts simulated under high moment load, corroborate with experimental observations. Wang [254] used Gupta's approach to investigate the effects of bearing parameters and working conditions on BB performances judged by different parameters such as contact angle, contact stiffness, edge angle and edge distance. One of the novelties is the consideration of time-varying contact stiffness. Nogi [196] also used Gupta's formalism to study the cage dynamical stability in a ball bearing submitted to purely axial load. Usual EHD theories are employed excepted for cage-race interaction where instead of short journal bearing HD theory, only physical contact is calculated with Palmgren formula for normal load and with a constant coefficient for friction forces. Ball-race damping is also considered to stabilise contact load fluctuation. Evolution of cage center orbital motion and whirl velocities with traction coefficient, bearing speed or balls separation confirms previous studies observations about cage stability, particularly Kingsbury's [152] one. The authors also postulated that cage instability occurs when cage friction coefficient is greater than a critical coefficient μ_c formulated as a function of cage mass, ball-race traction, cage

rotational velocity, ball-cage contact stiffness and number of balls.

Recently, for bearings working under radial clearance and dominant radial load, Razpotnik [216] found an efficient method to solve instability problems due to ball-race contact transitions. As for that, when contact deformation gets closer to zero, they proposed to replace this deformation by a smoothed expression which is a function of radial displacement. With such procedure, deformation, force and stiffness are continuous functions and continuously differentiable. Such model showed significant stability improvements and a reduction in computational time. And, even if it was applied in a vibrational study of shaft-bearing-housing assembly, it may be rapidly extended to dynamical ACBB studies with cage and lubrication. Yao [274] modelled four-contact points ball bearings on a multibody dynamic software. Hertzian contact, dry Coulomb friction and damping forces are defined at ball-race, ball-pocket and cage-ring contacts. Dynamical results show that under pure radial load there is always four-point contact at ball-race, whereas under combined loads there is four-point contact in the loaded zone and two in the non-loaded zone. Load distribution is also influenced by applied moment load. As well, with four-contact points there is always a pair of opposite contact-points that present major dynamic load and contact angle compared to a secondary pair of contact-points. Han [118] developed an ACBB planar dynamical model that considers cage unbalance forces. Results show that increasing cage mass unbalance improves cage center regular motion and increases whirl radii. On the contrary, cage unbalance has no effect on ball-to-pocket contact forces, but increases cage-guiding race forces which results in cage guiding surface wear.

2.4 Skidding issues in dynamics

Most skidding studies are in quasi-statics, they usually use kinematic assumptions and cannot be used to study the influence of time variation. Gupta [85], [86] conducted a dynamical skidding study that formulates in 3D the generalized equations of motion of a ball in a thrust loaded ACBB. Especially, EHD lubrication and three possible traction models were implemented. Results showed that ORC hypothesis does not hold for given EHL conditions and especially under low traction coefficient that allows for gyroscopic slip. Inner ring acceleration enabled to better understand skidding mechanism in dynamics. The program also proved its ability to determine the required preload to prevent skidding and to compute the product of normal load by slip velocity in order to estimate wear due to skidding. The limit is that cage is not considered yet, whereas it has an important influence on ball dynamics. Later, Jain [139] developed a simpler model where ball distribution of load is first solved in quasi-static and then skidding is investigated in dynamics for ACBB under combined loads. As for that, centrifugal forces, gyroscopic moments and usual ball-race interactions are considered, whereas a 1-DOF cage is represented by springs of very high stiffness interacting between balls. Results showed that under radial load, skidding is not equally distributed over the bearing. It is especially higher in unloaded zones and maximum at the entry to load-zone where contact load is minimum. Also, compared to pure axial load, a larger force is needed to minimize skidding. And, if increasing loads can reduce the length of skid zone, it cannot totally eliminate skidding. Nevertheless, this model is limited since it neglects cage inertia which has an important effect on cage speed, especially for time-varying operating conditions. Consequently, Tu

[247] developed a planar dynamical model to investigate skidding during acceleration. The model is very basic since it neglects lubrication and only centrifugal forces, gravity, Hertzian normal forces and Coulomb friction forces at ball-race and ball-to-pocket contacts are considered. However, it is reliable and enables to better understand the effect of radial load and acceleration on skidding. The limit is that it does not consider the fact that ball spinning axis is not aligned with bearing axis, whereas spinning greatly influences skidding. Then, Chen and Shao [37], [233] studied skidding of rolling elements entering the loaded zone of a radially loaded bearing with and without lubrication. They showed that lubrication decreases the length of the loaded zone and the amplitude of rolling elements own rotational speeds, but increases slip velocities and time duration of slip.

Wang [258] and Han [117] both developed very complete dynamical 3D models for ACBB under combined loads. They both considered spinning motion, centrifugal forces, EHD lubrication, traction and drag forces. Ball-cage interactions are again represented by springs of high stiffness. Wang's results confirm those of previous studies with spinning motion explanation. They also confirm the importance of lubrication parameters, of centrifugal expansion that reduces skidding threshold and of bearing rotational speed that severs skidding. Han [117] observed that constant radial load decreases slipping velocities in high-loaded bearing zones whereas it increases them in lower loaded zones, then it makes skidding become more serious. Nevertheless, for a given region, increasing time-variant radial load can increase slipping velocities during a cycle but decrease it at next cycle. Then, no conclusion can be drawn on the effect of time-variant load on skidding, excepted that it increases maximal slipping velocity. Later, Wang [259] added ball rolling friction and film thickness thermal effects to this dynamical model. The purpose was to study the race conformity influence on ball skidding and ball-race contact forces. It appears that under light axial load, open inner race and tight outer race conformities are preferred to limit skidding whereas under important loads, tight inner and outer races are preferred to limit contact pressure, then to improve bearing fatigue life. Starting from the original model [258], they also modified traction forces by the use of curve-fitted EHL parameters to consider the effect of surface roughness and temperature rise due to sliding [260]. Under low axial load, results show that raceway surface roughness reduces sliding velocity and spinning speed then limits skidding especially on the inner ring. However, for any axial load, increasing raceway surface roughness reduces film thickness, worsen lubrication performances, induce stress fluctuation in the substrate and stress concentration near the surface. Then, smooth surfaces are preferred under high axial load. More recently, Fang [68] developed a quasi-static 3D model with all of previous effects and with cage-guiding race interactions in addition. A thermal model was also implemented to show severe influence of skidding on temperature rise. Results also confirm skidding increasing with bearing speed, and the existence of an optimum preload to minimize it.

For the first time, Ma [174] developed a 3D-dynamical model for four contact point ball bearing (FCPBB) with EHD traction forces and 3-DOF cage. He showed that when axial load increases, bearing changes from 3 contact points with important skidding, to 2 contact points without skidding. The third contact-point on the outer race has important spin-to-roll ratio that generates heat and risks of burn or failure even if main contact has the largest PV (contact pressure x sliding speed) value. Under important radial load, during one revolution, balls can have 2, 3 or 4 contact points. Under two contact points,

PV factor is maximum on main contact, whereas it is maximum at sub-contact under four contact points. Ma [173] also used this model to investigate FCPBB optimum working conditions and outer race optimum geometry. At high speeds, working under three contact points better distributes centrifugal forces, limits contact angles differences, weakens the softening effect of high speed on stiffness, increases fatigue life, but also increases friction forces. Generally, an optimum curvature center eccentricity exists to improve fatigue life, whereas under skidding conditions, larger eccentricity and smaller groove curvature coefficient are preferable to limit PV factor, sliding and to increase fatigue life.

2.5 Improved models for surface defects

Bearings are subjected to localized defects like pits, cracks or spalls that lead to vibrations when the ball rolls over them. To prevent resulting failures, condition monitoring and fault diagnosis have recently become important subjects of research. Most models that consider surface defects are in quasi-statics or do not take into account 3D motion, ball-race slipping, lubrication or cage contribution [168]. However, under high-speed such effects are substantial for accurate defect modeling. Ashtekar and Sadeghi [10] added in DBM [79] effects of dents with sinusoidal profiles. In this dry contact elastic model they modified the Hertzian force-deflection relationship with a different exponent n function of dent geometry and loading. It appears that balls rolling over dent generates vibrations that have negative effects on balls, rings and cage behaviour. And, inner race speed increasing, dent size increasing, offset of dent from race centerline or the presence of a cluster worsen such vibrational phenomena. Later, they also modelled in DBM bumps, dents, spalls and debris represented by spherical defects [11]. They used the superposition principle to add or subtract to Hertzian contact force or pressure, an Hertzian force or pressure due to defect height or depth. Results confirm that localized defects modify contact force amplitude, direction and dynamical behaviour of all bearing components.

As well, employing Gupta's formalism [91], Niu [33] developed a dynamical model for high-speed ball bearing with ball-races normal load, relative slip and simplified traction forces. Raceways localized surface defects are accurately represented by the addition of a deflection due to material absence and by the modification of Hertzian contact stiffness and contact forces direction due to curvature changes. Later, cage was added and surface defect model was improved by considering the finite size of the ball instead of a point mass contact [193]. Results show the influence of rotational speed, axial and radial forces, initial contact angle and defect size on motions and ball passing frequencies especially under skidding operating conditions.

Qin [213] also modelled fault dynamics for high-speed ACBB. As for that, Jones-Harris quasi-static problem with inertial effects is solved for a planar ACBB. Then, balls dynamic is simulated with the use of a B-spline fitting displacement excitation to represent the fault. Later, 5-DOF were considered for inner ring, and cage was added with ball-to-pocket interactions represented by spring-damper systems [212]. The displacement excitation function was also replaced by a half-sine function to characterize the defect. These models accurately represent the real excitation and enable to observe that impulse duration, amplitude and ball-to-pocket forces increase with defect size. As well, with rotational speed and radial load increasing, the amplitude of acceleration vibration increases and cage motion changes from regular to erratic.

Wen [263] also modified their quasi-dynamic ACBB model [265] in dynamics and to implement a localized outer-race surface defect with a constraint on depth profile. They added EHL damping by short bearing theory for planar cage-guiding race interaction and by a constant for other components. For axial or combined loads, results showed the negative influence of surface defect scale and position, on angular misalignment, ball-to-pocket collisions, ball-race contact loads and traction forces over cycles. Then, they modified this model by representing ball-raceway contact with starved lubrication [264]. As for that, Masjedi and Khonsari's [177] mixed EHL theory is used to modify smooth and fully lubricated oil film thickness. It considers effects of surface roughness and of the degree of starvation which describes changes of mass flow rate. Traction forces and momentums are also revised to take into account asperities effects and previous planar cage model is transformed in 3 dimensions. Results show that ball-raceway starvation severity reduces oil-film thickness, increases ball-to-pocket impact load for combined loads and influences skidding behaviour and traction forces which modifies sliding, spinning velocities then gyroscopic effects at each race.

2.6 Cage elastic behaviour

With the development of high-speed bearings with cages made of lighter but softer materials, the necessity to model cage flexibility became essential. With PADRE, Boesiger [22] was the first one to consider cage elasticity locally. As for that, Hertzian ball-to-pocket penetration is considered in series with pocket web bending deflection and Hertzian race-retainer deflexion in series with radial flexing of the retainer. In each case, bending and radial deflexion are determined by finite element method (FEM) and the resulting contact force is modified by a displacement-proportional energy loss term or damping. The limit of this model is that it neglects cage global deformation.

Later, Hahn [107] developed a dynamical DGBB model that considers 3D cage elasticity with a FEA approach limited to linear-elastic materials. The macroscopic deformation of cage structure is defined as a deflection between pockets contact surfaces, whereas only micro-elastic deformations are allowed at ball-to-pocket iso-viscous contacts. Many phenomena are also considered such as squeeze-film damping effects, combined loads, misalignment or manufacturing inaccuracies.

Pederson and Sadeghi [203], [204] introduced a planar Flexible Cage Model in DBM code designed for DGBB [79], [221]. As schematised in Figure 1.5, the cage is divided into N spring-mass-damper translational systems where masses are centered on pockets. Torsional springs are also present between three consecutive pockets to provide a restoring moment. These stiffnesses are computed on the FEM software ANSYS, then a lumped mass model is solved for the cage and is finally inserted in DBM global system. Results show the importance of cage flexibility modelling. Indeed, rigid cage model predicts significantly higher ball-to-pocket contact forces and larger minimum ball-to-pocket clearances required to reduce normal forces and instabilities like whirl.

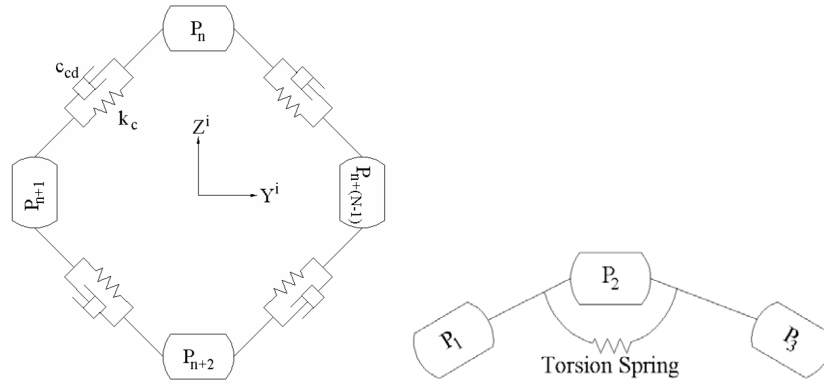


Figure 1.5 : Pederson's flexibility modeling [203], [204]

For DGBB and ACBB, Weinzapfel and Sadeghi [262] developed in DBM another model of deformable cage in a plan but with three-dimensional motion. As for that, pockets are assumed to be rigid, bridges are divided into finite elements linked by viscoelastic fibers comparable to spring-damper systems and massless rigid beams connect pockets to bridges as represented in Figure 1.6. Damping coefficient is derived from empirical relationships and stiffness is computed from a force-deflection relationship of a FE model. Resulting efforts are then introduced in DBM system of equations.

Results confirms the significant reduction of ball-to-pocket contact forces and ball-race slip velocities with flexible cage. Tilt angle also presents smaller amplitude, steady state is reached faster and whirl radius increases with elastic modulus. In contrast, flexibility does not change whirl frequencies, cage motion or velocity in case of radial load. This study also confirms Walters' [253] and Meeks' [180] conclusions about the role of centrifugal forces in making the cage maintain its radial position by overcoming cage friction forces and by increasing whirl radius to a constant value.

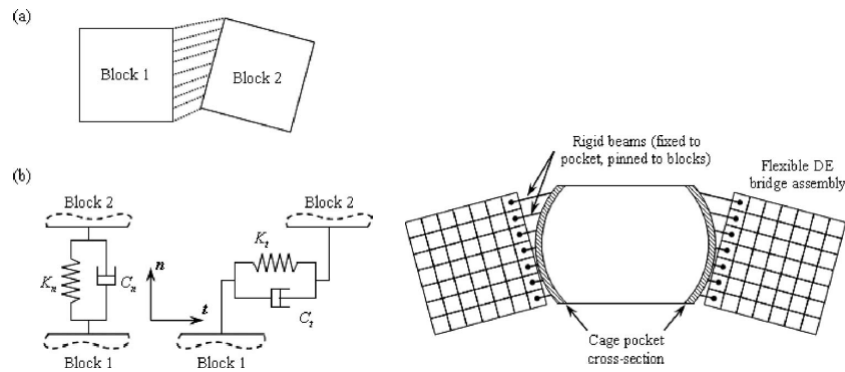


Figure 1.6 : Weinzapfel's flexibility modeling [262]

Ashtekar and Sadeghi [9] continued to work on DBM and combined this discrete element ball bearing dynamic model (DEM) with a 3D explicit finite element model (EFEM) of cage. As for that, the bearing cage is analytically meshed and the FE problem with boundary conditions and applied forces is solved at each RK4 time step in order to compute velocities and displacements at each node. An accurate and continuous procedure is also implemented to link DEM to EFEM problem, especially at ball-to-pocket contact

because ball forces acts at several pocket nodes. Results analysis confirmed Weinzapfel and Sadeghi's [262] observations. As well, for flexible cage, elastic deformations appear to be at the origin of multiple oscillations at ball-to-pocket impacts, centrifugal forces to be responsible for global cage expansion, deformation and resulting stresses. Moment load also increases magnitude and duration of ball-to-pocket impacts that generates stress cycles in the bridge and rail cage sections leading to fatigue failures. It's worth noting that those three models developed in DBM by Sadeghi's team, particularly improved flexible cage understanding and modelling. However, they were limited to ball guided cages, then cage-race interactions were not considered.

For NTN company, Sakaguchi [222], [223], [224] developed planar flexible cage models for tapered and needle roller bearings. However, 2D or 3D bearing geometry and bodies interaction forces are modelled on MSC. ADAMS, a multibody dynamic analysis software. If damping effects are neglected, elastic deformations and resultant cage stresses are derived in different points by Component Mode Synthesis method in ADAMS. Later, these two models were combined and organized on a simplified interface called IBDAS (Integrated Bearing Dynamic Analysis System) [231]. This system was extended to any kind of bearing and a Guyan reduction was applied to the FE cage system in order to reduce computation time. A comparison with a FE model shows that the accuracy of this CMS method highly depends on eigenmodes and boundary points chosen. We should also precise that these models proved that unequal steady distribution of rolling elements had an effect on stable whirl motion and particularly increases whirl radius.

For TIMKEN, Houpert developed CAGEDYN [129], [130], [131], a planar dynamical model for roller bearings with flexible cages. As schematised in Figure 1.7, cage 2D-elasticity is represented at ball-to-pocket impact by an equivalent stiffness that comprises Hertzian contact stiffness and bridge structural stiffness responsible for its bending. This last one is determined analytically if the beam has a simple shape and numerically by FEA otherwise. As well, cage-guiding ring Hertzian contact stiffness is added in series with a contact stiffness defined by standard load-ring ovalization relationship. If structural damping is neglected, effects of sliding, rolling, friction, traction or lubrication are particularly well considered. Model validation proves its high efficiency and confirms the importance of implementing bridge structural stiffness when the latter is small. It also shows its effectiveness in predicting cage damage by computing impact force on bridges, then Von Misses stresses to compare them to cage material fatigue limit.

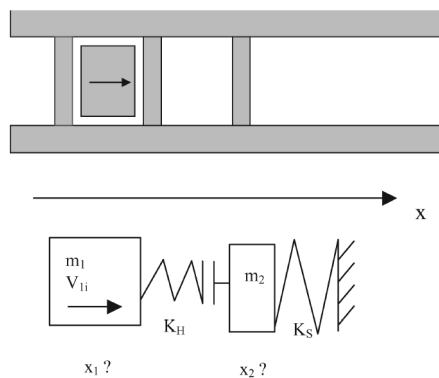


Figure 1.7 : Houpert's flexibility modeling [129]

Qian [211] also developed CyBeSime, a 3D dynamical Simulation code for CRB with any cage type. It is based on the multibody dynamic software SIMPACK where forces and solid or lubricated interactions are precisely defined in FORTRAN routines. Cage deformation and pocket-to-roller stiffness are computed in real time on Abaqus, and results obtained are automatically exported on SIMPACK for global bearing resolution. Contrary to other studies, results between rigid and flexible cages do not show differences in terms of roller-to-pocket contact forces or slip velocities. However, CyBeSime proves to be an efficient tool to optimise cage pocket geometry or structural design, to predict cage wear and vibrations, to better understand bearing behaviour as instabilities (whirl or squeal), motions, speeds and to investigate effects of parameters (misalignment, radial load, clearances, materials, type of cage, etc.) on contact forces, pitch and yaw angles.

Li [161] developed a 3D dynamical model of high-speed ball bearing with flexible cage lintel represented by 3D beam elements with 6-DOF at each node as represented in Figure 1.8. To model global cage flexibility, nodal displacements, force vectors and stiffness matrices are defined locally before being converted into the overall coordinate system. To compute ball-to-pocket interactions, geometric displacements are considered with the addition of the term BPWL that represents the amount of ball-to-pocket wear loss. Then, beams static equilibrium is solved on nodal displacements and on beam deformation, is this way, ball-to-pocket position and contact-force interactions are recalculated, and the procedure is repeated until forces does not vary anymore. As well, ball-to-raceway and cage-race contact and friction forces are computed with usual theories. Finally, the resulting system of dynamical equations on balls, cage and rings is solved by an RK4 scheme. Results show the influence of BPWL on cage center trajectory, on skidding ratio fluctuation and on total cage forces, then on bearing elements interactions.

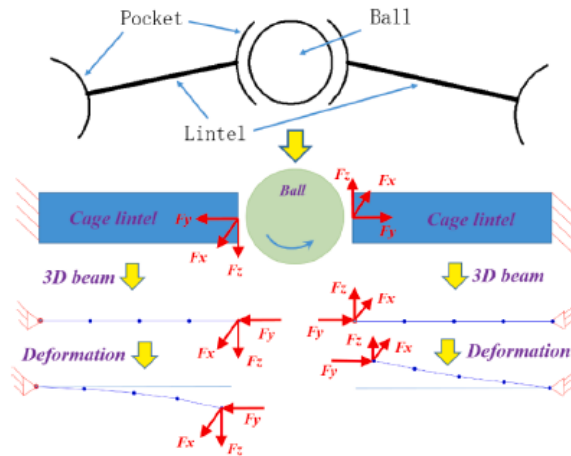


Figure 1.8 : Li's flexible cage model[161]

Liu [167] developed a planar dynamical model to investigate the influence of cage flexibility and impact load on skidding performances. As for that, dried and Hertzian contacts are considered for ball-race and ball-to-pocket interactions whereas races do not act on cage. To represent cage flexibility, cage pockets are lumped to springs with stiffnesses calculated by FEM as schematised in Figure 1.9. Note that cage-to-pocket clearance is ignored, then springs can only be compressed and they only work under contact conditions. Results confirms that high radial load and small inner ring rotational

speed limits skidding. A comparison between rigid and flexible cage model shows that neglecting cage elasticity underestimates cage skidding and overestimates rolling element skidding in self-rotational direction. Indeed, if ball-race contact forces do not change between the two models, ball-race friction forces and ball-to-pocket normal forces are higher for the flexible cage because ball-race slipping velocities are also higher. Another consequence is that it takes less time to reach a stable motion state with the flexible cage model. This study also shows that increasing cage stiffness reduces cage and rolling element-race slipping velocities, then it limits skidding.

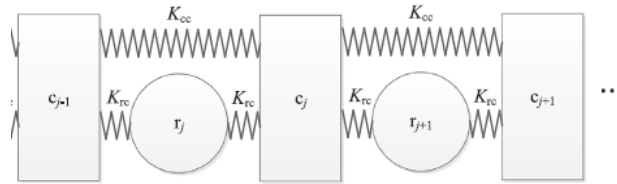


Figure 1.9 : Liu's flexibility modeling [167]

Then, cage flexibility is a subject that has been investigated only recently. Few studies interest in ACCB guided by inner or outer race, many flexible cage models are planar or based on a multibody dynamic analysis software. That is why, starting from Leblanc's previous work [158], authors aim at developing their own dynamical flexible cage model for ACBB with 2, 3 or 4 contact point in the future.

2.7 Squeeze-film damping modeling

A new feature to consider in dynamics is damping effect that can come from different sources as material hysteresis, fluid film or dry friction. From the first research, like those of Vichard [251] or Dareing [54], it was shown that lubricant film damping is one of the most important source of total damping and that it is primarily generated by squeeze-film mechanism in EHL contacts. Later, for cage-race interaction, Gupta [84] extended short journal bearing theory by adding a squeeze-film term that depends on film thickness evolution over time. Subsequently, for an ACBB subjected to an oscillating radial load, Walford and Stone [252] proposed to model ball-race interaction by the Hertzian contact stiffness K_c in parallel with the squeeze-film damping at the entry of contact zone f_e as schematised in Figure 1.10. Analysis of radial and axial stiffness and damping and comparison with experiments shows that damping magnitude is preload dependant and that bearing joints are another source of bearing damping that should be considered in dynamical modelling especially at high-speed.

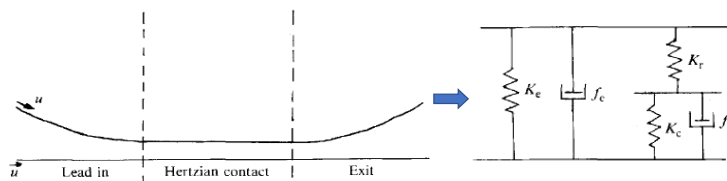


Figure 1.10 : Walford's squeeze-film modeling [252]

Hagiu and Gafitanu [106] added inlet zone rigidity k_{ef} in parallel with elastic Hertzian stiffness k_c and entry zone squeeze-film damping h_{ef} as represented in Figure 1.11. They also considered EHD lubrication film thickness h_{min} by Hamrock Dowson [113] formula multiplied by Wilson and Murch [185] thermal factor and Olaru [200] starvation factor. ACBB axial, radial and angular stiffnesses and dampings were investigated. And, experimental comparison shows that shaft-inner ring and housing-outer ring should be additional sources of damping under high-speed conditions.

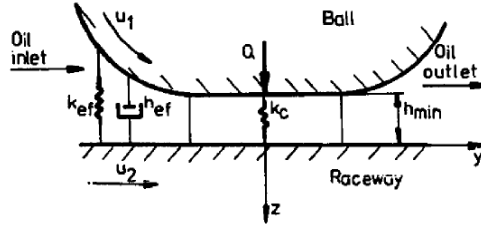


Figure 1.11 : Hagiu's squeeze-film modeling [106]

To compute squeeze-film damping, some studies are based on the change of mutual approach like those of Hagiu [106] or Sarangi [225] whereas others are based on the change of film thickness like those of Wijnant [267], Nonato [198], Wensing [266], Dietl [57] or Zhang [284]. They generally follow the same procedure that consists in solving a transient EHL line or point contact problem, usually by Van Nijenbanning's [192] or Venner's [249] multigrid method in order to compute lubricant and structural elements vibration response. From the logarithmic decrement of the response, squeeze film damping is calculated. Then, various numerical data are curve fitted by least square method to obtain a general expression on oil-film damping between roller and race. A similar expression is usually proposed for stiffness, in this way each ball-race interaction is described by a spring-damper system as schematised in Figure 1.13. These systems are then inserted in a whole dynamical bearing model.

Mostofi [183] followed this procedure, solved EHL point contact problem numerically and proposed a film thickness expression as a function of contact parameters and especially of integrated pressure which depends on squeeze velocity. Later, Rahnejat [215] reused this theory and computed in axial and radial direction, the vibrational response and squeeze film damping of a rotating shaft supported by two lubricated DGBB. Increasing the number of balls reduces film thickness and damping coefficient in unloaded region, whereas increasing load increases squeeze-film damping coefficient.

For an EHL-line contact problem, Dietl [57], [58] also derived an equivalent oil-film damping coefficient c_{EHL} at the inlet zone of the contact. In parallel, he estimated viscous material damping coefficient c_h due to dry Hertzian contact. This coefficient depends on a loss factor, on local contact stiffness and on frequency vibration. The system was then applied at each ball-race contact, as schematised in Figure 1.12. Damping matrix was also computed for the whole 5-DOF bearing. Experimental comparisons confirmed efficiency of these two formulations to predict bearing damping. Results also show that the damping coefficient increases with axial preload, lubricant viscosity, roller number or contact surface, but decreases with starvation, with an excessive amount of oil or with rotational speed. Damping is also highly dependant on lubricant temperature, since temperature depends on rotational speed but influences oil viscosity.

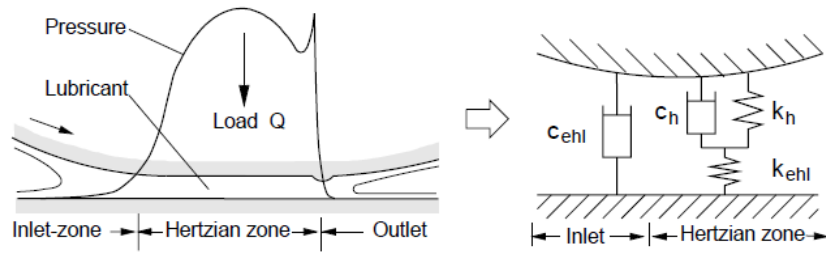


Figure 1.12 : Dietl's squeeze-film modeling [57], [58]

Wensing [266] solved time-dependant EHL point contact problem and proposed a curve fitted formula for damping coefficient as a function of dimensionless contact parameters (geometry, materials, load, frequency). Spring-damper systems were inserted in a whole dynamical bearing model where shaft, housing and outer ring are modelled by finite element method. Results show that two dampers are necessary for the ball to damp principal bearing resonances. And, viscosity increases damping values whereas starvation, load or speed decreases them significantly.

Wijnant [267] also used this methodology to investigate dry contact and lubricated contact under fully flooded or starved condition and for circular or elliptic EHL contacts. Curve fitted expressions were proposed for contact stiffness and viscous damping as a function of Moes-Venner parameters [248] with damping computed from solutions for sinusoidally varying loads.

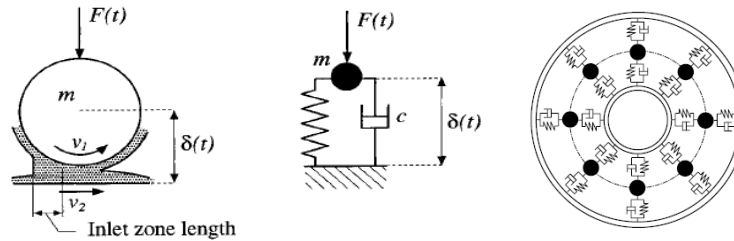


Figure 1.13 : Wijnant's squeeze-film modeling [267]

For EHL point contact problem with consideration of surface roughness, Sarangi [225], [226] derived empirical formulas on lubricant stiffness and damping of a single ball-race contact. Analysis of these expressions indicates that stiffness and damping increase with load capacity, but decrease with speed, material or ellipticity parameters. They are also a function of hydrodynamic roughness and surface pattern parameters. Damping is also inversely proportional to a geometrical parameter that conforms with ball-race contact. Then, the overall stiffness and damping matrices of the radially loaded bearing can be computed by replacing each ball by an equivalent spring-damper system made of two spring-dampers in series, as represented in Figure 1.14. Results show that damping cannot be neglected for lubricated ball bearings dynamic modelling. Later, Sarangi [227] reused the same approach to compute lubricant stiffness and damping for mixed lubricated point contact problem. As for that, contact asperities were considered in pressure computation with the use of Greenwood and Tripp model. Consequently, an additional parameter on contact stiffness K' was added in curve-fitted formulas on lubricant stiffness K_l and

damping C_l at entry contact region. And, an additional stiffness formula K_a was curve-fitted to represent asperity contact stiffness at the center of contact as schematised in Figure 1.15. Physically, when the contact stiffness parameter K' increases, more asperities are in contact then contact stiffness K_a increases, whereas lubricant stiffness K_l and damping C_l decrease considerably. As well, contact stiffness K_a increases with roughness pattern parameter or load capacity. Then, a dynamical, planar and non-linear ball bearing model [228] was developed to study the influence of previous parameters on vibrational response. Especially, the effect of EHL damping in reducing ball bearing vibrations was shown.

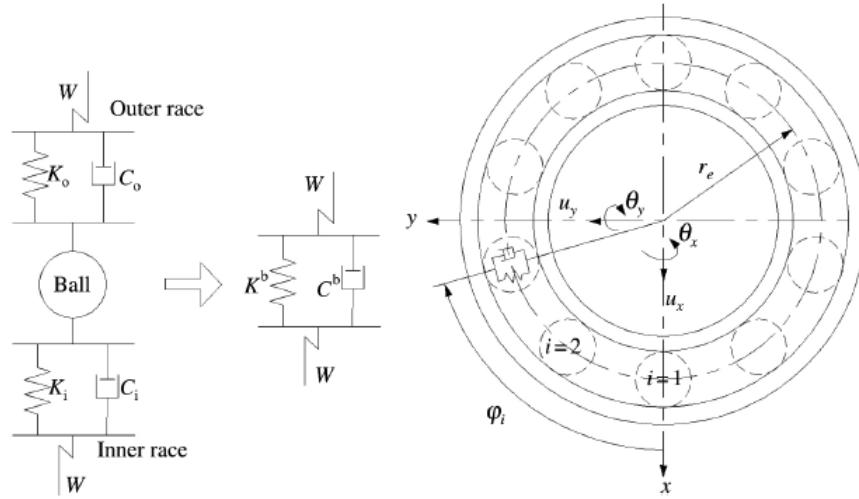


Figure 1.14 : Sarangi's squeeze-film modeling [225] under pure EHD lubrication

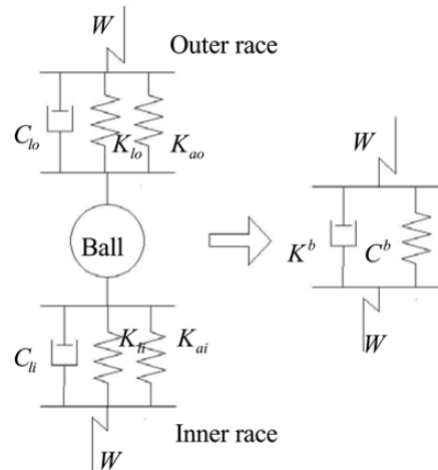


Figure 1.15 : Sarangi's squeeze-film modeling [227] under mixed EHD lubrication

Zhang [284] also derived stiffness and damping coefficients for transient EHL and free vibration models and under wider load and speed ranges than previous studies. Another feature is the consideration of the influence of working load and speed on inlet length and natural frequency computation. Such considerations significantly modify damping results,

especially under heavy load and high speed. It is also shown that stiffness and damping increases with lubricant ambient viscosity, whereas damping decreases with pressure-viscosity coefficient. Nonato [197], [198] also derived non-linear stiffness and linear viscous damping expressions to model EHD film effects under harmonic loading. Then, these effects were implemented in a planar DGBB model to compute resulting restoring and dissipative forces. Bizarre [20] also used this method to solve EHD contact problem in parallel with 5-DOF ACBB equilibrium based on Harris and Mindel's kinematic approach [123]. One of the differences with the DGBB model is the distinction of contact angles between inner and outer raceways, then the necessity to compute damping and stiffness at each contact over the bearing. Results differences between dry and EHD approaches show the necessity to consider these EHD dynamic parameters. And, computational efficiency was also shown which can be interesting to introduce this model in a rotor system with lubricated ACBB. Dong [60] also solved steady and transient EHL contact problem, considered energy conservation theory, a harmonic sinusoidal load, and curve fitted mutual approach and damping coefficient as a function of load and entrainment velocity. These EHD effects were implemented in a 3D dynamic, axially loaded ball bearing model based on Gupta's formalism [91]. Results between dry and EHD model are significantly different under low axial load because contact forces are low, ball motion is unsteady then damping effects are important. Guessasma [83] proposed a dynamical 3D discrete element model for radial ball bearing where, under mixed lubrication, material damping and Walford's [252] fluid film damping are considered in parallel. Feature of this model is that at each contact, each time step, lubrication regime is accurately and smoothly determined from fluid parameter and friction coefficient analysis on Stribeck curve [241]. Results show that lubrication regimes highly depend on inner ring rotational speed whereas radial load and diametral clearance have minor effects. Sun [242] also solved EHD point contact problem with the use of multi-grid method to compute pressure and film thickness distributions over the contact. Then, damping is calculated by the ratio between the change of force and the contact velocity. An experimental study was led in parallel in order to validate theoretical results. It was confirmed that damping increases with radial load, but decreases with rotational speed.

3 Conclusions

Ball bearing is an old mechanism that has known important development these past eighty years in parallel with aero-spatial evolutions. Indeed, bearings were subjected to get larger diameters, higher speeds, higher temperatures or wider load range (axial, radial, moment loads). Such modifications significantly change physical behaviour. Many models and experiences have been led to optimise their design. Especially, several quasi-static and quasi-dynamic models have been developed to better understand Angular Contact Ball Bearing behaviour. For different working conditions (speeds, axial, radial loads, misalignments, bearing geometry, etc.), these models allowed to study balls equilibrium, contact angles distribution, pitch angle evolution or ball kinematics. Importance of accurately considering EHD lubrication through film thickness, traction, starvation, dynamic viscosity definitions or thermal considerations was shown. First models like those of Jones, Harris or Crecelius are still considered as references. However, many researches have been led to improve them and especially to get rid of raceway control hypothesis. Some of them use geometric assumptions to compute pitch angle, others are minimizing contact friction or directly solving ball torque equilibrium. Depending on model applications, some authors investigated parameters influencing skidding, others interested in spindle bearings, or in calculating running torque. Few models interested in 3 or 4 contact point ball-bearing or considered yaw angle. Quasi-static and quasi-dynamic models are time-computational efficient and give a first outlook of ball-race equilibrium. However, analysis of cage motion, of accelerations or of accurate behaviour under important radial load or misalignment, requires dynamical studies.

ADORE and BEAST were among the first bearing dynamics computer codes developed. Their continuous improvements until today makes them one of the most important. More recently, Purdue University searchers, supervised by Sadeghi, developed DBM and made major advances in the domain. Chinese tribologist community also led many studies and brought important knowledges on the subject. Most dynamical models have same structures and considers more or less same interactions at ball-race, cage-race and ball-to-pocket contacts. Nevertheless, depending on authors, different bearing behaviours are studied under different working conditions. Especially, cage center of mass motion and ball-to-pocket interactions have been analysed for different ball-race friction models, cage speeds, cage unbalances, cage guidances, ball-to-pocket or cage-race clearances, lubricant types, lubricated conditions, raceway conformities, surface roughness, temperatures, gravity, axial, radial and moment loads. Is this way, bearing behaviour could be understood more precisely and working conditions to get stable cage whirl and to avoid skidding could be identified. To consider dynamic effects of EHD lubrication, some studies interested in modelling squeeze-film damping, especially at ball-race contacts. As well, to avoid bearing failures, more and more authors are modelling in dynamics, surface defects like dents, bumps, spalls or debris. Recently, with polymeric cages development, searchers started to implement cage flexibility in their models. If such investigations stay limited at the moment, improvements are expected in the coming years.

Chapter 2

Quasi-static model with balls and rings

Contents

1	Markers definition	47
1.1	Global coordinate system \mathcal{R}_G	47
1.2	Inner ring coordinates systems	47
1.3	Balls coordinates systems	49
2	Geometric equations	53
2.1	Geometric closure on outer ring	54
2.2	Geometric closure on inner ring	54
2.3	Geometric closure on inner and outer ring	55
2.4	Choice of equations depending on rings truncations	56
3	Ball kinematic	56
3.1	Detailed computation for outer race, side 2	58
3.2	Kinematic synthesis at 4 contacts	59
3.3	Point of pure rolling	60
4	Forces definition	61
4.1	External forces on the inner ring	61
4.2	Forces due to ball motion	61
4.3	Coulomb's friction	62
5	Friction forces computation	65
5.1	Analytic expressions	65
5.2	Validation	72
6	Quasi-static resolutions	77
6.1	R1 Resolution	77
6.2	R2 Resolution	80
6.3	New features of BB20 version 5	86

7	Results analysis	88
7.1	Investigation of existing bearings	88
7.2	Comparison with literature	94
8	Summary	101

In this section, the quasi-static model of Angular Contact Ball Bearing developed by Leblanc, Nelias and Lacroix [156], [157], [158] is improved. In such study the bearing is double-arched, then 1, 2, 3 or 4 contact points are present between balls and rings. The bearing has 5 degrees of freedom (3 translations, 2 rotations) due to external loads. Inner ring rotates at shaft speed Ω_i and outer ring at speed Ω_o in global coordinates system. The analysis is static with consideration of inertial effects. Consequently, only balls and rings are considered since cage is a dynamic body.

1 Markers definition

1.1 Global coordinate system \mathcal{R}_G

The formalism described in Lacroix's thesis [155] is reused here. The orientation of bearing axis \mathbf{x}_G is reversed in order to work in a direct coordinate system as represented in Figure 2.1. Then, \mathcal{R}_G is the global coordinate system of the bearing. It is considered as Galilean and it defines bodies positions under initial conditions without external forces applied. In this system, the center G represents bearing center, outer ring center and inner ring center initially. \mathbf{x}_G axis is bearing rotational axis, whereas \mathbf{y}_G and \mathbf{z}_G define outer ring medium plan.

1.2 Inner ring coordinates systems

1.2.1 Inner ring position \mathcal{R}_{i1}

In this study, rings are supposed to be rigid, only local deformations at ball-race contacts are considered. Because of external loads, inner ring center G_{i1} moves relative to bearing center G . To model corresponding degrees of freedom, the inner ring local coordinate system \mathcal{R}_{i1} is defined as represented in Figure 2.1. Then, inner ring has 3 degrees of freedom in translation $\delta_x, \delta_y, \delta_z$ and 2 degrees of freedom in rotation θ_y, θ_z . Because those displacements and rotations are small, \mathcal{R}_G and \mathcal{R}_{i1} systems are almost equivalent. Then, for the sake of simplicity, future projections related to inner ring will be defined in the global coordinate system \mathcal{R}_G .

$$\mathcal{R}_G = \{G, \mathbf{x}_G, \mathbf{y}_G, \mathbf{z}_G\} \quad (2.1)$$

$$\mathcal{R}_{i1} = \{G_{i1}, \mathbf{x}_{i1}, \mathbf{y}_{i1}, \mathbf{z}_{i1}\} \quad (2.2)$$

$$\boldsymbol{\delta} = \mathbf{G} \mathbf{G}_{i1} = \begin{bmatrix} \delta_x \\ \delta_y \\ \delta_z \end{bmatrix}_{\mathcal{R}_G} \quad (2.3)$$

$$\theta_y = (\mathbf{x}_G, \mathbf{x}_{i1}') = (\mathbf{z}_G, \mathbf{z}_{i1}) \quad (2.4)$$

$$\theta_z = (\mathbf{x}_{i1}', \mathbf{x}_{i1}) = (\mathbf{y}_G, \mathbf{y}_{i1}) \quad (2.5)$$

1.2.2 Inner ring rotation \mathcal{R}_i

Because of shaft speed, inner ring also rotates around its own axis (G_{i1}, \mathbf{x}_{i1}) at rotational speed ω_i . To model this motion, the coordinate system \mathcal{R}_i is defined such as represented in Figure 2.2. Note that rotational speed ω_i is the time derivative of $\theta_{i/i1}$ angle. Again, because of small inner ring motion, it can be considered that \mathbf{x}_{i1} is equivalent to \mathbf{x}_G , then that inner ring rotates around bearing axis (G, \mathbf{x}_G).

$$\mathcal{R}_i = \{G_{i1}, \mathbf{x}_{i1}, \mathbf{y}_i, \mathbf{z}_i\} \quad (2.6)$$

$$\theta_{i/i1} = (\mathbf{y}_{i1}, \mathbf{y}_i) = (\mathbf{z}_{i1}, \mathbf{z}_i) \quad (2.7)$$

$$\boldsymbol{\Omega}_{i/i1} = \dot{\theta}_{i/i1} \cdot \mathbf{x}_{i1} = \omega_i \cdot \mathbf{x}_{i1} \quad (2.8)$$

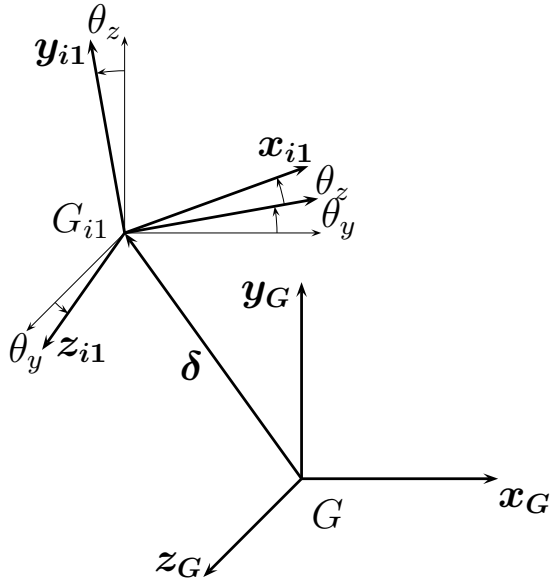


Figure 2.1 : Inner ring motions relative to bearing center

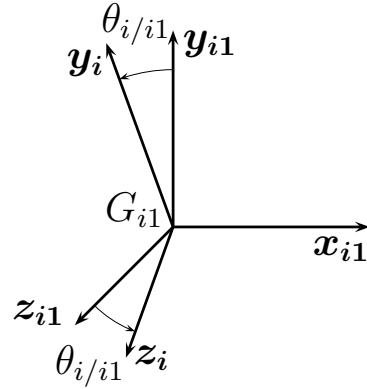


Figure 2.2 : Inner ring self-rotation

1.3 Balls coordinates systems

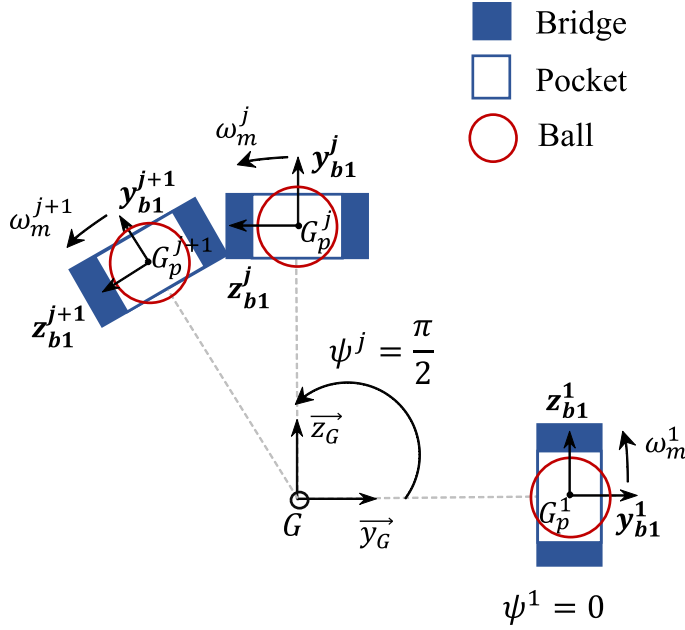


Figure 2.3 : Balls orbital positions and precession speeds in the bearing

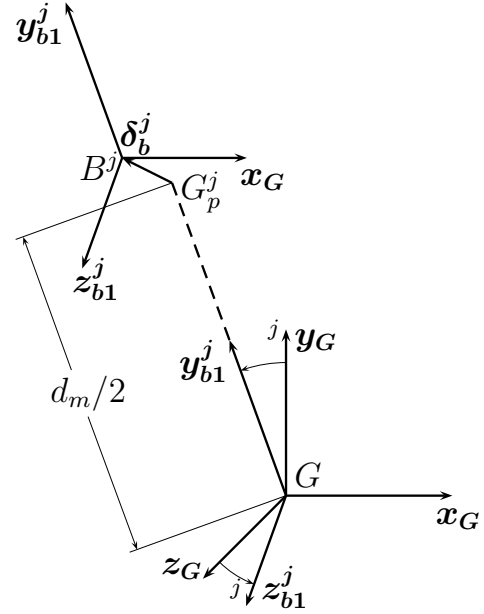


Figure 2.4 : Balls translations

1.3.1 Balls positions \mathcal{R}_{b1}^j

In global coordinate system \mathcal{R}_G , each ball j rotates around (G, \mathbf{x}_G) axis. This motion is called ball orbit or precession. As schematized in Figure 2.3, corresponding local coordinates systems are \mathcal{R}_{b1}^j . They define each ball orbital position ψ^j at pocket center G_p^j such that initially, balls are equally distributed around the bearing (cf. expression (2.10), where ψ_c is angular position of the first ball). Time derivative of ball position B^j is ball precession speed ω_m^j , that can differ from one ball to another one. That is why, in quasi-static, we suppose that the average of ball precession speeds is cage rotational speed as expressed in (2.11).

$$\mathcal{R}_{b1}^j = \{G_p^j, \mathbf{x}_G, \mathbf{y}_{b1}^j, \mathbf{z}_{b1}^j\} \quad (2.9)$$

$$\psi^j = \psi_c + \frac{2\pi}{N}(j-1) = (\mathbf{y}_G, \mathbf{y}_{b1}^j) = (\mathbf{z}_G, \mathbf{z}_{b1}^j) \quad (2.10)$$

$$\omega_c = \sum_{j=1}^N \frac{\omega_m^j}{N} \quad (2.11)$$

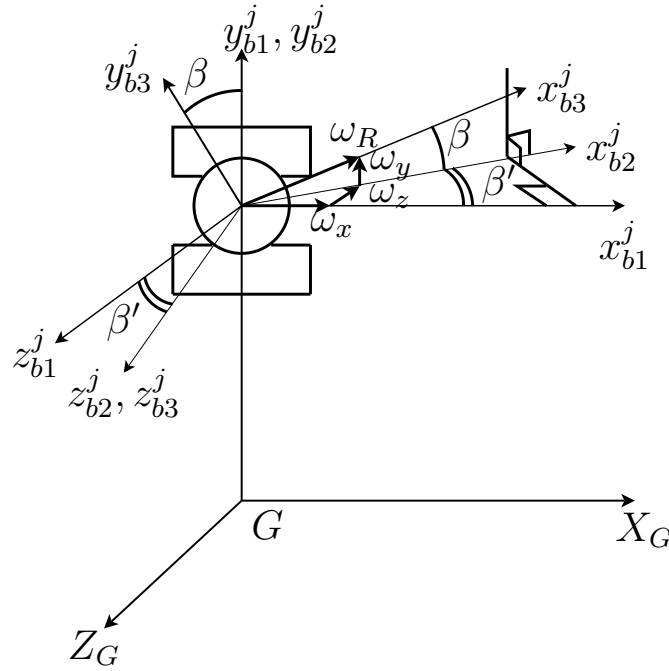


Figure 2.5 : Ball self-rotations

As well, ball orbital position or pocket position G_p^j is located at a distance $d_m/2$ from bearing center G , where d_m is the initial average bearing diameter. From this position, ball center B^j can translate of a distance δ_b^j as represented in Figure 2.4. Note that in quasi-static, ball orthoradial displacement is neglected, then δ_b^j does not have a component along z_{b1}^j axis. Such hypothesis is no longer valid in quasi-dynamics because of cage contribution and ball-to-pocket interactions.

$$\mathbf{GB}^j = \begin{bmatrix} x_G^j \\ y_G^j \\ z_G^j \end{bmatrix}_{\mathcal{R}_G} = \begin{bmatrix} \delta_{bx}^j \\ \frac{d_m}{2} + \delta_{by}^j \\ 0 \end{bmatrix}_{\mathcal{R}_{b1}^j} \quad (2.12)$$

1.3.2 Balls own rotations $\mathcal{R}_{b2}^j, \mathcal{R}_{b3}^j$

Each ball rotates in three directions around its own axis. The first rotation is around (B^j, \mathbf{x}_{b3}^j) axis and related to ω_R^j the ball own rotational speed. The second rotation is around (B^j, \mathbf{z}_{b2}^j) axis and related to β^j . This angle is caused by centrifugal forces. The last rotation is around (B^j, \mathbf{y}_{b1}^j) and related to β'^j . This angle is caused by gyroscopic effects. To define these three consecutive rotations, coordinates systems \mathcal{R}_{b2}^j and \mathcal{R}_{b3}^j are introduced as schematized in Figure 2.5. Consequently, ball rotational speed is expressed by relation (2.17) in ball coordinate system \mathcal{R}_{b1}^j .

$$\mathcal{R}_{b2}^j = \{B^j, \mathbf{x}_{b2}^j, \mathbf{y}_{b2}^j, \mathbf{z}_{b2}^j\} \quad (2.13)$$

$$\mathcal{R}_{b3}^j = \{B^j, \mathbf{x}_{b3}^j, \mathbf{y}_{b3}^j, \mathbf{z}_{b3}^j\} \quad (2.14)$$

$$\beta^j = (\mathbf{x}_{b2}^j, \mathbf{x}_{b3}^j) = (\mathbf{y}_{b2}^j, \mathbf{y}_{b3}^j) \quad (2.15)$$

$$\beta'^j = (\mathbf{x}_{b1}^j, \mathbf{x}_{b2}^j) = (\mathbf{z}_{b1}^j, \mathbf{z}_{b2}^j) \quad (2.16)$$

$$\boldsymbol{\omega}_R^j = \begin{bmatrix} \omega_x^j \\ \omega_y^j \\ \omega_z^j \end{bmatrix}_{\mathcal{R}_{b1}^j} = \begin{bmatrix} \omega_R^j \cos \beta^j \cos \beta'^j \\ \omega_R^j \sin \beta^j \\ -\omega_R^j \cos \beta \sin \beta'^j \end{bmatrix}_{\mathcal{R}_{b1}^j} \quad (2.17)$$

1.3.3 Ball-raceway contacts $\bar{\mathcal{R}}_{km}^j$

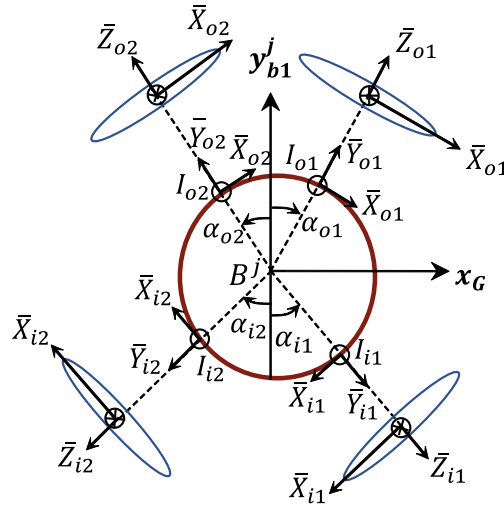


Figure 2.6 : Contacts orientations

Each ball can have 1, 2, 3 or 4 contact points with races in I_{km}^j . Thereafter, index k equal to i or o will refer to inner or outer race, and index m equal to 1 or 2 will refer to contact side 1 or 2. Coordinates systems $\bar{\mathcal{R}}_{km}^j$ are introduced to orient each contact and resulting ellipse on ball j . As schematized in Figure 2.6, in this system, \bar{Y}_{km}^j defines the contact normal that faces outwards from ball. \bar{X}_{km}^j is directed along major ellipse axis and \bar{Z}_{km}^j along minor ellipse axis.

$$\bar{\mathcal{R}}_{km}^j = \{I_{km}^j, \bar{X}_{km}^j, \bar{Y}_{km}^j, \bar{Z}_{km}^j\} \quad (2.18)$$

For these contacts definitions, we assume that all contact points belong to the same plan $\{B^j, \mathbf{x}_G, \mathbf{y}_{b1}^j\}$. As well, contact angles α_{km}^j can take positive or negative values between $-\pi/2$ and $+\pi/2$. By convention, an angle α_{km}^j is positive if it is directed from \mathbf{y}_{b1}^j axis to \bar{Y}_{km}^j axis. Then, a positive angle α_{k1}^j at side 1 corresponds to a contact at the right side whereas a negative angle α_{k1}^j corresponds to a contact at the left side. The inverse applies for contact angle α_{k2}^j at side 2.

$$\alpha_{km}^j = (\mathbf{y}_{b1}^j, \bar{Y}_{km}^j) \quad (2.19)$$

Consequently, several contact combinations can be modelled. They are associated to a Contact Configuration ($LMCC^j$) value and summarized in Table 2.1. However, physically, because of centrifugal forces, a total detachment from outer ring cannot occur. Then, cases $LMCC^j = 6$ and $LMCC^j = 12$ are not allowed. As well, inner race and outer race contacts cannot take place on the same side. That is why, case $LMCC^j = 3$ is allowed if α_{i1}^j and α_{o2}^j have same signs and $LMCC^j = 8$ if α_{i2}^j and α_{o1}^j have same signs. Case $LMCC^j = 10$ is allowed if α_{i1}^j and α_{o1}^j have opposite signs and case $LMCC^j = 11$ is allowed if α_{i2}^j and α_{o2}^j have opposite signs.

$LMCC^j$	Contacts			
0	I1	I2	O1	O2
1			O1	
				O2
2			O1	O2
3*	I1			O2
4	I1		O1	O2
5	I1	I2		O2
6*				
7		I2	O1	O2
8*		I2	O1	
9	I1	I2	O1	
10*	I1		O1	
11*		I2		O2
12**	I1	I2		
		I2		
	I1			

Table 2.1 : Overview of ball-raceway possible contacts

Besides, a deformation δ_{km}^j and a film thickness h_{km}^j are defined at each possible contact point I_{km}^j . These components are directed along \bar{Y}_{km}^j axis. For the sake of simplicity, we speak about contact when δ_{km}^j computed is positive. Then, film thickness h_{km}^j that separates ball from race is calculated from Hamrock Dowson theory [116], with a thermal reduction factor from Gupta [101]. On the contrary, when δ_{km}^j is equal to zero or negative, we consider that no contact occurs. Then, δ_{km}^j defines the gap between ball and race whereas film thickness h_{km}^j is set to zero.

$$\delta_{km}^j = \delta_{km}^j \bar{Y}_{km}^j \quad (2.20)$$

$$h_{km}^j = h_{km}^j \bar{Y}_{km}^j \quad (2.21)$$

2 Geometric equations

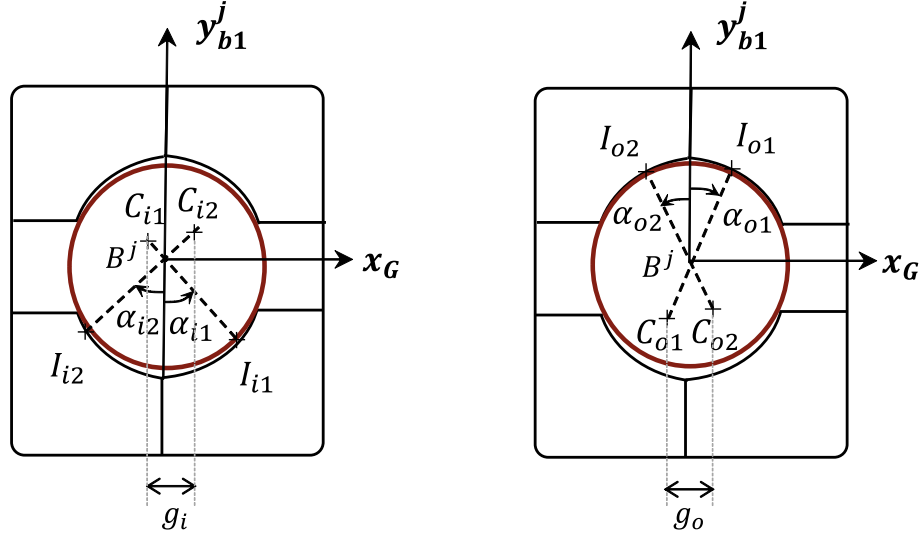


Figure 2.7 : Curvature centres at inner and outer ring

In this study, rings are supposed to be rigid, only local deformations at ball-race contacts are considered. As well, ring curvature centers are supposed to be fixed in inner ring coordinate system \mathcal{R}_{i1} and to remain in $(B^j, \mathbf{x}_G, \mathbf{y}_{b1}^j)$ plan related to each ball. Then, curvature centers displacement along \mathbf{z}_{b1}^j axis is neglected.

Geometric equations are based on geometric closures on $\mathbf{B}^j \mathbf{C}_{km}^j$. These vectors define the distance between raceway curvature center and ball center as schematized on Figure 2.7. They are expressed by relation (2.22) where δ_{km}^j is the ball displacement induced by contact point deformation, and h_{km}^j is the corresponding lubricant film thickness.

$$|\mathbf{B}^j \mathbf{C}_{km}^j| = GE_{km}^j = (f_k - 0.5) D + \delta_{km}^j - h_{km}^j \text{ with } k = o, i \text{ and } m = 1, 2 \quad (2.22)$$

To cope with projections on \mathbf{x}_G axis when α_{km}^j becomes negative, λ coefficients have also been introduced. They are equal to ± 1 and expressed in (2.23), (2.24), (2.25) and (2.26). They are based on *sign* function such that $\text{sgn}(x) = \frac{x}{|x|}$.

$$\lambda_o^j = \begin{cases} \text{sgn}(F_X) & \text{if } GE_{o1}^j \sin \alpha_{o1}^j + GE_{o2}^j \sin \alpha_{o2}^j = 0 \\ \text{sgn}(GE_{o1}^j \sin \alpha_{o1}^j + GE_{o2}^j \sin \alpha_{o2}^j) & \text{otherwise} \end{cases} \quad (2.23)$$

$$\lambda_i^j = \begin{cases} \text{sgn}(F_X) & \text{if } GE_{i1}^j \sin \alpha_{i1}^j + GE_{i2}^j \sin \alpha_{i2}^j = 0 \\ \text{sgn}(GE_{i1}^j \sin \alpha_{i1}^j + GE_{i2}^j \sin \alpha_{i2}^j) & \text{otherwise} \end{cases} \quad (2.24)$$

$$\lambda_{o2}^j = \begin{cases} \text{sgn}(F_X) & \text{if } GE_{o2}^j \sin \alpha_{o2}^j = 0 \\ \text{sgn}(GE_{o2}^j \sin \alpha_{o2}^j) & \text{otherwise} \end{cases} \quad (2.25)$$

$$\lambda_{i1}^j = \begin{cases} \text{sgn}(F_X) & \text{if } GE_{i1}^j \sin \alpha_{i1}^j = 0 \\ \text{sgn}(GE_{i1}^j \sin \alpha_{i1}^j) & \text{otherwise} \end{cases} \quad (2.26)$$

2.1 Geometric closure on outer ring

First geometric closure involves that outer ring does not move :

$$\mathbf{C}_{o1}^j \mathbf{C}_{o2}^j = g_o \mathbf{x}_G \quad (2.27)$$

In this equation, we introduce ball center B^j in order to get functions of $\mathbf{B}^j \mathbf{C}_{om}^j$ vectors:

$$\mathbf{C}_{o1}^j \mathbf{B}^j + \mathbf{B}^j \mathbf{C}_{o2}^j = g_o \mathbf{x}_G \quad (2.28)$$

Finally, we project relation (2.28) on \mathbf{x}_G and \mathbf{y}_{b1}^j axis to obtain two geometric equations (2.29), (2.30) on the outer ring.

$$f_{ORx}^j = GE_{o1}^j \sin \alpha_{o1}^j + GE_{o2}^j \sin \alpha_{o2}^j - g_o \lambda_o^j = 0 \quad (2.29)$$

$$f_{ORy}^j = GE_{o1}^j \cos \alpha_{o1}^j - GE_{o2}^j \cos \alpha_{o2}^j = 0 \quad (2.30)$$

2.2 Geometric closure on inner ring

Second geometric closure involves that inner ring rotates :

$$\mathbf{C}_{i1}^j \mathbf{C}_{i2}^j = g_i \mathbf{x}_{i1} \quad (2.31)$$

Similarly, we introduce ball center B^j in order to get functions of $\mathbf{B}^j \mathbf{C}_{im}^j$ vectors:

$$\mathbf{C}_{i1}^j \mathbf{B}^j + \mathbf{B}^j \mathbf{C}_{i2}^j = g_i \mathbf{x}_{i1} \quad (2.32)$$

We express \mathbf{x}_{i1} vector in ball coordinate system \mathcal{R}_{b1}^j :

$$\mathbf{x}_{i1} = \begin{bmatrix} \cos \theta_y \cos \theta_z \\ \cos \psi^j \sin \theta_z - \sin \psi^j \sin \theta_y \cos \theta_z \\ -\sin \psi^j \sin \theta_z - \cos \psi^j \sin \theta_y \cos \theta_z \end{bmatrix}_{\mathcal{R}_{b1}^j} \quad (2.33)$$

Finally, we project relation (2.32) on \mathbf{x}_G and \mathbf{y}_{b1}^j axis to obtain two geometric equations (2.34), (2.35) on the inner ring.

$$f_{IRx}^j = GE_{i1}^j \sin \alpha_{i1}^j + GE_{i2}^j \sin \alpha_{i2}^j - g_i \lambda_i^j \cos \theta_z \cos \theta_y = 0 \quad (2.34)$$

$$f_{IRy}^j = -GE_{i1}^j \cos \alpha_{i1}^j + GE_{i2}^j \cos \alpha_{i2}^j - g_i \lambda_i^j (\cos \psi^j \sin \theta_z - \sin \psi^j \sin \theta_y \cos \theta_z) = 0 \quad (2.35)$$

2.3 Geometric closure on inner and outer ring

To consider relative displacements between inner and outer ring, we make a geometric closure that uses a curvature center on each ring and each side:

$$\mathbf{C}_{i1}^j \mathbf{B}^j + \mathbf{B}^j \mathbf{C}_{o2}^j + \mathbf{C}_{o2}^j \mathbf{C}_{i1}^{j\text{ini}} = \mathbf{C}_{i1}^j \mathbf{G}_{i1} + \mathbf{G}_{i1} \mathbf{G} + \mathbf{G} \mathbf{C}_{i1}^{j\text{ini}} \quad (2.36)$$

Then, we detail each component of equation (2.36):

$$\mathbf{C}_{i1}^j \mathbf{B}^j + \mathbf{B}^j \mathbf{C}_{o2}^j = GE_{i1}^j \begin{bmatrix} \sin \alpha_{i1}^j \\ -\cos \alpha_{i1}^j \\ 0 \end{bmatrix}_{\mathcal{R}_b^j} + GE_{o2}^j \begin{bmatrix} \sin \alpha_{o2}^j \\ -\cos \alpha_{o2}^j \\ 0 \end{bmatrix}_{\mathcal{R}_b^j} \quad (2.37)$$

$$\mathbf{C}_{o2}^j \mathbf{C}_{i1}^{j\text{ini}} = \begin{bmatrix} -(\frac{g_o}{2} \lambda_{o2}^j + \frac{g_i}{2} \lambda_{i1}^j) \\ A \cos \alpha_f \\ 0 \end{bmatrix}_{\mathcal{R}_b^j}, \text{ with } A = |\mathbf{C}_{o2}^j \mathbf{C}_{i1}^{j\text{ini}}| = (f_o + f_i - 1)D \quad (2.38)$$

$$\begin{aligned} \mathbf{C}_{i1}^j \mathbf{G}_{i1} &= \begin{bmatrix} \frac{g_i}{2} \lambda_i^j \\ -(\frac{d_m}{2} + (f_i - 0.5)D \cos \alpha_f) \cos \psi^j \\ -(\frac{d_m}{2} + (f_i - 0.5)D \cos \alpha_f) \sin \psi^j \end{bmatrix}_{\mathcal{R}_{i1}} = \begin{bmatrix} -R_1 \\ -R_2 \cos \psi^j \\ -R_2 \sin \psi^j \end{bmatrix}_{\mathcal{R}_{i1}} \\ &= \begin{bmatrix} -R_1 \cos \theta_y \cos \theta_z + R_2 \cos \psi^j \cos \theta_y \sin \theta_z - R_2 \sin \psi^j \sin \theta_y \\ -R_1 \sin \theta_z - R_2 \cos \psi^j \cos \theta_z \\ R_1 \sin \theta_y \cos \theta_z - R_2 \cos \psi^j \sin \theta_z \sin \theta_y - R_2 \sin \psi^j \cos \theta_y \end{bmatrix}_{\mathcal{R}_G} \end{aligned} \quad (2.39)$$

$$\mathbf{G}_{i1} \mathbf{G} = \begin{bmatrix} -\delta_x \\ -\delta_y \\ -\delta_z \end{bmatrix}_{\mathcal{R}_G} \quad (2.40)$$

$$\mathbf{G} \mathbf{C}_{i1}^{j\text{ini}} = \begin{bmatrix} R_1 \\ R_2 \cos \psi^j \\ R_2 \sin \psi^j \end{bmatrix}_{\mathcal{R}_G} \quad (2.41)$$

Finally, we add these vectors and project the sum on \mathbf{x}_G and \mathbf{y}_{b1}^j to get geometric equations (2.42), (2.43) on inner and outer rings.

$$\begin{aligned} f_{I\text{ROR}x}^j &= -GE_{i1}^j \sin \alpha_{i1}^j - GE_{o2}^j \sin \alpha_{o2}^j + \left(\frac{g_o}{2} \lambda_{o2}^j + \frac{g_i}{2} \lambda_{i1}^j \right) \\ &\quad - \delta_x + R_1 - R_1 \cos \theta_y \cos \theta_z + R_2 \cos \psi^j \cos \theta_y \sin \theta_z - R_2 \sin \psi^j \sin \theta_y \end{aligned} \quad (2.42)$$

$$\begin{aligned} f_{I\text{ROR}y}^j &= GE_{i1}^j \cos \alpha_{i1}^j + GE_{o2}^j \cos \alpha_{o2}^j + [-\delta_y - R_1 \sin \theta_z - R_2 \cos \psi^j \cos \theta_z] \cos \psi^j \\ &\quad - A \cos \alpha_f + [-\delta_z + R_1 \sin \theta_y \cos \theta_z - R_2 \cos \psi^j \sin \theta_y \sin \theta_z - R_2 \sin \psi^j \cos \theta_y] \sin \psi^j + R_2 \end{aligned} \quad (2.43)$$

2.4 Choice of equations depending on rings truncations

Depending on bearing type and especially depending on ring truncations, certain races will never get more than one contact point. In such a case, geometric equations presented above are no longer valid. That is why, for each bearing we distinguish four possible configurations that are function of ring truncations. Then, depending on the bearing studied, a set of geometric equations adapted to truncations is applied. Description of these configurations and corresponding equations are summarized in Table 2.2.

Note that configuration 0 defines DGBB. Configuration 2 defines ACBB that are mostly used in high speed applications. Configuration 3 describes bearings less frequently used like those present in wind turbines or tower cranes.

Configuration	0	1	2	3
Truncations	$g_i = g_o = 0$ No truncation	$g_i = 0, g_o \neq 0$ OR truncated	$g_i \neq 0, g_o = 0$ IR truncated	$g_i \neq 0, g_o \neq 0$ OR+IR truncated
Contacts	0-1 point on IR 1 point on OR	0-1 point on IR 1-2 points on OR	0-2 points on IR 1 point on OR	0-2 points on IR 1-2 points on OR
$LMCC^j$	1, 3, 8, 10 or 11	1, 2, 3, 4, 7, 8, 10 or 11	1, 3, 5, 8, 9, 10 or 11	1, 2, 3, 4, 5, 7, 8, 9, 10 or 11
Geometric equations	$\alpha_{i2}^j = \delta_{i2}^j = 0$	$\alpha_{i2}^j = \delta_{i2}^j = 0$	IR along $\mathbf{x}_G, \mathbf{y}_{b1}^j$	IR along $\mathbf{x}_G, \mathbf{y}_{b1}^j$
	$\alpha_{o1}^j = \delta_{o1}^j = 0$	OR along $\mathbf{x}_G, \mathbf{y}_{b1}^j$	$\alpha_{o1}^j = \delta_{o1}^j = 0$	OR along $\mathbf{x}_G, \mathbf{y}_{b1}^j$
	IR - OR along $\mathbf{x}_G, \mathbf{y}_{b1}^j$	IR - OR along $\mathbf{x}_G, \mathbf{y}_{b1}^j$	IR - OR along $\mathbf{x}_G, \mathbf{y}_{b1}^j$	IR - OR along $\mathbf{x}_G, \mathbf{y}_{b1}^j$

Table 2.2 : Bearing configurations and corresponding equations

3 Ball kinematic

Ball kinematic is directly related to interactions with inner and outer race, especially with ω_i and ω_o , the relative angular velocity of inner and outer race. The operating pitch diameter \bar{d}_m , represented in Figure 2.8, is defined by :

$$\bar{d}_m = d_m + 2[(f_o - 0.5)D + \delta_{o2}] \cos \alpha_{o2} - 2(f_o - 0.5)D \cos \alpha_f \quad (2.44)$$

At each ball-race contact, R_k defines the radius of deformed pressure surface in plane of major axis of pressure ellipse. It is calculated by averaging radii of balls and raceway curvatures:

$$R_k = \frac{2f_k D}{2f_k + 1} \text{ with } k = i, o \quad (2.45)$$

3.1 Detailed computation for outer race, side 2

On contact ellipse located at the outer race, side 2, because of outer race relative rotation, each point (X_{o2}, Z_{o2}) on ball j has the translational velocity $\mathbf{V}_{b/o2}(I_{o2})$:

$$\begin{aligned}\mathbf{V}_{b/o2}(I_{o2}) &= \mathbf{V}_{b/o2}(G_{i1}) + \mathbf{I}_{o2} \mathbf{G}_{i1} \wedge \boldsymbol{\Omega}_{b/o2} \\ &= \mathbf{0} - \left(\frac{\bar{d}_m}{2} \mathbf{y}_{b1}^j + \bar{r}_{o2} \bar{\mathbf{Y}}_{o2} \right) \wedge -\omega_o \mathbf{x}_G \\ \mathbf{V}_{b/o2}(I_{o2}) &= \left(-\frac{\bar{d}_m}{2} \omega_o - \bar{r}_{o2} \omega_o \cos \alpha_{o2} \right) \bar{\mathbf{Z}}_{o2}\end{aligned}\tag{2.47}$$

As well, each point (X_{o2}, Z_{o2}) on ball j has the translational velocity $\mathbf{V}_b(I_{o2})$ due to ball self-rotation:

$$\begin{aligned}\mathbf{V}_b(I_{o2}) &= \mathbf{V}_b(B^j) + \mathbf{I}_{o2} \mathbf{B}^j \wedge \boldsymbol{\omega}_R \\ &= \mathbf{0} - \bar{r}_{o2} \bar{\mathbf{Y}}_{o2} \wedge \omega_R \mathbf{x}_{b3}^j \\ \mathbf{V}_b(I_{o2}) &= \begin{bmatrix} -\bar{r}_{o2} \omega_z \\ 0 \\ \bar{r}_{o2} (\omega_x \cos \alpha_{o2} + \omega_y \sin \alpha_{o2}) \end{bmatrix}_{\bar{\mathbf{R}}_{o2}}\end{aligned}\tag{2.48}$$

Then, at side 2, V_{Xo2} and V_{Zo2} , ball velocities relative to outer race in $\bar{\mathbf{X}}_{o2}$ and $\bar{\mathbf{Z}}_{o2}$ directions, are expressed by :

$$V_{Xo2} = \left(\mathbf{V}_{b/o2}(I_{o2}) + \mathbf{V}_b(I_{o2}) \right) \cdot \bar{\mathbf{X}}_{o2} = -\bar{r}_{o2} \omega_z\tag{2.49}$$

$$V_{Zo2} = \left(\mathbf{V}_{b/o2}(I_{o2}) + \mathbf{V}_b(I_{o2}) \right) \cdot \bar{\mathbf{Z}}_{o2} = -\frac{\bar{d}_m}{2} \omega_o - \bar{r}_{o2} \omega_o \cos \alpha_{o2} + \bar{r}_{o2} (\omega_x \cos \alpha_{o2} + \omega_y \sin \alpha_{o2})\tag{2.50}$$

Similarly, each point (X_{o2}, Z_{o2}) on ball j has the rotational speed $\boldsymbol{\Omega}_{b/o2}$ due to outer race relative rotation and $\boldsymbol{\Omega}_b$ due to ball self-rotation.

$$\boldsymbol{\Omega}_{b/o2} = -\omega_o \mathbf{x}_G = \begin{bmatrix} -\omega_o \cos \alpha_{o2} \\ \omega_o \sin \alpha_{o2} \\ 0 \end{bmatrix}_{\bar{\mathbf{R}}_{o2}}\tag{2.51}$$

$$\boldsymbol{\Omega}_b = \omega_r \mathbf{x}_{b3}^j = \begin{bmatrix} \omega_x \cos \alpha_{o2} + \omega_y \sin \alpha_{o2} \\ -\omega_x \sin \alpha_{o2} + \omega_y \cos \alpha_{o2} \\ \omega_z \end{bmatrix}_{\bar{\mathbf{R}}_{o2}}\tag{2.52}$$

Then, ball-race rolling speed ω_{Ro2} and spinning speed ω_{So2} are calculated:

$$\omega_{Ro2} = \left(\boldsymbol{\Omega}_{b/o2} + \boldsymbol{\Omega}_b \right) \cdot \bar{\mathbf{X}}_{o2} = -\omega_o \cos \alpha_{o2} + \omega_x \cos \alpha_{o2} + \omega_y \sin \alpha_{o2}\tag{2.53}$$

$$\omega_{So2} = \left(\boldsymbol{\Omega}_{b/o2} + \boldsymbol{\Omega}_b \right) \cdot \bar{\mathbf{Y}}_{o2} = \omega_o \sin \alpha_{o2} - \omega_x \sin \alpha_{o2} + \omega_y \cos \alpha_{o2}\tag{2.54}$$

3.2 Kinematic synthesis at 4 contacts

- Relative speeds on outer race, side 2

In above kinematic relations, we can replace ball-self rotations ω_x , ω_y , ω_z by their developed expressions (2.17). Then, ball kinematics at outer race, side 2 can be expressed by:

$$V_{Xo2} = \omega_R \bar{r}_{o2} \cos \beta \sin \beta' \quad (2.55)$$

$$V_{Zo2} = -\frac{\bar{d}_m \omega_o}{2} + \bar{r}_{o2} \omega_o \left[-\cos \alpha_{o2} + \frac{\omega_R}{\omega_o} (\cos \beta \cos \beta' \cos \alpha_{o2} + \sin \beta \sin \alpha_{o2}) \right] \quad (2.56)$$

$$\omega_{Ro2} = \omega_o \left[-\cos \alpha_{o2} + \frac{\omega_R}{\omega_o} (\cos \beta \cos \beta' \cos \alpha_{o2} + \sin \beta \sin \alpha_{o2}) \right] \quad (2.57)$$

$$\omega_{So2} = -\omega_o \left[-\sin \alpha_{o2} + \frac{\omega_R}{\omega_o} (\cos \beta \cos \beta' \sin \alpha_{o2} - \sin \beta \cos \alpha_{o2}) \right] \quad (2.58)$$

Using different projections, same procedure is applied at the three other ball-race contacts to compute translational velocities, spinning and rolling speeds. Corresponding expressions are synthesized below by relations (2.59) to (2.70).

- Relative speeds on outer race, side 1

$$V_{Xo1} = \omega_R \bar{r}_{o1} \cos \beta \sin \beta' \quad (2.59)$$

$$V_{Zo1} = -\frac{\bar{d}_m \omega_o}{2} + \bar{r}_{o1} \omega_o \left[-\cos \alpha_{o1} + \frac{\omega_R}{\omega_o} (\cos \beta \cos \beta' \cos \alpha_{o1} - \sin \beta \sin \alpha_{o1}) \right] \quad (2.60)$$

$$\omega_{Ro1} = \omega_o \left[-\cos \alpha_{o1} + \frac{\omega_R}{\omega_o} (\cos \beta \cos \beta' \cos \alpha_{o1} - \sin \beta \sin \alpha_{o1}) \right] \quad (2.61)$$

$$\omega_{So1} = -\omega_o \left[\sin \alpha_{o1} - \frac{\omega_R}{\omega_o} (\cos \beta \cos \beta' \sin \alpha_{o1} + \sin \beta \cos \alpha_{o1}) \right] \quad (2.62)$$

- Relative speeds on inner race, side 1

$$V_{Xi1} = \omega_R \bar{r}_{i1} \cos \beta \sin \beta' \quad (2.63)$$

$$V_{Zi1} = -\frac{\bar{d}_m \omega_i}{2} + \bar{r}_{i1} \omega_i \left[\cos \alpha_{i1} - \frac{\omega_R}{\omega_i} (\cos \beta \cos \beta' \cos \alpha_{i1} + \sin \beta \sin \alpha_{i1}) \right] \quad (2.64)$$

$$\omega_{Ri1} = \omega_i \left[\cos \alpha_{i1} - \frac{\omega_R}{\omega_i} (\cos \beta \cos \beta' \cos \alpha_{i1} + \sin \beta \sin \alpha_{i1}) \right] \quad (2.65)$$

$$\omega_{Si1} = -\omega_i \left[\sin \alpha_{i1} + \frac{\omega_R}{\omega_i} (-\cos \beta \cos \beta' \sin \alpha_{i1} + \sin \beta \cos \alpha_{i1}) \right] \quad (2.66)$$

- Relative speeds on inner race, side 2

$$V_{Xi2} = \omega_R \bar{r}_{i2} \cos \beta \sin \beta' \quad (2.67)$$

$$V_{Zi2} = -\frac{\bar{d}_m \omega_i}{2} + \bar{r}_{i2} \omega_i \left[\cos \alpha_{i2} - \frac{\omega_R}{\omega_i} (\cos \beta \cos \beta' \cos \alpha_{i2} - \sin \beta \sin \alpha_{i2}) \right] \quad (2.68)$$

$$\omega_{Ri2} = \omega_i \left[\cos \alpha_{i2} - \frac{\omega_R}{\omega_i} (\cos \beta \cos \beta' \cos \alpha_{i2} - \sin \beta \sin \alpha_{i2}) \right] \quad (2.69)$$

$$\omega_{Si2} = -\omega_i \left[-\sin \alpha_{i2} + \frac{\omega_R}{\omega_i} (\cos \beta \cos \beta' \sin \alpha_{i2} + \sin \beta \cos \alpha_{i2}) \right] \quad (2.70)$$

Note that these kinematic results are different than those presented in literature by Jones [144] or Harris [121]. It is because we define ball motion in a direct coordinate system whereas Jones and Harris work in an indirect one.

3.3 Point of pure rolling

When ball and race translational velocities are equal, pure rolling occurs at the effective rolling radius r'_{km} :

$$\mathbf{V}_b(\mathbf{I}_{km}) = \mathbf{V}_{b/km}(\mathbf{I}_{km}) \quad (2.71)$$

Consequently, kinematic relations (2.72) to (2.75) applies.

$$-\omega_i \cos \alpha_{i1} \left(\frac{\bar{d}_m}{2 \cos \alpha_{i1}} - r'_{i1} \right) = r'_{i1} (\omega_x \cos \alpha_{i1} + \omega_y \sin \alpha_{i1}) \quad (2.72)$$

$$-\omega_i \cos \alpha_{i2} \left(\frac{\bar{d}_m}{2 \cos \alpha_{i2}} - r'_{i2} \right) = r'_{i2} (\omega_x \cos \alpha_{i2} - \omega_y \sin \alpha_{i2}) \quad (2.73)$$

$$-\omega_o \cos \alpha_{o1} \left(\frac{\bar{d}_m}{2 \cos \alpha_{o1}} - r'_{o1} \right) = -r'_{o1} (\omega_x \cos \alpha_{o1} - \omega_y \sin \alpha_{o1}) \quad (2.74)$$

$$-\omega_o \cos \alpha_{o2} \left(\frac{\bar{d}_m}{2 \cos \alpha_{o2}} - r'_{o2} \right) = -r'_{o2} (\omega_x \cos \alpha_{o2} + \omega_y \sin \alpha_{o2}) \quad (2.75)$$

Such equations can be written in a different way as in (2.76) to (2.83). However, in this quasi-static problem, r'_{i1} and r'_{o2} are the unknowns of the Newton-Raphson scheme. Then, ξ_1 and ξ_2 are computed with relations (2.76) and (2.79) and r'_{i2} and r'_{o1} are calculated with relations (2.81) and (2.82). In these relations, r'_{km} define the effective rolling radius which is the distance between ball center and a point of pure rolling. This point is not necessarily located on surface ellipse, especially if ball-race sliding occurs. r'_{km} is not to be confused with \bar{r}_{km} , the distance between ball center B^j and a point \bar{X}_{km} on surface ellipse.

$$\xi_1 = \frac{\omega_R}{\omega_i} = \frac{-\frac{\bar{d}_m}{2r'_{i1}} + \cos \alpha_{i1}}{\cos \beta \cos \beta' \cos \alpha_{i1} + \sin \beta \sin \alpha_{i1}} \quad (2.76)$$

$$\xi_1 = \frac{\omega_R}{\omega_i} = \frac{-\frac{\bar{d}_m}{2r'_{i2}} + \cos \alpha_{i2}}{\cos \beta \cos \beta' \cos \alpha_{i2} - \sin \beta \sin \alpha_{i2}} \quad (2.77)$$

$$\xi_2 = \frac{\omega_R}{\omega_o} = \frac{\frac{\bar{d}_m}{2r'_{o1}} + \cos \alpha_{o1}}{\cos \beta \cos \beta' \cos \alpha_{o1} - \sin \beta \sin \alpha_{o1}} \quad (2.78)$$

$$\xi_2 = \frac{\omega_R}{\omega_o} = \frac{\frac{\bar{d}_m}{2r'_{o2}} + \cos \alpha_{o2}}{\cos \beta \cos \beta' \cos \alpha_{o2} + \sin \beta \sin \alpha_{o2}} \quad (2.79)$$

$$r'_{i1} = \frac{-\frac{\bar{d}_m}{2}}{\xi_1 (\cos \beta \cos \beta' \cos \alpha_{i1} + \sin \beta \sin \alpha_{i1}) - \cos \alpha_{i1}} \quad (2.80)$$

$$r'_{i2} = \frac{-\frac{\bar{d}_m}{2}}{\xi_1 (\cos \beta \cos \beta' \cos \alpha_{i2} - \sin \beta \sin \alpha_{i2}) - \cos \alpha_{i2}} \quad (2.81)$$

$$r'_{o1} = \frac{\frac{\bar{d}_m}{2}}{\xi_2 (\cos \beta \cos \beta' \cos \alpha_{o1} - \sin \beta \sin \alpha_{o1}) - \cos \alpha_{o1}} \quad (2.82)$$

$$r'_{o2} = \frac{\frac{\bar{d}_m}{2}}{\xi_2 (\cos \beta \cos \beta' \cos \alpha_{o2} + \sin \beta \sin \alpha_{o2}) - \cos \alpha_{o2}} \quad (2.83)$$

From inner and outer race rotational speeds Ω_i and Ω_o , and from above kinematic relations, we can compute races relative speeds ω_i and ω_o , ball precession speed ω_m and ball self-rotational speed ω_R . Is this way, all ball kinematics is defined.

$$\omega_o = \frac{\xi_1}{\xi_2 - \xi_1} (\Omega_i - \Omega_o) \quad (2.84)$$

$$\omega_i = (\Omega_i - \Omega_o) + \omega_o \quad (2.85)$$

$$\omega_m = \Omega_o - \omega_o \quad (2.86)$$

$$\omega_R = \frac{(\Omega_i - \Omega_o) \xi_2 \xi_1}{(\xi_2 - \xi_1)} \quad (2.87)$$

4 Forces definition

4.1 External forces on the inner ring

Inner ring is subject to external forces caused by many factors such as preloads or shaft misalignments. Corresponding torsor $\mathcal{T}_{ext/IR}^j$ is defined at bearing center G in global coordinate system \mathcal{R}_G .

$$\mathcal{T}_{ext/IR}^j = \left\{ \begin{array}{ccc} -F_X & -F_Y & -F_Z \\ 0 & -M_Y & -M_Z \end{array} \right\}_{\mathcal{R}_G} \quad (2.88)$$

4.2 Forces due to ball motion

Ball self-rotation and ball orbital motion result in inertia and drag forces gathered in torsor $\mathcal{T}_{/b}^j$ defined at ball center B^j in ball coordinate system \mathcal{R}_{b1}^j .

$$\mathcal{T}_{/b}^j = \left\{ \begin{array}{ccc} 0 & F_c^j & F_{dr}^j \\ 0 & M_{GY}^j & M_{GZ}^j \end{array} \right\}_{\mathcal{R}_{b1}^j} \quad (2.89)$$

Indeed, because of their orbital motion, each ball of mass m_b , is subject to a centrifugal force F_c^j directed along the outer normal \mathbf{y}_{b1}^j :

$$F_c^j = m_b \frac{\bar{d}_m}{2} (\omega_m^j)^2 \quad (2.90)$$

As well, because of their self-rotation, each ball of inertia momentum I_b , is subject to a gyroscopic momentum M_{GY}^j along \mathbf{y}_{b1}^j and M_{GZ}^j along \mathbf{z}_{b1}^j :

$$M_{GY}^j = -I_b \omega_R^j \omega_m^j \cos \beta^j \sin \beta'^j \quad (2.91)$$

$$M_{GZ}^j = -I_b \omega_R^j \omega_m^j \sin \beta^j \quad (2.92)$$

Similarly, because of their orbital motion, balls move throughout lubricant in ortho-radial direction \mathbf{z}_{b1}^j . This creates an oleodynamic force or drag force F_{dr}^j in the opposite direction. This force can be expressed by relation (2.93) with a simple drag model defined in SI units. From experimental results, Harris' [121] developed a comparable relation expressed in (2.94) in anglo-saxon units (lb, inch, s).

$$F_{dr}^j = -\frac{1}{2} C_d \rho_m \left(\frac{\pi D^2}{4} \right) \left(\frac{\omega_m^j \bar{d}_m}{2} \right)^2 \quad (2.93)$$

$$F_{dr}^j = -\frac{C_d \pi \rho_m D^2 (\omega_m^j \bar{d}_m)^{1.95}}{32g} \quad (2.94)$$

In both expressions, C_d is the drag coefficient set by BB20 user. Its value varies with Reynolds number such as reported by Schlichting [229]. As well, ρ_m is air/oil lubricant mixture density. If f_{oil} , the oil fraction in the mixture, is known, ρ_m can be calculated by relation (2.95). Otherwise, if W_{lub} , the lubricant flow, is known, XCAV, the oil percentage in the mixture, can be calculated from Parker [202] relation defined in (2.96). In this expression XCAV is in percent, W_{lub} in cm^3/min , d_m in mm and N_i in rpm .

$$\rho_m = f_{oil} \rho_{oil} + (1 - f_{oil}) \rho_{air} \quad (2.95)$$

$$XCAV = 100 \rho_m = \frac{10^7 (W_{lub})^{0.37}}{N_i d_m^{1.7}} \quad (2.96)$$

4.3 Coulomb's friction

At each ball-race contact, from the unknown δ_{km}^j , Hertzian theory is applied to compute contact parameters such as normal force Q_{km}^j , contact stiffness K , pressure P_{km}^j or semi-major and semi-minor axes of ellipse a_{km}^j , b_{km}^j .

$$Q_{km}^j = K (\delta_{km}^j)^{\frac{3}{2}} \quad (2.97)$$

Friction forces also act at each contact, they are defined by Coulomb's model presented in Jones' study [144]. In this model, macro-sliding due to ball-race kinematics is considered. Shear stress that depends on contact pressure, is integrated on each point of ellipse surface and corresponding forces are projected along each axis. Especially, as expressed in (2.99), F_{Xkm}^j and M_{Rkm}^j correspond to friction along $\bar{\mathbf{X}}_{km}^j$, F_{Zkm}^j and M_{Zkm}^j along $\bar{\mathbf{Z}}_{km}^j$ and M_{Skm}^j along $\bar{\mathbf{Y}}_{km}^j$. Regarding directions, forces of races on balls are opposed to ball-race velocity at contact such as schematised on Figures 2.9 and 2.10. Consequently, each ball-race contact is represented by the torsor $\mathcal{T}_{km/b}^j$ defined at ball center B^j , in ball-race contact coordinate system $\bar{\mathcal{R}}_{km}^j$.

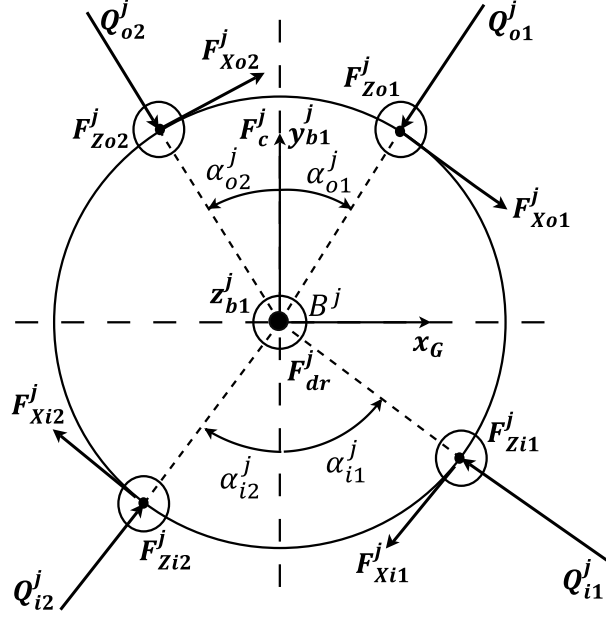


Figure 2.9 : Contact forces acting on each ball

$$\mathcal{T}_{km/b}^j = \left\{ \begin{array}{ccc} F_{Xkm}^j & -Q_{km}^j & F_{Zkm}^j \\ M_{Rkm}^j & M_{Skm}^j & M_{Zkm}^j \end{array} \right\}_{\bar{\mathcal{R}}_{km}^j} \quad (2.98)$$

$$\begin{aligned} F_{Xkm}^j &= \frac{3Q_{km}^j\mu}{2\pi} \int_{-1}^1 \int_{-\sqrt{1-q^2}}^{\sqrt{1-q^2}} \sqrt{1-q^2-t^2} \sin \varphi \, dt dq \\ F_{Zkm}^j &= \frac{3Q_{km}^j\mu}{2\pi} \int_{-1}^1 \int_{-\sqrt{1-q^2}}^{\sqrt{1-q^2}} \sqrt{1-q^2-t^2} \cos \varphi \, dt dq \\ M_{Rkm}^j &= \frac{3Q_{km}^j\mu}{2\pi} \int_{-1}^1 \int_{-\sqrt{1-q^2}}^{\sqrt{1-q^2}} \bar{r} \sqrt{1-q^2-t^2} \cos \varphi \, dt dq \\ M_{Skm}^j &= \frac{3Q_{km}^j\mu a}{2\pi} \int_{-1}^1 \int_{-\sqrt{1-q^2}}^{\sqrt{1-q^2}} \sqrt{1-q^2-t^2} \sqrt{q^2 + \frac{t^2}{k^2}} \cos(\varphi - \theta) \, dt dq \\ M_{Zkm}^j &= \frac{3Q_{km}^j\mu}{2\pi} \int_{-1}^1 \int_{-\sqrt{1-q^2}}^{\sqrt{1-q^2}} \bar{r} \sqrt{1-q^2-t^2} \sin \varphi \, dt dq \end{aligned} \quad (2.99)$$

with

$$\begin{aligned} q &= \frac{X}{a}, \quad t = \frac{Z}{b}, \quad k = \frac{a}{b}, \quad \tan \theta = \left(\frac{Z}{X} \right) = \left(\frac{t}{kq} \right) \\ \tan \varphi &= \left(\frac{\rho \omega_S^j \sin \theta + V_X^j}{-\rho \omega_S^j \cos \theta - V_Z^j} \right) = \left(\frac{Z \omega_S^j + V_X^j}{-X \omega_S^j - V_Z^j} \right) = \left(\frac{\frac{t}{k} + \frac{V_X^j}{a \omega_S^j}}{-q - \frac{V_Z^j}{a \omega_S^j}} \right) \end{aligned} \quad (2.100)$$

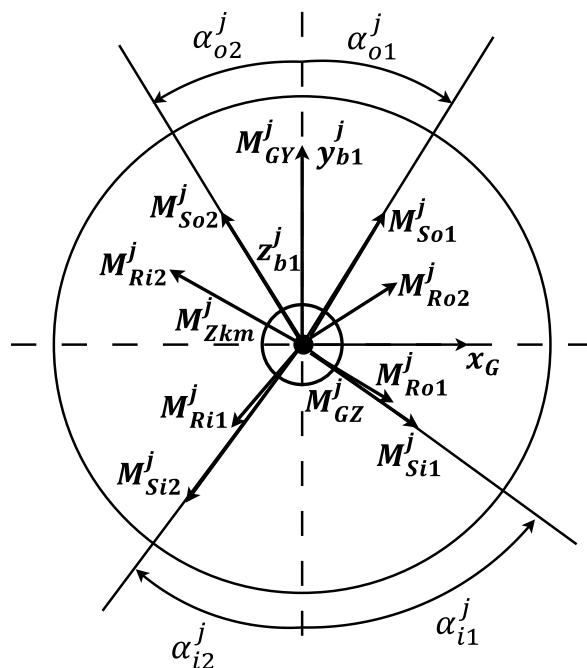


Figure 2.10 : Contact momentums acting on each ball

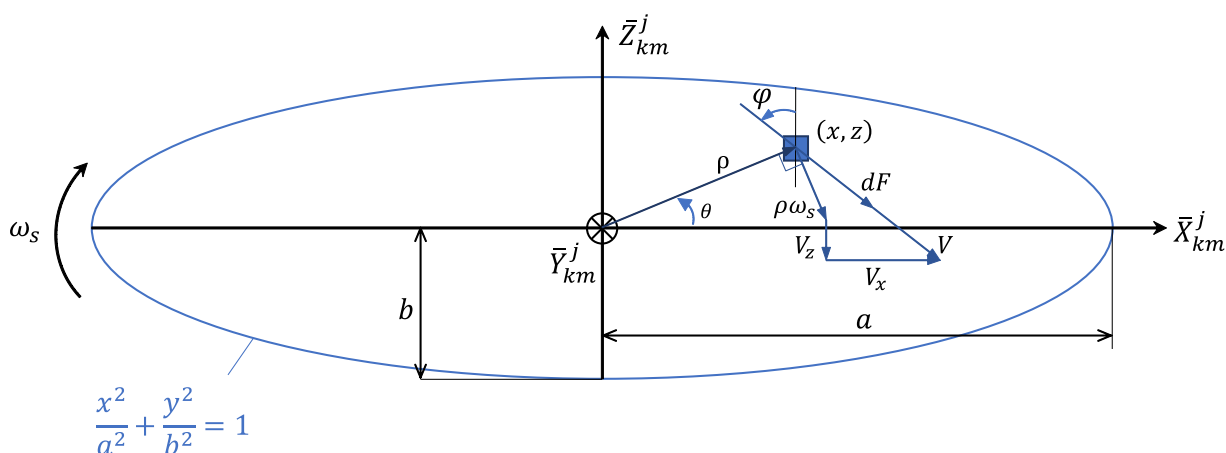


Figure 2.11 : Coulomb's parameters definition

Note that in previous BB20 (version 4), $\cos\varphi$, $\sin\varphi$ and $\cos(\varphi-\theta)$ were calculated by trigonometric relations. However, we noticed that these relations, just like *arctan* function, were valid on $] -\frac{\pi}{2}; \frac{\pi}{2}[$ interval. That is why, in this new version, φ and θ are calculated by *arctan2* function which is valid on $] -\pi; \pi[$ interval.

As well, in BB20V4, F_{Xkm}^j , F_{Zkm}^j and M_{Rkm}^j were projected in an opposite direction than in BB20V5. Is this way torsor $\mathcal{T}_{km/b}^j$ was defined like in Jones' model. However, to have opposite friction forces and sliding speeds, torsor defined in (2.98) is according to us the correct one.

5 Friction forces computation

5.1 Analytic expressions

Integrals (2.99) must be solved numerically. To begin, we express all of them by the general form (2.101). Then, variable change $x = a\bar{x}$ and $z = b\tilde{z}\sqrt{1-\bar{x}^2}$ is applied to get relation (2.102). To solve this last one, different methods with more or less advantages can be used.

$$I = \int_{-a}^a \int_{-b\sqrt{1-(\frac{x}{a})^2}}^{b\sqrt{1-(\frac{x}{a})^2}} \sqrt{1-\left(\frac{x}{a}\right)^2 - \left(\frac{z}{b}\right)^2} f(x, z) dz dx \quad (2.101)$$

$$I = ab \int_{-1}^1 (1-\bar{x}^2) \int_{-1}^1 \sqrt{1-\tilde{z}^2} f(a\bar{x}, b\tilde{z}\sqrt{1-\bar{x}^2}) d\tilde{z} d\bar{x} \quad (2.102)$$

5.1.1 Gupta's method

To solve such integrals, Gupta [91] proposed to apply the polar variable change $x = ar \cos \theta$ and $z = br \sin \theta$, in order to get relation (2.103), also written in (2.104).

$$I = ab \int_0^1 r \sqrt{1-r^2} \int_0^{2\pi} f(ar \cos \theta, br \sin \theta) d\theta dr \quad (2.103)$$

$$I = ab \int_0^1 \sqrt{1-r^2} F(r) dr \text{ with } F(r) = r \int_0^{2\pi} f(ar \cos \theta, br \sin \theta) d\theta \quad (2.104)$$

To evaluate the inner integral $F(r)$, midpoint method is applied. It consists in dividing integration domain into $2m$ equal sections. Integral of each section $[c; d]$ is approximated by a rectangle centered in the middle as expressed by relation (2.105). The whole integral is obtained by adding all of these contributions.

$$\int_c^d f(x) dx = (d-c) f\left(\frac{c+d}{2}\right) \quad (2.105)$$

Brought back to our problem, $F(r)$ integral is partitioned into $2m$ rectangles from 0 to 2π , and midpoint method is applied to get relation (2.106). Geometrically, m represents the number of equally spaced points on a circle of radius r .

$$F(r) \approx \frac{\pi r}{m} \sum_{i=1}^{2m} f\left(ar \cos\left(\frac{\pi i}{m}\right), br \sin\left(\frac{\pi i}{m}\right)\right) \quad (2.106)$$

Regarding outer integral, by its form, it can be approximated by Gauss-Chebyshev quadrature but limited to $[0; 1]$ interval instead of $[-1; 1]$. Then, expression (2.107) is obtained where w_j and r_j are weights and roots related to this quadrature. Corresponding values for $n = 5$ are synthesized in Table 2.3.

$$\int_0^1 \sqrt{1-r^2} F(r) dr \approx \sum_{j=1}^n w_j F(r_j) \quad (2.107)$$

j	r_j	w_j
1	0.04455946723	0.1123147489
2	0.2186940824	0.2209876009
3	0.4743109864	0.2392785529
4	0.7358891185	0.1615816193
5	0.929067427	0.05123564139

Table 2.3 : Roots and weights for $n = 5$

Finally, from inner and outer integral estimations, the initial double integral I is expressed by the following double summation:

$$I \approx ab \sum_{j=1}^n \left[w_j \frac{\pi r_j}{m} \sum_{i=1}^{2m} f \left(ar_j \cos \left(\frac{\pi i}{m} \right), br_j \sin \left(\frac{\pi i}{m} \right) \right) \right] \quad (2.108)$$

Gupta estimated that $m = 72$ and $n = 5$ were adequate to get a good accuracy. However, if this method is time effective, it is also less robust because contact ellipse is meshed with equal elements. Indeed, if mesh can be improved by increasing m or n values, all elements are fixed at the same size. This can cause important integral computation errors when points of zero sliding are met because it causes discontinuous derivatives.

5.1.2 Gauss-Legendre's method

Development of this method was initially inspired by Legrand's work [159] implemented in RBL4 code. However, study of contact ellipses led us to use different Gaussian quadratures and to define different partitioning with other directions and with computations adapted to BB20 coordinate systems and kinematics.

To know which quadrature using in order to integrate functions defined in (2.99), we studied evolution of these functions over contact ellipses. As for that, asymptotic expansions of integrands were calculated when ellipse coordinates (x, z) gets closer to values that cancel sliding velocities $(z\omega_S^j + V_X^j)$ and $(-x\omega_S^j - V_Z^j)$. Asymptotic expansions obtained presented finite values. Sliding velocities quotient that corresponds to $\tan \varphi$ function were also plotted for the bearing defined in Table 2.4. For example, $\tan \varphi$ function obtained for first ball is reported in Figure 2.12. All results confirmed that $\tan \varphi$ has finite values. This indicates that integrands do not present singularities over contact ellipses. Then, classical Gauss-Legendre quadrature is suitable to integrate these functions. This quadrature has the advantage to refine mesh at integration limits -1 and 1 .

In this problem, to compute accurately integrals (2.99), mesh should be refined in regions where integrands vary significantly. To identify these regions, integrands of F_{Xkm}^j , F_{Zkm}^j , M_{Skm}^j , M_{Rkm}^j , M_{Zkm}^j and corresponding sliding speeds were plotted. Analysis of integrands showed important variations along x when sign of $(-x\omega_S^j - V_Z^j)$ changes and along z when sign of $(z\omega_S^j + V_X^j)$ changes. This is noticeable if we compare evolution of sliding lines of Figure 2.13, with F_{Xkm}^j integrands of Figure 2.14 and with sliding speeds

of Figure 2.15. This phenomena indicates that zero sliding lines and instantaneous centre of rotation will have to be identified to partition contact ellipses. Then, integrals will be calculated on each portion with Gauss-Legendre quadrature that will improve mesh density in regions where integrand vary significantly. Is this way, discontinuities and errors sources found with Gupta's method will be avoided.

N	D (m)	d_m (m)	J_d (mm)	f_i	f_o	g_i	g_o	F_X (N)	F_Y (N)	Ω_i (rpm)
20	0.019	0.15	0.13	0.52	0.51	$\neq 0$	0	15 000	14 000	17 500

Table 2.4 : Bearing dimensions and working conditions

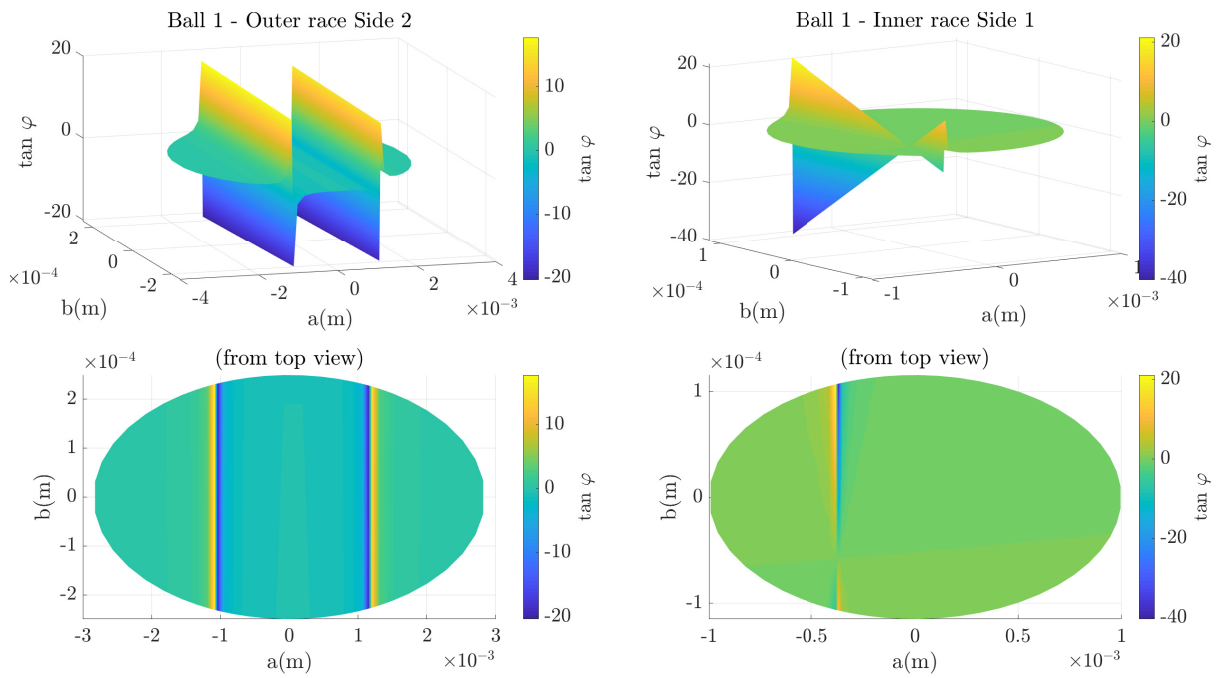


Figure 2.12 : $\tan \varphi$ functions over contact ellipses

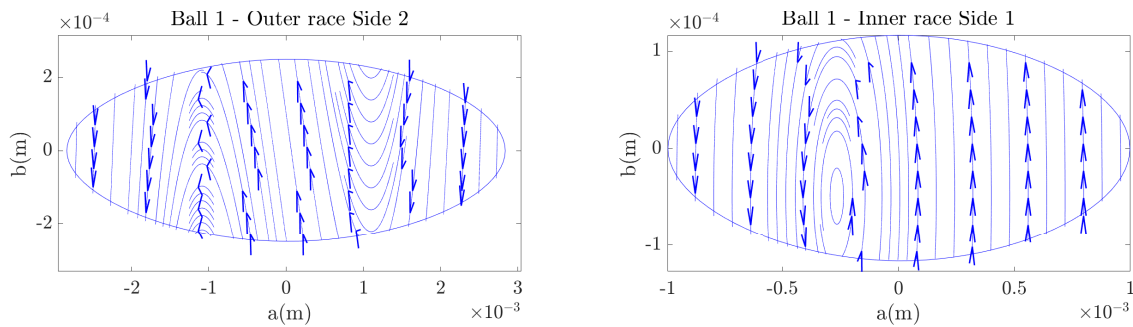


Figure 2.13 : Sliding lines on contact ellipses

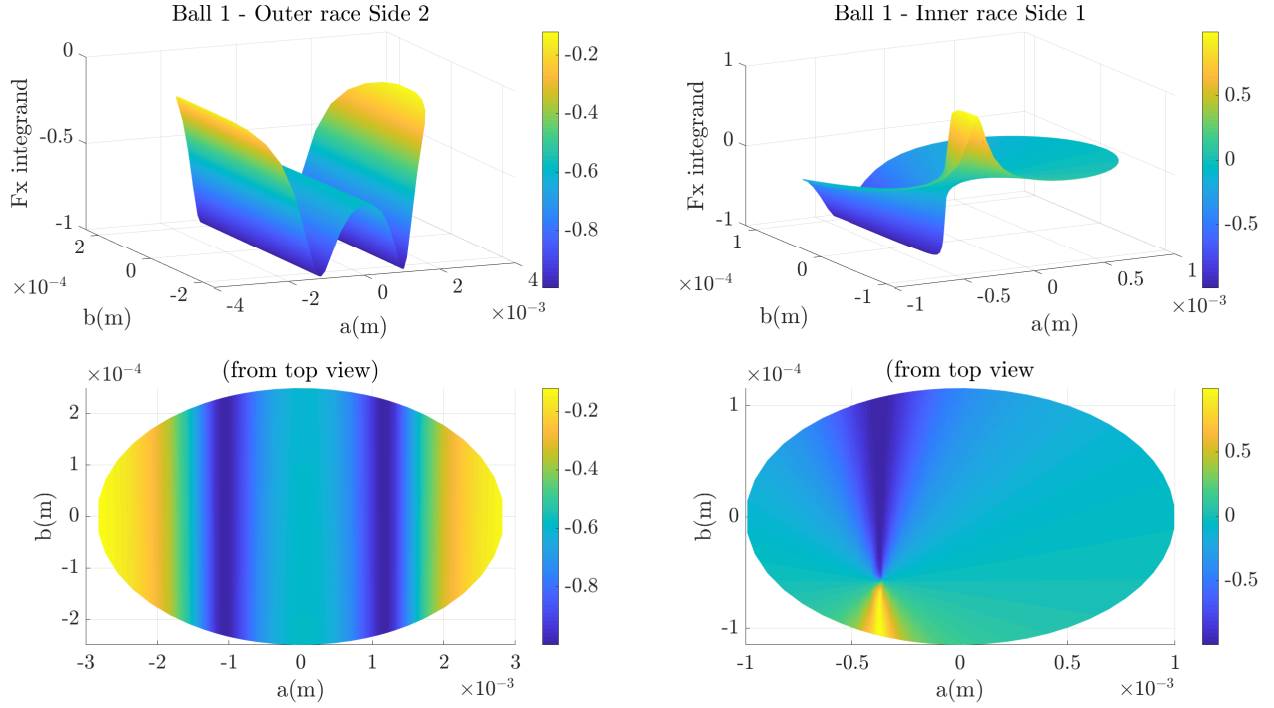


Figure 2.14 : F_{Xkm} integrands over contact ellipses

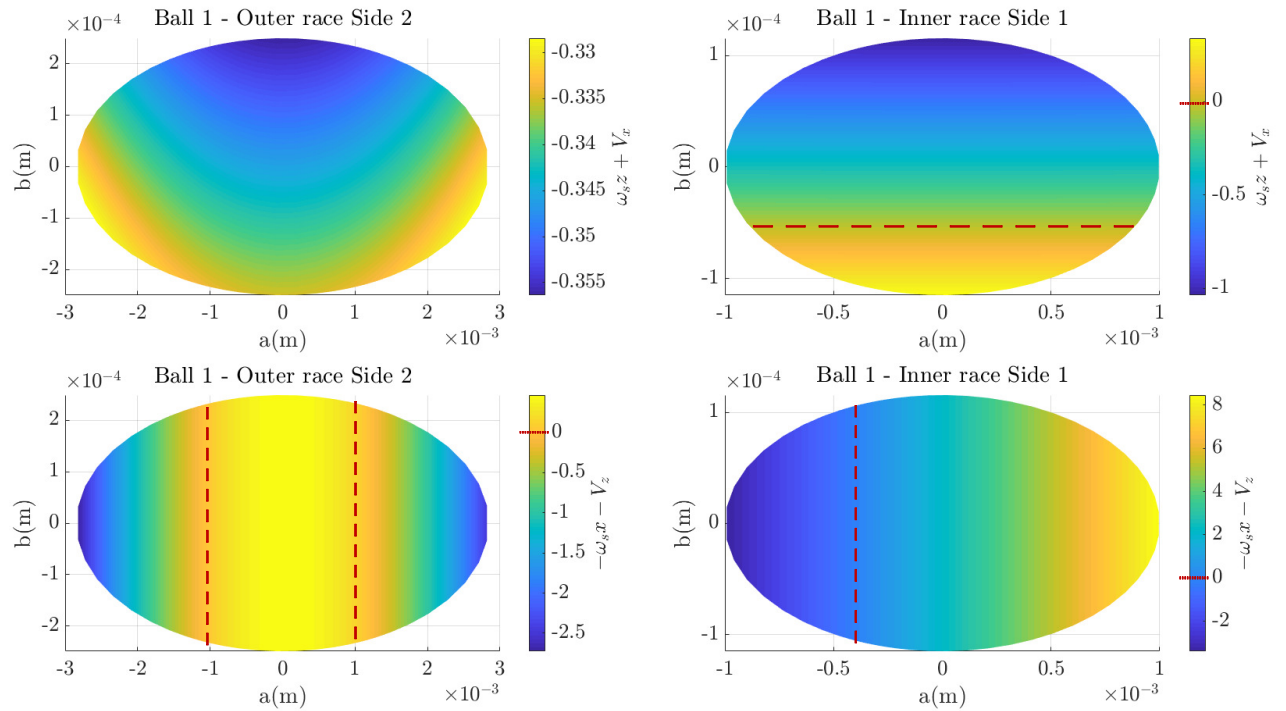


Figure 2.15 : Sliding speeds $-x\omega_s^j - V_Z^j$ and $z\omega_s^j + V_X^j$ over contact ellipses

To begin integral computation, we seek on contact ellipse, for which abscissas x , transverse speeds become equal to zero. According to kinematic relations, V_{Zkm} is a function of x such that:

$$V_{Zkm}(x) = \gamma_1 + \bar{r}_{km}\gamma_2 \text{ with } \bar{r}_{km} = \sqrt{R_k^2 - x^2} + \gamma_3 \quad (2.109)$$

$$\text{and } \gamma_1 = -\frac{\bar{d}_m}{2}\omega_k \quad (2.110)$$

$$\gamma_2 = \begin{cases} \omega_o \left[-\cos \alpha_{o2} + \frac{\omega_R}{\omega_o} (\cos \beta \cos \beta' \cos \alpha_{o2} + \sin \beta \sin \alpha_{o2}) \right] & \text{if } km = o2 \\ \omega_o \left[-\cos \alpha_{o1} + \frac{\omega_R}{\omega_o} (\cos \beta \cos \beta' \cos \alpha_{o1} - \sin \beta \sin \alpha_{o1}) \right] & \text{if } km = o1 \\ \omega_i \left[\cos \alpha_{i1} - \frac{\omega_R}{\omega_i} (\cos \beta \cos \beta' \cos \alpha_{i1} + \sin \beta \sin \alpha_{i1}) \right] & \text{if } km = i1 \\ \omega_i \left[\cos \alpha_{i2} - \frac{\omega_R}{\omega_i} (\cos \beta \cos \beta' \cos \alpha_{i2} - \sin \beta \sin \alpha_{i2}) \right] & \text{if } km = i2 \end{cases} \quad (2.111)$$

$$\gamma_3 = -\sqrt{R_k^2 - a_{km}^2} + \sqrt{\left(\frac{D}{2}\right)^2 - a_{km}^2} \quad (2.112)$$

Consequently, equation (2.113), that defines zero transverse speed, has two solutions x_1 and x_2 expressed in (2.114).

$$-V_{Zkm}(x) - x\omega_{skm} = 0 \quad (2.113)$$

$$x_{1,2} = \frac{-\omega_{skm}(\gamma_1 + \gamma_2\gamma_3) \pm \gamma_2\sqrt{R_k^2(\omega_{skm}^2 + \gamma_2^2) - (\gamma_1 + \gamma_2\gamma_3)^2}}{\omega_{skm}^2 + \gamma_2^2} \quad (2.114)$$

We define $\bar{x}_{1,2} = x_{1,2}/a$ and consider that a solution $\bar{x}_{1,2}$ is correct, that is to say belongs to contact ellipse, if $\bar{x}_{1,2}^2 \leq 1$. In such a case, we set:

$$q_1 = \max(-1, \min(\bar{x}_1, \bar{x}_2)) \quad (2.115)$$

$$q_2 = \min(\max(\bar{x}_1, \bar{x}_2), 1) \quad (2.116)$$

Then, we partition contact ellipse into 1, 2 or 3 zones located between zero sliding abscissas \bar{x}_1 and \bar{x}_2 :

$$\text{zone 1 } \bar{x} \in [v_{1,1}, v_{1,2}] \text{ with } v_{1,1} = -1 \quad v_{1,2} = q_1 \quad (2.117)$$

$$\text{zone 2 } \bar{x} \in [v_{2,1}, v_{2,2}] \text{ with } v_{2,1} = q_1 \quad v_{2,2} = q_2 \quad (2.118)$$

$$\text{zone 3 } \bar{x} \in [v_{3,1}, v_{3,2}] \text{ with } v_{3,1} = q_2 \quad v_{3,2} = 1 \quad (2.119)$$

Mathematically, by partitioning the integral along \bar{x} , expression (2.102) of double integral I becomes:

$$I = ab \sum_{k=1}^3 \left[\int_{v_{k,1}}^{v_{k,2}} (1 - \bar{x}^2) \int_{-1}^1 \sqrt{1 - \bar{z}^2} f(a\bar{x}, b\bar{z}\sqrt{1 - \bar{x}^2}) d\bar{z} d\bar{x} \right] \quad (2.120)$$

Regarding outer integral, variable change $v = \bar{x}$ and $u = \tilde{z}$ gives:

$$J = \int_{v_1}^{v_2} F(v) dv \quad \text{with } F(v) = (1-v^2) \int_{-1}^1 \sqrt{1-u^2} f(av, bu\sqrt{1-v^2}) du \quad (2.121)$$

To apply Gaussian quadrature, J integral must be limited to $[-1; 1]$ interval. That is why variable change $s = \frac{2v-v_1-v_2}{v_2-v_1}$ is applied and we obtain :

$$J = \frac{v_2-v_1}{2} \int_{-1}^1 G(s) ds \quad \text{with } G(s) = F\left(\frac{(v_2-v_1)s + v_2 + v_1}{2}\right) \quad (2.122)$$

This integral can be approximated by Gauss-Legendre quadrature such that:

$$J \approx \frac{v_2-v_1}{2} \sum_{j=1}^{N_k} w_j G(s_j) \quad (2.123)$$

In this expression, w_j and s_j are weights and roots of the quadrature. They are calculated numerically for a given quadrature order N_k . This order corresponds to the number of sections to mesh contact ellipse in each zone k . It is fixed between 2 and 30 and calculated in (2.124) such that total number of sections is close to N_t , the value specified by user.

$$N_k = \begin{cases} \max\left(2, \frac{N_t(v_{k,2}-v_{k,1})}{2}\right) & \text{if } (v_{k,2} - v_{k,1}) > 0 \\ 0 & \text{if } (v_{k,2} - v_{k,1}) \leq 0 \end{cases} \quad (2.124)$$

To compute inner integral, we seek in x_1 or x_2 , if longitudinal speed ($z\omega_s + V_X$) gets equal to zero. In such a case, an instantaneous centre of rotation (ICR) is present on contact ellipse, partitioning along z direction is necessary. This is especially visible on Figure 2.14, for inner ring side 1, where important integrand variations occurs along both x and z directions when approaching the ICR.

To compute ordinates z_1 or z_2 , respectively related to x_1 or x_2 , we apply relation (2.125).

$$z_{1,2} = -\frac{V_{Xkm}(x_{1,2})}{\omega_{skm}(x_{1,2})} \quad (2.125)$$

Then, we define $\bar{z}_{1,2} = z_{1,2}/b$ and consider that an ICR belongs to contact ellipse if $\bar{x}_{1,2}^2 + \bar{z}_{1,2}^2 \leq 1$. In such a case, we set relations (2.126), (2.127), otherwise we set $p_1 = -1$ and/or $p_2 = 1$ to do not partition along z .

$$p_1 = \max(-1, \min(\bar{z}_1, \bar{z}_2)) \quad (2.126)$$

$$p_2 = \min(\max(\bar{z}_1, \bar{z}_2), 1) \quad (2.127)$$

Then, we divide contact ellipse into 1, 2 or 3 zones located between zero sliding ordinates \bar{z}_1 and \bar{z}_2 :

$$\text{zone 1} \quad \bar{z} \in [u_{1,1}, u_{1,2}] \quad \text{with} \quad u_{1,1} = -1 \quad u_{1,2} = p_1 \quad (2.128)$$

$$\text{zone 2} \quad \bar{z} \in [u_{2,1}, u_{2,2}] \quad \text{with} \quad u_{2,1} = p_1 \quad u_{2,2} = p_2 \quad (2.129)$$

$$\text{zone 3} \quad \bar{z} \in [u_{3,1}, u_{3,2}] \quad \text{with} \quad u_{3,1} = p_2 \quad u_{3,2} = 1 \quad (2.130)$$

By partitioning inner integral along z , $F(v)$ expression (2.121) becomes:

$$F(v) = (1-v^2) \sum_{k'=1}^3 \left[\int_{u_{k',1}}^{u_{k',2}} \sqrt{1-u^2} f(av, bu\sqrt{1-v^2}) du \right] \quad (2.131)$$

Again, to limit integral to $[-1;1]$ interval, variable change $s' = \frac{2u-u_1-u_2}{u_2-u_1}$ is applied and we obtain :

$$F(v) = (1-v^2) \sum_{k'=1}^3 \left(\frac{u_{k',2}-u_{k',1}}{2} \int_{-1}^1 H(s') ds' \right) \quad (2.132)$$

with $H(s') = \sqrt{1-u^2} f(av, bu\sqrt{1-v^2})$ and $u = \frac{s'(u_{k',2}-u_{k',1}) + u_{k',2} + u_{k',1}}{2}$

This integral can be approximated by Gauss-Legendre quadrature such that:

$$F(v) \approx (1-v^2) \sum_{k'=1}^3 \left(\frac{u_{k',2}-u_{k',1}}{2} \sum_{j'=1}^{N_{k'}} w_{j'} H(s_{j'}) \right) \quad (2.133)$$

Here again, $w_{j'}$ and $s_{j'}$ are weights and roots of the quadrature calculated numerically for a given quadrature order $N_{k'}$ defined in (2.124). Note also that $F(v)$ defines a pressure density that vary significantly in regions around $v_{k,1}$, $v_{k,2}$, $u_{k',1}$ and $u_{k',2}$. However, with this method, finer mesh is modeled at integral limits, then in these required regions.

Finally, from above ellipse partitions and integrals approximations, the initial double integral I can be expressed by the following quadruple summation:

$$I = ab \sum_{k=1}^3 \frac{v_{k,2}-v_{k,1}}{2} \left[\sum_{j=1}^{N_k} \left(w_j (1-v_j^2) \left(\sum_{k'=1}^3 \frac{u_{k',2}-u_{k',1}}{2} \sum_{j'=1}^{N_{k'}} w_{j'} H(s_{j'}) \right) \right) \right] \quad (2.134)$$

with $H(s_{j'}) = \sqrt{1-u_{j'}^2} f(av_{j'}, bu_{j'}\sqrt{1-v_{j'}^2})$

and $v_j = \frac{(v_{k,2}-v_{k,1})s_j + v_{k,2} + v_{k,1}}{2}$; $u_{j'} = \frac{(u_{k',2}-u_{k',1})s_{j'} + u_{k',2} + u_{k',1}}{2}$

5.1.3 Monte-Carlo's method

To compute a double integral, Monte-Carlo's method generates N_{MC} random points (x_i, y_j) over the integration domain $[a, b] \times [c, d]$. Then, integrand f is evaluated in each point and total integral is estimated by summing all these evaluations $f(x_i, y_j)$ and by multiplying it by the ratio domain area/number of points, such as defined in relation (2.135).

Brought back to our problem, integral I , defined in (2.101), can be approximated by expression (2.136). This method is easy to program and gives very accurate results without meshing problems found with previous methods. However, to avoid important computational errors, lot of points N_{MC} are required. Then, $f(x_i, y_j)$ must be evaluated many times which is very time consuming.

$$I = \int_c^d \int_{a(y)}^{b(y)} f(x, y) dx dy \approx \frac{(d-c)}{N_{MC}} \sum_{i,j} (b(y_j) - a(y_j)) f(x_i, y_j) \quad (2.135)$$

$$I \approx \frac{4ab}{N_{MC}} \sum_{i,j} \sqrt{1 - \left(\frac{x_i}{a}\right)^2} \sqrt{1 - \left(\frac{x_i}{a}\right)^2 - \left(\frac{z_j}{b}\right)^2} f(x_i, z_j) \quad (2.136)$$

5.2 Validation

5.2.1 Friction without spinning or transverse sliding

• Analytic solutions

To validate integration methods, we first study a case without spinning ω_{Skm}^j or transverse sliding V_{Xkm}^j . In such a case, friction forces F_{Xkm}^j , M_{Zkm}^j , M_{Skm}^j are equal to zero. Pure longitudinal sliding V_{Zkm}^j occurs whereas β^j , β'^j angles and gyroscopic momentums are negligible. As illustrated on Figure 2.16, on contact ellipse, sliding speeds get equal to zero in a maximum of two points located in c_1 and c_2 along \bar{X} axis. On each side of these points, directions of longitudinal speed V_{Zkm}^j or friction force F_{Zkm}^j are opposite. That is why ellipse can be partitioned in three zones and forces can be expressed by relations (2.138) and (2.139). After computation, analytic solutions (2.140), (2.141) on F_{Zkm}^j and M_{Rkm}^j are obtained.

$$F_{Xkm}^j = M_{Zkm}^j = M_{Skm}^j = 0 \quad (2.137)$$

$$F_{Zkm}^j = \frac{3Q_{km}^j \mu}{2\pi} \sum_{k=1}^3 \pm \left(\int_{v_{1,k}}^{v_{2,k}} \int_{-\sqrt{1-q^2}}^{\sqrt{1-q^2}} \sqrt{1-q^2-t^2} \text{sign}(V_{Z0}^j) dt dq \right) \quad (2.138)$$

with $\begin{cases} v_{1,1} = -1 & v_{2,1} = c_1 \\ v_{1,2} = c_1 & v_{2,2} = c_2 \\ v_{1,3} = c_2 & v_{2,3} = 1 \end{cases}$

$$M_{Rkm}^j = \frac{3Q_{km}^j \mu}{2\pi} \int_{-1}^1 \int_{-\sqrt{1-q^2}}^{\sqrt{1-q^2}} \bar{r}_{km} dF_{Zkm}^j \quad (2.139)$$

$$F_{Zkm}^j = Q_{km}^j \mu \left(1 - \frac{3}{2}(c_2 - c_1) + \frac{1}{2}(c_2^3 - c_1^3) \right) \text{sign}(V_{Z0}^j) \quad (2.140)$$

$$M_{Rkm}^j = F_{Zkm}^j \left[\sqrt{\left(\frac{D}{2}\right)^2 - a^2} - \sqrt{R_k^2 - a^2} \right] + \frac{3Q_{km}^j \mu}{4} R_k \text{sign}(V_{Z0}^j) \quad (2.141)$$

with $\sin \lambda_1 = \frac{ac_1}{R_k}$; $\sin \lambda_2 = \frac{ac_2}{R_k}$; $\sin \lambda_3 = \frac{a}{R_k}$

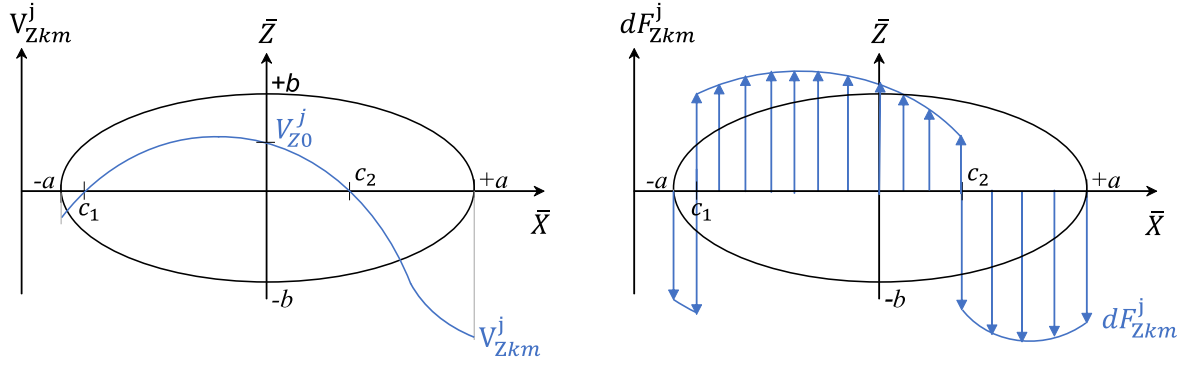


Figure 2.16 : Sliding speed V_{Zkm}^j and friction force F_{Zkm}^j without spinning or transverse sliding

• Methods comparison

To get a numerical solution with pure transversal sliding, bearing presented in Table 2.4 is reused excepted that pure axial load $F_X = 150N$ is applied and that friction coefficient is divided by 10. Under these conditions, BB20 quasi-static code converges to a solution with all balls identicals and with sliding lines distribution of Figure 2.17.

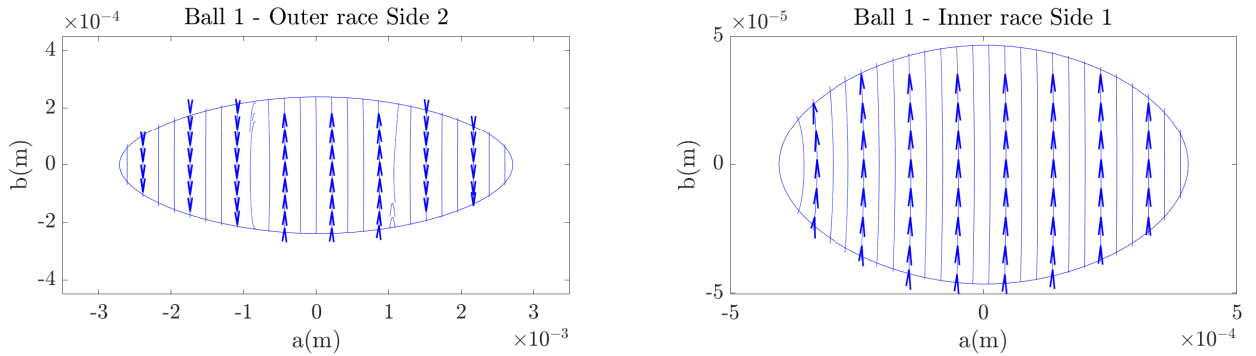


Figure 2.17 : Sliding lines on contact ellipses

This test case has been run 3 times with friction forces calculated either by Gupta, Gauss-Legendre or Monte-Carlo method. We also ran this test case with analytical solution. However, system diverged because during first iterations, pure transversal sliding does not occur. Then this simplified model is not appropriate to solve a whole system. It can be used just as a way of comparison once we are sure there is no spinning or longitudinal sliding. To do that, we extracted BB20 solution outputs from Gauss-Legendre test and computed friction forces with each method. Results are synthesized on Table 2.5. As expected, Monte-Carlo method is the closest to analytical one. Gauss-Legendre method is very similar, Gupta's method is comparable excepted for F_{Z02}^j . For outer race, F_{X02}^j and M_{Z02}^j are not negligible which makes us think that, despite sliding lines profile, hypothesis of pure transverse sliding is not correct on this race.

	Gupta	Gauss-Legendre	Monte-Carlo	Analytic
F_{Zo2}^j	-30.40957	-1.07911	1.18925	0.47956
M_{Ro2}^j	-0.14691	5.43983E-2	1.16747E-2	6.01112E-2
F_{Xo2}^j	-15.50998	-17.42163	-16.91385	0
M_{Zo2}^j	-0.16505	-0.16505	-0.16123	0
M_{So2}^j	7.37064E-2	8.99466E-2	8.71947E-2	0
F_{Zi1}^j	7.12535	7.13742	7.14774	7.17893
M_{Ri1}^j	-1.66382E-4	6.79711E-2	6.80786E-2	6.83663E-2
F_{Xi1}^j	-1.74746E-2	-1.58402E-2	-1.79318E-2	0
M_{Zi1}^j	-1.50827E-4	-1.50827E-4	-1.570114E-4	0
M_{Si1}^j	2.39647E-5	2.03182E-5	1.78833E-5	0

Table 2.5 : Comparison of friction forces calculated with different methods

On Figure 2.18, for each method, we plotted evolution of friction forces over iterations. Note that we did not report M_{Rkm}^j and M_{Zkm}^j because they respectively have same profile as F_{Zkm}^j and F_{Xkm}^j . We can observe that Gupta's method gives similar results to Monte-Carlo excepted for M_{So2}^j . Indeed, this momentum oscillate and the system has difficulties to converge with a persistently small error. Gauss-Legendre and Monte-Carlo results are almost equal for inner race whereas important differences are observed for outer race, especially for M_{So2}^j . Final results on ball parameters are summarised in Table 2.6. Gauss-Legendre solution is particularly close to Monte-Carlo. Gupta's method is also comparable and differences does not physically change bearing behaviour.

To conclude, Monte-Carlo method appears to be the most accurate to compute friction forces. However, a million points N_{MC} had to be used to converge. Then, computations took several hours whereas other methods required less than 30 seconds. For this reason, Monte-Carlo method is not suitable in practice. Gauss-Legendre method is more adapted to our problem, it has the best accuracy-to-computation time ratio even if results calculated are not exactly equal to Monte-Carlo's.

5.2.2 Friction for combined axial and radial loads (rolling, sliding, spinning)

To study if spinning and transversal sliding are correctly considered in integral computations, bearing presented in Table 2.4 is used again with combined forces $F_X = 15\ 000\text{N}$ and $F_Y = 7\ 500\text{N}$, $F_Y = 10\ 500\text{N}$ or $F_Y = 14\ 000\text{N}$. Friction forces were plotted at first and last iteration of BB20 resolution. Results for outer race, $F_Y = 14\ 000\text{N}$, are reported on Figure 2.19. For all tests, we observed that Monte-Carlo and Gauss-Legendre methods were almost equal. Small differences are due to Monte-Carlo convergence difficulties. At first iteration, some differences are noticeable between Gupta and other methods, especially for outer race contact. These differences have cancelled at last iteration. Balls characteristics given in output were also plotted and very similar results were obtained between all methods.

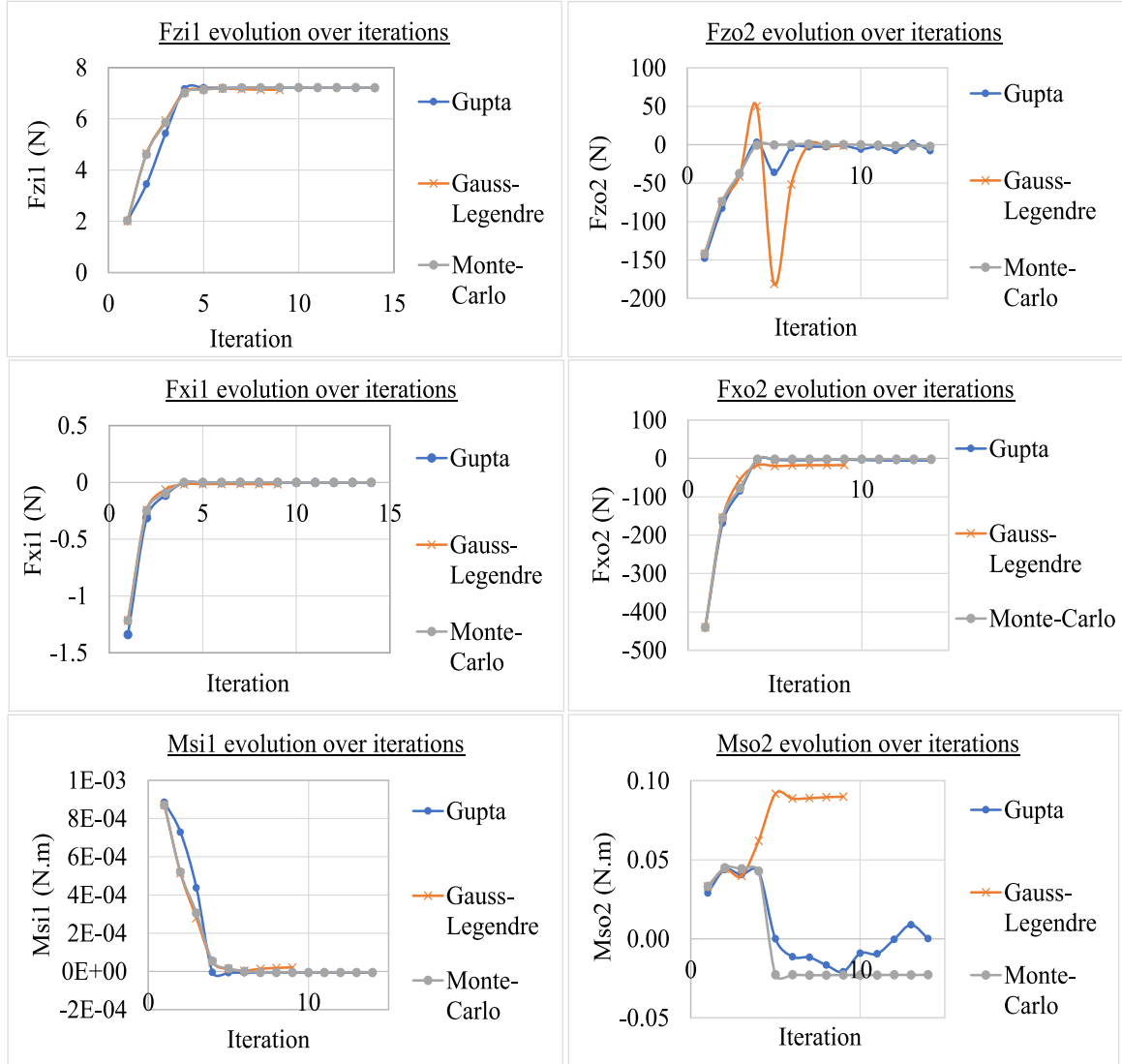


Figure 2.18 : For each method, friction calculated over iterations

	Gupta	Gauss-Legendre	Monte-Carlo
ω_m^j (rpm)	8553.6	8566.7	8580.9
ω_R^j (rpm)	-75871.5	-75963.1	-75963.0
β^j (°)	0.06123	0.14089	0.01427
β'^j (°)	0.0000409	0.0002156	0.0000171
α_{i1}^j (°)	4.2250	4.2250	4.2257
α_{o2} (°)	0.05535	0.09129	0.03414
δ_{i1}^j (μm)	0.45897	0.45944	0.46047
δ_{o2}^j (μm)	10.382	10.403	10.403

Table 2.6 : Results obtained with different methods

This confirms accuracy of Gauss-Legendre methods compared with Gupta's method, especially when pure rolling occurs. Note that Gupta's method is almost twice faster than Gauss-Legendre since no ellipse partitioning is done. However, Gauss-Legendre stays more recommended, particularly in case of critical operating conditions.

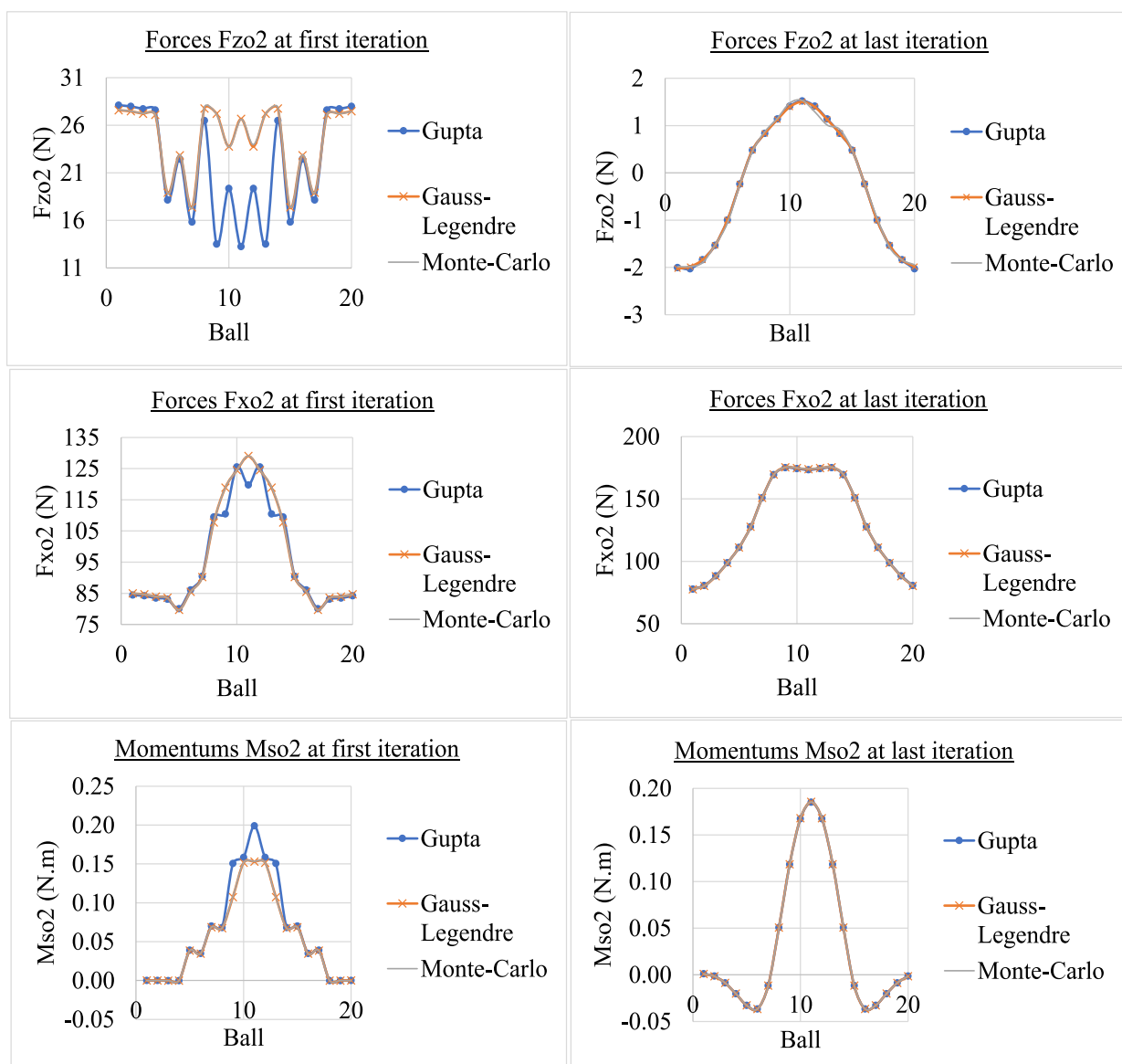


Figure 2.19 : For each method, outer race friction forces obtained for $F_X=15\ 000\text{N}$ and $F_Y=14\ 000\text{N}$

6 Quasi-static resolutions

6.1 R1 Resolution

Before solving the complete quasi-static system with balls and rings, a first resolution called R1, is led in order to get simple initial values. In this procedure, external forces on the inner ring, ball centrifugal forces and ball-race normal forces are the only one of concern. In other words, gyroscopic effects, drag forces and ball-race friction forces are neglected.

6.1.1 Inner race equilibrium

In this R1 resolution, inner ring is subject to external forces and ball-race normal forces coming from N balls, that is why forces equilibrium gives:

$$\mathbf{F}_{ext/IR} + \sum_{j=1}^N (\mathbf{Q}_{i1}^j + \mathbf{Q}_{i2}^j) = \mathbf{0} \quad (2.142)$$

After projecting normal forces in global coordinate system \mathcal{R}_G , equations on the sum of forces on the inner ring in \mathbf{x}_G , \mathbf{y}_G and \mathbf{z}_G directions are obtained:

$$-F_X - \sum_{j=1}^N (-\sin \alpha_{i1}^j Q_{i1}^j + \sin \alpha_{i2}^j Q_{i2}^j) = 0 \quad (2.143)$$

$$-F_Y - \sum_{j=1}^N (\cos \psi^j (\cos \alpha_{i1}^j Q_{i1}^j + \cos \alpha_{i2}^j Q_{i2}^j)) = 0 \quad (2.144)$$

$$-F_Z - \sum_{j=1}^N (\sin \psi^j (\cos \alpha_{i1}^j Q_{i1}^j + \cos \alpha_{i2}^j Q_{i2}^j)) = 0 \quad (2.145)$$

Momentum equilibrium on the inner ring is calculated at bearing center G such that:

$$\mathbf{M}_{/IR}(G) = \mathbf{M}_{ext/IR}(G) + \sum_{j=1}^N (\mathbf{Q}_{i1}^j \wedge \mathbf{GI}_{i1}^j + \mathbf{Q}_{i2}^j \wedge \mathbf{GI}_{i2}^j) = \mathbf{0} \quad (2.146)$$

To compute \mathbf{GI}_{im}^j , we use inner ring center G_I and consider the fact that inner ring translates of $\boldsymbol{\delta}$ and rotates of $[\theta]$, such that $\mathbf{GC}_{im}^{j'} = \boldsymbol{\delta} + [\theta] \mathbf{GC}_{im}^j$. We also know that

$$\mathbf{GC}_{i1}^j = \begin{bmatrix} R_1 \\ R_2 \cos \psi^j \\ R_2 \sin \psi^j \end{bmatrix}_{\mathcal{R}_G}, \quad \mathbf{GC}_{i2}^j = \begin{bmatrix} -R_1 \\ R_2 \cos \psi^j \\ R_2 \sin \psi^j \end{bmatrix}_{\mathcal{R}_G}, \quad \text{and} \quad \mathbf{GI}_{im}^j = \mathbf{GC}_{im}^{j'} + \mathbf{C}_{im}^{j'} \mathbf{I}_{im}^j.$$

Then, we can compute \mathbf{GI}_{im}^j coordinates:

$$\begin{bmatrix} x_1^j \\ y_1^j \\ z_1^j \end{bmatrix}_{\mathcal{R}_G} = \begin{bmatrix} R_1 \cos \theta_z \cos \theta_y + R_2 (-\cos \theta_y \sin \theta_z \cos \psi^j + \sin \theta_y \sin \psi^j) \\ R_1 \sin \theta_z + R_2 \cos \theta_z \cos \psi^j \\ -R_1 \sin \theta_y \cos \theta_z + R_2 (\sin \theta_z \sin \theta_y \cos \psi^j + \cos \theta_y \sin \psi^j) \end{bmatrix}_{\mathcal{R}_G} + \begin{bmatrix} +f_i D \sin \alpha_{i1}^j \\ -f_i D \cos \alpha_{i1}^j \cos \psi^j \\ -f_i D \cos \alpha_{i1}^j \sin \psi^j \end{bmatrix}_{\mathcal{R}_G} \quad (2.147)$$

$$\begin{bmatrix} x_2^j \\ y_2^j \\ z_2^j \end{bmatrix}_{\mathcal{R}_G} = \begin{bmatrix} -R_1 \cos \theta_z \cos \theta_y + R_2 (-\cos \theta_y \sin \theta_z \cos \psi^j + \sin \theta_y \sin \psi^j) \\ -R_1 \sin \theta_z + R_2 \cos \theta_z \cos \psi^j \\ +R_1 \sin \theta_y \cos \theta_z + R_2 (\sin \theta_y \sin \theta_z \cos \psi^j + \cos \theta_y \sin \psi^j) \end{bmatrix}_{\mathcal{R}_G} + \begin{bmatrix} -f_i D \sin \alpha_{i2}^j \\ -f_i D \cos \alpha_{i2}^j \cos \psi^j \\ -f_i D \cos \alpha_{i2}^j \sin \psi^j \end{bmatrix}_{\mathcal{R}_G} \quad (2.148)$$

Consequently, from relations (2.146), (2.147), (2.148), equations on the sum of momentums on the inner ring in \mathbf{y}_G and \mathbf{z}_G directions, at bearing center G are obtained:

$$-M_Y + \sum_{j=1}^N \left(z_1^j \sin \alpha_{i1}^j Q_{i1}^j - z_2^j \sin \alpha_{i2}^j Q_{i2}^j + \sin \psi^j (x_1^j \cos \alpha_{i1}^j Q_{i1}^j + x_2^j \cos \alpha_{i2}^j Q_{i2}^j) \right) = 0 \quad (2.149)$$

$$-M_Z + \sum_{j=1}^N \left(-\cos \psi^j (x_1^j \cos \alpha_{i1}^j Q_{i1}^j + x_2^j \cos \alpha_{i2}^j Q_{i2}^j) - y_1^j \sin \alpha_{i1}^j Q_{i1}^j + y_2^j \sin \alpha_{i2}^j Q_{i2}^j \right) = 0 \quad (2.150)$$

6.1.2 Balls equilibrium

In this R1 resolution, each ball is subject to centrifugal forces and ball-race normal forces coming from four contacts, then forces equilibrium gives:

$$\mathbf{F}_c^j + \mathbf{Q}_{i1}^j + \mathbf{Q}_{i2}^j + \mathbf{Q}_{o1}^j + \mathbf{Q}_{o2}^j = \mathbf{0} \quad (2.151)$$

After projecting in ball coordinate system \mathcal{R}_{b1}^j , equations on the sum of forces on each ball j in \mathbf{x}_G and \mathbf{y}_{b1}^j directions are obtained:

$$F_{R1/bx}^j = -Q_{i1}^j \sin \alpha_{i1}^j + Q_{i2}^j \sin \alpha_{i2}^j - Q_{o1}^j \sin \alpha_{o1}^j + Q_{o2}^j \sin \alpha_{o2}^j = 0 \quad (2.152)$$

$$F_{R1/by}^j = Q_{i1}^j \cos \alpha_{i1}^j + Q_{i2}^j \cos \alpha_{i2}^j - Q_{o1}^j \cos \alpha_{o1}^j - Q_{o2}^j \cos \alpha_{o2}^j + F_c^j = 0 \quad (2.153)$$

Note that ball forces equilibrium along \mathbf{z}_{b1}^j and ball momentums equilibrium are not solved in R1 resolution. Instead, ball kinematics is assumed such that effective rolling radius r_{km}^j are equal to ball radius. Kinematic parameters ξ_1^j and ξ_2^j are deduced from relations (2.76) and (2.79). Races relative speeds ω_i^j , ω_o^j , ball precession speeds ω_m^j and ball self-rotation speeds ω_R^j result from kinematic relations (2.84) to (2.87). As well, ball self rotation β'^j is supposed to be equal to zero whereas outer race control (ORC) hypothesis is applied to compute β^j . Indeed, β^j is assumed to be balanced between left and right outer race contact angles such as defined by relation (2.154).

$$\beta^j = -\gamma_{o1} \beta_{o1}^j + \gamma_{o2} \beta_{o2}^j \text{ with } \begin{cases} \gamma_{ok} = \left| \frac{Q_{ok}^j}{\sqrt{(Q_{o1}^j)^2 + (Q_{o2}^j)^2}} \right| \\ \beta_{ok}^j = \arctan \left(\frac{\sin \alpha_{ok}^j}{\cos \alpha_{ok}^j + \frac{D}{d_m}} \right) \end{cases} \quad (2.154)$$

Nevertheless, for final R1 iteration, if $LMCC^j = 3$, that is to say if ball contacts each race in one point, β^j is calculated without ORC hypothesis. Indeed, Dusserre and Nélías [64] showed that ball angle β^j was shared between inner race control angle β_i^j and outer race control angle β_o^j such that power loss at ball-race contact is minimum. Then, β^j calculated is shared between β_i^j and β_o^j such that ball energy equilibrium is satisfied. Is this way, accuracy of β^j predicted for R2 initialisation is enhanced.

$$\beta_o^j = \arctan \left(\frac{\sin \alpha_{o2}^j}{\cos \alpha_{o2}^j + \frac{D}{d_m}} \right) \quad (2.155)$$

$$\beta_i^j = \arctan \left(\frac{\sin \alpha_{i1}^j}{\cos \alpha_{i1}^j - \frac{D}{d_m}} \right) \quad (2.156)$$

6.1.3 Numerical procedure

R1 procedure consists in solving a set of $8N+5$ equations with

- 5 equilibrium equations on inner ring: (2.143), (2.144), (2.145), (2.149), (2.150).
- 2N equilibrium equations on balls: (2.152), (2.153).
- 6N geometric equations between balls and rings: (2.29), (2.30), (2.34), (2.35), (2.42), (2.43).

Related unknowns are:

- 3 displacements, 2 rotations on inner ring ($\delta_x, \delta_y, \delta_z, \theta_y, \theta_z$) or 3 forces, 2 momentums (F_X, F_Y, F_Z, M_Y, M_Z) or 3 displacements, 2 momentums ($\delta_x, \delta_y, \delta_z, M_Y, M_Z$) depending if input parameters are forces, moments, displacements or rotations.
- 4N ball-race contact angles ($\alpha_{i1}^j, \alpha_{i2}^j, \alpha_{o1}^j, \alpha_{o2}^j$).
- 4N Hertzian deformations at ball-race contacts ($\delta_{i1}^j, \delta_{i2}^j, \delta_{o1}^j, \delta_{o2}^j$).

This system is solved numerically by a Newton-Raphson algorithm. However, convergence difficulties occurs when the bearing support important radial load or misalignment. In such a case, balls located at the opposite of the load tend to lose contact with inner race. To solve this problem, a numerical procedure is implemented to increase incrementally radial and misalignment input parameters. Is this way, system is solved step-by-step by initialising unknowns of the next step with previous solution that is less radially loaded or less misaligned.

6.1.4 Stiffness matrix computation

At the end of R1 resolution, bearing stiffness matrix \mathbf{K}_{Stiff} defined in (2.157) is calculated. Note that this matrix could be calculated at the end of R2 resolution. However equations are much complicated in R2, computation time would be significantly increased without important accuracy improvement. Procedure to compute stiffness matrix was developed by Leblanc in 2008 [158]. We just corrected few mistakes and adapted it to equations modifications brought in this version.

$$\mathbf{K}_{Stiff} = \begin{bmatrix} \frac{\partial F_X}{\partial \delta_x} & \frac{\partial F_X}{\partial \delta_y} & \frac{\partial F_X}{\partial \delta_z} & \frac{\partial F_X}{\partial \theta_y} & \frac{\partial F_X}{\partial \theta_z} \\ \frac{\partial F_Y}{\partial \delta_x} & \dots & \dots & \dots & \dots \\ \frac{\partial F_Z}{\partial \delta_x} & \dots & \dots & \dots & \dots \\ \frac{\partial M_Y}{\partial \delta_x} & \dots & \dots & \dots & \dots \\ \frac{\partial M_Z}{\partial \delta_x} & \dots & \dots & \dots & \dots \end{bmatrix} \quad (2.157)$$

6.2 R2 Resolution

R2 resolution uses R1 results to initialise unknowns. In this procedure, R1 kinematic hypothesis on ball parameters do not hold anymore. Instead, complete ball equilibrium is solved to compute accurately β^j , β'^j , r_{km}^j , then ω_o^j , ω_i^j , ω_m^j and ω_R^j . As well, now all external forces $\mathcal{T}_{ext/IR}^j$, ball motion forces $\mathcal{T}_{/b}^j$ and ball-race contact forces $\mathcal{T}_{km/b}^j$ including friction are considered.

6.2.1 Inner ring equilibrium

Inner ring is subject to external forces, ball-race normal and friction forces arising from N balls, that is why forces equilibrium is given by:

$$\mathbf{F}_{ext/IR} + \sum_{j=1}^N (\mathbf{F}_{b/i1} + \mathbf{F}_{b/i2}) = \mathbf{0} \quad (2.158)$$

After projecting each contribution in global coordinate system \mathcal{R}_G , quasi-static equations on the sum of forces on the inner ring in \mathbf{x}_G , \mathbf{y}_G and \mathbf{z}_G directions are obtained:

$$F_{QS/IRx} = -F_X - \sum_{j=1}^N \left(-\sin \alpha_{i1}^j Q_{i1}^j - \cos \alpha_{i1}^j F_{Xi1}^j + \sin \alpha_{i2}^j Q_{i2}^j - \cos \alpha_{i2}^j F_{Xi2}^j \right) = 0 \quad (2.159)$$

$$\begin{aligned} F_{QS/IRy} = -F_Y - \sum_{j=1}^N \left(\cos \psi^j (\cos \alpha_{i1}^j Q_{i1}^j - \sin \alpha_{i1}^j F_{Xi1}^j + \cos \alpha_{i2}^j Q_{i2}^j + \sin \alpha_{i2}^j F_{Xi2}^j) \right. \\ \left. - \sin \psi^j (F_{Zi1}^j + F_{Zi2}^j) \right) = 0 \end{aligned} \quad (2.160)$$

$$F_{QS/IRz} = -F_Z - \sum_{j=1}^N \left(\sin \psi^j (\cos \alpha_{i1}^j Q_{i1}^j - \sin \alpha_{i1}^j F_{X i1}^j + \cos \alpha_{i2}^j Q_{i2}^j + \sin \alpha_{i2}^j F_{X i2}^j) + \cos \psi^j (F_{Z i1}^j + F_{Z i2}^j) \right) = 0 \quad (2.161)$$

To compute momentum equilibrium on the inner ring, the point G_I is not used like in R1 resolution. Indeed, Coulomb's friction momentums are expressed at ball center B^j . That is why momentums are transposed in this point:

$$\mathbf{M}_{/IR}(G) = \mathbf{M}_{ext/IR}(G) + \sum_{j=1}^N \left(\mathbf{M}_{b/i1}(B^j) + \mathbf{M}_{b/i2}(B^j) + (\mathbf{F}_{b/i1} + \mathbf{F}_{b/i2}) \wedge \mathbf{G} \mathbf{B}^j \right) \quad (2.162)$$

To compute $\mathbf{G} \mathbf{B}^j$, intermediate point C_{o2}^j is used. This curvature center is the most relevant point because a total ball detachment cannot happen on the outer ring. And, if the outer race contact is lost at side 2, formulas remain valid since δ_{o2}^j can take negative values.

$$\mathbf{G} \mathbf{B}^j = \mathbf{G} \mathbf{C}_{o2}^j + \mathbf{C}_{o2}^j \mathbf{B}^j \quad (2.163)$$

$$\mathbf{G} \mathbf{B}^j = \begin{bmatrix} +\frac{g_o}{2} \lambda_o^j \\ \frac{d_m}{2} - (f_o - 0.5) D \cos \alpha_f \\ 0 \end{bmatrix}_{\mathcal{R}_b^j} + \begin{bmatrix} -G E_{o2} \sin \alpha_{o2}^j \\ G E_{o2} \cos \alpha_{o2}^j \\ 0 \end{bmatrix}_{\mathcal{R}_b^j} \quad (2.164)$$

The projection in global coordinate system \mathcal{R}_G gives ball center coordinates:

$$\begin{bmatrix} x_G^j \\ y_G^j \\ z_G^j \end{bmatrix}_{\mathcal{R}_G} = \begin{bmatrix} +\frac{g_o}{2} \lambda_o^j - G E_{o2} \sin \alpha_{o2}^j \\ (\frac{d_m}{2} - (f_o - 0.5) D \cos \alpha_f + G E_{o2} \cos \alpha_{o2}^j) \cos \psi^j \\ (\frac{d_m}{2} - (f_o - 0.5) D \cos \alpha_f + G E_{o2} \cos \alpha_{o2}^j) \sin \psi^j \end{bmatrix}_{\mathcal{R}_G} \quad (2.165)$$

Note again that, in the above expression, ball orthoradial displacements along \mathbf{z}_{b1}^j are neglected. Such hypothesis will be revised in quasi-dynamics because of cage contribution and ball-to-pocket interactions.

Finally, after combining equations (2.162) and (2.165), quasi-static equations on the sum of momentums on the inner ring in \mathbf{y}_G and \mathbf{z}_G directions are obtained:

$$M_{QS/IRy} = -M_Y - \sum_{j=1}^N \left[\left(-\sin \alpha_{i1}^j M_{R i1}^j - \cos \alpha_{i1}^j M_{S i1}^j + \sin \alpha_{i2}^j M_{R i2}^j - \cos \alpha_{i2}^j M_{S i2}^j \right) \cos \psi^j - \sin \psi^j (M_{Z i1}^j + M_{Z i2}^j) + z_G^j \left(-\cos \alpha_{i1}^j F_{X i1}^j - \sin \alpha_{i1}^j Q_{i1}^j - \cos \alpha_{i2}^j F_{X i2}^j + \sin \alpha_{i2}^j Q_{i2}^j \right) - x_G^j \left((-\sin \alpha_{i1}^j F_{X i1}^j + \cos \alpha_{i1}^j Q_{i1}^j + \sin \alpha_{i2}^j F_{X i2}^j + \cos \alpha_{i2}^j Q_{i2}^j) \sin \psi^j + \cos \psi^j (F_{Z i1}^j + F_{Z i2}^j) \right) \right] = 0 \quad (2.166)$$

$$\begin{aligned}
 M_{QS/IRz} = -M_Z - \sum_{j=1}^N \left[(-\sin \alpha_{i1}^j M_{Ri1}^j - \cos \alpha_{i1}^j M_{Si1}^j + \sin \alpha_{i2}^j M_{Ri2}^j - \cos \alpha_{i2}^j M_{Si2}^j) \sin \psi^j \right. \\
 + \cos \psi^j (M_{Zi1}^j + M_{Zi2}^j) + x_G^j \left((-\sin \alpha_{i1}^j F_{Xi1}^j + \cos \alpha_{i1}^j Q_{i1}^j + \sin \alpha_{i2}^j F_{Xi2}^j + \cos \alpha_{i2}^j Q_{i2}^j) \cos \psi^j \right. \\
 \left. \left. - \sin \psi^j (F_{Zi1}^j + F_{Zi2}^j) \right) - y_G^j (-\cos \alpha_{i1}^j F_{Xi1}^j - \sin \alpha_{i1}^j Q_{i1}^j - \cos \alpha_{i2}^j F_{Xi2}^j + \sin \alpha_{i2}^j Q_{i2}^j) \right] = 0
 \end{aligned} \tag{2.167}$$

6.2.2 Balls equilibrium

Each ball is subject to forces due to their motion and to ball-race normal and friction forces coming from four contacts. Then, forces equilibrium on each ball gives:

$$\mathbf{F}_{/b}^j + \mathbf{F}_{i1/b}^j + \mathbf{F}_{i2/b}^j + \mathbf{F}_{o1/b}^j + \mathbf{F}_{o2/b}^j = \mathbf{0} \tag{2.168}$$

After projecting in ball coordinate system \mathcal{R}_{b1}^j , quasi-static equations on the sum of forces on each ball j in \mathbf{x}_G , \mathbf{y}_{b1}^j and \mathbf{z}_{b1}^j directions are obtained:

$$\begin{aligned}
 F_{QS/bx}^j = -Q_{i1}^j \sin \alpha_{i1}^j + Q_{i2}^j \sin \alpha_{i2}^j - Q_{o1}^j \sin \alpha_{o1}^j + Q_{o2}^j \sin \alpha_{o2}^j \\
 - F_{Xi1}^j \cos \alpha_{i1}^j - F_{Xi2}^j \cos \alpha_{i2}^j + F_{Xo1}^j \cos \alpha_{o1}^j + F_{Xo2}^j \cos \alpha_{o2}^j = 0
 \end{aligned} \tag{2.169}$$

$$\begin{aligned}
 F_{QS/by}^j = Q_{i1}^j \cos \alpha_{i1}^j + Q_{i2}^j \cos \alpha_{i2}^j - Q_{o1}^j \cos \alpha_{o1}^j - Q_{o2}^j \cos \alpha_{o2}^j \\
 - F_{Xi1}^j \sin \alpha_{i1}^j + F_{Xi2}^j \sin \alpha_{i2}^j - F_{Xo1}^j \sin \alpha_{o1}^j + F_{Xo2}^j \sin \alpha_{o2}^j + F_c^j = 0
 \end{aligned} \tag{2.170}$$

$$F_{QS/bz}^j = F_{Zi1}^j + F_{Zi2}^j + F_{Zo1}^j + F_{Zo2}^j + F_{dr}^j = 0 \tag{2.171}$$

Computation of momentum equilibrium on each ball j is straightforward since torsors $\mathcal{T}_{km/b}^j$ and \mathcal{T}_b^j are expressed at ball center B^j :

$$\mathbf{M}_{/b}^j(B^j) + \mathbf{M}_{i1/b}^j(B^j) + \mathbf{M}_{i2/b}^j(B^j) + \mathbf{M}_{o1/b}^j(B^j) + \mathbf{M}_{o2/b}^j(B^j) = \mathbf{0} \tag{2.172}$$

After projecting in ball coordinate system \mathcal{R}_{b1}^j , quasi-static equations on the sum of momentums on the ball j in \mathbf{x}_G , \mathbf{y}_{b1}^j and \mathbf{z}_{b1}^j directions, are obtained:

$$\begin{aligned}
 M_{QS/bx}^j = +M_{Si1}^j \sin \alpha_{i1}^j - M_{Si2}^j \sin \alpha_{i2}^j + M_{So1}^j \sin \alpha_{o1}^j - M_{So2}^j \sin \alpha_{o2}^j \\
 - M_{Ri1}^j \cos \alpha_{i1}^j - M_{Ri2}^j \cos \alpha_{i2}^j + M_{Ro1}^j \cos \alpha_{o1}^j + M_{Ro2}^j \cos \alpha_{o2}^j = 0
 \end{aligned} \tag{2.173}$$

$$\begin{aligned}
 M_{QS/by}^j = -M_{Si1}^j \cos \alpha_{i1}^j - M_{Si2}^j \cos \alpha_{i2}^j + M_{So1}^j \cos \alpha_{o1}^j + M_{So2}^j \cos \alpha_{o2}^j \\
 - M_{Ri1}^j \sin \alpha_{i1}^j + M_{Ri2}^j \sin \alpha_{i2}^j - M_{Ro1}^j \sin \alpha_{o1}^j + M_{Ro2}^j \sin \alpha_{o2}^j + M_{GY}^j = 0
 \end{aligned} \tag{2.174}$$

$$M_{QS/bz}^j = M_{Zi1}^j + M_{Zi2}^j + M_{Zo1}^j + M_{Zo2}^j + M_{GZ}^j = 0 \tag{2.175}$$

6.2.3 Numerical procedure

BB20 solves in quasi-static a system of 12N+5 equations with:

- 5 equilibrium equations on inner ring: (2.159), (2.160), (2.161), (2.166), (2.167).
- 6N equilibrium equations on balls: (2.169), (2.170), (2.171), (2.173), (2.174), (2.175).
- 6N geometric equations between balls and rings: (2.29), (2.30), (2.34), (2.35), (2.42), (2.43).

The related unknowns are:

- 3 displacements, 2 rotations on inner ring ($\delta_x, \delta_y, \delta_z, \theta_y, \theta_z$) or 3 forces, 2 momentums (F_X, F_Y, F_Z, M_Y, M_Z) or 3 displacements, 2 momentums ($\delta_x, \delta_y, \delta_z, M_y, M_z$).
- 4N ball-race contact angles ($\alpha_{i1}^j, \alpha_{i2}^j, \alpha_{o1}^j, \alpha_{o2}^j$).
- 4N Hertzian deformations at ball-race contacts ($\delta_{i1}^j, \delta_{i2}^j, \delta_{o1}^j, \delta_{o2}^j$).
- 2N ball position angles induced by gyroscopic and centrifugal motions (β^j, β'^j).
- 2N effective rolling radius at ball-race contacts (r_{i1}^j, r_{o2}^j).

Besides, to improve numerical resolution and especially Jacobian conditioning, each equation and each unknown are nondimensionalized by a parameter given in Table 2.7.

Equation	Parameter	Unknown	Parameter
$F_{QS/IRx} : (2.159)$	$\sqrt{F_X^2 + F_Y^2 + F_Z^2}$	δ_x	$\frac{D}{2}$
$F_{QS/IRy} : (2.160)$		δ_y	
$F_{QS/IRz} : (2.161)$		δ_z	
$M_{QS/IRy} : (2.166)$	$\frac{d_m}{2} \sqrt{F_X^2 + F_Y^2 + F_Z^2}$	θ_y	$\frac{\pi}{N}$
$M_{QS/IRz} : (2.167)$		θ_z	
$F_{QS/bx}^j : (2.169)$	$N \sqrt{F_X^2 + F_Y^2 + F_Z^2}$	α_{o2}^j	α_f
$F_{QS/by}^j : (2.170)$		δ_{o2}^j	$\frac{D}{2}$
$F_{QS/bz}^j : (2.171)$		r_{o2}^j	$\frac{D}{2}$
$M_{QS/bx}^j : (2.173)$	$\frac{d_m}{2} N \sqrt{F_X^2 + F_Y^2 + F_Z^2}$	r_{i1}^j	$\frac{D}{2}$
$M_{QS/by}^j : (2.174)$		β'^j	α_f
$M_{QS/bz}^j : (2.175)$		β^j	α_f
$f_{ORx}^j : (2.29)$	$\frac{D}{2}$	α_{o1}^j	α_f
$f_{IRx}^j : (2.34)$		α_{i2}^j	
$f_{IORx}^j : (2.42)$		α_{i1}^j	
$f_{ORy}^j : (2.30)$	$\frac{D}{2}$	δ_{o1}^j	$\frac{D}{2}$
$f_{IRy}^j : (2.35)$		δ_{i2}^j	
$f_{IORy}^j : (2.43)$		δ_{i1}^j	

Table 2.7 : Parameters used to nondimensionalize related equation or unknown

6.2.4 Ball-to-inner race detachment

- Initial observations

To validate BB20, we interest in four bearings currently mounted on aircraft engines designed by Safran company. Their main characteristics are given in Table 2.8.

Bearing	N	D (m)	d_m (m)	J_d (mm)	f_i	f_o	g_i	g_o	Ω_i (rpm)	F_X (kN)	F_Y (kN)
A	20	0.019	0.15	0.13	0.52	0.51	$\neq 0$	0	17 500	[1;15]	[0.1;15]
B	17	0.018	0.12	0.14	0.52	0.51	$\neq 0$	$\neq 0$	23 900	[1;300]	[0.1;30]
C	24	0.029	0.25	0.13	0.51	0.51	$\neq 0$	0	5 000	[1;100]	[1;15]
D	20	0.045	0.35	0.17	0.51	0.51	$\neq 0$	$\neq 0$	3 700	[10;200]	[0.1;100]

Table 2.8 : Bearing data

We run BB20 with these four bearings under different axial and radial loads between minimums and maximums accepted by each one. For all bearings, under important axial load, system always converges rapidly. It generally takes around 16 iterations for R1 and 10 for R2. However, when axial-to-radial load ratio gets closer to 1, for balls located at the opposite of radial load, a fall in precession ω_m^j and self-rotation speed ω_R^j is observed. This fall is illustrated on Figure 2.20 where results for bearing A under an axial load $F_X=7500\text{N}$ and an increasing radial load F_Y are reported. If this fall does not prevent algorithm to converge, such solutions are not physically possible.

When radial load gets larger than axial load, balls located at the opposite from radial load detach from inner race and BB20 computes values equal to zero for ω_m^j and ω_R^j . Algorithm diverges or converge towards non physical solutions. Nevertheless, we observed that bearing C, which is made to work with important radial loads, converges for bigger radial-to-axial load ratios. In practice, all these bearings never work with radial loads larger than $\frac{2}{3}$ of axial loads. However, bearing designers are asking for a computer code that works for the load panel presented.

In previous version of BB20, when a ball detached from inner race, equations (2.171) to (2.175) on ball equilibrium were not solved. Instead, β^j and β'^j angles were set at zero and effective rolling radius r_{i1}^j, r_{o2}^j were supposed to be equal to ball radius. In this new version, we deleted all locks that forced convergence. However, after many researches and algorithm improvements, we did not find a solution that solves this ball-detachment problem. We assume that, in quasi-static and if we only consider balls and rings, the system is not designed for important radial loads. Indeed, when a ball detach from inner race, it only gets in contact with outer race and get positioned at groove middle such that β^j and β'^j are equal to zero and that α_{o2}^j is equal to zero if outer ring is not truncated or that α_{o1}^j and α_{o2}^j are equal if it is truncated. If inner race does not drive the ball anymore, cage is supposed to take over this role. Since cage is not considered yet in BB20, this explains why it cannot converge under these conditions. Mathematically, when a ball detach from inner race, friction forces on inner race and gyroscopic momentums get equal to zero. Then, in ball equilibrium equations (2.169) to (2.175), no momentum is present to balance outer race momentum.

Also, only drag force F_{dr}^j balances outer race friction F_{Zom}^j . This explains why ω_m^j and ω_R^j values tend to zero. This also confirms necessity to consider ball-cage forces. Dynamic modelling with additional inertial effects should also allow to solve this problem.

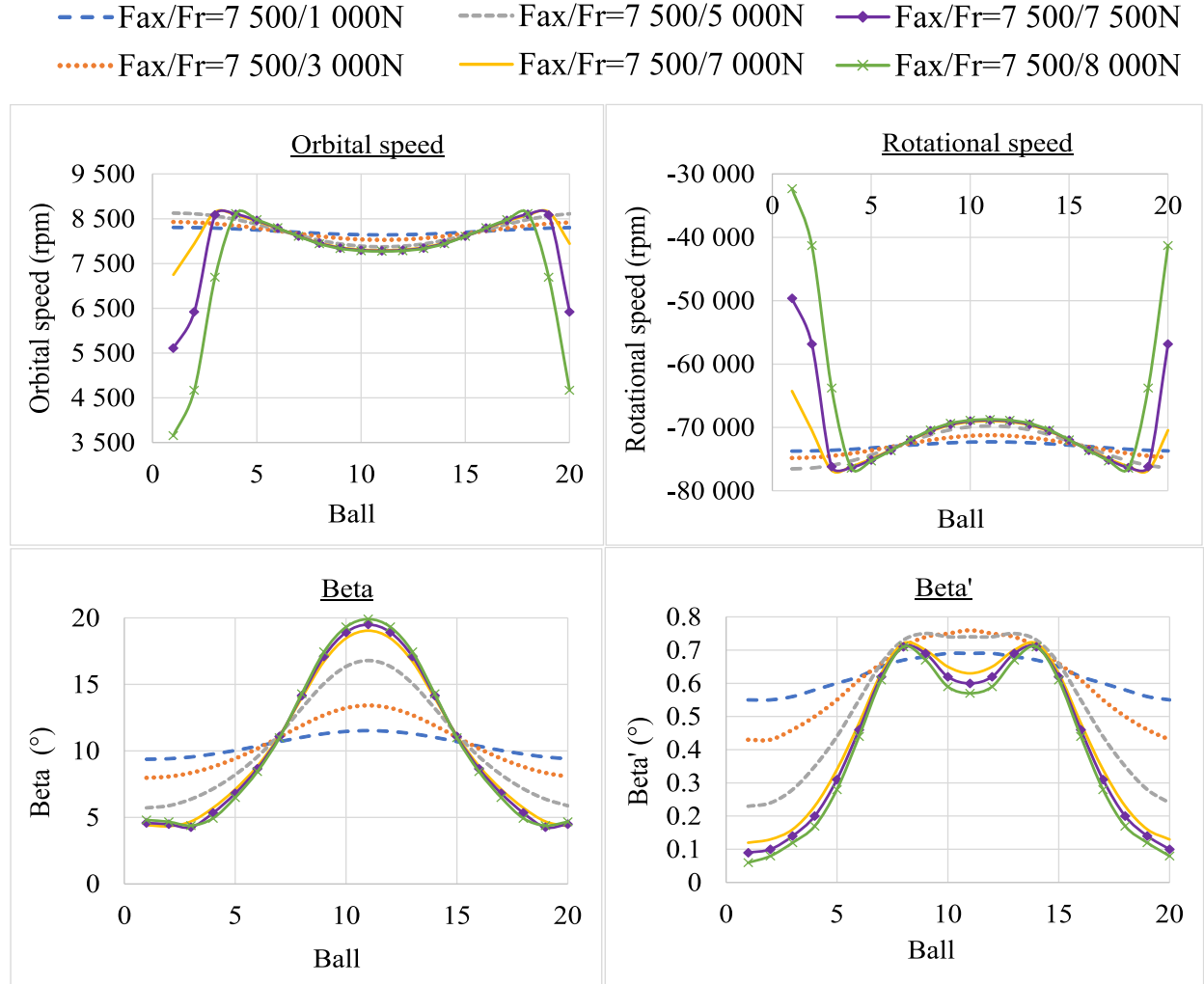


Figure 2.20 : Illustration of ball rotations fall for bearing A

- Solution proposed

Under important radial loads, bearing designers need a computer code that gives at least load distribution for all balls and a complete solution for balls that stay attached to inner race. To satisfy this demand, we differentiate two kind of balls; those in contact with inner race and those detached or at limit of contact. We consider that a ball belongs to this second category if its orbital speed ω_m^j is less than 20% of balls maximal one or if ball-to-inner race contact Q_{im}^j is less than 10% of balls maximal one. For these (almost) detached balls, we suppose that β^j , β'^j angles are equal to zero and that ω_i^j , ω_o^j , ω_m^j , ω_R^j speeds are equal to attached ball average one. Then, equations (2.171) to (2.175) on ball equilibrium are not solved anymore. Instead, β^j and β'^j angles are set to zero and ball radius are calculated by kinematic relations (2.72) and (2.75).

With this procedure, convergence is forced and solution on β^j , β'^j , ω_m^j , ω_R^j is approximated for (almost) detached balls. Nevertheless, this solution gives a first outlook of bearing equilibrium before modelling cage. Indeed, tests were rerun with these modifications and convergence improvements are noticeable. For these four bearings, more than 1000 tests have been done and less than 5% diverged. Computational difficulties mainly happen when axial-to-radial load ratio gets closer to 1. Modification of Newton-Raphson relaxation criteria makes converge some of these cases but makes diverge other ones. This shows that remaining diverging cases are only due to numerical limitations and not to physical errors in the model.

Ball results obtained for bearing A are presented in Figure 2.21. When radial load F_Y is less or equal than 7 000N, all balls are attached to inner race. All curves (excepted those of β'^j) have sinusoidal shapes. For $F_Y=7$ 000N, a small fall already occurs. For $F_Y=9$ 000N, balls 1, 2, 19, 20 are detached and balls 3, 4, 5, 6, 17, 18 are almost detached from inner race, then their computation is forced. For $F_Y=10$ 000N, balls 1, 2, 3, 19, 20 are detached and balls 4, 5, 6, 16, 17, 18 are almost detached. This detachment has no influence on outer race loads and contact angles computed. For inner race, as expected, contact angles and loads tend to zero. Ball speeds are particularly impacted by this detachment since they are prescribed. Consequently, curves obtained does not have sinusoidal shape anymore.

Note also that instead of forcing ω_i^j , ω_o^j , ω_m^j , ω_R^j to be equal to attached ball average ones, we have tried to force these speeds to be equal to maximal one. Is this way we thought we could get results closer to a sinusoid. However, system did not succeed to converge. We suppose that such method does not work because it overestimates cage speed ω_c . In any case, new solution proposed to manage ball detachment appears to be satisfying as a first approach to always make the system converge and have a first idea of bearing equilibrium.

6.3 New features of BB20 version 5

Quasi-static model presented above was not entirely developed during this thesis. Indeed, basis were already present in BB20 version 4. However, some mistakes have been found in previous system, algorithm was not optimal with important numerical discontinuities, computer code was over-constrained in order to make it converge towards a solution that was not always physically correct. These limits were not visible while working with important axial load. However, they appeared to be problematic while trying to add cage contributions.

To solve these problems, we first transposed the whole system in a direct coordinate system since previous version was based on Jones' indirect system [144]. Unknowns and coordinate systems were also defined to only work with positive axial loads and positive angles. This limited working conditions but also forced the solution to converge toward false values. Indeed, depending on speed and combined loads, contact angles α_{km}^j or ball self-rotation angles β^j , β'^j can take negative values even if axial load is positive. That is why, this new definition of contact angles, of ball rotations and adaptation of equations to negative values were necessary.

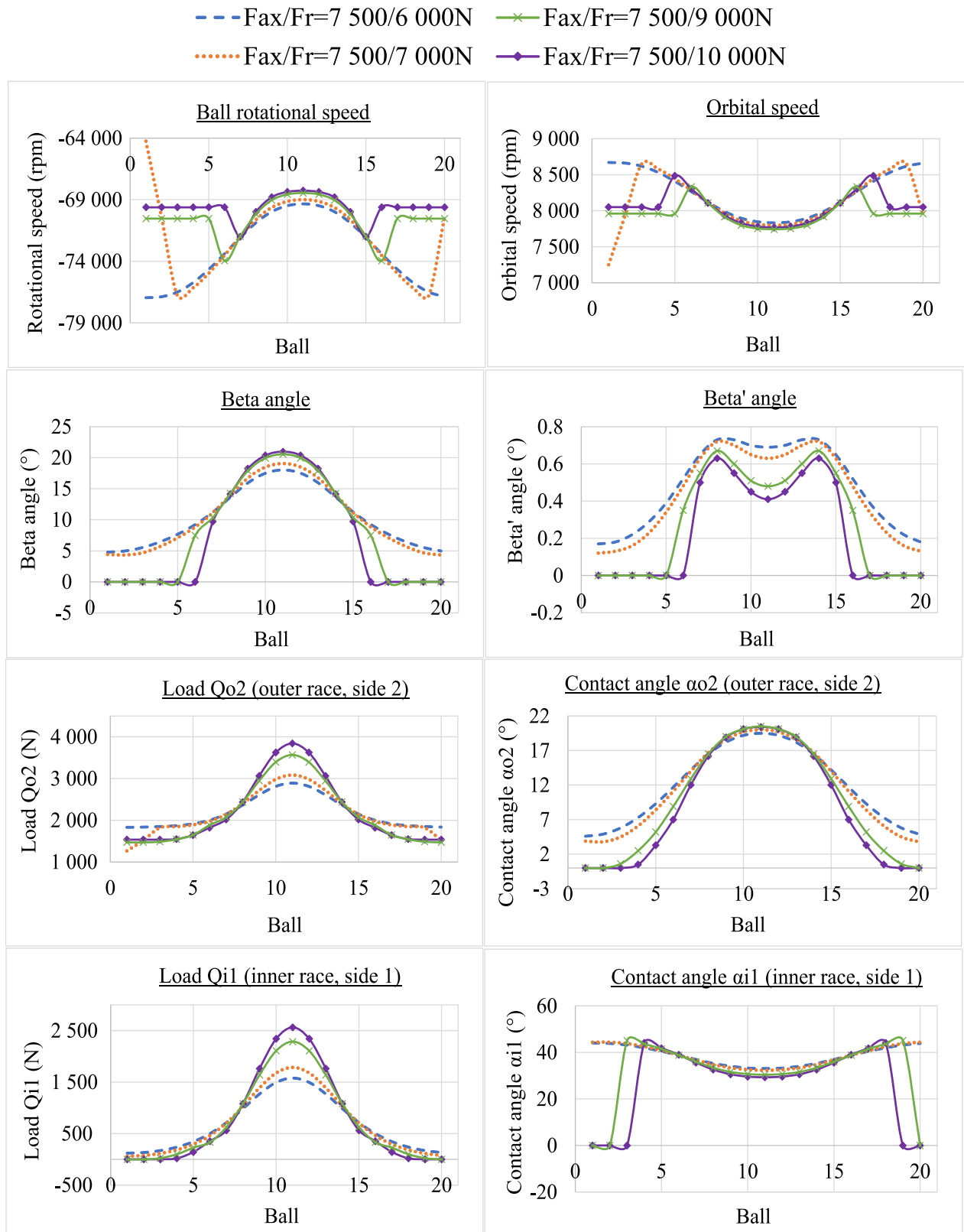


Figure 2.21 : Results for bearing A after ball detachment improvements

In BB20V4, when a ball lost a contact with a race, elastic deformation δ_{km}^j was put to zero. Then, at each iteration, depending on ball-race contacts and $LMCC^j$ values, geometric equations had to be adapted which created important numerical discontinuities. Now, with consideration of film thickness h_{km}^j and negative δ_{km}^j , an unique system of equation is solved. To deal with different ring truncations and to work with a continuous system of equations, we also created the whole procedure presented in section 2.4. Then, numerical resolution is smooth and contact differentiations with $LMCC^j$ is only used to relax Newton-Raphson scheme between two successive iterations in order to avoid aberrant contacts.

As well, we optimised drag model to consider lubricant flow effect. We verified and improved the whole procedure of friction forces computation. Especially, we completely revised Gauss-Legendre's method and implemented Monte-Carlo's one. To optimise computational efficiency, converging loops of R1 and R2 have also been deeply revised. Projections of friction forces were changed. We revised stiffness matrix computation and procedure to deal with ball-to-inner race detachments. Equations and unknowns nondimensionalization is also a novelty in BB20V5. Order of equations and unknowns in the program has also been modified to associate each equation with its corresponding unknown. All these modifications brought us to verify and adapt all equations and computational code. In this way, quasi-static BB20 is made of a unique system of equations, it is better conditioned, it better deals with contact changes over iterations and does not force any solution. It is adapted to larger working conditions in terms of bearing geometry, speed or load. Previous errors have been rectified, then cage should be modelled without problems.

7 Results analysis

7.1 Investigation of existing bearings

7.1.1 Pure axial load

To pursue BB20 validation, we run four tests on bearing A where we vary axial load F_X , shaft speed N_i and friction coefficient μ such as indicated in Table 2.9. Main results obtained are gathered in Appendix B, Table B.1.

Test	A	B	C	D
F_X (N)	15 000	15 000	150	150
Ω_i (rpm)	17 500	1 750	17 500	17 500
μ	0.065	0.065	0.065	0.65

Table 2.9 : Operating conditions applied for bearing A under pure axial load

We work under pure axial load, then all balls have same kinematics with two contact points and with sliding lines of Figure 2.22. Spinning direction is clearly visible on ellipses of test B. In this way we can verify that ω_{Si1}^j , M_{Si1}^j and ω_{So2}^j , M_{So2}^j are opposite.

As well, on inner race of tests C and D, pure sliding occurs in a constant direction, then we verify that V_{Zi1}^j and F_{Zi1}^j are opposite. From Table B.1, we also confirm that F_{Xkm}^j and M_{Zkm}^j are opposite to M_{GZ}^j in order to balance this gyroscopic momentum, as predicted by Figures 2.9 and 2.10. We also check that M_{Skm}^j and ω_{Skm}^j are always opposite. We expected M_{Rkm}^j and ω_{Rkm}^j to be in reverse directions. However, if M_{Ro2}^j and ω_{Ro2}^j have opposite signs, M_{Ri1}^j and ω_{Ri1}^j have same signs. Then, if we can validate all friction forces directions, this last one stays questionable. Note however that ω_{Rkm}^j is not involved in any BB20 computation.

Besides, we can observe on sliding lines profile of test A, that under high speed, high axial load, ball rolls, spins and slides on both races. When speed is reduced, spinning ω_s^j then gyroscopic momentums decrease whereas contact angles tend to be equal. When axial load is reduced, as shown in Figure 2.22 for test C, on the inner race, pure rolling point translates longitudinally and skidding occurs since spinning is negligible compared to transversal sliding. When friction is increased and axial load stays small, as represented on Figure 2.22 for test D, skidding occurs on both races. All these results confirms that BB20 models physical behaviour expected from an ACBB submitted to pure axial load.

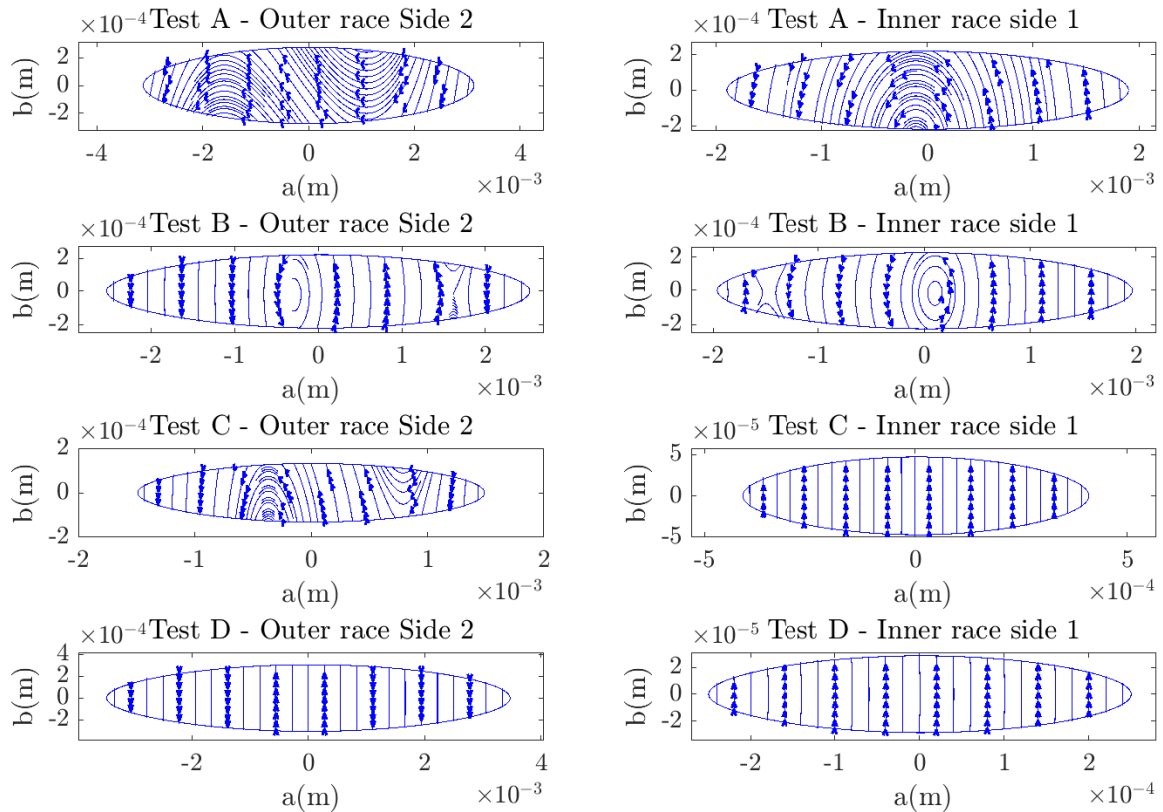


Figure 2.22 : Sliding lines for bearing A, under different working conditions

7.1.2 Combined axial and radial loads

First results on bearing behaviour under combined loads were presented in section 6.2.4. When radial load is less or equal than axial load, results are in adequacy with literature. Indeed, we can observe on Figure 2.21, for $F_Y = 6\,000\text{N}$, that inner race contact angle α_{i1}^j is always larger than outer race α_{o2}^j whereas inner race normal load Q_{i1}^j is less than outer race Q_{o2}^j . Attitude angle β^j is comprised between inner and outer race contact angles. Since radial load is applied on ball 11, it is the one with the higher normal loads and contact angles. Orbital speed plot also confirms that balls decelerate when they enter the loaded zone and accelerate when they come out.

On Figures 2.23 and 2.24, for different radial loads, we reported sliding lines profile of few balls. Under small radial loads, all balls roll, spin and slide on both races as illustrated on Figure 2.23. When radial load increases, normal load increases then outer race ellipse gets larger whereas inner race ellipse gets smaller. For first balls, point of pure rolling on the inner race translates longitudinally and skidding occurs as visible on Figure 2.24 for balls 1 and 5 under radial load of $7\,000\text{N}$. Note that these balls are those subjected to ω_m^j and ω_R^j fall. For even larger radial loads, as under $F_Y = 8\,000\text{N}$, on radially loaded balls, spinning occurs at inner race contact then outer race controls ball.

7.1.3 Comparison BB20 Version 4 vs 5

To compare this new version of BB20 with previous one, we interest in bearing D under an axial load of $100\,000\text{N}$ and an increasing radial load. Results obtained with both versions are presented in Figure 2.25. Note that results reported for BB20V5 are shifted of 10 balls. Indeed, this new model is defined in a direct coordinate system, then axis z_{b1}^j has rotated of 180° . So to compare same loaded balls as BB20V4, either we set the first ball with ψ_c at 180° or we inverse the sign of applied radial load. As well, we would have expected to get opposite signs of β^j between BB20V4 and V5. But since F_{Xkm}^j , F_{Zkm}^j and M_{Rkm}^j directions were reversed, same signs for β^j are obtained with both versions.

On Figure 2.25, for radial loads of $50\,000\text{N}$ or $75\,000\text{N}$, we can observe that orbital speeds ω_m^j and ball rotational speeds ω_R^j are significantly higher for BB20V4, especially for radially loaded balls. Pitch angles β^j , yaw angles β'^j , contact angles α_{o2}^j and normal loads Q_{o1}^j also have more important variations in version 4. We also ran BB20V5 with previous friction forces projections and obtained very close results to BB20V4. This shows that amplitude differences between BB20V4 and V5 are directly due to F_{Xkm}^j , F_{Zkm}^j and M_{Rkm}^j projections. For radial load of $100\,000\text{N}$, in BB20V4, balls 9 to 13 have detached from inner race whereas in BB20V5, only ball 11 has detached and balls 8, 9, 10, 12, 13, 14 are at limit of detachment. Considering almost detached balls gives smoother curves on orbital and rotational speeds such as noticeable in Figure 2.25 where peaks on 8th and 14th balls decreased of a factor 5 between V4 and V5. Finally, different kinematics are calculated between BB20V4 and V5. We cannot say if new results are more or less correct than previous ones. As we will see in next sections, no model in literature has exactly the same physics to be compared with BB20. And, leading experimental study on quasi-static parameters like pitch, yaw or contact angles is a complicated task. However, we will see that obtaining less important orbital speed variations is preferable for future cage computations.

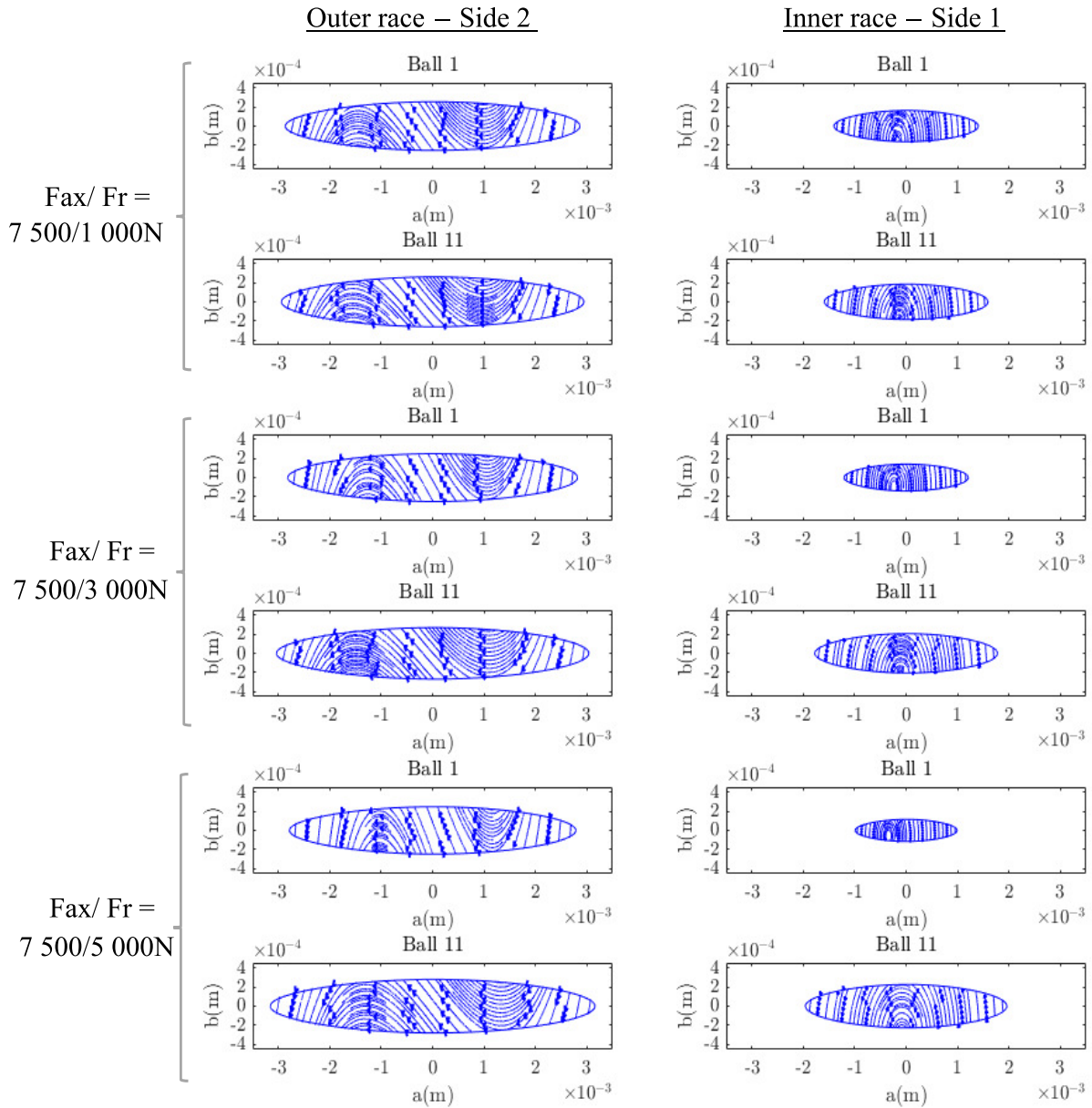


Figure 2.23 : Sliding lines for bearing A under low radial loads

7.1.4 Power loss

At the moment, only power loss due to ball-race friction is calculated by formula (2.176). Under different operating conditions, experiences have been led by bearing designers at Safran, to measure driving torque and rings temperatures. Especially, hybrid bearing defined in Table 2.10, was tested under an oil shut-off. After results exploitation, a power loss of 6587W was estimated. Same test is run with BB20 without considering film thickness or drag forces. A power loss P of 9 658W is obtained.

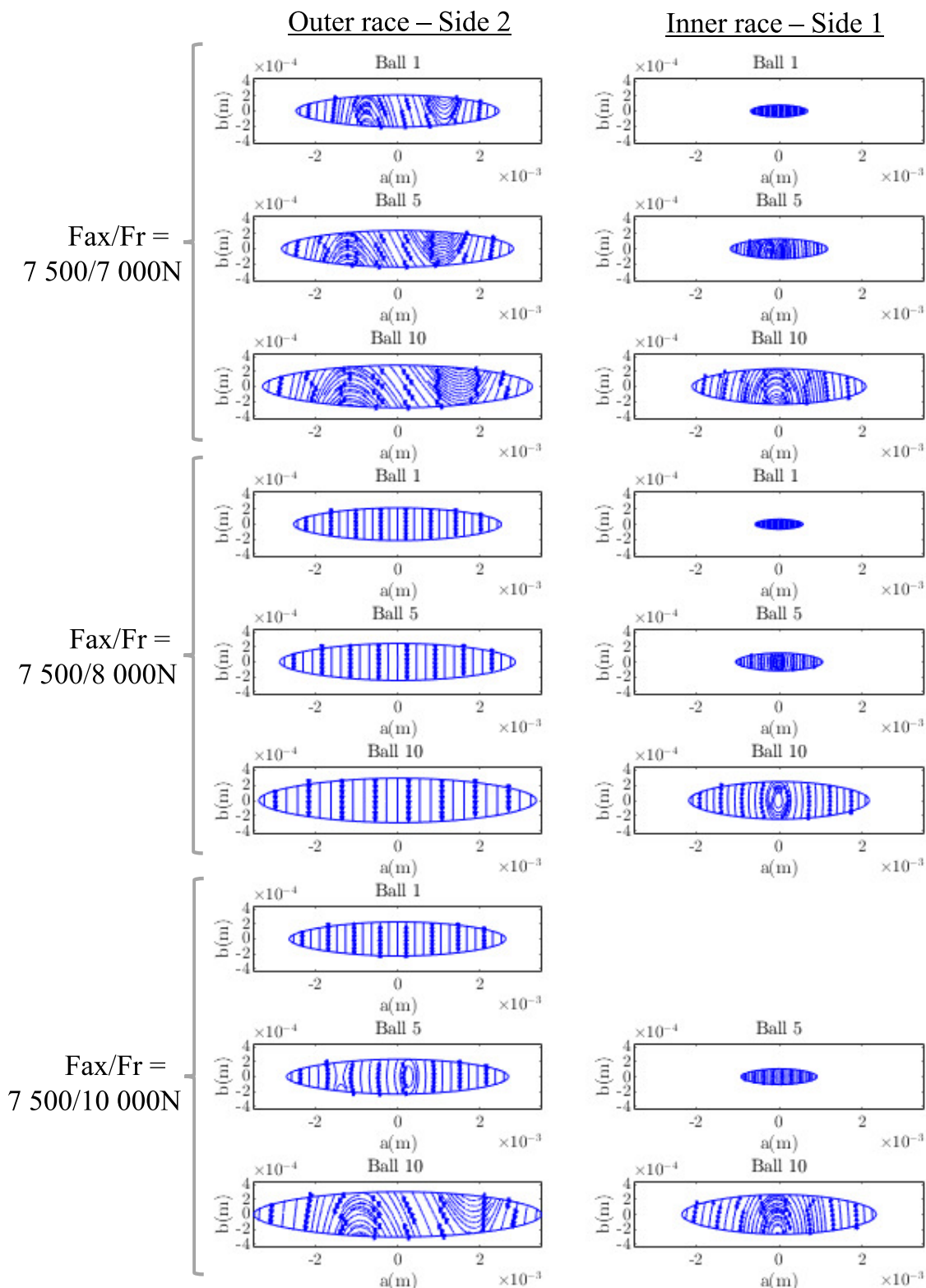


Figure 2.24 : Sliding lines for bearing A under important radial loads

— V5 - Fr=0N — V5 - Fr=50 000N — V5 - Fr=75 000N — V5 - Fr=100 000N
 - - - V4 - Fr=0N - - - V4 - Fr=50 000N - - - V4 - Fr=75 000N - - - V4 - Fr=100 000N

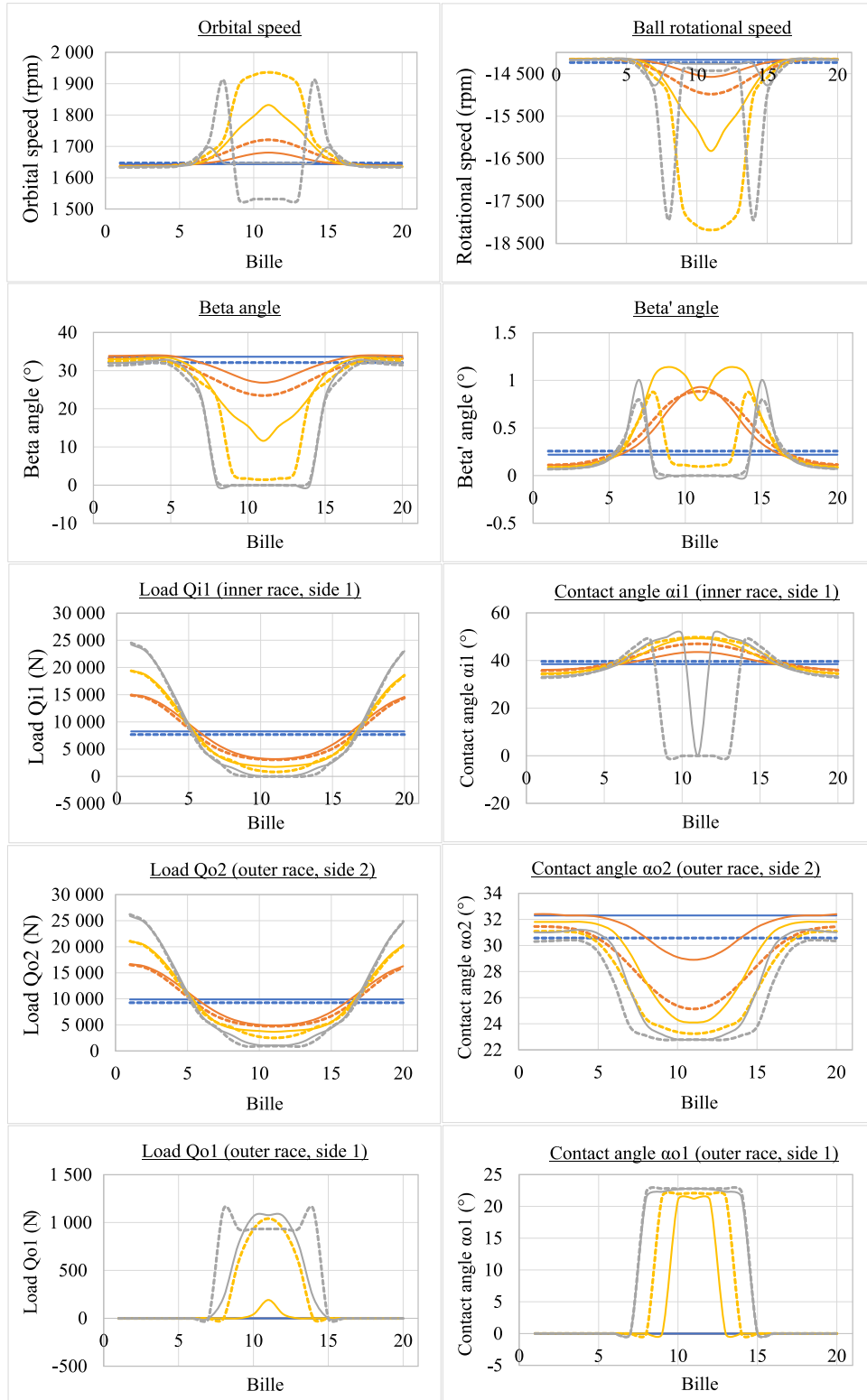


Figure 2.25 : Comparison of BB20V4/V5 for bearing D under $F_X = 100\,000\text{N}$

Then, 31% difference is observed between experiments and model. This difference is acceptable and may be due to the fact that friction coefficient considered is equal to 0.065. This is an important value, a coefficient around 0.04 may have given closer results. This analysis shows that power loss is a useful tool to validate a model. It is easily measured experimentally and calculated numerically. That is why, power dissipated at all contacts and arising from dry and lubricated effects, will have to be added in future versions of BB20.

$$P = \sum_{j=1}^N \sum_{m=1,2} \omega_i^j \left(-M_{Sim}^j \sin \alpha_{im}^j + M_{Rim}^j \frac{\bar{d}_m^j - r_{im}^j \cos \alpha_{im}^j}{r_{im}^j} \right) + \omega_o^j \left(M_{Som}^j \sin \alpha_{om}^j + M_{Rom}^j \frac{\bar{d}_m^j + r_{om}^j \cos \alpha_{om}^j}{r_{om}^j} \right) \quad (2.176)$$

N	D (m)	d_m (m)	J_d (mm)	f_i	f_o	g_i	g_o	Ω_i (rpm)	F_X	F_Y
21	0.045	0.34	0.14	0.508	0.513	$\neq 0$	$\neq 0$	3050	347 300	15 000

Table 2.10 : Data of bearing tested

7.2 Comparison with literature

7.2.1 Reference analytical models

In order to validate our model with two contact points, an investigation is led to compare BB20 outputs with Harris [121] and ADORE quasi-static [91] results.

Gupta developed a quasi-static code to solve bearing equilibrium without cage. All of kinematic effects considered in BB20 quasi-static, are also modelled in ADOREQS except for drag force and β'^j angle. To compute orientation of ball angular velocity vector, depending on user choice, Raceway Control Hypothesis (RCH) or Minimum Energy Hypothesis (NRJ) are applied. This last method was developed recently by Gupta [100]. For a given lubrication model, it consists in searching for β^j angle such that frictional energy dissipated at ball-race contacts is minimum. This iterative procedure is much time consuming than RCH. However, rolling and spinning are considered at both raceways, more than one point of pure rolling can be present and point of pure rolling is not obviously located at ellipse center. Gupta has shown that QS results obtained with this method are much closer to dynamical results than those given by RCH method.

- Shaft speed effects

In 1971, Harris developed a model based on Jones' work [144] in order to study ACBB without making raceway control hypothesis (RCH). In his first model [120], such as represented on Figure 2.16, he supposed that only longitudinal sliding and spinning occur. Then, he only calculated friction forces F_{Zkm}^j , M_{Rkm}^j and M_{Skm}^j . To get rid of double integral, as we did in section 5.2.1, he supposed that a maximum of two lines of pure rolling occurs in surface ellipse. He also supposed that angle θ_n is small. This angle is defined between ball-center-to-ellipse center axis and ball center-to point of pure sliding

axis as expressed by relation (2.177). In this way, analytic expressions on F_{Zkm}^j , M_{Rkm}^j and M_{Skm}^j are obtained. Since M_{Zkm}^j is not considered, ball momentum equation on z_{b1}^j is not solved, β'^j angles and gyroscopic momentums M_{GZ}^j are supposed to be equal to zero. Consequently, friction coefficient is calculated such that this gyroscopic slippage gets equal to zero. Note that Harris defined these parameters with different names, but for the sake of clarity, we adapted them to our model.

$$\sin \theta_n = \frac{x'_n}{r_n} \quad (2.177)$$

Then, he led a parametric study on bearing defined in Table 2.11, and made vary shaft speed from 0 to 10 000 rpm. We also run these tests on BB20 and ADOREQS computer code. As for that, we applied a constant friction coefficient $\mu=0.065$. Results from all tests are synthesized in Figures 2.26 to 2.29.

N	D (mm)	d_m (mm)	α_f (°)	f_i	f_o	g_i	g_o	F_X (N)	F_Y (N)
14	8.731	48.54	24.5	0.52	0.52	0	0	442	0

Table 2.11 : Bearing design data from Harris' first study [120]

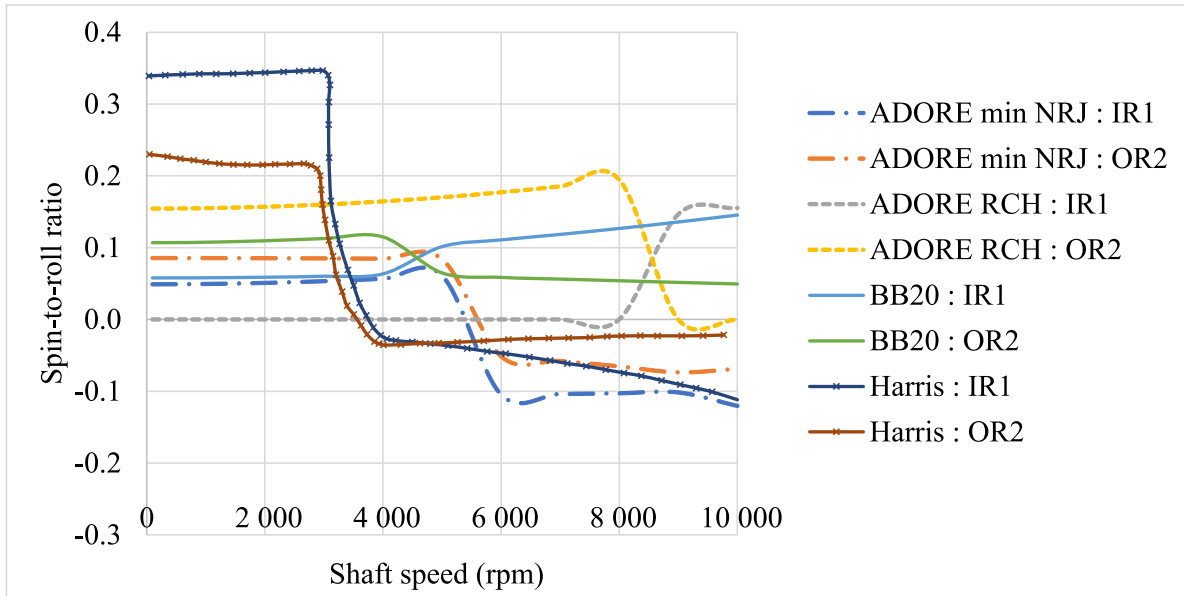


Figure 2.26 : Evolution of spin-to-roll ratio at inner and outer race with shaft speed

Figure 2.26 presents with shaft speed N_i , evolution of spin-to-roll ratio $\frac{\omega_{Skm}}{\omega_{Rkm}}$ for inner race (IR1) and outer race (OR2). We can observe that ADORE RCH compute a solution with inner race control ($\omega_{So2} \neq 0, \omega_{Si1} = 0$) at speeds below 8 000 rpm and outer race control ($\omega_{So2} = 0, \omega_{Si1} \neq 0$) at higher speeds.

BB20 curves have similar shapes excepted that control is always slightly shared between both races at low and high speeds. For speeds lower than 4 000 rpm, balls mainly spin on

outer race, whereas they mainly spin on inner race for higher speeds. For speeds higher than 10 000 rpm, BB20 curve on SR-OR2 seems to tend to zero, then to outer race control. At low speed, ADOREQS with minimum energy hypothesis gives results comparable to BB20. For higher speeds, SR ratio changes in sign which is surprising. However, SR-OR2 tend to zero such as predicted by RCH.

SR ratio computed by Harris is significantly larger than other ones. We suppose that this difference comes from friction coefficient that is not prescribed but calculated such that gyroscopic momentum M_{GZ}^j is minimum. As well, at low speeds, balls mainly spin on inner race which is at the opposite from other models. This difference may be due to the fact that θ_n is neglected which seems to be an important approximation. For speeds higher than 4 000 rpm, SR ratios change in sign and SR-OR2 tend to get equal to zero, which is comparable to ADORE with minimum energy hypothesis.

At this point, we cannot say if sign inversion of SR ratio with speed should be expected or not. However, we believe that Harris' model is too much simplified to correctly model ball spinning and rolling. Gupta's model with minimum energy hypothesis is the one that model physics the most accurately. BB20 is closer to this model which comforts us in its correctness. Note that measuring experimentally spinning and rolling motions at each contact is almost impossible. No article about such experience has been found in literature.

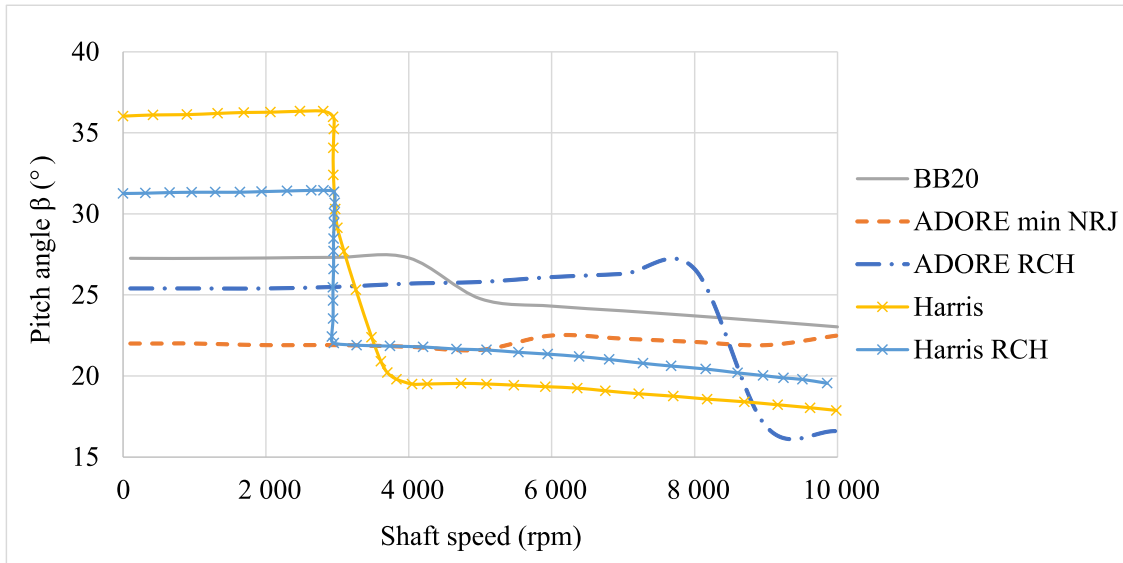


Figure 2.27 : Evolution of pitch angle β with shaft speed

Figure 2.27 presents evolution of pitch angle β^j with shaft speed. For all models, we can observe an abrupt change of this angle at same speeds values as abrupt spin-to-roll ratio change. Differences in speeds between BB20 and Harris may be due to friction coefficient definition. BB20 and ADORE RCH have same shape as Harris but different amplitudes. We can ask ourselves if these differences are due to BB20 mistakes, to hypothesis in ADORE RCH or to Harris' model hypothesis. Especially, neglecting β'^j angle and transversal speed may have significant impact on β^j computation.

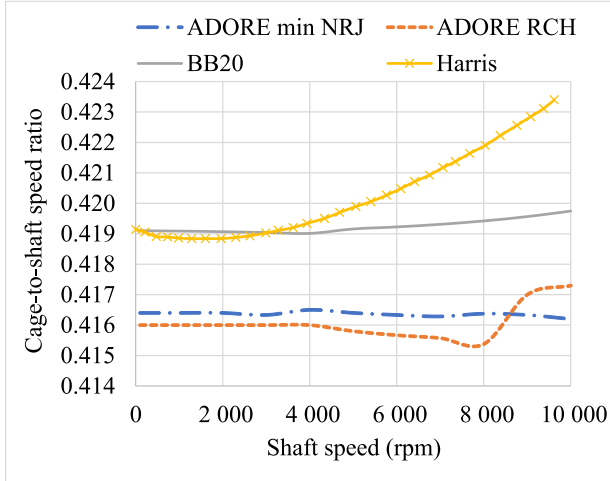


Figure 2.28 : Evolution of cage-to-shaft speed ratio $\frac{\omega_c}{N_i}$ with shaft speed

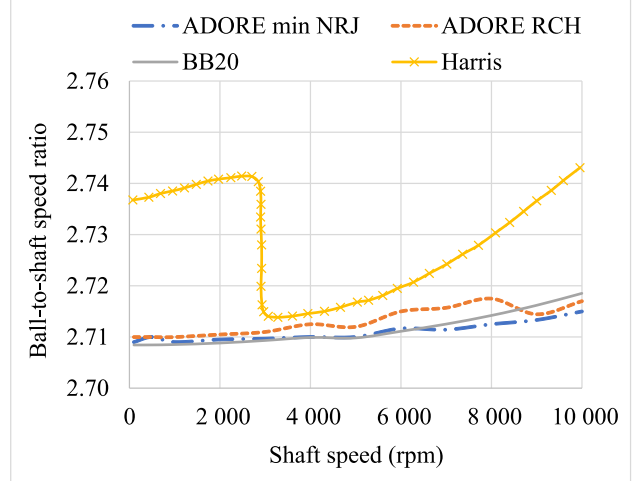


Figure 2.29 : Evolution of ball-to-shaft speed ratio $\frac{\omega_R}{N_i}$ with shaft speed

Figure 2.28 presents evolution of cage-to-shaft speed ratio $\frac{\omega_c}{N_i}$ with shaft speed. BB20 is close to Harris at low speeds. ADORE results are different at all speeds even if magnitude stays comparable. We can assume that differences between models are due to friction coefficient and drag force considerations. Indeed, these elements have direct effects on cage speed ω_c . Drag is not considered in ADOREQS and Harris did not mention it either.

Figure 2.29 presents evolution of ball rotation-to-shaft speed ratio $\frac{\omega_R}{N_i}$ with shaft speed. Same order of magnitude is obtained with all models. BB20 and ADOREQS curves are very close.

- Axial load effects

Later, Harris improved this model to include EHD film thickness and drag forces [119]. However, he did not specify values taken by drag coefficient C_d or oil fraction in the mixture. He considered all friction forces F_{Xkm}^j , F_{Zkm}^j , M_{Rkm}^j , M_{Zkm}^j , M_{Skm}^j without simplifying double integrals like previously. He led a novel parametric study on same bearing but fixed shaft speed at 27 000 rpm and varied axial load between 400N and 1900N. We also run these tests with ADOREQS and BB20 and obtained results of Figures 2.30 and 2.31.

Figure 2.30 presents evolution of spin-to-roll ratio with axial load F_X . We can observe that all curves have similar shapes but different amplitudes. ADORE RCH computes a solution with outer race control. ADORE with minimum energy hypothesis is close to BB20 with same amplitude difference on SR-I1. For SR-O2 ratio, results given by ADORE min NRJ are questionable since SR-O2 is far from zero and becomes larger than SR-I1 for $F_X = 800N$. This indicates an unexpected change in raceway control. Harris amplitudes are also very different than other models. This may be due to friction coefficient and drag forces definition.

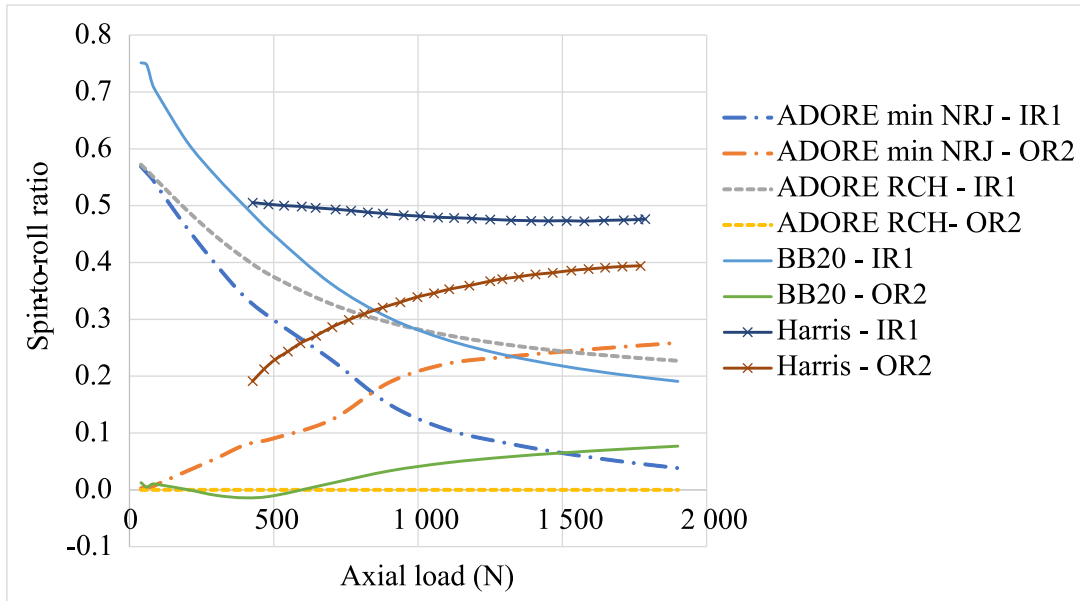


Figure 2.30 : Evolution of spin-to-roll ratio at inner and outer race with axial load

Figure 2.31 presents evolution of cage-to-shaft speed ratio with axial load F_X . We can observe that ADORE and Harris with RCH have similar results. BB20 is also close but with amplitude differences under low axial loads. For all models, cage speed decreases with axial load whereas it increases for Harris' one. This phenomena is due to drag effect that decelerates cage speed under low axial load. Indeed, as illustrated on Figure 2.32, when drag coefficient C_d is increased in BB20, cage slows down more and more under low axial loads. Same behaviour is observed on Figure 2.33 when friction coefficient μ is decreased. Then, Harris differences observed in Figure 2.31 are also due to the fact that friction coefficient is prescribed differently.

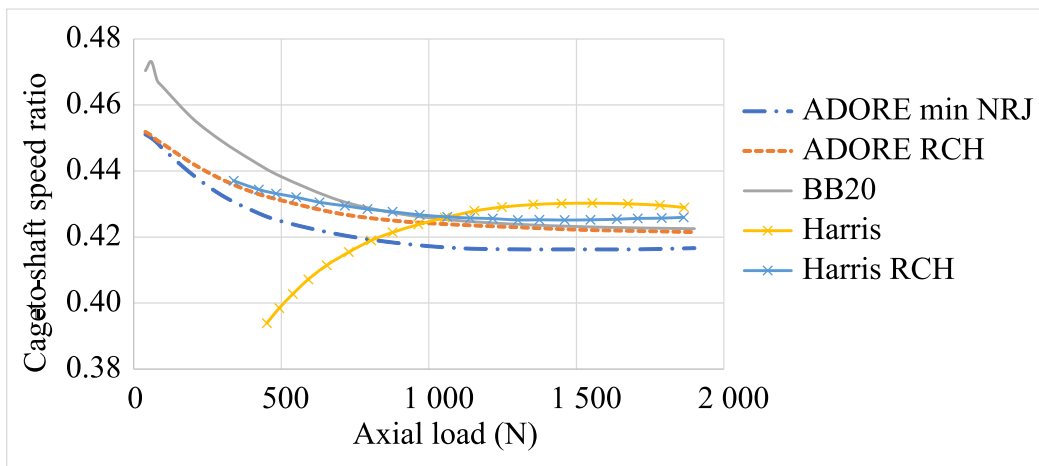


Figure 2.31 : Evolution of cage-to-shaft speed ratio $\frac{\omega_c}{N_i}$ with axial load

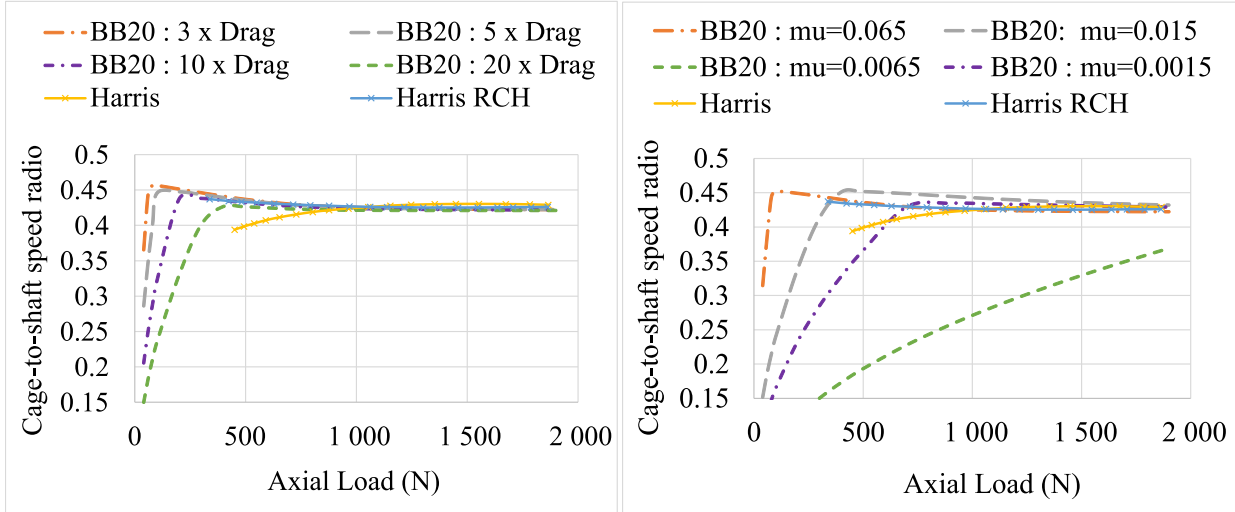


Figure 2.32 : Influence of drag coefficient C_d on cage speed ω_c **Figure 2.33 :** Influence of friction coefficient μ on cage speed ω_c

7.2.2 Experience measuring pitch angle β^j

After comparing BB20 with Harris and Gupta's studies, many questions remain outstanding. Comparing results between different models is a tricky thing since each model has its own hypothesis that significantly influence resulting behaviour. Another way of validating BB20 is to compare with experiments. Many parameters calculated in quasi-static (spinning, rolling, ball rotations, normal loads or contact angles) are very difficult to be measured experimentally. However, in 1990, Kawamura [150] succeeded to measure 3D ball motion by magnetizing an unbalanced ball drilled with a hole and by measuring 3D voltage with the use of Hall elements. Cage and shaft speeds were also recorded. For axial load of 392N or 588N, for ACBB defined in Table 2.12, shaft speed was varied between 400 and 12 000 rpm. Data were recorded for ball A which has an unbalance eccentricity of $3\mu m$ and for ball B which has $0.3\mu m$ unbalance eccentricity. Results obtained by Kawamura and BB20 are reported on Figures 2.34 and 2.35. For this bearing, Kawamura showed that friction coefficient μ was comprised between 0.006 and 0.02. That is why BB20 is run in this range.

N	D (mm)	ID x OD x width (mm)	α_f (°)	f_i	f_o	g_i	g_o	W_{lub} (L/min)
9	19.058	50 x 110 x 27	30	0.52	0.52	0	0	0.4

Table 2.12 : Bearing design data from Kawamura's study [150]

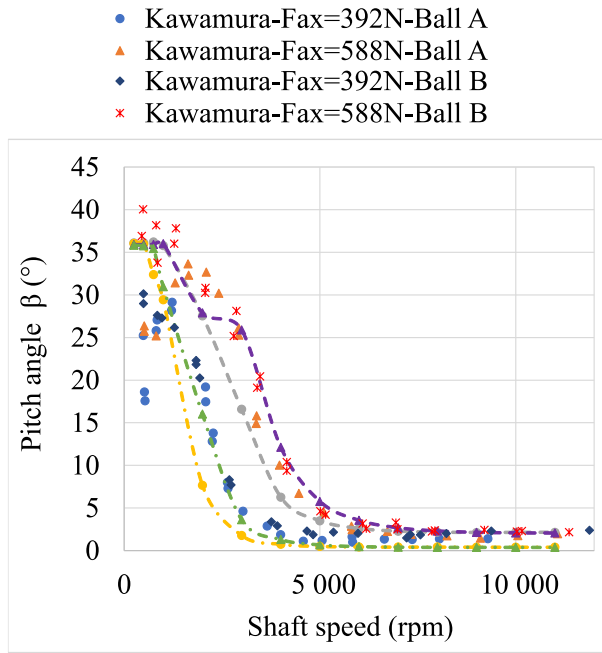


Figure 2.34 : Evolution of pitch angle β^j with shaft speed

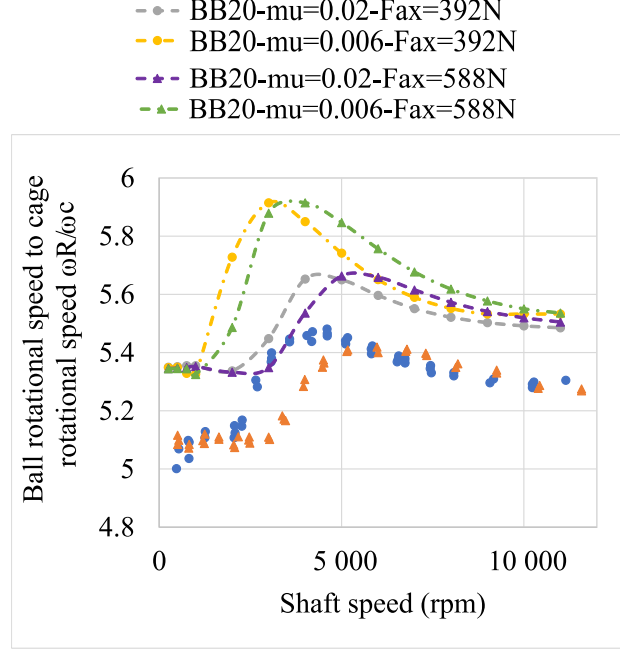


Figure 2.35 : Evolution of ball-to-cage rotational speeds $\frac{\omega_R^j}{\omega_c}$ with shaft speed

Concerning pitch angle plotted on Figure 2.34, for $F_X = 392\text{N}$, experimental results are very close to BB20 with $\mu = 0.006$. For $F_X = 588\text{N}$, they are very close to BB20 with $\mu = 0.02$. At low speed, results from ball B are closer to BB20 than results from ball A. This is logical because unbalance is not considered in BB20, then ball B which has the less unbalance eccentricity is the closest one to BB20. And, Kawamura has shown that unbalance eccentricity affected regularity and stability of ball motion at low speeds.

On Figure 2.35, only ball A is reported because comparable results were measured experimentally with ball B. This shows that unbalance does not influence ball rotation to cage rotation speeds ratio. Results between BB20 and experiments are very close especially under high friction coefficient. If curve shapes are similar, a small vertical shift is observed. This is probably due to the fact that cage is not considered yet, then its rotational speed ω_c is underestimated. In any case, BB20 and experimental results for β and ω_R are comparable which makes us think that BB20 correctly models ball self-rotations under pure axial load.

8 Summary

To conclude, ACBB with 1, 2, 3 or 4 contact points are modelled by solving balls and rings quasi-static equilibrium. Lubrication, inertia, external forces on inner ring, ball-race normal and friction forces are considered. Compared with models in the literature, important feature of BB20 is the possibility to get more than 2 ball-race contact points and the consideration of yaw angle β'^j due to gyroscopic momentum M_{GY}^j . Another specificity is that no raceway control hypothesis is done to compute kinematics. Then, nothing is neglected and all balls degrees of freedom are calculated by solving bearing equilibrium.

Ball-race interactions are accurately modelled by considering spinning, rolling, macro-sliding at contact and by integrating shear stress on each point of surface ellipse. All these elements significantly complicate kinematic behaviour and numerical resolution, but improve model accuracy. It was also shown that modifications brought in this version reduce constraints, improves numerical continuity, robustness, computational time and allows to work under a larger panel of operating conditions.

Results obtained under pure axial load or moderated radial loads, are in agreement with physics expected. When radial load becomes larger than axial load, model limitations are reached. Then, cage and dynamical effects should be considered to compute balls rotations without making important hypothesis. Results validation by comparison with literature is complicated since each model has its own considerations. However, comparable behaviours were observed and makes us believe on model correctness even if few questions remain and should be kept in mind while pursuing development. Validation by experiments is also limited by difficulties to measure kinematic parameters of interest. However, satisfying results were obtained while comparing BB20 with power loss measured by Safran, or with pitch angle, ball and cage rotations experienced by Kawamura.

Chapter 3

Quasi-dynamic model with cage

Contents

1	Markers definition	104
1.1	Cage coordinate systems	104
1.2	Relative displacements	106
2	Ball-to-pocket interactions	108
2.1	Interactions in (G_p^j, y_p^j, z_p^j) plan	109
2.2	Interaction in (G_p^j, z_p^j, x_p^j) plan	114
2.3	Total interactions	117
3	Cage-ring interactions	117
3.1	General model	117
3.2	Computation for whole cage	119
3.3	Computation for each pocket	121
4	Rigid cage resolution	123
4.1	Inner Ring equilibrium	123
4.2	Balls equilibrium	124
4.3	Cage equilibrium	124
4.4	Numerical procedure	124
5	Flexible cage resolution	126
5.1	Cage elasticity definition	126
5.2	Pocket equilibrium	128
5.3	Numerical procedure	128
5.4	Cage center motions and pocket elastic deformations	128
6	Results analysis	130
6.1	Investigation of existing bearings	130
6.2	Comparison with a 4 contact-points literature model	142
7	Summary	148

1 Markers definition

1.1 Cage coordinate systems

1.1.1 Cage center \mathcal{R}_c

Cage can be considered as a rigid or flexible body in three-dimensions. In any case, it has six degrees of freedom as represented in Figure 3.1. Indeed, cage center G_c translates of x_c , y_c , z_c and rotates of θ_{cx} , θ_{cy} , θ_{cz} relative to bearing center G . \mathcal{R}_c is the coordinate system related to these motions. As mentioned previously, cage also rotates around bearing axis \mathbf{x}_G at ω_c speed. In quasi-static and quasi-dynamic, this speed is supposed to be the average of balls precessions.

$$\mathcal{R}_C = \{G_C, \mathbf{x}_C, \mathbf{y}_C, \mathbf{z}_C\} \quad (3.1)$$

$$\delta_c = \mathbf{G}G_c = \begin{bmatrix} x_c \\ y_c \\ z_c \end{bmatrix}_{\mathcal{R}_G} \quad (3.2)$$

$$\theta_{cx} = (\mathbf{y}_G, \mathbf{y}_c) = (\mathbf{z}_G, \mathbf{z}_c) \quad (3.3)$$

$$\theta_{cy} = (\mathbf{z}_G, \mathbf{z}_c) = (\mathbf{x}_G, \mathbf{x}_c) \quad (3.4)$$

$$\theta_{cz} = (\mathbf{x}_G, \mathbf{x}_c) = (\mathbf{y}_G, \mathbf{y}_c) \quad (3.5)$$

$$\omega_c = \sum_{j=1}^N \frac{\omega_m^j}{N} \quad (3.6)$$

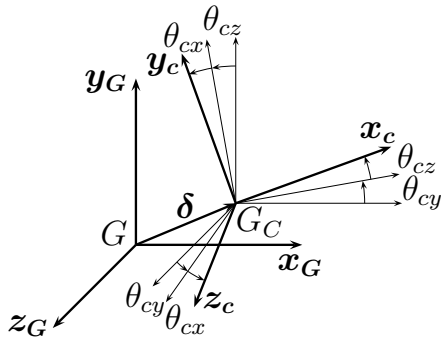


Figure 3.1 : Cage center motions

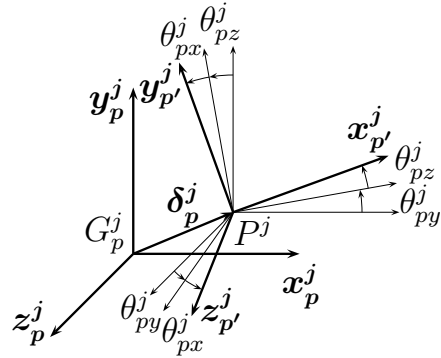


Figure 3.2 : Pocket center motions

1.1.2 Pocket initial position \mathcal{R}_p^j

Cage presents N cylindrical holes, or pockets, equally distributed around circumference. Initially, when cage is centered on the bearing and has not moved yet, each pocket is located in G_p^j and defined locally by coordinate system \mathcal{R}_p^j . Since cage rotational speed is supposed to be the average of balls precessions, this coordinate system is equivalent to ball position coordinate system \mathcal{R}_{b1}^j .

$$\mathcal{R}_p^j \equiv \mathcal{R}_{b1}^j = \{G_p^j, \mathbf{x}_G, \mathbf{y}_p^j, \mathbf{z}_p^j\} \quad (3.7)$$

$$\psi^j = \psi_c + \frac{2\pi}{N}(j-1) = (\mathbf{y}_G, \mathbf{y}_p^j) = (\mathbf{z}_G, \mathbf{z}_p^j) \quad (3.8)$$

1.1.3 Pocket removed position $\mathcal{R}_{p'}^j$

Like cage, pockets have six degrees of freedom as schematized in Figure 3.2. In global coordinate system, pocket centers P^j translates of δ_{px}^j , δ_{py}^j , δ_{pz}^j and rotates of θ_{px}^j , θ_{py}^j , θ_{pz}^j relative to pocket initial position G_p^j . $\mathcal{R}_{p'}^j$ is the coordinate system that defines this removed position.

$$\mathcal{R}_{p'}^j = \{P^j, \mathbf{x}_{p'}^j, \mathbf{y}_{p'}^j, \mathbf{z}_{p'}^j\} \quad (3.9)$$

$$\mathbf{G}_p^j \mathbf{P}^j = \delta_p^j = \begin{bmatrix} \delta_{px}^j \\ \delta_{py}^j \\ \delta_{pz}^j \end{bmatrix}_{\mathcal{R}_G} \quad (3.10)$$

$$\theta_{px}^j = (\mathbf{y}_p^j, \mathbf{y}_{p'}^j) = (\mathbf{z}_p^j, \mathbf{z}_{p'}^j) \quad (3.11)$$

$$\theta_{py}^j = (\mathbf{z}_p^j, \mathbf{z}_{p'}^j) = (\mathbf{x}_p^j, \mathbf{x}_{p'}^j) \quad (3.12)$$

$$\theta_{pz}^j = (\mathbf{x}_p^j, \mathbf{x}_{p'}^j) = (\mathbf{y}_p^j, \mathbf{y}_{p'}^j) \quad (3.13)$$

1.1.4 Bridge position \mathcal{R}_{br}^j

Each bridge is defined at its center G_{br}^j , by coordinate system \mathcal{R}_{br}^j . As illustrated in Figure 3.3, this position corresponds to initial pocket position with an additional rotation of $-\frac{\pi}{N}$.

$$\mathcal{R}_{br}^j \equiv \mathcal{R}_{b1}^j = \{G_{br}^j, \mathbf{x}_G, \mathbf{y}_{br}^j, \mathbf{z}_{br}^j\} \quad (3.14)$$

$$\psi_{br}^j = \psi_c + \frac{2\pi}{N}(j-1.5) = (\mathbf{y}_G, \mathbf{y}_{br}^j) = (\mathbf{z}_G, \mathbf{z}_{br}^j) \quad (3.15)$$

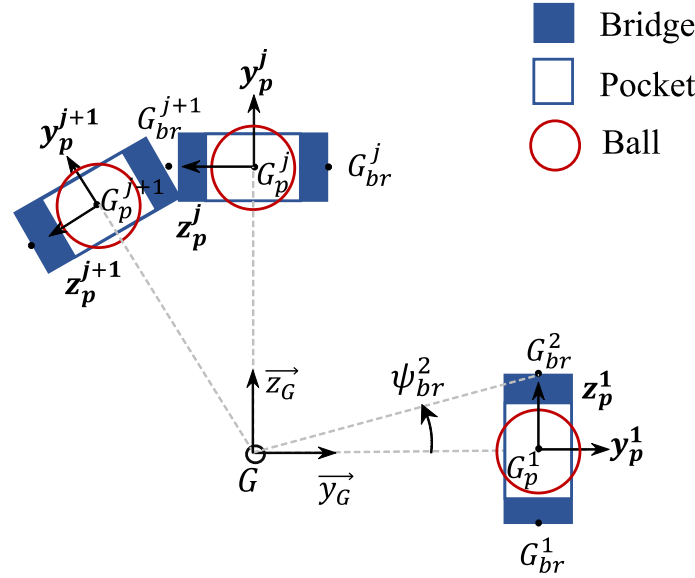


Figure 3.3 : Pocket centers and bridge centers positions

1.2 Relative displacements

1.2.1 Balls positions

In quasi-static, ball position was defined by relation (2.12). However, ball orthoradial displacement δ_{bz}^j was neglected, which is no longer valid with cage contribution. Indeed, as represented on Figure 3.4, pocket center P^j and ball center B^j are not combined anymore and ball-to-pocket interactions can occur. Nevertheless, determination of δ_{bz}^j is tricky since ball motion is already entirely defined. Adding another unknown would overstress the system. The solution found to estimate these variables is to consider ball number 1 as reference with δ_{bz}^1 set to 0. Then, we suppose that following balls have a displacement δ_{bz}^j equal to previous ball displacement δ_{bz}^{j-1} with an additional increment Δ_{bz}^j . This increment, defined by relation (3.16), corresponds to ball acceleration between two positions. To compute it, we assume that time step $\Delta\tau$ between two balls is the average time travelled by cage. With such definition, balls accelerations ω_m^j are approximated as a function of positions and speeds instead of real time. That is why we speak about quasi-dynamics of cage. Note that a coefficient λ_c is introduced in this expression. It is normally equal to 1 but during numerical procedure, it will be used as a relaxation coefficient comprised between 10^{-6} and 1.

$$\Delta_{bz}^j = \frac{\omega_m^j - \omega_m^{j-1}}{2} \frac{d_m}{2} \Delta\tau \text{ with } \Delta\tau = \frac{2\pi}{N\omega_c} \quad (3.16)$$

$$\delta_{bz}^j = \begin{cases} 0 & \text{if } j = 1 \\ \delta_{bz}^{j-1} + \lambda_c \frac{\omega_m^j - \omega_m^{j-1}}{\omega_c} \frac{\pi}{N} \frac{d_m}{2} & \text{otherwise} \end{cases} \quad (3.17)$$

Now that balls orthoradial displacements are known from expression (3.17), coordinates of ball mass center are updated with relation (3.18) and balls displacements relative to initial pockets centers are assessed by relation (3.19).

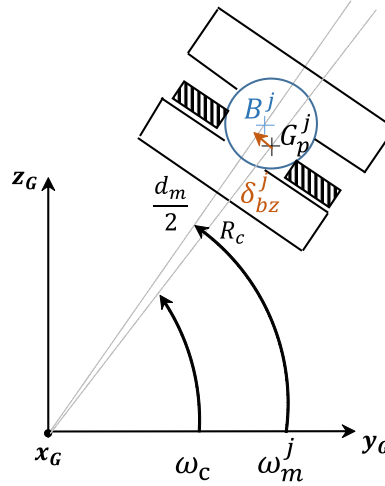


Figure 3.4 : Ball tangential displacement

$$GB^j = \begin{bmatrix} x_G^j \\ y_G^j \\ z_G^j \end{bmatrix}_{\mathcal{R}_G} = \begin{bmatrix} \delta_{bx}^j \\ \frac{d_m}{2} + \delta_{by}^j \\ \delta_{bz}^j \end{bmatrix}_{\mathcal{R}_{b1}^j} = \begin{bmatrix} \frac{g_o}{2} \lambda_o^j - GE_{o2} \sin \alpha_{o2}^j \\ (\frac{d_m}{2} - (f_o - 0.5)D \cos \alpha_f + GE_{o2} \cos \alpha_{o2}^j) \cos \psi^j - \delta_{bz}^j \sin \psi^j \\ (\frac{d_m}{2} - (f_o - 0.5)D \cos \alpha_f + GE_{o2} \cos \alpha_{o2}^j) \sin \psi^j + \delta_{bz}^j \cos \psi^j \end{bmatrix}_{\mathcal{R}_G} \quad (3.18)$$

$$G_p^j B^j = \delta_b^j = \begin{bmatrix} \delta_{bx}^j \\ \delta_{by}^j \\ \delta_{bz}^j \end{bmatrix}_{\mathcal{R}_G} = \begin{bmatrix} x_G^j \\ y_G^j - \frac{d_m}{2} \cos \psi^j \\ z_G^j - \frac{d_m}{2} \sin \psi^j \end{bmatrix}_{\mathcal{R}_G} \quad (3.19)$$

1.2.2 Pockets motions

When cage is considered as rigid, pocket displacements δ_p^j and rotations θ_p^j are only due to cage rigid motion. That is why, δ_c and θ_c are unknowns of the problem and δ_p^j , θ_p^j are deduced from relations (3.20) and (3.21).

$$G_p^j P^j = \begin{bmatrix} \delta_{px}^j \\ \delta_{py}^j \\ \delta_{pz}^j \end{bmatrix}_{\mathcal{R}_G} = \begin{bmatrix} x_c - R_c \cos \psi^j \theta_{cz} + R_c \sin \psi^j \theta_{cy} \\ y_c - R_c \sin \psi^j \theta_{cx} \\ z_c + R_c \cos \psi^j \theta_{cx} \end{bmatrix}_{\mathcal{R}_G} \quad (3.20)$$

$$\begin{bmatrix} \theta_{px}^j \\ \theta_{py}^j \\ \theta_{pz}^j \end{bmatrix}_{\mathcal{R}_G} = \begin{bmatrix} \theta_{cx} \\ \theta_{cy} \\ \theta_{cz} \end{bmatrix}_{\mathcal{R}_G} \quad (3.21)$$

On the contrary, as illustrated in Figure 3.5, when cage is considered as flexible, pocket motions δ_p^j , θ_p^j , are the contribution of cage rigid body modes δ_c^j , θ_c^j and of elastic deformations δ_{el}^j , θ_{el}^j . That is why, δ_p^j and θ_p^j cannot be expressed directly and becomes unknowns of elastic problem instead of δ_c , θ_c .

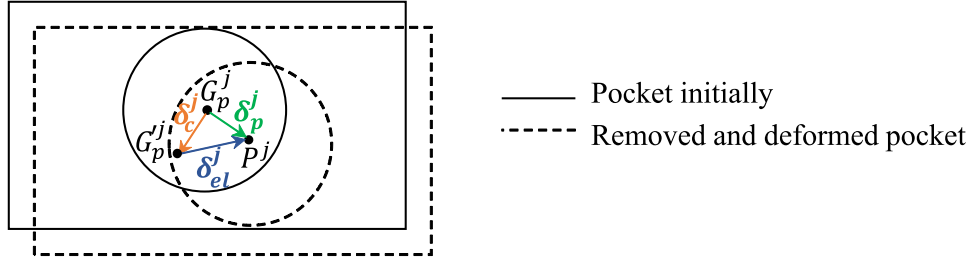


Figure 3.5 : Pocket motion and deformation

1.2.3 Ball-to-pocket geometric approach

From ball and pocket respective displacements, we can compute ball-to pocket displacements δ_{pb}^j by relation (3.22). We also define C_b^j the closer point on ball that approaches the point on pocket C_p^j . We suppose that ball-to-pocket interaction occurs in $(P^j, \mathbf{x}_p^j, \mathbf{z}_p^j)$ plan. Then, we assume that film thickness h_f^j , geometric approach Δpb^j and normal contact force do not have component along \mathbf{y}_p^j . Consequently, geometric approach Δ_{pb}^j is the projection of δ_{pb}^j in $(P^j, \mathbf{x}_p^j, \mathbf{z}_p^j)$ plan, as expressed in (3.23). As well, we define direction of ball-to-pocket approach by ϕ^j angle such as reported in Figure 3.6 and in expression (3.24). We will also suppose for the future, that ball-to-pocket clearance is a geometric constant, that is to say that ball and pocket macroscopic deformations are neglected even when cage is considered as flexible.

$$\mathbf{PB}^j = \delta_{pb}^j = \begin{bmatrix} PB_x^j \\ PB_y^j \\ PB_z^j \end{bmatrix}_{\mathcal{R}_G} = \begin{bmatrix} \delta_{bx}^j - \delta_{px}^j \\ \delta_{by}^j - \delta_{py}^j \\ \delta_{bz}^j - \delta_{pz}^j \end{bmatrix}_{\mathcal{R}_G} \quad (3.22)$$

$$\Delta_{pb}^j = \sqrt{(PB_x^j)^2 + (-PB_y^j \sin \psi^j + PB_z^j \cos \psi^j)^2} \quad (3.23)$$

$$\begin{cases} \cos \phi^j = \frac{PB_x^j}{\Delta_{pb}^j} \\ \sin \phi^j = \frac{-PB_y^j \sin \psi^j + PB_z^j \cos \psi^j}{\Delta_{pb}^j} \end{cases} \quad (3.24)$$

2 Ball-to-pocket interactions

Balls have complex motions with three self-rotations. That is why, ball-to-pocket interactions involve two phenomenon:

- Hydrodynamic (HD) or elastohydrodynamic (EHD) contact due to rotation $\omega_{yp}^j = \omega_R^j \sin \beta^j$ in $(G_p^j, \mathbf{y}_p^j, \mathbf{z}_p^j)$ plan.
- Short journal bearing effect due to rotation $\omega_{xp}^j = \omega_R^j \cos \beta^j \cos \beta'^j$ in $(G_p^j, \mathbf{z}_p^j, \mathbf{x}_p^j)$ plan.

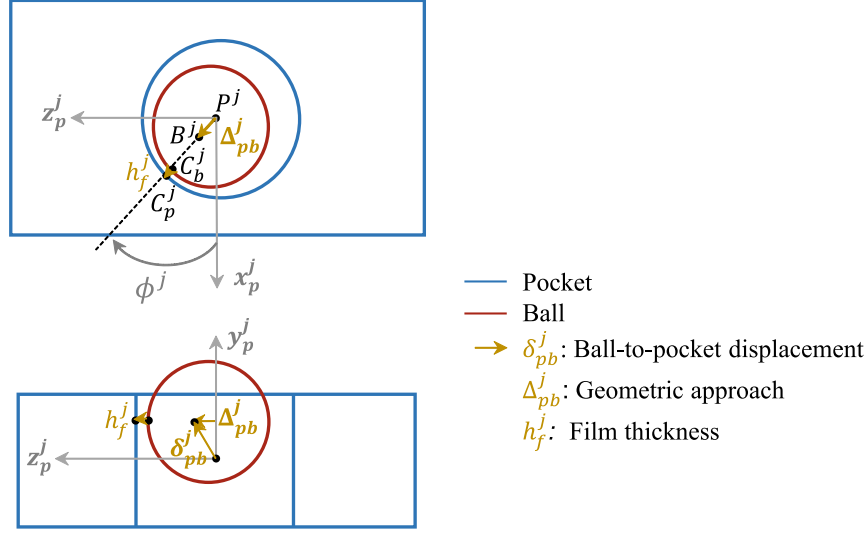


Figure 3.6 : Ball-to-pocket geometric interaction

2.1 Interactions in (G_p^j, y_p^j, z_p^j) plan

2.1.1 Barrel-plan HD contact

Ball-to-pocket hydrodynamic interaction in (G_p^j, y_p^j, z_p^j) plan is equivalent to a barrel-plan contact as schematized in Figure 3.7. This theory, developed in Nelias' thesis [186], gives HD normal force (3.25) and friction force (3.26) expressions of a fully lubricated contact between a barrel and a plan. To assess these forces, the relative velocity U (3.27) projected in (G_p^j, y_p^j, z_p^j) plan and equivalent radius R_x, R_y (3.28) are computed. Barrel-plan forces also depends on lubricant dynamic viscosity μ , on half length of the contact l , here half cage thickness h_c and above all on film thickness h_0 at the given contact.

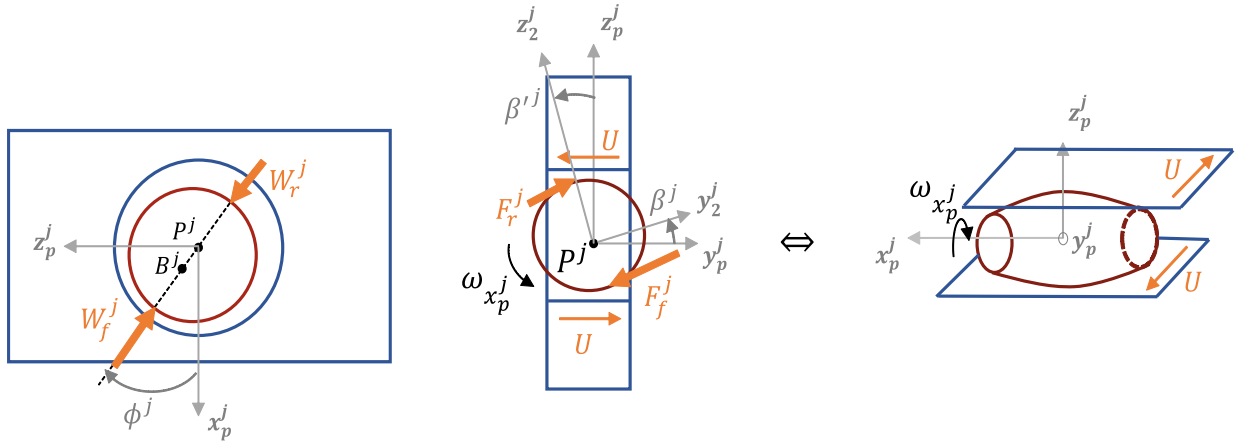


Figure 3.7 : Barrel-plan contact

$$W = \frac{2\pi\mu UR_y}{1 + \frac{2}{3}\frac{R_y}{R_x}} \sqrt{\frac{2R_x}{h_0}} \quad (3.25)$$

$$F = 2\mu U \sqrt{R_x R_y} \int_{-3}^3 \frac{1}{\sqrt{\frac{1}{L^2} + \eta^2}} \arctan \left(\frac{1}{\sqrt{\frac{1}{L^2} + \eta^2}} \right) d\eta \text{ with } L = \frac{l}{\sqrt{2R_y h_0}} \quad (3.26)$$

$$U = \frac{D}{2} \omega_R^j \cos \beta^j \cos \beta'^j \quad (3.27)$$

$$\begin{cases} R_x = \frac{R_p R_b}{R_p - R_b} \\ R_y = R_b \end{cases} \text{ with } R_b = \frac{D}{2} \text{ and } R_p = \frac{c_p + D}{2} \quad (3.28)$$

2.1.2 Dry contact

When two bodies get closer and film thickness gets smaller, contact interaction changes from hydrodynamic to elastohydrodynamic, then bodies deform with an elastic deformation δ_H^j . In such case, barrel-plan HD theory does not apply and normal contact force is characterised by Hertzian theory (3.29) instead.

$$W_H^j = K_H (\delta_H^j)^{\frac{3}{2}} \quad (3.29)$$

As well, by curve-fitting numerical solutions from 2D contact under EHD or PE (piezo-viscous elastic) lubrication regimes, Hamrock and Dowson [116] developed formula (3.30). It links film thickness with contact parameters such as load, speed or materials properties written in (3.31). More details about rheological parameters defined in these relations and in all BB20 interactions are presented in Appendix C.

$$H_{HD} = 1.69 U'^{0.67} G'^{0.53} W'^{-0.067} (1 - 0.61 e^{-0.73 k'}) R_y \quad (3.30)$$

with $k' = 1.03 \left(\frac{R_x}{R_y} \right)^{0.64}$

$$\left\{ \begin{array}{l} \text{Young's equivalent modulus } \frac{1}{E'} = \frac{1}{2} \left(\frac{1-\nu_b^2}{E_b} + \frac{1-\nu_c^2}{E_c} \right) \\ \text{Dimensionless velocity } U' = \frac{\mu U}{E' R_y} \\ \text{Dimensionless force } W' = \frac{W}{E' R_y^2} \\ \text{Dimensionless elasticity modulus : } G' = \alpha^* E' \end{array} \right. \quad (3.31)$$

Besides, when bodies deform elastically and when ball slips on pocket at relative speed U , shearing of solid fluid film occurs. Resulting shear force F_τ^j is calculated by considering non-Newtonian behaviour and by integrating shear stress limit τ_L on contact ellipse. This stress τ_L is defined by an isothermal, Maxwell-type, traction model with a Ree-Eyring visco-elastic formulation. Corresponding expression is reported in (3.32), where a , c are ellipse semi-axes and P is the average contact pressure. Lubricant parameters τ_{L0} , α_τ , β_τ , T_0 come from Nelias' experimental results [187] obtained for Mobil Jet-oil II with MIL-L-23699 specification.

$$F_\tau^j = \int_{\text{ellipse}} \tau_L dS = \pi a c \tau_L(T, P) \text{ with } \tau_L(T, P) = \tau_{L0} e^{(\alpha_\tau P + \beta_\tau (\frac{1}{T} - \frac{1}{T_0}))} \quad (3.32)$$

2.1.3 Contact forces continuity

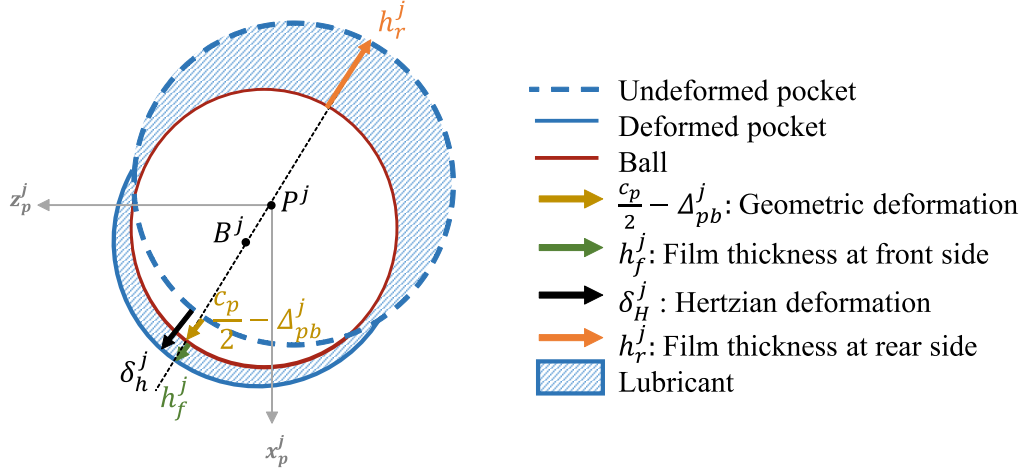


Figure 3.8 : Contact at each side

As schematized in Figure 3.8, ball-to-pocket interaction in (G_p^j, y_p^j, z_p^j) plan takes place at two locations:

- at front side where ball gets closer to pocket.
- at rear side which is opposite and where ball moves away from pocket.

At rear side, film thickness h_r^j arises from geometric relation (3.33), normal force W_r^j and friction force F_r^j are deduced from barrel-plan relations (3.25) and (3.26).

$$h_r^j = \frac{c_p}{2} + \Delta_{pb}^j \quad (3.33)$$

At front side, computation of normal and friction forces is tedious. Depending on ball-to-pocket relative positions, different contact model applies and transition from one model to another one results in important numerical discontinuities.

Indeed, as represented on the right part of graphics 3.9, when film thickness (or positive gap: $h_f^j = \frac{c_p}{2} - \Delta_{pb}^j$) decreases to get closer to zero, barrel-plan normal load W_{BP}^j tends to infinity. This is due to the fact that W_{BP}^j is inversely proportional to the root of film thickness. Such exponential increase generates discontinuities when film thickness changes between two iterations. This also confirms that barrel-plan HD theory does not apply below a minimal film thickness.

On the left part of graphics 3.9, Hertzian load W_H^j is plotted by supposing that elastic deformation is equal to ball-to-pocket penetration: $\delta_H^j = -\frac{c_p}{2} + \Delta_{pb}^j$. Then, it can be observed that normal load increases rapidly with penetration. This is due to the fact that W_H^j is proportional to δ_H^j at power 1.5. Note that physically, ball never penetrates pocket, a film is always present between bodies and gap cannot be negative. However, such case can be numerically encountered before reaching a converged state.

Analysis of these two curves in zero, also shows a discontinuity of normal load between barrel-plan and Hertzian model when changing from HD to EHD contact. Many procedures have been tested to find a solution to this problem. Optimal method selected is to define h_{tr}^j , the film thickness transition from HD to EHD regime. This transition occurs when Moes-Venner parameter M' , defined by relation (3.34), becomes greater than 10. Then, h_{tr}^j is calculated by Hamrock Dowson film thickness formula (3.30) with W' fixed such that $M' = 10$.

$$M' = W' U'^{-0.75} \quad (3.34)$$

Is this way, we consider that barrel-plan HD theory applies when gap is greater than h_{tr}^j . For lower values, Hertzian theory is applied with a δ_H^j value translated of h_{tr}^j . This translation does not introduce important error on load computation since W_H^j is particularly small when $\delta_H^j = h_{tr}^j$. This equivalent model is represented by the grey plot on Figure 3.9. With such model, transition between HD and EHD regimes is smooth and normal load does not take infinite values when film thickness tends to zero.

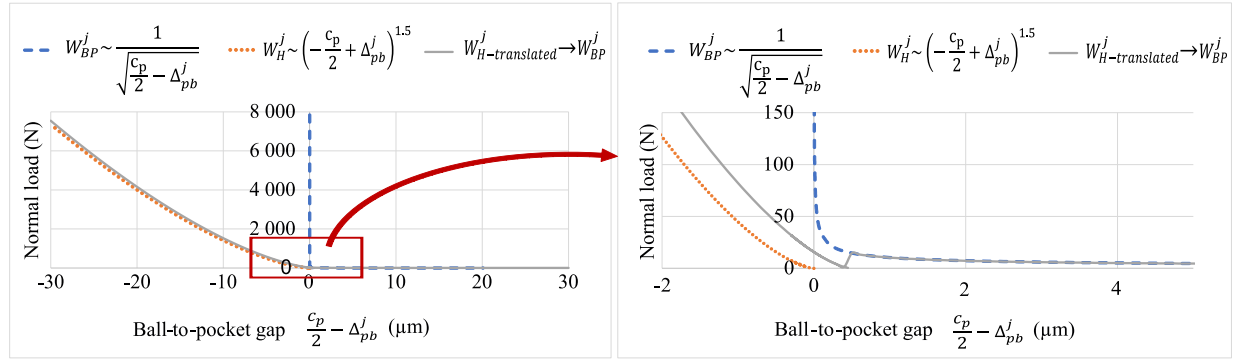


Figure 3.9 : Normal load evolution with ball-to-pocket gap $\frac{c_p}{2} - \Delta_{pb}^j$, for different contact models

Consequently, depending on ball-to-pocket positions and pocket clearance c_p , the following procedure is applied to compute contact forces at the front side:

- Hydrodynamic contact prevails if $\frac{c_p}{2} - \Delta_{pb}^j \geq h_{tr}^j$:

Then, film thickness h_f^j is calculated from geometric relation (3.35), HD normal force W_{BP}^j and friction force F_f^j are deduced from barrel-plan relations (3.25) and (3.26). From the knowledge of film thickness h_f^j , Hamrock-Dowson formula (3.30) is used in the reversed direction to compute dry normal load W_H^j . Then, Hertzian deformation δ_H^j is calculated by applying relation (3.29) in the reversed direction. From dry contact parameters, shear force F_τ^j is obtained by relation (3.32).

$$h_f^j = \frac{c_p}{2} - \Delta_{pb}^j \quad (3.35)$$

- Dry contact prevails if $\frac{c_p}{2} - \Delta_{pb}^j < h_{tr}^j$:

Then, Hertzian deformation is calculated geometrically by translated expression (3.36), dry normal load W_H^j by relation (3.29) and shear force F_τ^j by (3.32). Using normal load W_H^j , film thickness h_f^j is assessed by Hamrock Dowson formula (3.30). From film thickness, hydrodynamic normal force W_{BP}^j and friction force F_f^j are deduced from barrel-plan relations (3.25) and (3.26).

$$\delta_H^j = \left| \frac{c_p}{2} - \Delta_{pb}^j - h_{tr}^j \right| \quad (3.36)$$

Finally, for any lubrication regime, from HD and EHD contributions, equivalent normal load at front side is estimated by relation (3.37). Similarly, friction force at front side is expressed in (3.38) and shear force in (3.39).

$$W_f^j = W_{BP}^j \left(\frac{h_f^j}{h_f^j + \delta_H^j} \right) + W_H^j \left(\frac{\delta_H^j}{h_f^j + \delta_H^j} \right) \quad (3.37)$$

$$F_f^j = F_f^j \left(\frac{h_f^j}{h_f^j + \delta_H^j} \right) \quad (3.38)$$

$$F_\tau^j = F_\tau^j \left(\frac{\delta_H^j}{h_f^j + \delta_H^j} \right) \quad (3.39)$$

2.1.4 Forces summary

To summarize, ball-to-pocket forces acting in $(G_p^j, \mathbf{y}_p^j, \mathbf{z}_p^j)$ plan are normal and friction forces at front and rear side ($W_f^j, W_r^j, F_f^j, F_r^j$) and shear forces F_τ^j at front side. They act such that friction and shear are opposed to sliding speed U and that normal forces are directed toward the body of interest. Then, contact forces and momentums of pocket-on-ball at ball center B^j , in ball coordinate system \mathcal{R}_{b1}^j , are expressed by:

$$\mathbf{F}_{bp/b}^j = \begin{bmatrix} (W_f^j - W_r^j) \cos \phi^j - \sin \beta^j \cos \beta'^j (F_r^j - F_f^j - F_\tau^j) \\ (F_r^j - F_f^j - F_\tau^j) \cos \beta^j \\ (W_f^j - W_r^j) \sin \phi^j + \sin \beta^j \sin \beta'^j (F_r^j - F_f^j - F_\tau^j) \end{bmatrix}_{\mathcal{R}_{b1}^j} \quad (3.40)$$

$$\mathbf{M}_{bp/b}^j(B^j) = \begin{bmatrix} \frac{D}{2} (F_r^j + F_f^j + F_\tau^j) \sin \phi^j \cos \beta^j \\ \frac{D}{2} (\sin \phi^j \cos \beta'^j + \cos \phi^j \sin \beta'^j) (F_r^j + F_f^j + F_\tau^j) \sin \beta^j \\ -\frac{D}{2} (F_r^j + F_f^j + F_\tau^j) \cos \phi^j \cos \beta^j \end{bmatrix}_{\mathcal{R}_{b1}^j} \quad (3.41)$$

Forces and momentums of ball-on-pocket are opposed to pocket-on-ball ones. They are projected in global coordinate system \mathcal{R}_G because equilibrium equations on pocket or cage will be defined in this system. Ball-on-pocket momentums are also transposed at pocket center P^j .

$$\mathbf{F}_{bp/p}^j = -\mathbf{F}_{bp/b}^j \quad (3.42)$$

$$\mathbf{M}_{bp/p}^j(P^j) = -\mathbf{M}_{bp/b}^j(B^j) + \mathbf{P}B^j \wedge \mathbf{F}_{bp/p}^j \quad (3.43)$$

Then, contact forces and momentums of ball-on-pocket at pocket center P^j , in global coordinate system \mathcal{R}_G , are expressed by:

$$\mathbf{F}_{bp/p}^j = \begin{bmatrix} -F_{bp/bx}^j \\ -F_{bp/by}^j \cos \psi^j + F_{bp/bz}^j \sin \psi^j \\ -F_{bp/by}^j \sin \psi^j - F_{bp/bz}^j \cos \psi^j \end{bmatrix}_{\mathcal{R}_G} \quad (3.44)$$

$$\mathbf{M}_{bp/p}^j(P^j) = \begin{bmatrix} -M_{bp/bx}^j + PB_y^j F_{bp/pz}^j - PB_z^j F_{bp/py}^j \\ -M_{bp/by}^j \cos \psi^j + M_{bp/bz}^j \sin \psi^j + PB_z^j F_{bp/px}^j - PB_x^j F_{bp/pz}^j \\ -M_{bp/by}^j \sin \psi^j - M_{bp/bz}^j \cos \psi^j + PB_x^j F_{bp/py}^j - PB_y^j F_{bp/px}^j \end{bmatrix}_{\mathcal{R}_G} \quad (3.45)$$

2.2 Interaction in (G_p^j, z_p^j, x_p^j) plan

Considering forces acting in (G_p^j, z_p^j, x_p^j) plan is essential to gain in accuracy and to understand all mechanisms involved in cage behaviour. To model these interactions, we assume that corresponding contact is lightly loaded, that fluid is Newtonian and that bodies deformations are negligible. We also suppose that ball and pocket are co-axial and that the ratio cage thickness h_c to ball diameter D is less than $1/6$. Then, this interaction can be assimilated to an infinitely short hydrodynamic journal bearing. Note that in fact the ratio cage thickness to ball diameter h_c/D is between $1/3$ and $1/2$. That is why an improvement of this model could be considered a posteriori.

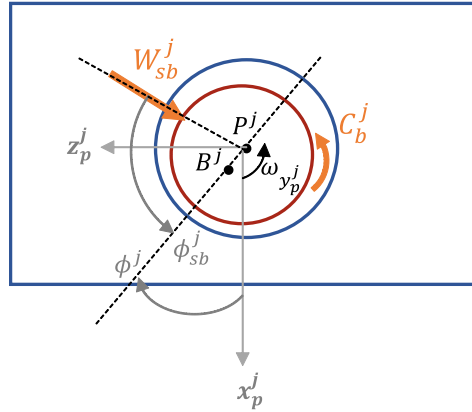


Figure 3.10 : Short journal bearing interaction

2.2.1 Short journal bearing modeling for HD contact

When film thickness h_f^j is greater than or equal to h_{tr}^j , lubrication regime is hydrodynamic and short journal bearing (SJB) theory applies directly. In this problem, we consider ball as a shaft of radius $R_1 = R_b$ and pocket as a pad of radius $R_2 = R_p$. Ball rotates around y_p^j at speed $\omega_1 = \omega_{y_p}^j = \omega_R^j \sin \beta^j$ whereas pocket does not rotate around y_p^j : $\omega_2 = 0$.

Contact width is equal to cage thickness h_c and eccentricity is equal to geometric approach Δ_{pb}^j . We also define in (3.46) eccentricity ratio ϵ as the ratio between eccentricity and radial clearance.

$$\epsilon = \frac{2\Delta_{pb}^j}{c_p} \quad (3.46)$$

Then, application of SJB theory gives attitude angle ϕ_{sb}^j , hydrodynamic load W_{sb}^j , friction torque on ball C_b^j and friction torque on pocket C_p^j as expressed in (3.47), (3.48), (3.49), (3.50).

$$\tan \phi_{sb}^j = \frac{\pi}{4} \frac{\sqrt{1-\epsilon^2}}{\epsilon} \text{sign}(\omega_R^j \sin \beta^j) \quad (3.47)$$

$$W_{sb}^j = \frac{\mu |\omega_R^j \sin \beta^j| R_p h_c^3}{c_p^2} \frac{\epsilon}{(1-\epsilon^2)^2} \sqrt{16\epsilon^2 + \pi^2(1-\epsilon^2)} \quad (3.48)$$

$$C_b^j = -\frac{\mu R_p^3 \omega_R^j \sin \beta^j h_c}{c_p} \frac{2\pi(2+\epsilon)}{(1+\epsilon)\sqrt{1-\epsilon^2}} \quad (3.49)$$

$$C_p^j = -C_b^j + \Delta_{pb}^j W_{sb}^j \sin \phi_{sb}^j \quad (3.50)$$

These contact parameters are schematized in Figure 3.10. Note that, because of fluid rotation ω_{yp}^j , hydrodynamic load W_{sb}^j is directed by attitude angle ϕ_{sb}^j . This direction is different than ϕ^j that orient contact approach with normal load W_f^j such as illustrated in Figure 3.7. Indeed, according to SJB theory, attitude angle ϕ_{sb}^j is defined by relation (3.51).

$$\phi_{sb}^j = (\mathbf{W}_{sb}^j, \mathbf{W}_f^j) \quad (3.51)$$

2.2.2 Extension of short journal bearing theory to EHD contact

When film thickness h_f^j is less than h_{tr}^j , lubrication regime is elastohydrodynamic, SJB theory does not apply anymore. Indeed, when film thickness reduces, Δ_{pb}^j gets closer to half pocket clearance $\frac{c_p}{2}$, relative eccentricity ϵ tends to 1, $(1-\epsilon^2)$ tends to zero, load W_{sb}^j and torques C_b^j , C_p^j tend to infinity. Nevertheless, a detailed analysis of SJB theory enables to understand that component $\frac{c_p}{2}(1-\epsilon)$ characterises shaft-pad minimum film thickness. Then, SJB theory can be extended to EHD contact by replacing $\frac{c_p}{2}(1-\epsilon)$ by h_f^j and ϵ by 1. In this way, relations (3.52) to (3.56) are obtained.

$$\epsilon = 1 \quad (3.52)$$

$$\phi_{sb}^j = 0 \quad (3.53)$$

$$W_{sb}^j = \frac{\mu |\omega_R^j \sin \beta^j| R_p h_c^3}{(h_f^j)^2} \quad (3.54)$$

$$C_b^j = -\frac{3\pi}{2} \frac{\mu R_p^3 \omega_R^j \sin \beta^j h_c}{\sqrt{2c_p h_f^j}} \quad (3.55)$$

$$C_p^j = -C_b^j \quad (3.56)$$

2.2.3 Forces summary

For both HD and EHD regimes, when fluid flow changes from laminar to turbulent, that is to say when Reynolds number R_e gets greater than 3 000, a correction on friction torques C_b^j and C_p^j is applied such that:

$$C_{turb}^j = C_{lam}^j (1 + 0.0012 R_e^{0.94}) \text{ with } R_e = \frac{\rho |\omega_R^j \sin \beta^j| D c_p}{4\mu} \quad (3.57)$$

Besides, from attitude angle definition (3.51), relation (3.58) can be deduced and load W_{sb}^j can be projected in ball coordinate system \mathcal{R}_{b1}^j . However, to avoid the use of arctangente function that can introduce numerical errors, explicit expression of ϕ^j is not calculated. Instead, $\sin \phi^j$ and $\cos \phi^j$ expressed in (3.24), are combined with trigonometric relations to project W_{sb}^j in \mathcal{R}_{b1}^j system.

$$(\mathbf{x}_p^j, \mathbf{W}_{sb}^j) = \phi^j - \phi_{sb}^j + \pi \quad (3.58)$$

Is this way, SJB forces and momentums of pocket-on-ball, at ball center B^j , in ball coordinate system \mathcal{R}_{b1}^j , are expressed by:

$$\mathbf{F}_{sb/b}^j = \begin{bmatrix} -W_{sb}^j (-\cos \phi^j \cos \phi_{sb}^j - \sin \phi^j \sin \phi_{sb}^j) \\ 0 \\ -W_{sb}^j (-\sin \phi^j \cos \phi_{sb}^j + \cos \phi^j \sin \phi_{sb}^j) \end{bmatrix}_{\mathcal{R}_{b1}^j} \quad (3.59)$$

$$\mathbf{M}_{sb/b}^j(B^j) = \begin{bmatrix} 0 \\ C_b^j \\ 0 \end{bmatrix}_{\mathcal{R}_{b1}^j} \quad (3.60)$$

SJB forces and momentums of ball-on-pocket, at pocket center P^j , in global coordinate system \mathcal{R}_G , are expressed by:

$$\mathbf{F}_{sb/p}^j = \begin{bmatrix} -F_{sb/bx}^j \\ F_{sb/bz}^j \sin \psi^j \\ -F_{sb/bz}^j \cos \psi^j \end{bmatrix}_{\mathcal{R}_G} \quad (3.61)$$

$$\mathbf{M}_{bp/p}^j(P^j) = \begin{bmatrix} 0 \\ C_p^j \cos \psi^j \\ C_p^j \sin \psi^j \end{bmatrix}_{\mathcal{R}_G} \quad (3.62)$$

2.3 Total interactions

To conclude on ball-to-pocket total interactions, resulting forces and momentums are the sum of contributions in $(G_p^j, \mathbf{y}_p^j, \mathbf{z}_p^j)$ and $(G_p^j, \mathbf{z}_p^j, \mathbf{x}_p^j)$ plans as expressed in relations (3.63) to (3.66).

$$\mathbf{F}_{p/b}^j = \mathbf{F}_{bp/b}^j + \mathbf{F}_{sb/b}^j \quad (3.63)$$

$$\mathbf{M}_{p/b}^j(B^j) = \mathbf{M}_{bp/b}^j(B^j) + \mathbf{M}_{sb/b}^j(B^j) \quad (3.64)$$

$$\mathbf{F}_{b/p}^j = \mathbf{F}_{bp/p}^j + \mathbf{F}_{sb/p}^j \quad (3.65)$$

$$\mathbf{M}_{b/p}^j(P^j) = \mathbf{M}_{bp/p}^j(P^j) + \mathbf{M}_{sb/p}^j(P^j) \quad (3.66)$$

Moreover, since rigid cage equilibrium will be defined at cage center G_c , ball-to-pocket momentum $\mathbf{M}_{b/p}^j(P^j)$ is transposed in this point:

$$\mathbf{M}_{b/c}^j(G_c) = \mathbf{M}_{b/p}^j(P^j) + \mathbf{G}_c \mathbf{P}^j \wedge \mathbf{F}_{b/p}^j \quad (3.67)$$

$$\mathbf{M}_{b/c}^j(G_c) = \begin{bmatrix} M_{b/px}^j(P^j) + R_c \cos \psi^j F_{b/pz}^j - R_c \sin \psi^j F_{b/py}^j \\ M_{b/py}^j(P^j) + R_c \sin \psi^j F_{b/pz}^j \\ M_{b/pz}^j(P^j) - R_c \cos \psi^j F_{b/px}^j \end{bmatrix}_{\mathcal{R}_G} \quad (3.68)$$

3 Cage-ring interactions

3.1 General model

If cage-inner race clearance c_{IR} is less than cage-outer race clearance c_{OR} , cage is guided by inner ring and hydrodynamic interaction occurs between these solids. Otherwise, cage is guided by outer ring and hydrodynamic interaction occurs with this ring. In any case, guiding clearance is defined by relation (3.69) and cage interactions with left and right races are considered independently. Is this way, different shoulder diameters can be considered at each side of a given ring: de_{il} , de_{ir} for left, right inner race and de_{ol} , de_{or} for left, right outer race. This distinction of upstream and downstream races is also an alternative to model a dissymmetry in cage temperature.

$$c_G = \min(c_{IR}, c_{OR}) \text{ with } \begin{cases} c_{IR} = D_{ci} - 0.5(de_{il} + de_{ir}) \\ c_{OR} = 0.5(de_{ol} + de_{or}) - D_{co} \end{cases} \quad (3.69)$$

To model these interactions, we assume that contact between cage and guiding race is lightly loaded, that fluid is Newtonian and that bodies deformations are negligible. We also suppose that cage and guiding race are co-axial and that the ratio race width L_{km} to shoulder diameter de_{km} is less than 1/6. Then, this interaction can be assimilated to an infinitely short hydrodynamic journal bearing in $(G, \mathbf{y}_G, \mathbf{z}_G)$ plan. With such hypothesis ring misalignment is not considered. Its implementation should be done in future versions.

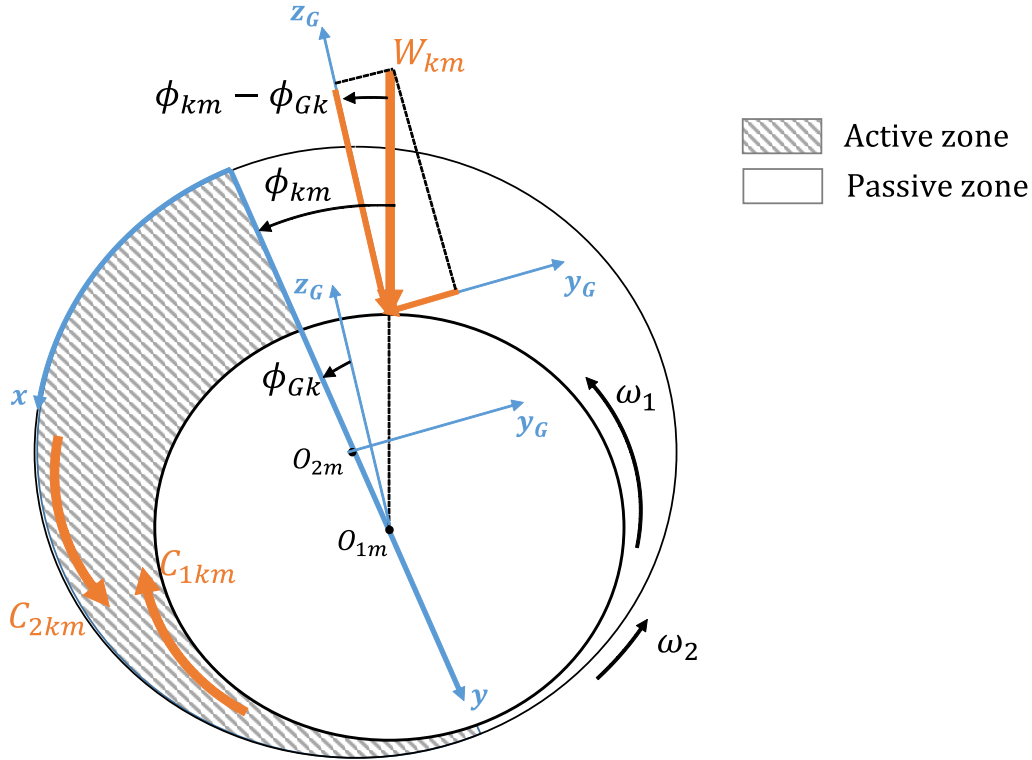


Figure 3.11 : Short journal bearing parameters

If short journal bearing theory is used to compute both cage-inner races or cage-outer races interactions, parameters definition is specific to each interaction. This parametrisation is illustrated in Figure 3.11.

When $c_{IR} \leq c_{OR}$, cage-inner races interactions occur, then cage-outer races forces $\mathbf{F}_{c/OR}$, $\mathbf{M}_{c/OR}$ are set to zero. To apply SJB theory to cage and inner races, we consider that left or right inner race is shaft (solid 1) of radius $R_1 = 0.5de_{im}$, rotational speed $\omega_1 = \Omega_i$ and that cage is pad (solid 2) of radius $R_2 = 0.5D_{ci}$, rotational speed $\omega_2 = \omega_c$. From cage and inner ring coordinates in $(G, \mathbf{y}_G, \mathbf{z}_G)$ plan, eccentricity is defined by relation (3.70).

$$e = O_{1m}O_{2m} = \sqrt{(\delta_y - y_c)^2 + (\delta_z - z_c)^2} \quad (3.70)$$

On the contrary, when $c_{OR} > c_{IR}$, cage-outer races interactions occur, then cage-inner races forces $\mathbf{F}_{c/IR}$, $\mathbf{M}_{c/IR}$ are set to zero. To apply SJB theory to cage and outer races, we consider that left or right outer race is pad (solid 2) of radius $R_2 = 0.5de_{om}$, rotational speed $\omega_2 = \Omega_o$ and that cage is shaft (solid 1) of radius $R_1 = 0.5D_{co}$, rotational speed $\omega_1 = \omega_c$. Since outer ring is supposed to be centered on the bearing in G , from cage coordinates in $(G, \mathbf{y}_G, \mathbf{z}_G)$ plan, eccentricity is defined by relation (3.71).

$$e = O_{1m}O_{2m} = \sqrt{y_c^2 + z_c^2} \quad (3.71)$$

For both interactions, relative eccentricity is defined in (3.72) as the ratio between eccentricity and half guiding clearance.

$$\epsilon = \frac{2e}{c_G} \quad (3.72)$$

From bearing geometry, contact widths L_{km} at left and right side of both rings are calculated by relation (3.73). In this expression, k refers to inner or outer race and m to left or right side. w_{Bk} is ring width, f_k is race conformity and C_{km,x_G} , C_{km,y_{b1}^j} are raceway curvature center positions along \mathbf{x}_G and \mathbf{y}_{b1}^j .

$$L_{km} = \left| 0.5w_{Bk} + \lambda C_{km,x_G} - \sqrt{(f_k D)^2 - (C_{km,y_{b1}^j} - 0.5de_{km})^2} \right| \text{ with } \lambda = +/ - 1 \text{ for } m = l/r \quad (3.73)$$

This theory applies to model both rigid and elastic cages. However, for rigid cage, quasi-dynamic resolution consists in solving cage equilibrium at cage center G_c . On the contrary, for flexible cage, quasi-dynamic resolution consists in solving pocket equilibrium at pocket center G_p^j . That is why computation of cage-ring interactions has to be done for whole cage on one hand, and for each pocket on the other hand.

3.2 Computation for whole cage

For rigid cage resolution, SJB theory is applied directly to the whole cage to obtain at each race k , each side m , attitude angle ϕ_{km} , hydrodynamic load W_{km} , friction torque on shaft C_{1km} and friction torque on pad C_{2km} as expressed in (3.74), (3.75), (3.76), (3.77). Note also that cage and inner ring rotation speeds are high, then fluid flow is turbulent and correction (3.78) is applied on torque computation.

$$\tan \phi_{km} = \frac{\pi}{4} \frac{\sqrt{1-\epsilon^2}}{\epsilon} \text{sign}(\omega_1 - \omega_2) \quad (3.74)$$

$$W_{km} = \frac{\mu |\omega_1 R_1 - \omega_2 R_2| L_{km}^3}{c_G} \frac{\epsilon}{(1-\epsilon^2)^2} \sqrt{16\epsilon^2 + \pi^2(1-\epsilon^2)} \quad (3.75)$$

$$C_{1km} = -\frac{\mu R_2^3 (\omega_1 - \omega_2)}{c_G} \frac{2\pi L_{km} (2+\epsilon)}{(1+\epsilon)\sqrt{1-\epsilon^2}} \quad (3.76)$$

$$C_{2km} = -C_{1km} + e W_{km} \sin \phi_{km} \quad (3.77)$$

$$C_{turb}^j = C_{lam}^j (1 + 0.0012 R_e^{0.94}) \text{ with } R_e = \frac{\rho |\omega_1 R_1 - \omega_2 R_2| c_G}{2\mu} \quad (3.78)$$

To project normal force W_{km} in global coordinate system \mathcal{R}_G , angle ϕ_{Gk} is defined between \mathbf{z}_G and eccentricity direction $\mathbf{O}_{1m}\mathbf{O}_{2m}$ as schematized in Figure 3.11. This angle is calculated by relation (3.79) for cage-inner races interactions and by relation (3.80) for cage-outer races.

$$\phi_{Gi} = (\mathbf{z}_G; \mathbf{O}_{1m}\mathbf{O}_{2m}) \text{ such that } \begin{cases} \text{if } z_c - \delta_z \neq 0 : \tan \phi_{Gi} = \frac{y_c - \delta_y}{z_c - \delta_z} \\ \text{if } z_c - \delta_z = 0 \text{ and } \begin{cases} \text{if } y_c - \delta_y = 0 : \phi_{Gi} = 0 \\ \text{if } y_c - \delta_y < 0 : \phi_{Gi} = \frac{\pi}{2} \\ \text{if } y_c - \delta_y > 0 : \phi_{Gi} = -\frac{\pi}{2} \end{cases} \end{cases} \quad (3.79)$$

$$\phi_{Go} = (z_G; \mathbf{O}_{1m} \mathbf{O}_{2m}) \text{ such that } \begin{cases} \text{if } z_c \neq 0 : \tan \phi_{Go} = \frac{y_c}{z_c} \\ \text{if } z_c = 0 \text{ and } \begin{cases} \text{if } y_c = 0 : \phi_{Go} = 0 \\ \text{if } y_c > 0 : \phi_{Go} = \frac{\pi}{2} \\ \text{if } y_c < 0 : \phi_{Go} = -\frac{\pi}{2} \end{cases} \end{cases} \quad (3.80)$$

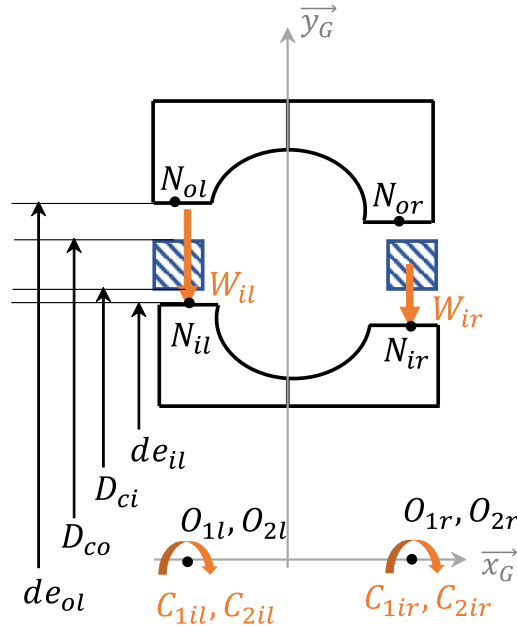


Figure 3.12 : Cage-inner races interactions

Finally, to compute cage-race forces we suppose that each force apply at the middle width of the race in N_{km} . We also assume that torques apply in O_{1m} or O_{2m} such as illustrated in Figure 3.12.

Consequently, forces and momentums of cage on inner race, at bearing center G , are expressed by:

$$\mathbf{F}_{c/IR} = \sum_{m=l,r} \begin{bmatrix} 0 \\ W_{im} \sin(\phi_{im} - \phi_{Gi}) \\ W_{im} \cos(\phi_{im} - \phi_{Gi}) \end{bmatrix}_{\mathcal{R}_G} \quad (3.81)$$

$$\mathbf{M}_{c/IR}^j(G) = \sum_{m=l,r} \left(\mathbf{M}_{c/IRm}^j(O_{1m}) + \mathbf{G} \mathbf{N}_{im} \wedge \mathbf{F}_{c/IRm} \right) \quad (3.82)$$

$$\mathbf{M}_{c/IR}(G) = \sum_{m=l,r} \begin{bmatrix} C_{1im} \\ -W_{im} \cos(\phi_{im} - \phi_{Gi}) (\delta_x + 0.5\lambda(w_{IR} - L_{im})) \\ W_{im} \sin(\phi_{im} - \phi_{Gi}) (\delta_x + 0.5\lambda(w_{IR} - L_{im})) \end{bmatrix}_{\mathcal{R}_G} \quad \begin{array}{l} \text{with } \lambda = -/+1 \\ \text{for } m = l/r \end{array} \quad (3.83)$$

Forces and momentums of inner race on cage at cage center G_c are expressed by:

$$\mathbf{F}_{IR/c} = -\mathbf{F}_{c/IR} \quad (3.84)$$

$$\mathbf{M}_{IR/c}^j(G_c) = \sum_{m=l,r} \left(\mathbf{M}_{IR/cm}^j(O_{2m}) + \mathbf{G}_c \mathbf{N}_{im} \wedge \mathbf{F}_{IR/cm} \right) \quad (3.85)$$

$$\mathbf{M}_{IR/c}(G_c) = \sum_{m=l,r} \left[\begin{array}{c} C_{2im} \\ W_{im} \cos(\phi_{im} - \phi_{Gi}) (\delta_x + 0.5\lambda(w_{IR} - L_{im})) \\ -W_{im} \sin(\phi_{im} - \phi_{Gi}) (\delta_x + 0.5\lambda(w_{IR} - L_{im})) \end{array} \right]_{\mathcal{R}_G} \quad \begin{array}{l} \text{with } \lambda = -/+1 \\ \text{for } m = l/r \end{array} \quad (3.86)$$

Forces and momentums of outer race on cage at cage center G_c are expressed by:

$$\mathbf{F}_{OR/c} = \sum_{m=l,r} \left[\begin{array}{c} 0 \\ W_{om} \sin(\phi_{om} - \phi_{Go}) \\ W_{om} \cos(\phi_{om} - \phi_{Go}) \end{array} \right]_{\mathcal{R}_G} \quad (3.87)$$

$$\mathbf{M}_{OR/c}^j(G_c) = \sum_{m=l,r} \left(\mathbf{M}_{OR/cm}^j(O_{1m}) + \mathbf{G}_c \mathbf{N}_{om} \wedge \mathbf{F}_{OR/cm} \right) \quad (3.88)$$

$$\mathbf{M}_{OR/c}(G_c) = \sum_{m=l,r} \left[\begin{array}{c} C_{1om} \\ -W_{om} \cos(\phi_{om} - \phi_{Go}) (0.5\lambda(w_{OR} - L_{om})) \\ W_{om} \sin(\phi_{om} - \phi_{Go}) (0.5\lambda(w_{OR} - L_{om})) \end{array} \right]_{\mathcal{R}_G} \quad \begin{array}{l} \text{with } \lambda = -/+1 \\ \text{for } m = l/r \end{array} \quad (3.89)$$

Note that forces and momentums of cage on outer race are not calculated because no equilibrium is made on outer race.

3.3 Computation for each pocket

Computation of cage-race forces for flexible cage is more complicated since cage is segmented in N elements. Forces of each race section on each pocket must be calculated. As for that, SJB theory is revised from the beginning. Indeed, in general theory, normal load and friction torque are calculated by integrating respectively, hydrodynamic pressure and shear stress, on the whole bearing. Now, to compute normal load W_{km}^j and friction torque C_{km}^j on each pocket j , hydrodynamic pressure and shear stress are only integrated on each element. Corresponding integration interval is defined in (3.90) and taken as bridge angular position on both sides of a pocket.

$$[a^j; b^j] = [\psi_{br}^j; \psi_{br}^{j+1}] = \left[\frac{2\pi}{N}(j - 1.5) + \psi_c; \frac{2\pi}{N}(j - 0.5) + \psi_c \right] \quad (3.90)$$

Pockets are separated into two categories depending on their orbital position:

- Pockets in active zone where $\phi_{Gk} + \frac{\pi}{2} \leq \psi^j \leq \phi_{Gk} + \frac{3\pi}{2}$, hydrodynamic pressure is positive and normal load is calculated by pressure integration on $[a^j; b^j]$.
- Pockets in passive zone where $\phi_{Gk} + \frac{3\pi}{2} \leq \psi^j \leq \phi_{Gk} + \frac{5\pi}{2}$, pressure and normal load are supposed to be equal to zero.

Each zone also presents a different shear stress. Then, after computation, different normal load W_{km}^j and friction torque C_{km}^j are obtained for pockets located in each zone. Corresponding expressions are summarised by relations (3.91) to (3.95). Note that torque correction (3.78) is again applied on C_{km}^j since fluid flow is turbulent.

$$W_{km}^j = \begin{cases} \sqrt{(W_{tkm}^j)^2 + (W_{rkm}^j)^2} & \text{if } \psi^j \in \text{active zone} \\ 0 & \text{if } \psi^j \in \text{passive zone} \end{cases} \quad (3.91)$$

$$W_{tkm}^j = \frac{\mu |\omega_1 R_1 - \omega_2 R_2| L_{km}^3}{c_G^2} \frac{2\epsilon}{(1-\epsilon^2)^2} \left(\frac{(\cos \psi_b^j)^2 - (\cos \psi_a^j)^2}{2} - \epsilon (\cos \psi_b^j - \cos \psi_a^j) \right) \quad (3.92)$$

$$W_{rkm}^j = \frac{\mu |\omega_1 R_1 - \omega_2 R_2| L_{km}^3}{c_G^2} \frac{\epsilon}{(1-\epsilon^2)^{1.5}} \left(\psi_b^j - \psi_a^j - \frac{\sin(2\psi_b^j) - \sin(2\psi_a^j)}{2} \right) \quad (3.93)$$

$$C_{km}^j = \begin{cases} \frac{\mu R_2^3 (\omega_1 - \omega_2)}{c_G} \frac{2L_{km}}{\sqrt{1-\epsilon^2}} (\psi_b^j - \psi_a^j) & \text{if } j \in \text{active zone} \\ \frac{\mu R_2^3 (\omega_1 - \omega_2)}{c_G} \frac{2L_{km}}{(1+\epsilon)\sqrt{1-\epsilon^2}} (\psi_b^j - \psi_a^j - \epsilon(\sin \psi_b^j - \sin \psi_a^j)) & \text{if } j \in \text{passive zone} \end{cases} \quad (3.94)$$

$$\begin{cases} \cos \psi_c^j = \frac{\epsilon + \cos c}{1 + \epsilon \cos c} \\ \sin \psi_c^j = \frac{\sqrt{1-\epsilon^2} \sin c}{1 + \epsilon \cos c} \\ \sin(2\psi_c^j) = \frac{\sqrt{1-\epsilon^2} \sin(2c)}{1 + \epsilon \cos(2c)} \end{cases} \quad \text{with } c = a^j, b^j \quad (3.95)$$

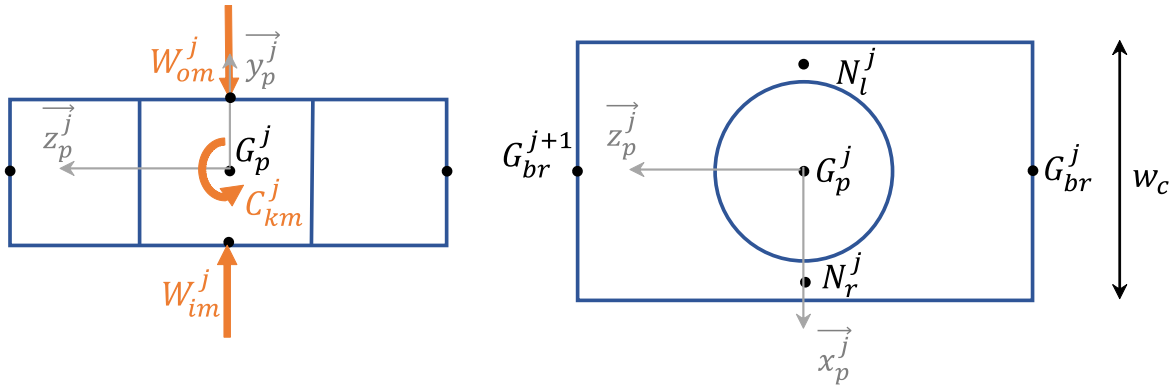


Figure 3.13 : Races-Pocket interactions

Finally, to compute race-to-pocket forces, we suppose that each force apply at the middle length of a pocket in N_m^j such as schematized in Figure 3.13. Normal load W_{km}^j is directed along \mathbf{y}_p^j and friction torque C_{km}^j around \mathbf{x}_G .

Consequently, forces and momentums of inner race on pocket j , at pocket center G_p^j , are expressed by:

$$\mathbf{F}_{IR/p}^j = \sum_{m=l,r} \begin{bmatrix} 0 \\ W_{im}^j \cos \psi^j \\ W_{im}^j \sin \psi^j \end{bmatrix}_{\mathcal{R}_G} \quad (3.96)$$

$$\mathbf{M}_{IR/p}^j(G_p^j) = \sum_{m=l,r} \left(\mathbf{M}_{IR/pm}^j(G_p^j) + \mathbf{G}_p^j \mathbf{N}_m^j \wedge \mathbf{F}_{IR/pm}^j \right) \quad (3.97)$$

$$\mathbf{M}_{IR/p}^j(G_p^j) = \sum_{m=l,r} \begin{bmatrix} C_{im}^j \\ -0.25\lambda W_{im}^j \sin \psi^j (w_c + D_p) \\ 0.25\lambda W_{im}^j \cos \psi^j (w_c + D_p) \end{bmatrix}_{\mathcal{R}_G} \quad \begin{array}{l} \text{with } \lambda = -/+1 \\ \text{for } m = l/r \end{array} \quad (3.98)$$

Similarly, forces and momentums of outer race on pocket j , at pocket center G_p^j , are expressed by:

$$\mathbf{F}_{OR/p}^j = \sum_{m=l,r} \begin{bmatrix} 0 \\ -W_{om}^j \cos \psi^j \\ -W_{om}^j \sin \psi^j \end{bmatrix}_{\mathcal{R}_G} \quad (3.99)$$

$$\mathbf{M}_{OR/p}^j(G_p^j) = \sum_{m=l,r} \left(\mathbf{M}_{OR/pm}^j(G_p^j) + \mathbf{G}_p^j \mathbf{N}_m^j \wedge \mathbf{F}_{OR/pm}^j \right) \quad (3.100)$$

$$\mathbf{M}_{OR/p}^j(G_p^j) = \sum_{m=l,r} \begin{bmatrix} -C_{om}^j \\ 0.25\lambda W_{om}^j \sin \psi^j (w_c + D_p) \\ -0.25\lambda W_{om}^j \cos \psi^j (w_c + D_p) \end{bmatrix}_{\mathcal{R}_G} \quad \begin{array}{l} \text{with } \lambda = +/ -1 \\ \text{for } m = l/r \end{array} \quad (3.101)$$

4 Rigid cage resolution

Quasi-dynamic (QD) resolution of ACBB with rigid cage is straightforward and consists in adding cage-race forces and pocket-to-ball forces in previous quasi-static (QS) equations on inner ring and balls. Six equations on cage are also added to solve its equilibrium.

4.1 Inner Ring equilibrium

In QD, sum of forces and momentums that apply on the inner ring, at bearing center G , in \mathbf{x}_G , \mathbf{y}_G and \mathbf{z}_G directions, includes QS contribution and cage-to-inner race interactions such that:

$$F_{QD/IRx} = F_{QS/IRx} + F_{c/IRx} = 0 \quad (3.102)$$

$$F_{QD/IRy} = F_{QS/IRy} + F_{c/IRy} = 0 \quad (3.103)$$

$$F_{QD/IRz} = F_{QS/IRz} + F_{c/IRz} = 0 \quad (3.104)$$

$$M_{QD/IRy} = M_{QS/IRy} + M_{c/IRy} = 0 \quad (3.105)$$

$$M_{QD/IRz} = M_{QS/IRz} + M_{c/IRz} = 0 \quad (3.106)$$

4.2 Balls equilibrium

In QD, sum of forces and momentums that apply on each ball j at their center B^j , in \mathbf{x}_G , \mathbf{y}_{b1}^j and \mathbf{z}_{b1}^j directions, includes QS contribution and pocket-to-ball interactions such that:

$$F_{QD/bx}^j = F_{QS/bx}^j + F_{p/bx}^j = 0 \quad (3.107)$$

$$F_{QD/by}^j = F_{QS/by}^j + F_{p/by}^j = 0 \quad (3.108)$$

$$F_{QD/bz}^j = F_{QS/bz}^j + F_{p/bz}^j = 0 \quad (3.109)$$

$$M_{QD/bx}^j = M_{QS/bx}^j + M_{p/bx}^j = 0 \quad (3.110)$$

$$M_{QD/by}^j = M_{QS/by}^j + M_{p/by}^j = 0 \quad (3.111)$$

$$M_{QD/bz}^j = M_{QS/bz}^j + M_{p/bz}^j = 0 \quad (3.112)$$

In R2 resolution with cage, when balls (almost) detach from inner race, balls equations are not modified anymore. Then, no convergence is forced on β^j , β'^j , ω_m^j or ω_R^j .

4.3 Cage equilibrium

In QD, sum of forces and momentums on cage, that apply at its center G_c , in \mathbf{x}_G , \mathbf{y}_G and \mathbf{z}_G directions, includes cage-ring forces and ball-to-pocket forces coming from N balls. These equilibrium equations are expressed by:

$$F_{QD/cx} = F_{IR/cx} + F_{OR/cx} + \sum_{j=1}^N F_{b/px}^j = 0 \quad (3.113)$$

$$F_{QD/cy} = F_{IR/cy} + F_{OR/cy} + \sum_{j=1}^N F_{b/py}^j = 0 \quad (3.114)$$

$$F_{QD/cz} = F_{IR/cz} + F_{OR/cz} + \sum_{j=1}^N F_{b/pz}^j = 0 \quad (3.115)$$

$$M_{QD/cx} = M_{IR/cx} + M_{OR/cx} + \sum_{j=1}^N M_{b/cx}^j = 0 \quad (3.116)$$

$$M_{QD/cy} = M_{IR/cy} + M_{OR/cy} + \sum_{j=1}^N M_{b/cy}^j = 0 \quad (3.117)$$

$$M_{QD/cz} = M_{IR/cz} + M_{OR/cz} + \sum_{j=1}^N M_{b/cz}^j = 0 \quad (3.118)$$

4.4 Numerical procedure

Then, QS system of $12N+5$ equations becomes a QD system of $12N+5+6$ equations. Six additional equations are related to cage equilibrium with cage center positions x_c , y_c , z_c and cage rotations θ_{cx} , θ_{cy} , θ_{cz} as unknowns. These cage equations and unknowns are also nondimensionalized by parameters given in Table 3.1.

Then, this dimensionless system of $12N+11$ QD equations is solved with same Newton-Raphson scheme as QS one. Note that QS solution of R2 resolution is used to initialise balls and inner ring unknowns of QD problem. Regarding initialisation of cage unknowns, axial displacement x_c is set equal to balls average position along \mathbf{x}_G . If cage is guided by inner ring, it is assumed that other cage displacements and rotations are initially equal to inner ring ones. If cage is guided by outer ring, it is assumed that cage is initially centered on bearing, then all cage unknowns, except for x_c , are set to zero.

Equation	Parameter	Unknown	Parameter
$F_{QD/cx} : (3.113)$	$\sqrt{F_X^2 + F_Y^2 + F_Z^2}$	x_c	$\frac{c_G}{2}$
$F_{QD/cy} : (3.114)$		y_c	
$F_{QD/cz} : (3.115)$		z_c	
$M_{QD/cx} : (3.116)$	$\frac{d_m}{2} \sqrt{F_X^2 + F_Y^2 + F_Z^2}$	θ_{cx}	$\frac{\pi}{N}$
$M_{QD/cy} : (3.117)$		θ_{cy}	
$M_{QD/cz} : (3.118)$		θ_{cz}	

Table 3.1 : Cage parameters used to nondimensionalize related equations or unknowns

At first iterations of R2 resolution with cage, precession speeds calculated are far from real values because cage was not considered before. Under important radial load, consecutive balls can have important precession speeds differences. Consequently, ball-to-pocket orthoradial displacements δ_{bz}^j , defined in (3.17), can be very large. Then, in $(G_p^j, \mathbf{y}_p^j, \mathbf{z}_p^j)$ plan, radially loaded balls are under EHD regime. Elastic deformations δ_H^j and normal loads W_f^j are large compared with unloaded balls that are under HD regime. In $(G_p^j, \mathbf{z}_p^j, \mathbf{x}_p^j)$ plan, extended theory of short journal bearing is used for radially loaded balls. Film thickness is particularly small, then load W_{sb}^j and torques C_b^j , C_p^j are very large. Numerically, load differences between radially loaded and unloaded balls create an ill conditioned Jacobian matrix and cage does not succeed to balance itself.

This problem can be solved by improving numerical procedure. As for that, on the one hand, R2 resolution with cage is first solved without considering ball-to-pocket interactions in $(G_p^j, \mathbf{z}_p^j, \mathbf{x}_p^j)$ plan. Once cage is balanced, these forces are introduced in the system in order to refine solution. This is made possible by the fact that ball-to-pocket SJB interactions are of the second-order even if they can be responsible for converging problems when suddenly, film thickness gets particularly small. On the other hand, a coefficient λ_c is introduced in ball-to-pocket orthoradial displacement expression (3.17). This coefficient allows to relax δ_{bz}^j value when important precession differences occurs between two consecutive balls. This coefficient is comprised between 10^{-6} and 1. It is fixed at the beginning of each iteration such that all ball-to-pocket normal loads W_f^j are less than 5 000N. Numerically, we observe that λ_c is always equal to 1 under small radial loads. But, when radial load is increased, this coefficient gets smaller at first iterations. Then, it increases step by step as bearing with cage balances itself and as ball precession differences reduce. In any case, system is not considered as converged if λ_c is less than 1.

Over iterations, if system no longer changes because of too small λ_c , W_f^j is authorized to be larger than 5 000N and λ_c is increased incrementally. Note that if W_f^j can take values larger than 5 000N, once converged this normal load is never larger than a dozen Newtons. This is logical since in quasi-dynamics, ball-to-pocket impacts are not considered, then only small interactions occurs.

5 Flexible cage resolution

5.1 Cage elasticity definition

To model cage flexibility, we divide it into finite elements centered on each bridge. Each node corresponds to pocket center such as represented on Figure 3.14. In this finite element model, we suppose that nodal forces directly applies on the node. Is this way, use of shape functions is not necessary.

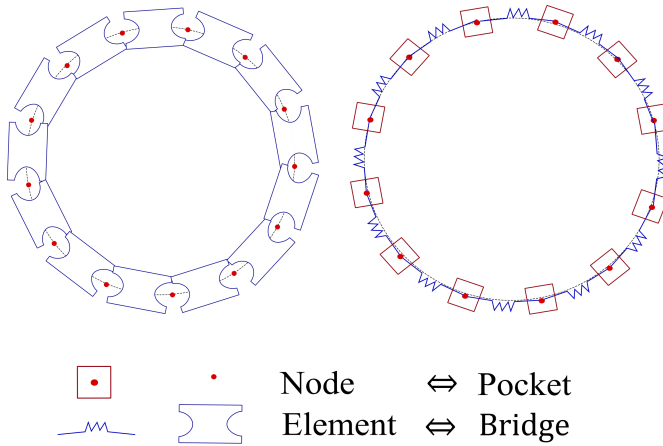


Figure 3.14 : Cage discretisation by finite elements

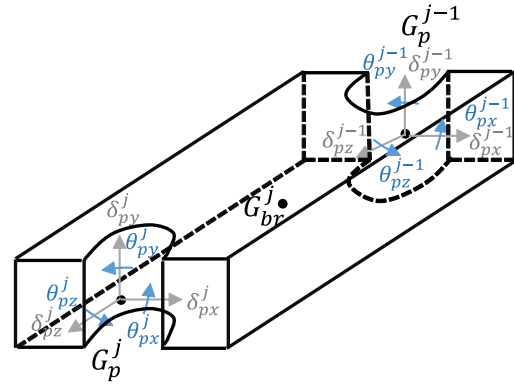


Figure 3.15 : 3D Beam element

Each bridge is defined by a 3D beam with 6 degrees of freedom at each node: δ_{pz}^j for traction, δ_{px}^j , δ_{py}^j , θ_{px}^j , θ_{py}^j for bending and θ_{pz}^j for torsion, such as schematized in Figure 3.15. Each element is defined by a stiffness matrix \mathbf{K}_{el} of size 12 by 12 and expressed in bridge coordinate system \mathcal{R}_{br}^j such as defined in (3.119). Transfer matrix \mathbf{P}_K^j defined in (3.120), enables to transpose \mathbf{K}_{el} in global coordinate system \mathcal{R}_G in order to obtain \mathbf{K}_G^j computed in (3.121). Numerically, assembling all these element matrix \mathbf{K}_G^j between all bridges, gives the global cage stiffness matrix \mathbf{K}_{cage} of size 6N by 6N and defined in global coordinate system \mathcal{R}_G . Multiplication of \mathbf{K}_{cage} by related degrees of freedom at each node gives nodal elastic deformation forces and momentums such as calculated in (3.122).

$$\mathbf{K}_{el} = \begin{bmatrix}
0 & \frac{12EI_x}{L_{br}^3} & 0 & -\frac{6EI_x}{L_{br}^2} & 0 & 0 & 0 & -\frac{12EI_x}{L_{br}^3} & 0 & -\frac{6EI_x}{L_{br}^2} & 0 & 0 \\
0 & 0 & \frac{ES}{L_{br}} & 0 & 0 & 0 & 0 & 0 & -\frac{ES}{L_{br}} & 0 & 0 & 0 \\
0 & -\frac{6EI_x}{L_{br}^2} & 0 & \frac{4EI_x}{L_{br}} & 0 & 0 & 0 & \frac{6EI_x}{L_{br}^2} & 0 & \frac{2EI_x}{L_{br}} & 0 & 0 \\
\frac{6EI_y}{L_{br}^2} & 0 & 0 & 0 & \frac{4EI_y}{L_{br}} & 0 & -\frac{6EI_y}{L_{br}^2} & 0 & 0 & 0 & \frac{2EI_y}{L_{br}} & 0 \\
0 & 0 & 0 & 0 & 0 & \frac{GJ}{L_{br}} & 0 & 0 & 0 & 0 & 0 & -\frac{GJ}{L_{br}} \\
-\frac{12EI_y}{L_{br}^3} & 0 & 0 & 0 & -\frac{6EI_y}{L_{br}^2} & 0 & \frac{12EI_y}{L_{br}^3} & 0 & 0 & 0 & -\frac{6EI_y}{L_{br}^2} & 0 \\
0 & -\frac{12EI_x}{L_{br}^3} & 0 & \frac{6EI_x}{L_{br}^2} & 0 & 0 & 0 & \frac{12EI_x}{L_{br}^3} & 0 & \frac{6EI_x}{L_{br}^2} & 0 & 0 \\
0 & 0 & -\frac{ES}{L_{br}} & 0 & 0 & 0 & 0 & 0 & \frac{ES}{L_{br}} & 0 & 0 & 0 \\
0 & -\frac{6EI_x}{L_{br}^2} & 0 & \frac{2EI_x}{L_{br}} & 0 & 0 & 0 & \frac{6EI_x}{L_{br}^2} & 0 & \frac{4EI_x}{L_{br}} & 0 & 0 \\
\frac{6EI_y}{L_{br}^2} & 0 & 0 & 0 & \frac{2EI_y}{L_{br}} & 0 & -\frac{6EI_y}{L_{br}^2} & 0 & 0 & 0 & \frac{4EI_y}{L_{br}} & 0 \\
0 & 0 & 0 & 0 & 0 & -\frac{GJ}{L_{br}} & 0 & 0 & 0 & 0 & 0 & \frac{GJ}{L_{br}}
\end{bmatrix} \mathbf{R}_{br}^j$$

with $\begin{cases} L_{br} = \frac{\pi(D_{co}+D_{ci})}{2N} & S = h_c w_c & G_c = \frac{E_c}{2(1+\nu_c)} \\ I_x = \frac{w_c h_c^3}{12} & I_y = \frac{h_c w_c^3}{12} & J = I_x + I_y \end{cases}$

(3.119)

$$\mathbf{P}_K^j = \begin{bmatrix} P_{br \rightarrow G}^j & 0 & 0 & 0 \\ 0 & P_{br \rightarrow G}^j & 0 & 0 \\ 0 & 0 & P_{br \rightarrow G}^j & 0 \\ 0 & 0 & 0 & P_{br \rightarrow G}^j \end{bmatrix} \text{ with } \mathbf{P}_{br \rightarrow G}^j = \begin{bmatrix} 1 & 0 & 0 \\ 0 & \cos \psi_{br}^j & \sin \psi_{br}^j \\ 0 & -\sin \psi_{br}^j & \cos \psi_{br}^j \end{bmatrix} \quad (3.120)$$

$$\mathbf{K}_G^j = \left(\mathbf{P}_K^j \right)^{-1} \mathbf{K}_{el} \mathbf{P}_K^j \quad (3.121)$$

$$\begin{bmatrix} \mathbf{F}_{el}^1 \\ \mathbf{M}_{el}^1(P^j) \\ \dots \\ \dots \\ \mathbf{F}_{el}^N \\ \mathbf{M}_{el}^N(P^j) \end{bmatrix}_{R_G} = \mathbf{K}_{cage} \begin{bmatrix} \boldsymbol{\delta}_p^1 \\ \boldsymbol{\theta}_p^1 \\ \dots \\ \dots \\ \boldsymbol{\delta}_p^N \\ \boldsymbol{\theta}_p^N \end{bmatrix}_{R_G} \quad (3.122)$$

5.2 Pocket equilibrium

In QD, sum of forces and momentums on each pocket j , that apply at its center P^j , in \mathbf{x}_G , \mathbf{y}_G and \mathbf{z}_G directions, includes race-to-pocket forces, ball-to-pocket forces and nodal elastic deformation forces. These equilibrium equations are expressed by:

$$F_{QD/px}^j = F_{IR/px}^j + F_{OR/px}^j + F_{b/px}^j - F_{elx}^j = 0 \quad (3.123)$$

$$F_{QD/py}^j = F_{IR/py}^j + F_{OR/py}^j + F_{b/py}^j - F_{ely}^j = 0 \quad (3.124)$$

$$F_{QD/pz}^j = F_{IR/pz}^j + F_{OR/pz}^j + F_{b/pz}^j - F_{elz}^j = 0 \quad (3.125)$$

$$M_{QD/px}^j = M_{IR/px}^j + M_{OR/px}^j + M_{b/px}^j - M_{elx}^j = 0 \quad (3.126)$$

$$M_{QD/py}^j = M_{IR/py}^j + M_{OR/py}^j + M_{b/py}^j - M_{ely}^j = 0 \quad (3.127)$$

$$M_{QD/pz}^j = M_{IR/pz}^j + M_{OR/pz}^j + M_{b/pz}^j - M_{elz}^j = 0 \quad (3.128)$$

5.3 Numerical procedure

Then, with flexible cage modelling, a QD system of 12N+5+6N equations is solved. Inner ring and ball equilibrium equations defined for rigid cage are the same for flexible cage. Nevertheless, 6 cage equilibrium equations (3.113) to (3.118) are replaced by 6N pocket equilibrium equations (3.123) to (3.128). Related unknowns are pockets displacements δ_{px}^j , δ_{py}^j , δ_{pz}^j and rotations θ_{px}^j , θ_{py}^j , θ_{pz}^j . These pocket equations and unknowns are also nondimensionalized by parameters given in Table 3.2. This system is solved with same Newton-Raphson scheme. Regarding initialisation, cage motions are initialised like in rigid cage problem. Then, pocket unknowns are initialised by applying relations (3.20) and (3.21).

Equation	Parameter	Unknown	Parameter
$F_{QD/px}^j : (3.123)$	$N \sqrt{F_X^2 + F_Y^2 + F_Z^2}$	δ_{px}^j	$\frac{c_p}{2}$
$F_{QD/py}^j : (3.124)$		δ_{py}^j	
$F_{QD/pz}^j : (3.125)$		δ_{pz}^j	
$M_{QD/px}^j : (3.126)$	$N R_p \sqrt{F_X^2 + F_Y^2 + F_Z^2}$	θ_{px}^j	$\frac{\pi}{N}$
$M_{QD/py}^j : (3.127)$		θ_{py}^j	
$M_{QD/pz}^j : (3.128)$		θ_{pz}^j	

Table 3.2 : Pocket parameters used to nondimensionalize related equation or unknown

5.4 Cage center motions and pocket elastic deformations

Pocket unknowns calculated numerically are made of one component related to rigid body motion (RBM) and another one related to elastic deformations such as defined in relation (3.129) and in Figure 3.5. But rigid body motion of each pocket δ_{RBM}^j is due to cage center rigid motion as expressed in (3.130).

$$\begin{bmatrix} \delta_p^1 \\ \theta_p^1 \\ \dots \\ \delta_p^N \\ \theta_p^N \end{bmatrix} = \begin{bmatrix} \delta^1 \\ \theta^1 \\ \dots \\ \delta^N \\ \theta^N \end{bmatrix}_{RBM} + \begin{bmatrix} \delta^1 \\ \theta^1 \\ \dots \\ \delta^N \\ \theta^N \end{bmatrix}_{elastic} \quad (3.129)$$

$$\delta_{RBM}^j = \delta_c^j = \delta_c + G_p^j G \wedge \theta_c \quad (3.130)$$

Consequently, from the knowledge of pockets center motions δ_p^j, θ_p^j , we can compute each of these component by searching for cage center motions δ_c, θ_c , such that pocket elastic deformations are minimum:

$$\min \begin{bmatrix} \delta_c \\ \theta_c \end{bmatrix} \left\| \begin{bmatrix} \delta^j \\ \theta^j \end{bmatrix}_{elastic} \right\|_2 \quad (3.131)$$

After computations we obtain rigid cage center motions defined in (3.132), rigid pocket motions in (3.133) and pocket elastic deformations in (3.134). Finally, with this post-treatment of pockets unknowns, we assess in three-dimensions the elastic and rigid body movement of the whole cage.

$$\begin{bmatrix} \delta_c \\ \theta_c \end{bmatrix} = (P^T P)^{-1} P^T \begin{bmatrix} \delta_p^1 \\ \theta_p^1 \\ \dots \\ \delta_p^N \\ \theta_p^N \end{bmatrix} \quad (3.132)$$

$$\begin{bmatrix} \delta^j \\ \theta^j \end{bmatrix}_{RBM} = P^j \begin{bmatrix} \delta_c \\ \theta_c \end{bmatrix} \text{ with } P^j = \begin{bmatrix} 1 & 0 & 0 & 0 & R_c \sin \psi^j & -R_c \cos \psi^j \\ 0 & 1 & 0 & -R_c \sin \psi^j & 0 & 0 \\ 0 & 0 & 1 & R_c \cos \psi^j & 0 & 0 \\ 0 & 0 & 0 & 1 & 0 & 0 \\ 0 & 0 & 0 & 0 & 1 & 0 \\ 0 & 0 & 0 & 0 & 0 & 1 \end{bmatrix} \text{ and } P = \begin{bmatrix} P^1 \\ \dots \\ P^N \end{bmatrix} \quad (3.133)$$

$$\begin{bmatrix} \delta_x^j \\ \delta_y^j \\ \delta_z^j \\ \theta_x^j \\ \theta_y^j \\ \theta_z^j \end{bmatrix}_{elastic} = \begin{bmatrix} \delta_{px}^j \\ \delta_{py}^j \\ \delta_{pz}^j \\ \theta_{px}^j \\ \theta_{py}^j \\ \theta_{pz}^j \end{bmatrix} - \begin{bmatrix} \delta_{cx} - R_c \cos \psi^j \theta_{cz} + R_c \sin \psi^j \theta_{cy} \\ \delta_{cy} - R_c \sin \psi^j \theta_{cx} \\ \delta_{cz} + R_c \cos \psi^j \theta_{cx} \\ \theta_{cx} \\ \theta_{cy} \\ \theta_{cz} \end{bmatrix}_{RBM} \quad (3.134)$$

6 Results analysis

6.1 Investigation of existing bearings

6.1.1 Pure axial load

- Cage interactions

To begin quasi-dynamic validation, tests are run with bearing A defined in Table 2.8. An axial load between 50 and 100 000N is applied. Cage has a pocket clearance of $525\mu\text{m}$ and a guiding clearance of 1.085mm. Outer race diameter is changed to consider in one case a cage centered on inner race and in another case a cage centered on outer race. These tests are also run with rigid and flexible cages. First results are gathered in Figure 3.16. For a given guidance, we can observe that rigid and flexible cage results are almost equal. This is due to the fact that under pure axial load, ball-to-pocket displacements and interactions are very small, cage stacks up against guiding race, then cage elastic deformations are negligible.

Cage rotation along bearing axis \mathbf{x}_G is reported on Figure 3.16 (a). As expected, because of cage-race SJB interactions, when cage is centered on IR, cage rotation θ_{cx} is positive, inner race drives the cage because its rotational velocity Ω_i is higher than ω_c . On the contrary, when cage is centered on OR, cage rotation θ_{cx} is negative since outer race does not rotate. Same phenomena can be observed on Figure 3.16 (c) where PB_x^j and PB_z^j , the ball-to-pocket positions along \mathbf{x}_p^j and \mathbf{z}_p^j , are reported. Axis orientation used is the same as in Figure 3.6. When cage is centered on IR, PB_z^j are negative which means that cage pulls balls whereas when cage is centered on OR, PB_z^j are positive, cage slows down balls. We can also note that, when cage is centered on IR, PB_x^j are positive whereas they are negative under OR guidance. This is because, as shown in Figure 3.16 (b), δ_{px}^j are more negative under IR guidance, then $\delta_{bx}^j - \delta_{px}^j$ are positive.

x_c and δ_x , cage and inner race displacements along \mathbf{x}_G , are plotted on Figure 3.16 (b). As expected, cage moves in same direction as inner race. Inner race displacements δ_x obtained are the same whatever cage guidance or cage model considered. When cage is centered on IR, x_c and δ_x are closer than under OR guidance since influence of IR is more important. Axial displacements increase with axial load because contact angles increase too.

Ball-to-pocket normal loads W_f are reported on Figure 3.16 (d). These loads are only the contribution of barrel-plan hydrodynamic effects since Hertzian deformations are negligible under pure axial load. In absolute value, normal loads W_f decrease with axial loads, then balls are better centered on pockets. Normal loads are higher for IR guidance since cage rotations θ_{cx} and ball-to-pocket displacements PB^j are also higher. These differences are due to lubricant drag forces and to the fact that balls are always guided by inner race. Note also that under low axial loads, a small spike is present on all curves. Same trend is observed if we plot the evolution of cage rotational speed ω_c . Indeed, under low axial loads, ω_c is small, ball skidding occurs because axial load is too small to drive balls in rotation.

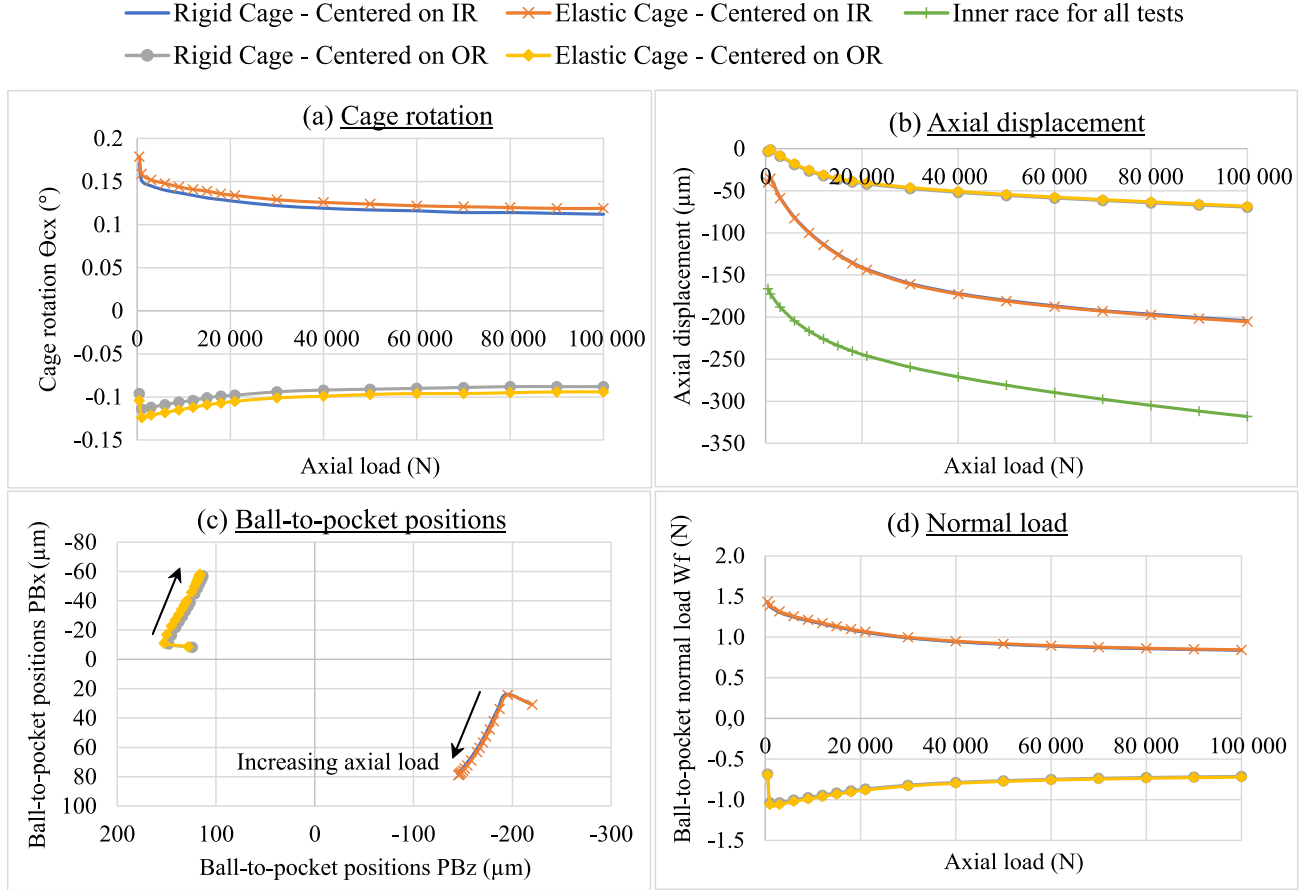


Figure 3.16 : Results for different type of cages under pure axial load

- Ball-race kinematics

For rigid cage centered on IR, ball-race kinematics is analysed in details. Main results are gathered on Figure 3.17. Ball-race contact loads and friction forces are plotted on Figure 3.17 (a). Because of centrifugal forces, ball-to-outer race contact load Q_{o2} is always larger than Q_{i1} , the inner race one. These loads increase linearly with axial load whereas friction forces F_{Xo2} and F_{Xi1} increase logarithmically. These friction forces oppose gyroscopic moment, then this momentum also increase with axial load. Friction forces along z_{b1}^j also increase with axial load but their value are significantly lower than F_{Xo2} , F_{Xi1} forces. Friction F_{Zi1} is also larger than F_{Zo2} even if Q_{i1} is less than Q_{o2} . This behaviour is in agreement with results presented in literature, like in Wen and Meng's article [264]. Few differences may be due to the fact that, in BB20, ball-race friction is modelled by a constant coefficient μ . In future works, to refine kinematics, this EHD model should be improved.

Ball-race contact angles α_{i1} , α_{o2} and ball self-rotations β are plotted in Figure 3.17 (b). As expected, inner race contact angle is always larger than outer race one. These angles increase with axial load even if α_{o2} increase is more important. β angle is always close to α_{o2} , which reflect a trend in outer race control. This trend is confirmed by Figure 3.17 (c) and (d), where spinning, sliding speeds and PV factors are plotted. Indeed, balls mainly slide and spin on the inner race, especially under low axial load. When axial load increases, sliding on the inner race decreases whereas it increases on the outer race.

PV factor follows the same tendency since spinning is directly related to this product. However, if tests are run until $F_X = 100\,000\text{N}$, this bearing usually works for much smaller loads around $15\,000\text{N}$. Then, results for loads larger than $40\,000\text{N}$ should be analysed with precaution. Note also that PV factor is an important criteria used by industry to design bearings because it is an indicator of wear and heat generation.

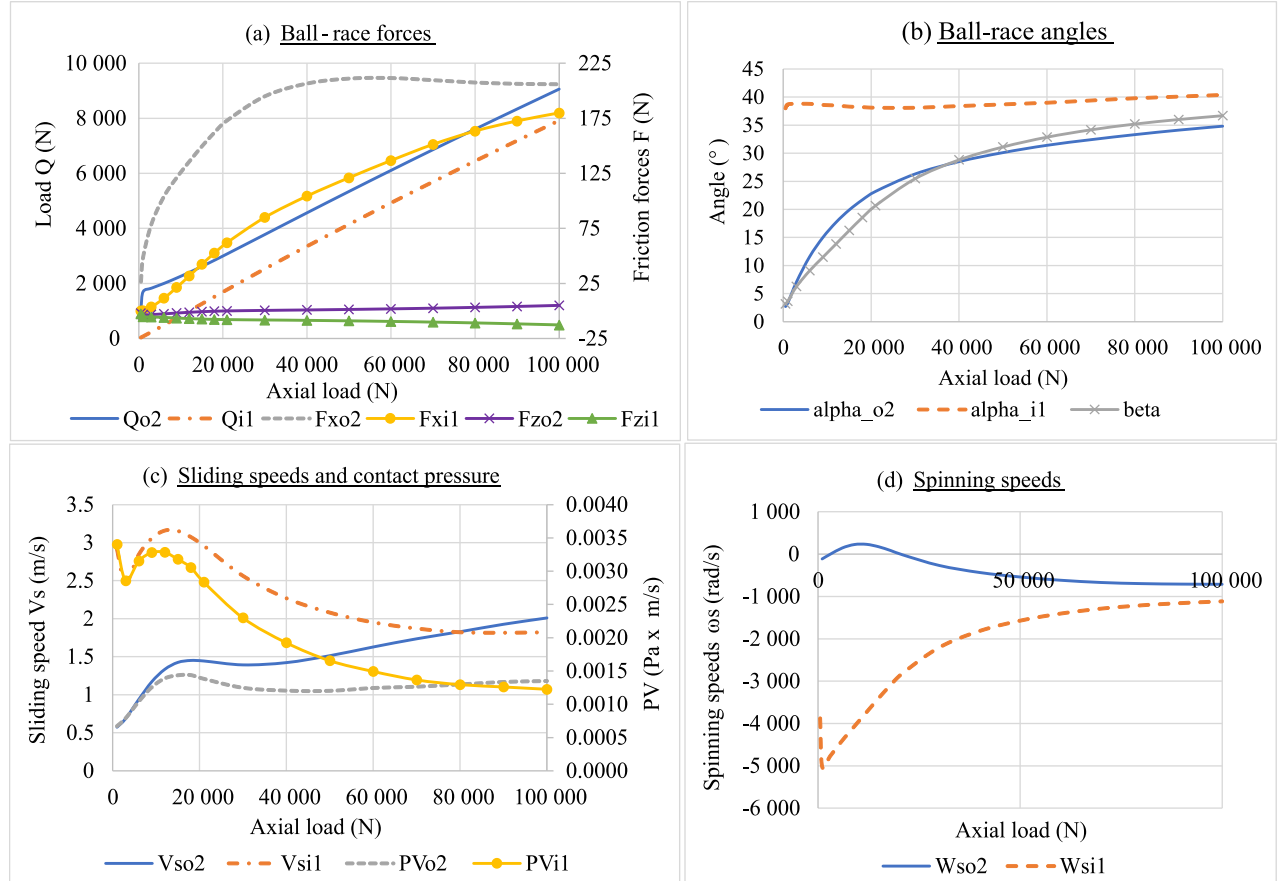


Figure 3.17 : Ball-race kinematics for rigid cage centered on IR

Besides, we are interested in the evolution of β' angle with axial load F_X and shaft speed Ω_i . We can observe on Figure 3.18 (a) that, for a given speed Ω_i , under small axial loads, β' increases abruptly until reaching a maximum. For larger axial loads, β' decreases more slowly. The higher the speed Ω_i , the more β' is large and reached for important loads. We can notice on Figure 3.18 (b) that, for a given axial load F_X , β' is close to zero at low speeds because gyroscopic momentum M_{GY}^j is too small to turn the ball in transverse direction. When speed increases, ball precession ω_m^j , gyroscopic momentum M_{GY}^j and β'^j angle increase until reaching a maximum. For larger speeds, β'^j decreases because ball sticks at outer race bottom, contact angle α_{o2}^j and β^j angle decrease too. As well, the higher the axial load, the more β' is large and reached at high-speeds.

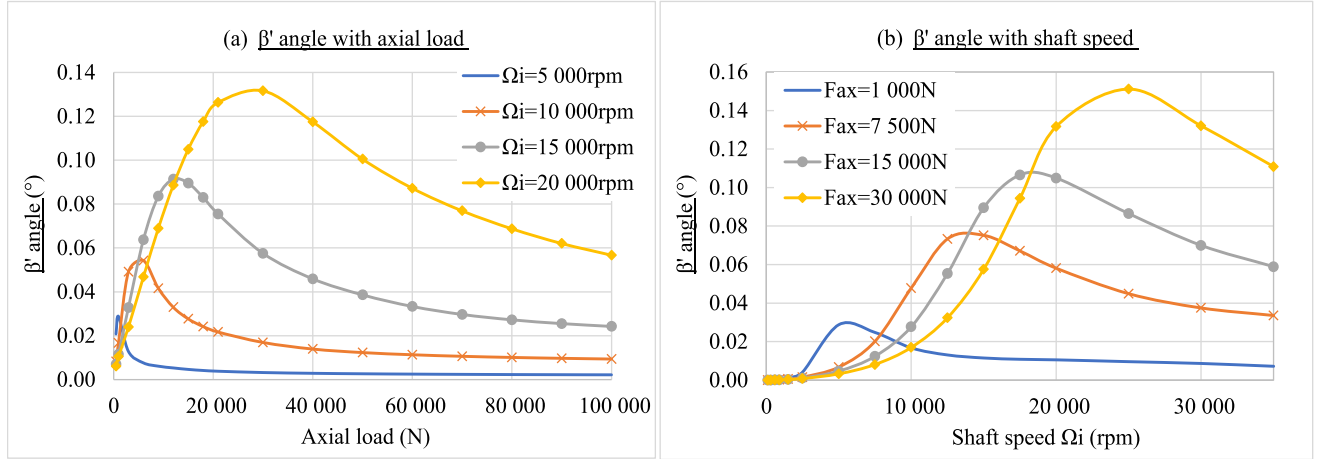


Figure 3.18 : Evolution of β' with axial load F_X and shaft speed Ω_i for rigid cage centered on IR

6.1.2 Combined loads with a rigid cage

In this section, bearing A centered on inner race, is investigated with a rigid cage. An axial load F_X of 15 000N and radial loads F_Y varying between 100 and 15 000N are applied. Since $-F_Y$ is applied on inner race, ball 11 is the most loaded.

- Cage center motion

Positions of cage center x_c, y_c, z_c and inner race centers $\delta_x, \delta_y, \delta_z$ are reported on Figure 3.19 (a). When radial load increases, cage and IR displacements decrease in a negative direction along x_G . Along y_G , cage and IR centers move of a few microns in a negative direction. IR center does not move along z_G whereas cage center significantly moves in a positive direction. This displacement of z_c is caused by cage-race SJB effects and by the fact that each ball has a different load. This phenomena is also observable in Figure 3.19 (b) where cage-to-inner race attitude angle ϕ_i , defined in (3.74), is plotted. As expected, when radial load is equal to zero, relative eccentricity ϵ is equal to 1, then ϕ_i is equal to 90° . When radial load increases, cage is more and more off-centered, relative eccentricity reduces, then attitude angle decreases.

In this test, cage-race clearance is large and equal to 1.085mm, then relative eccentricity stays close to 1 and attitude angle decreasing is small. Under important radial loads and small guiding clearances, this angle should tend to zero. In such conditions, cage-race dry contact almost occur. However, only SJB HD contact is considered in BB20. When cage-race dry contact is found, Newton-Raphson solution is relaxed until calculating cage-race HD interaction. Then, we did not succeed to make converge tests with small clearances and important radial loads. This indicates the necessity to model cage-race dry contact in future works. Even if we do not expect to converge towards such contact, it should be used in iterative process before converging towards quasi-dynamic solution. In any case, dynamical experiences have already shown cage-race collisions, then their consideration will be important when modelling dynamics. Note also that in SJB model, bearings are supposed to be coaxial. Such hypothesis does not hold when misalignment is applied on the inner ring. To solve such a case, SJB solutions with misaligned axis, like that of Gomez-Mancilla [81], should be implemented in the future.

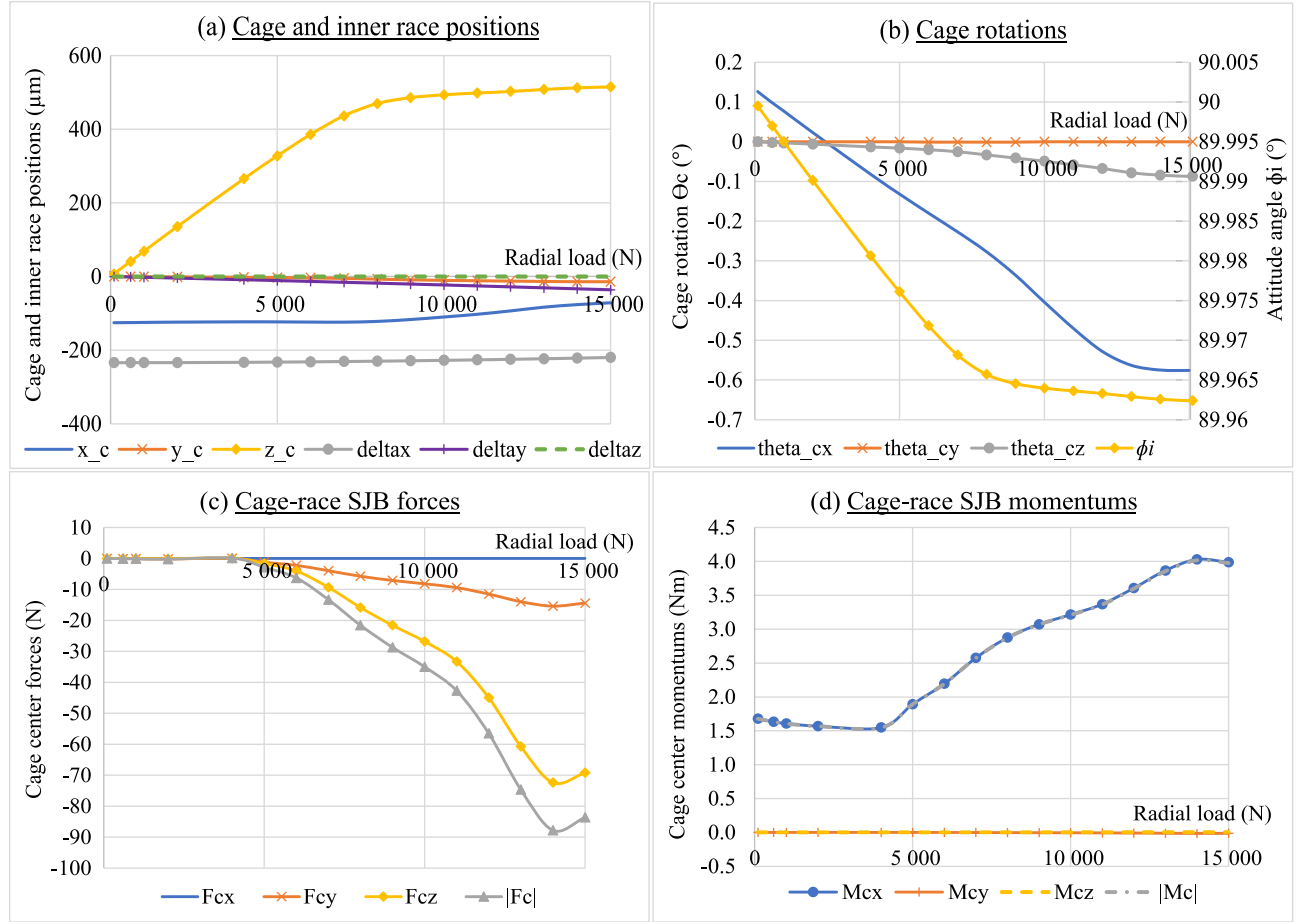


Figure 3.19 : Rigid cage results with an increasing radial load

Cage self rotations are plotted in Figure 3.19 (b). These rotations are almost equal to zero along y_G , they are very small along z_G but increase with F_Y . Rotation θ_{cx} is positive under low radial loads because cage is centered on the inner race that drives it. When radial load increases, contact angles are different on each ball which tends to slow down cage. Then, θ_{cx} decreases and gets negative for radial loads larger than 2 500N.

All these cage center motions are related to cage-race SJB forces reported in Figures 3.19 (c), (d). Indeed, according to SJB expressions (3.70) to (3.86), when radial load increases, cage-race eccentricity increases, then relative eccentricity gets closer to 1, cage-race hydrodynamic loads W_{km} and friction torques C_{1km} increase which explains that $F_{c/IRy}$, $F_{c/IRz}$ and $M_{c/IRx}$ increase too.

To better understand cage behaviour, we plotted in Figures 3.20 and 3.21, the evolution of $|G_I C_{i1}^j|$ and $|G_C C_{o2}^j|$ over the bearing. These scalars define the distance between inner or outer ring center and race curvature centers. These distances reflect ball-race contact point motion relative to ring center. On both Figures (d) we can observe that radial load does not influence location of ball-race contact points along y_G and z_G . On the contrary, as noticeable on Figures (a), (b), (c), when radial load is applied, ball-race contact points are shifted from pure axial load position, in x_G direction. This motion increase with radial load. It is directed in one direction for loaded balls and in opposite

direction for unloaded balls. It is always maximum for loaded ball 11 and unloaded ball 1. Variation $\mathbf{G}_I \mathbf{C}_{i1}^j \cdot \mathbf{x}_G$ is almost symmetric between loaded and unloaded balls whereas it is asymmetric for $\mathbf{G} \mathbf{C}_{o2}^j \cdot \mathbf{x}_G$. Indeed, under radial load of 15 000N, for ball-to-outer race contact, loaded balls move of $45\mu\text{m}$ maximum from pure axial load position, whereas unloaded balls move of $15\mu\text{m}$ maximum in opposite direction. For inner race contacts, these displacements are of $170\mu\text{m}$ for both balls 1 and 11. Then, we can also note that ball-to-inner race motion is 4 times larger than ball-to-outer race.

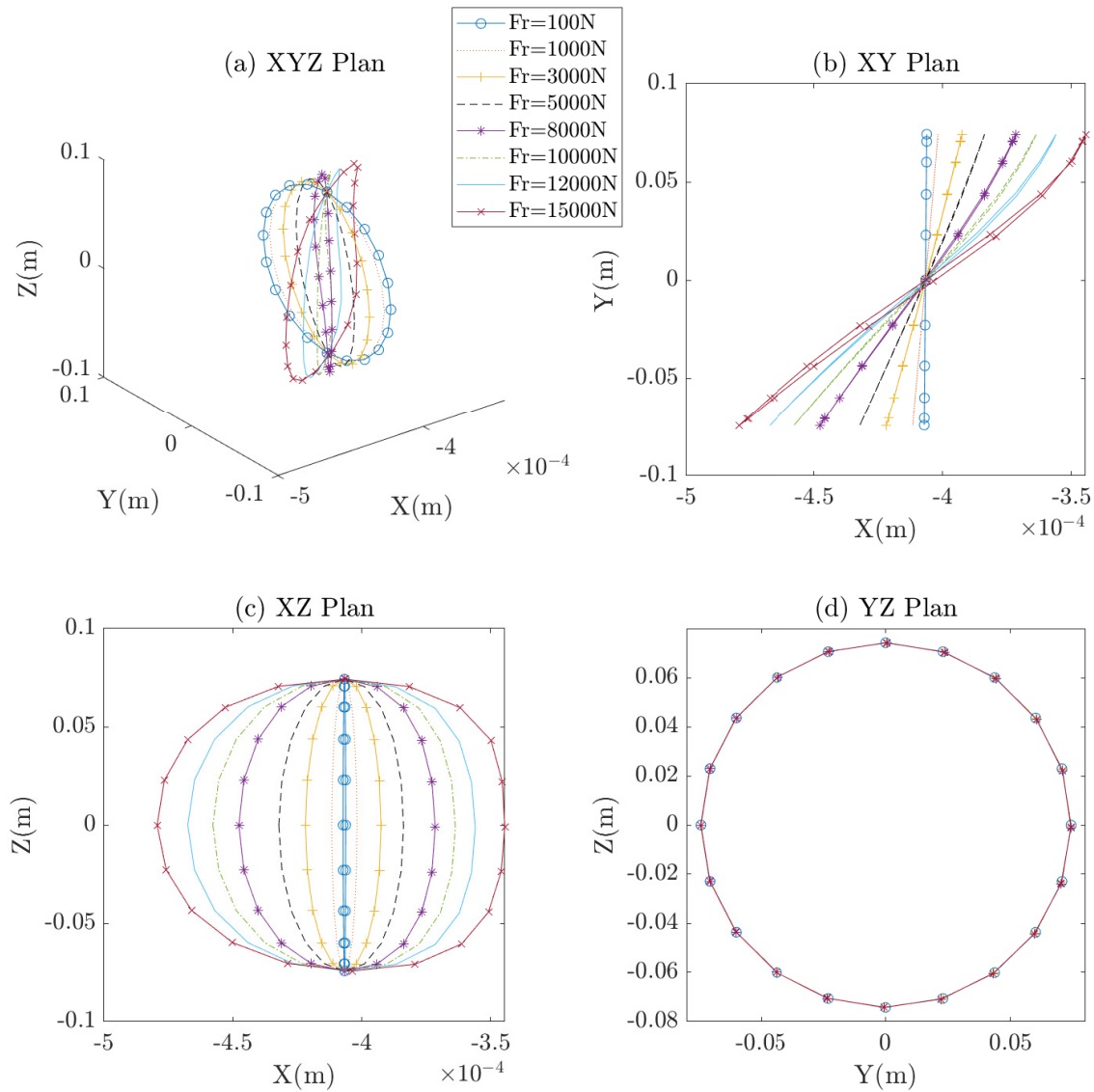


Figure 3.20 : Positions of ball-to-inner race contact points: $|\mathbf{G}_I \mathbf{C}_{i1}^j|$

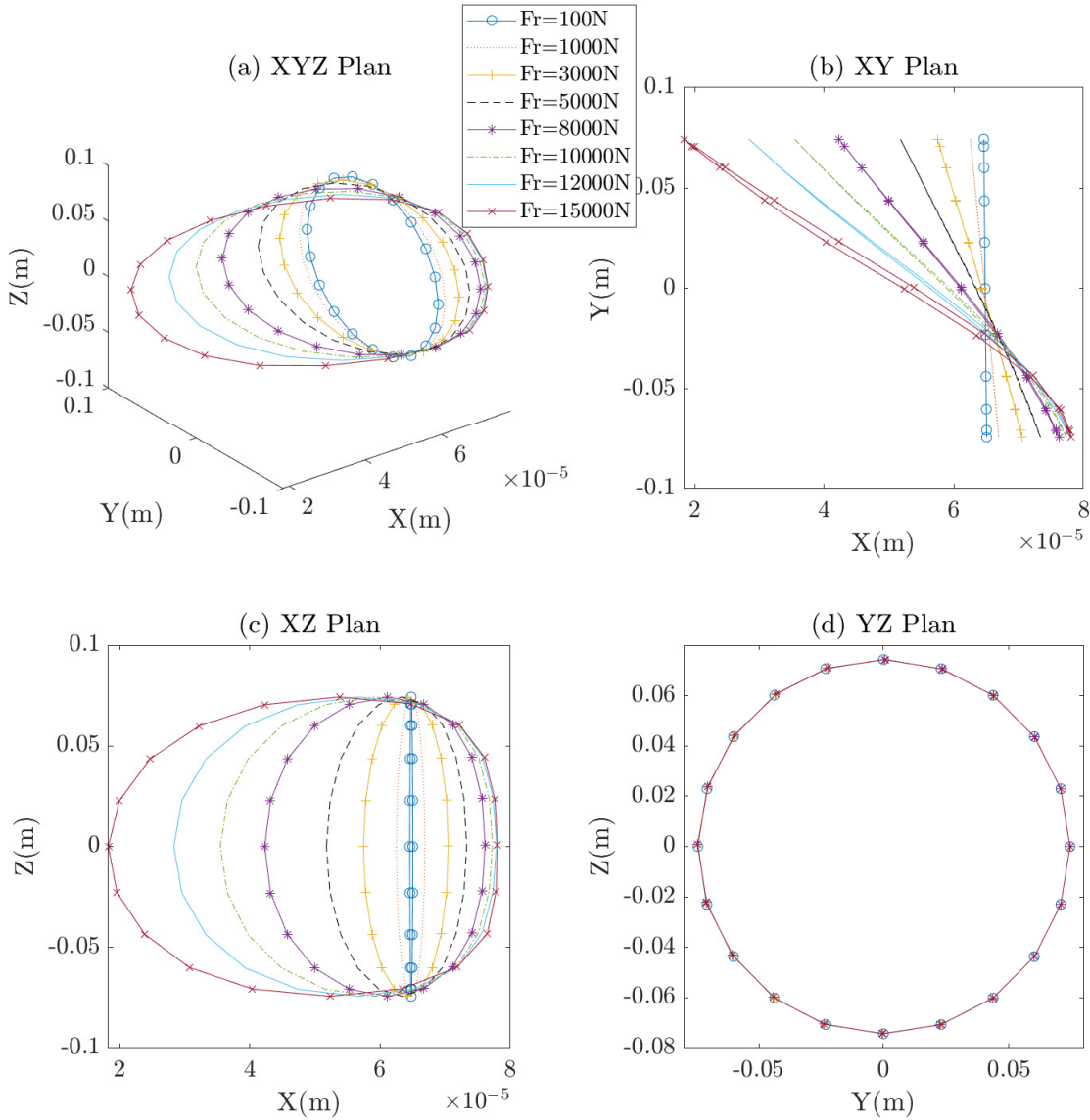


Figure 3.21 : Positions of ball-to-outer race contact points: $|GC_{o2}^j|$

- Ball-to-pocket motion

Ball-to-pocket positions along x_p^j and z_p^j are reported in Figure 3.22 by using same axis orientation as in Figure 3.6. Results are given for all balls of the bearing and for increasing radial loads. These positions are also plotted in Figures 3.23 (a), (b) as a function of ball number. Under small radial loads, all balls are positioned on the same side of the pocket. They are at the back side ($PB_z^j < 0$) which means that cage pull them. This position is mainly due to inner race guidance and to drag forces. When radial load increases, differences in ball-to-pocket positions between consecutive balls increase. Displacement PB_z^j increases in negative value for loaded balls, whereas it decreases and gets closer to zero for unloaded balls. When radial load gets larger than 10 000N, PB_x^j of unloaded balls is getting negative whereas PB_z^j is getting positive. Then, some balls locate at one side of the pocket whereas other balls get positioned at the opposite. Loaded balls are pulled by the cage, unloaded balls pull the cage.

If we look at Figure 3.23 (g) where balls precession ω_m^j are plotted, we can observe that balls decelerate when they enter the loaded zone and accelerate when they exit it. This is due to the fact that outer race contact angles α_{o2}^j decrease in loaded zone and increase in unloaded zone. These results agree with physical behaviour described in literature.

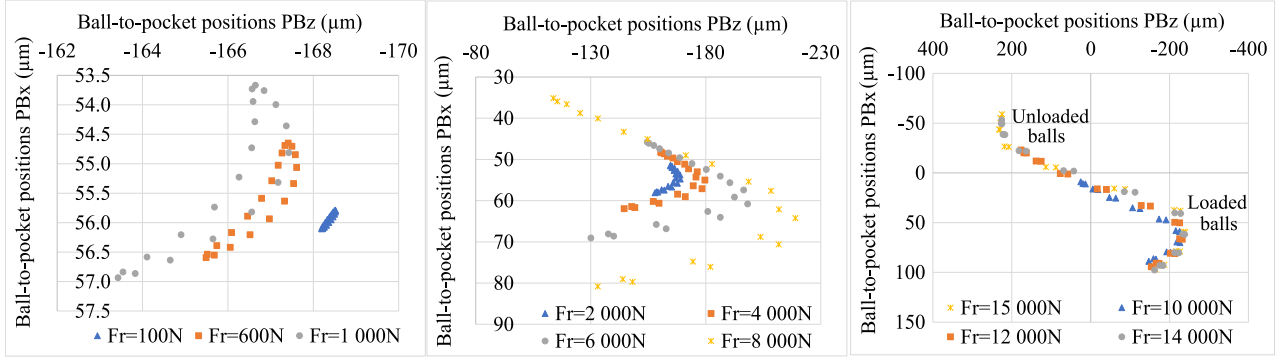


Figure 3.22 : Ball-to-pocket displacements in (G_p^j, z_p^j, x_p^j) plan, for rigid cage

$F_{p/bz}^j$ and $F_{p/bx}^j$, the ball-to-pocket forces along z_p^j and x_G , are plotted in Figure 3.23 (c) and (d). These forces are the contribution of barrel-plan normal and friction forces, Hertzian load, shear force and ball-to-pocket SJB forces. By comparing Figure 3.23 (a) with (c) and Figure (b) with (d), we can observe that evolution of PB_z^j is directly related to $F_{p/bz}^j$ since same tendencies (up to an overall sign) are observable. On the contrary, $F_{p/bx}^j$ does not have same evolution as PB_x^j which shows that ball-to-pocket position along x_G is influenced by other forces like those of adjacent balls.

Contribution of barrel-plan normal load W_f^j is plotted in Figure 3.23 (e) whereas contribution of ball-to-pocket SJB normal load W_{sb}^j is plotted on Figure 3.23 (f). Under small radial loads, W_f^j are centered around -1N whereas W_{sb}^j are centered on zero. When radial load increases, both loads vary around these values. However, if W_f^j amplitude does not exceed 2.5N, W_{sb}^j variation is 10 times larger. Then, ball-to-pocket SJB effect is predominant on barrel-plan effect when ball-to-pocket interaction is under HD lubrication. This phenomena is confirmed if we compare Figure 3.23 (c) with (f) under large radial loads. Indeed, same spikes around balls 8 and 14 are present on both plots which confirms that forces $F_{p/bz}^j$ are mainly due to SJB forces. In dynamics, because of EHD lubrication, we expect Hertzian loads to be larger than these SJB forces.

If we compare Figure 3.23 (a), (b) with (e), we can confirm that barrel-plan normal loads W_f^j are directly related to ball-to-pocket displacements. Under small radial loads, they are not equal to zero but almost constant because of small PB^j . Under important radial loads, they are maximum when PB^j are maximum and film thickness h_f^j are minimum. Ball-to-pocket SJB normal loads W_{sb}^j are related both to PB^j and to ball self-rotations β^j . Indeed, β^j are maximum for loaded balls and minimum for unloaded balls. On Figure 3.23 (f), we can observe that W_{sb}^j are equal to zero when radial load is equal to zero. Under combined loads, they are small for balls located in unloaded zone. In such cases, even if PB^j are not minimum, ball self-rotations β^j are small, then W_{sb}^j are small too. When balls are getting loaded, β^j increase, then, according to relations (3.47)

to (3.50), SJB effect is more important. However, because of small \mathbf{PB}^j , SJB forces of loaded balls 10, 11, 12 are almost equal to zero, even if β^j is maximum.

In Figure 3.23 (h), ball-to-pocket minimal clearance $\min_{j=1,N}(\frac{c_p}{2} - \Delta_{pb}^j)$, is plotted for increasing radial loads. Results are given for R2 resolution without cage and for R2 with rigid cage. We can observe that without considering cage, then by directly applying $\lambda_c = 1$, negative clearances are obtained for radial loads larger than 5 000N. This would mean that balls hit the pocket under such loads. By considering cage, then by increasing λ_c incrementally, cage equilibrates to get positive clearances until 15 000N. Physically, balls are not supposed to hit cage under relatively small radial loads. That is why, results with cage appears to be closer to reality and confirm the need to introduce it into the model.

Nevertheless, for radial loads larger than 15 000N, then for axial-to-radial load ratios smaller than 1, BB20 does not converge with cage. This is due to the fact that some balls start to detach from inner race, important precession differences ω_m^j are calculated between successive balls, then δ_{pb}^j are important, ball-to-pocket clearances are negative, pocket normal loads W_f^j are huge, cage does not succeed to equilibrate. Physically, we cannot say if these ball-to-pocket collisions really occur. Indeed, quasi-dynamic hypotheses on δ_{bz}^j and ω_c limit computation accuracy, especially under important radial loads. Then, we should not draw active conclusions on bearing behaviour under such conditions. By solving BB20 in dynamics, we should get rid of such hypotheses, then simulate a behaviour closer to reality and be able to answer these questions.

6.1.3 Combined loads with a flexible cage

- Steel cage

BB20 is run again with bearing A centered on inner race, with $F_X = 15\,000\text{N}$, with increasing radial loads F_Y but with a flexible cage made of steel. Results on cage motion, IR displacements, cage-race SJB interactions and ball-to-pocket minimal clearance are gathered in Figure 3.24. For radial loads smaller than 7 000N, comparable results are obtained between rigid and flexible cage. For larger loads, evolution of cage displacements x_c are more abrupt for flexible cage, SJB forces $F_{IR/cy}$, $F_{IR/cz}$ are slightly higher whereas $M_{IR/cx}$ and cage rotations θ_{cx} are smaller.

Nevertheless, these results were obtained without considering errors on pocket motions unknowns δ_p and θ_p . Then, converging conditions only depended on ball and inner race error variation between two iterations. We have also tried to run these tests by considering pockets errors, but it did not converge for radial loads larger than 7 000N. In such a case, even if errors on balls and IR were small, BB20 continued to solve the Newton Raphson scheme until relative variation of pocket unknowns over iterations were less than 10^{-3} . Finally, system did not equilibrate, the problem was over-relaxed because cage-race dry contacts were found. These results show again that cage-race collisions should be considered in future works and that numerical improvements are still needed. In particular, instead of post-treating cage RBM, implementing in the Newton-Raphson scheme the equation (3.132) on cage minimisation and cage center motions as unknowns may be a solution to improve numerical resolution of flexible cage. To return to Figure 3.24, we can now assume that differences between rigid and flexible cage, observed for radial loads larger than 7 000N, are due to the fact that system is not really converged.

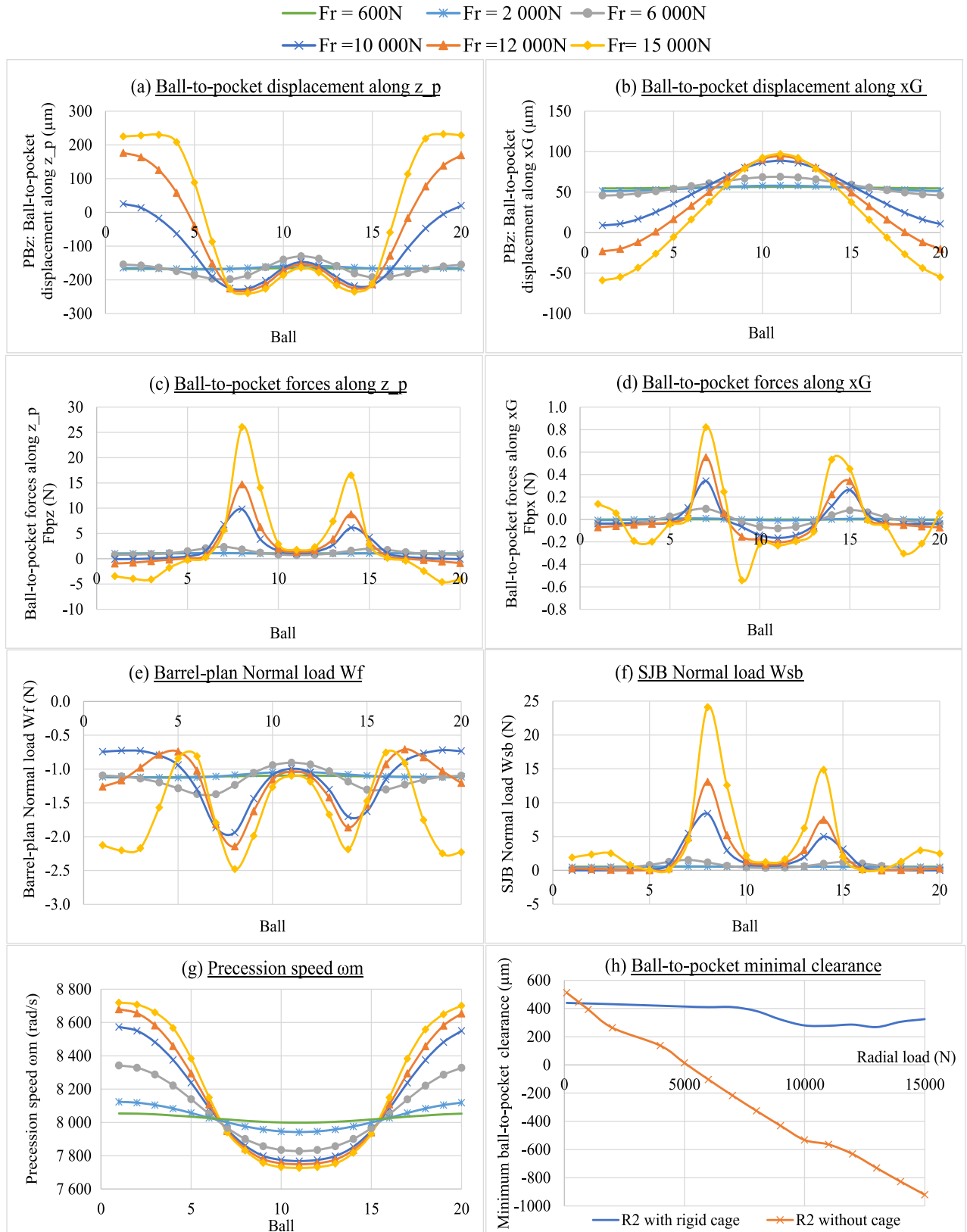


Figure 3.23 : Ball-to-pocket interactions under increasing radial loads

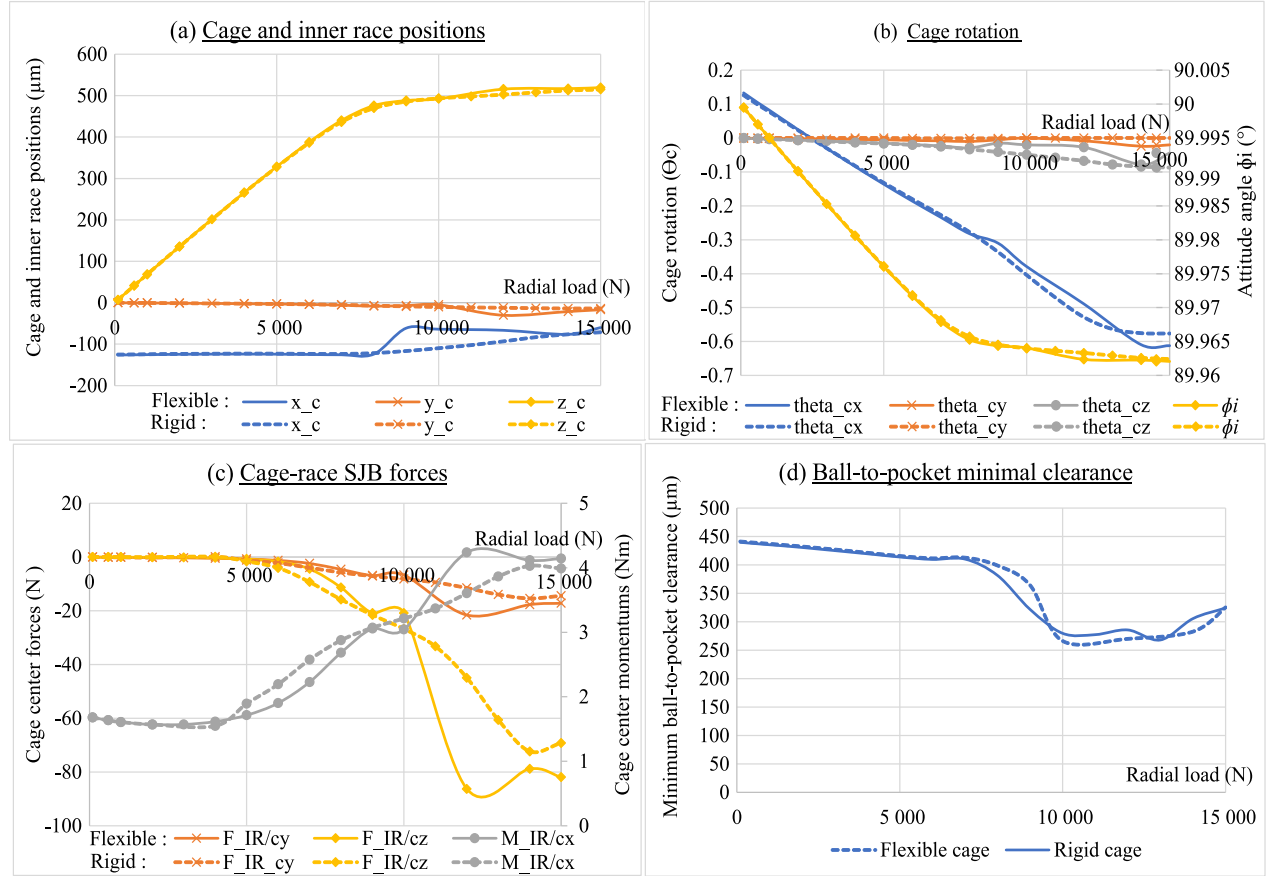


Figure 3.24 : Comparison between flexible and rigid cage for increasing radial loads

Ball-to-pocket displacements in (G_p^j, z_p^j, x_p^j) plan are synthesised in Figure 3.25. Results between rigid and flexible cage are again very similar. Under small radial loads, displacements PB_z^j are only 1 or $2\mu\text{m}$ smaller for flexible cage. For radial loads of 10 000N and 12 000N, displacements PB_x^j are always between 0 and $20\mu\text{m}$ for flexible cage whereas they vary between 0 and $100\mu\text{m}$ for rigid cage. Such differences are unexpected and prove that these two tests are not converged.

Besides, pocket elastic rotations θ_{elcx}^j , θ_{elcy}^j , θ_{elcz}^j obtained are always less than 0.005° , which is negligible. Pocket elastic deformations δ_{elcx}^j , δ_{elcy}^j , δ_{elcz}^j are plotted on Figure 3.26. Deformations δ_{elcx}^j , δ_{elcz}^j are equal to zero for the most loaded ball and the lowest loaded ball, whereas they are maximum for balls located in between. On the contrary, deformations δ_{elcy}^j are maximum for the most loaded ball and the lowest loaded ball. For all deformations, maximal amplitude increases with radial load. However, for $F_Y = 10\,000\text{N}$ and $F_Y = 12\,000\text{N}$, δ_{elcx} are smaller than under 8 000N. This confirm again that these two tests are not converged. In any case, elastic deformations have amplitudes of several hundred microns which is non negligible.

Consequently, in quasi-dynamics, if modelling cage flexibility does not influence cage center rigid body motions, it reveals that cage is subject to structural deformations even when ball-to-pocket and cage-race interactions are under HD regime. In dynamics, EHD interactions should happen, then influence of cage flexibility on cage motion and elastic deformations should be more important.

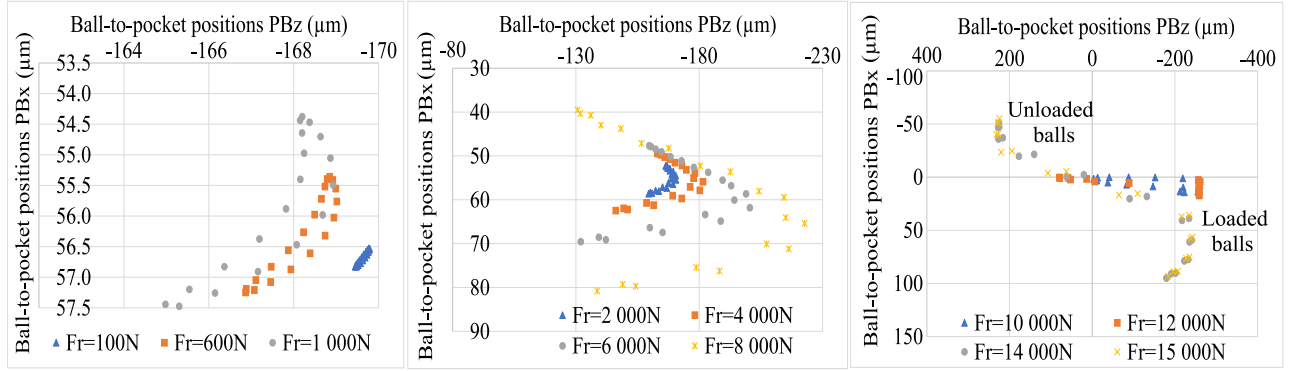


Figure 3.25 : Ball-to-pocket displacements in (G_p^j, z_p^j, x_p^j) plan, for flexible cage

- PEEK cage

These tests with varying radial loads are rerun with a cage made of PEEK. However, it only converged for radial loads less or equal than 8 000N because cage-race dry contacts were obtained for larger loads. Under radial loads lower than 8 000N, cage RBM, cage-race and ball-to-pocket interactions are comparable with steel ones. On the contrary, cage elastic deformations differs, as illustrated in Figure 3.27. Indeed, if δ_{elcx}^j are similar with both cages, δ_{elcy}^j and δ_{elcz}^j are larger with PEEK. In particular, for a radial load of 8 000N, these deformations are 30% larger with PEEK cage. This is due to the fact that PEEK elastic modulus is 52 times lower than steel and that Poisson's coefficient is 25% larger, such as reported in Table 3.3. Then, E and G_c parameters are smaller, components of stiffness matrix \mathbf{K}_{el} , defined in (3.119), are also smaller, PEEK cage is softer and subjected to larger deformations. We can also note that evolution of δ_{elcy}^j and δ_{elcz}^j with ball position is a sinusoid for steel cage whereas it is more erratic with PEEK.

Material	Elastic modulus (GPa)	Poisson's coefficient	Density (kg/m^3)
Steel	200	0.3	7850
PEEK	3.85	0.4	1300

Table 3.3 : Material properties of steel and PEEK

- Computational time

Regarding computational time, it is worth noting that R1 resolution of a single test, always lasts less than a second. R2 resolution without cage lasts around 90 seconds which is much lower than R2 with cage. Indeed, with cage consideration, because of the need to increase incrementally ball-to-pocket ortho-radial displacements δ_{bz}^j , number of iterations needed to converge is much important. To get an idea, under pure axial load, computational time is comprised between 500 and 700 seconds. It vary linearly with increasing radial load, to be larger than 4 000 seconds when $F_Y = 15\,000\text{N}$. This time is comparable whether if rigid or flexible cages are considered. If this time may seem important, we expect dynamic computations to be much more consuming. Besides, these results were obtained with jacobian matrix calculated numerically by a Fortran routine.

Computing analytic jacobian reduces this computational time of a factor 14 but gives less accurate results.

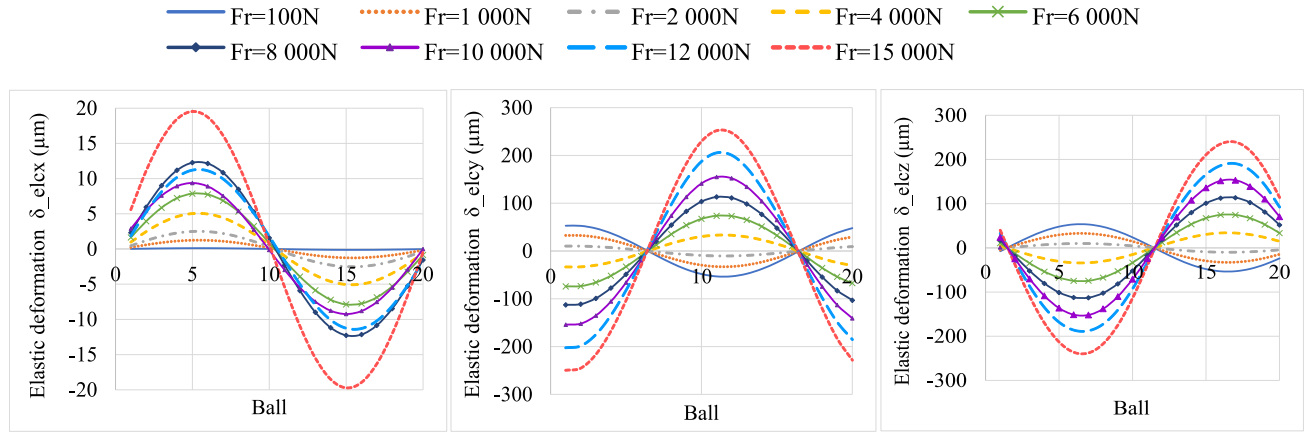


Figure 3.26 : Pocket elastic deformations with steel cage

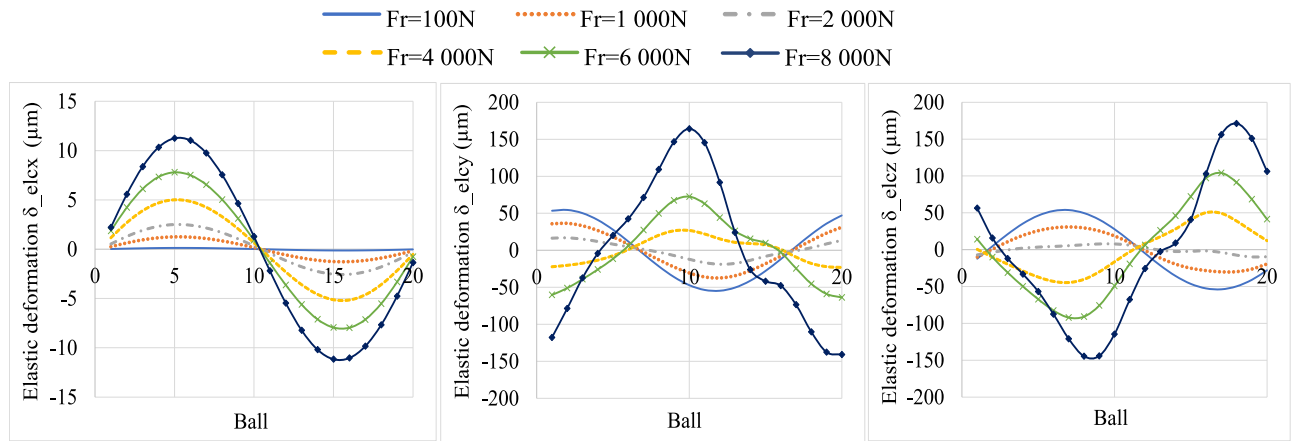


Figure 3.27 : Pocket elastic deformations with PEEK cage

6.2 Comparison with a 4 contact-points literature model

In this section, we are comparing BB20 with Ma's model [174] which is one of the only one to consider the dynamics of ACBB with up to 4 contact points. Compared with BB20, this model is solved in dynamics, cage has only 3 degrees of freedom, ball-race traction coefficient is defined by Kragelskii's model [154] with Gupta's coefficients [104] and ball-to-pocket interactions are only modelled by Hertzian contact for normal load and Coulomb's theorem for friction. Above all, ball gyroscopic momentums are not considered in this model. Tests are run with the bearing defined in Table 3.4, with outer race guidance and under high-speed ($\Omega_i = 5000rpm$), small loads (always lower than 3 000N).

Notation	Parameter	Unity	Value
N	Ball number		16
D	Ball diameter	mm	17.464
d_i	IR diameter	mm	84.925
d_o	OR diameter	mm	120.14
r_i	IR groove curvature radius ($r_i = f_i D$)	mm	9.15
r_o	OR groove curvature radius ($r_o = f_o D$)	mm	9.25
e_i	IR curvature eccentricity ($e_i = 0.5 g_i$)	mm	0.183
e_o	OR curvature eccentricity ($e_o = 0.5 g_o$)	mm	0.298
D_p	Pocket diameter	mm	17.7
D_{co}	Cage outer diameter	mm	111

Table 3.4 : Data of bearing tested

6.2.1 Pure axial load

To begin, tests are run with constant speed of 5 000rpm and pure axial loads varying between 100 and 3 000N. Results obtained with BB20 and Ma's model are gathered in Figure 3.28. On each plot, continuous line refers to BB20 and dashed line to Ma. Main contact corresponds to inner race side 1 (IR1) and outer race side 2 (OR2) whereas sub contact corresponds to inner race side 2 (IR2) and outer race side 1 (OR1). These secondary contacts are less loaded and occur under specific conditions.

Some parameters like material properties (elastic modulus, density), lubricant properties, drag coefficient C_d or friction coefficients are not specified in Ma's article. Consequently, in order to get comparable cage-to-shaft speed ratios $\frac{\omega_c}{\Omega_i}$, we fixed ball-race friction coefficient μ at 0.01, oil fraction in the mixture f_{oil} at 0.15 and drag coefficient C_d at 0.4. Such values do not seem aberrant even if we usually work with a coefficient $\mu=0.065$. These results for $\frac{\omega_c}{\Omega_i}$ are plotted in Figure 3.28 (g). As well, BB20 tests were first run with steel material. However, we obtained transitions from 3 to 2 contact-points for $F_X=7\,000\text{N}$ whereas it occurs at 2 400N with Ma's model. This reveal a difference in contact stiffness. Then, in BB20, we let rings and cage in steel but fixed ball elastic modulus at 10 GPa, Poisson's coefficient at 0.3 and density at $3\,950\text{kg}/\text{m}^3$. Is this way, as observable in Figure 3.28 (h), contact transition with BB20 occurs around 2 400N too.

- $F_X < 400\text{N}$

With both models, for axial loads smaller than 400N, 3 contact-points are present: two on outer race and one on inner race side 1. We can observe in Figure (g) that cage speed increases with axial load. In Figure (c), ball-to-inner race sliding speed in the rolling direction is very important but decreases with axial load. In figure (a), at 3 contacts, normal load increases with F_X because of centrifugal force increasing. Then, as observable in Figure (d), (e), (f), contact pressures and traction forces at 3 contacts increase too, whereas PV factor of inner-race contact is important and decrease because of sliding speed decrease.

All these results shows that, for axial loads smaller than 400N, ball skidding occurs because applied load is too small to develop sufficient EHD tractive force to overcome cage drag and prevent gyroscopic spin.

- $400\text{N} < F_X < 2\ 400\text{N}$

When axial load is larger than 400N but smaller than 2 400N, skidding does not occur anymore. Then, cage speed is more stable and sliding speeds of main contacts are very small. On the contrary, sliding speed of OR1 contact increases before falling down to zero when this contact is lost for $F_X=2\ 400\text{N}$. This increase is due to the fact that axial force changes ball angular velocity. Contact loads of main contacts increase linearly with axial load whereas OR1 contact load decreases to zero for $F_X=2\ 400\text{N}$. For main contact, inner race contact load is always a bit larger than outer race one which shows that centrifugal forces stay relatively small. Main contact loads are also at least one order of magnitude larger than sub contact. Contact pressures present same evolutions as contact loads excepted that curves are flatter because of non-linear relationship between contact stress and contact force. PV factors of main contacts are almost equal to zero since sliding speeds are very small whereas PV factor of OR1 increases until 1 900N and then decreases and gets equal to zero for 2 400N because contact is lost.

- $2\ 400\text{N} < F_X < 3000\text{N}$

When axial load is larger than 2400N, the sub contact on outer race is lost, related parameters are equal to zero. Only IR1 and OR2 contacts remain, corresponding parameters present same evolution as when $400\text{N} < F_X < 2\ 400\text{N}$.

- Differences analysis

Excepted for traction forces, BB20 and Ma's curves present same evolutions. Only differences are in amplitudes. In Figure 3.28 (a), we can observe that contact loads of main contacts are comparable between BB20 and Ma's model. Ma's loads are just about 40N larger than BB20. For sub contact OR1, contact loads are comparable under small axial loads. When axial load gets closer to 400N, Ma's contact load increase is larger than BB20, with a difference of a factor 2 at 400N. For larger loads, these differences decrease.

Concerning contact angles plotted in Figure 3.28 (b), with Ma's model these angles are almost constant, excepted for α_{o1}^j that fall to zero when contact is lost. Under 3 contact-points, outer race contact angles are almost equal whereas inner race contact angle is always larger than outer race ones. Outer-race contact angles obtained with BB20 are comparable whereas inner-race contact angle is 30% smaller than with Ma's model. In BB20, this angle also decrease with axial load and is smaller than outer race angles which is unexpected.

BB20 and Ma's sliding speeds of Figure 3.28 (c) are comparable for main contacts whereas sliding speed evolution for OR1 is rather linear with Ma and exponential with BB20. Contact pressures and PV factors obtained with Ma's model are four times larger than with BB20, such as illustrated in Figure 3.28 (d), (f).

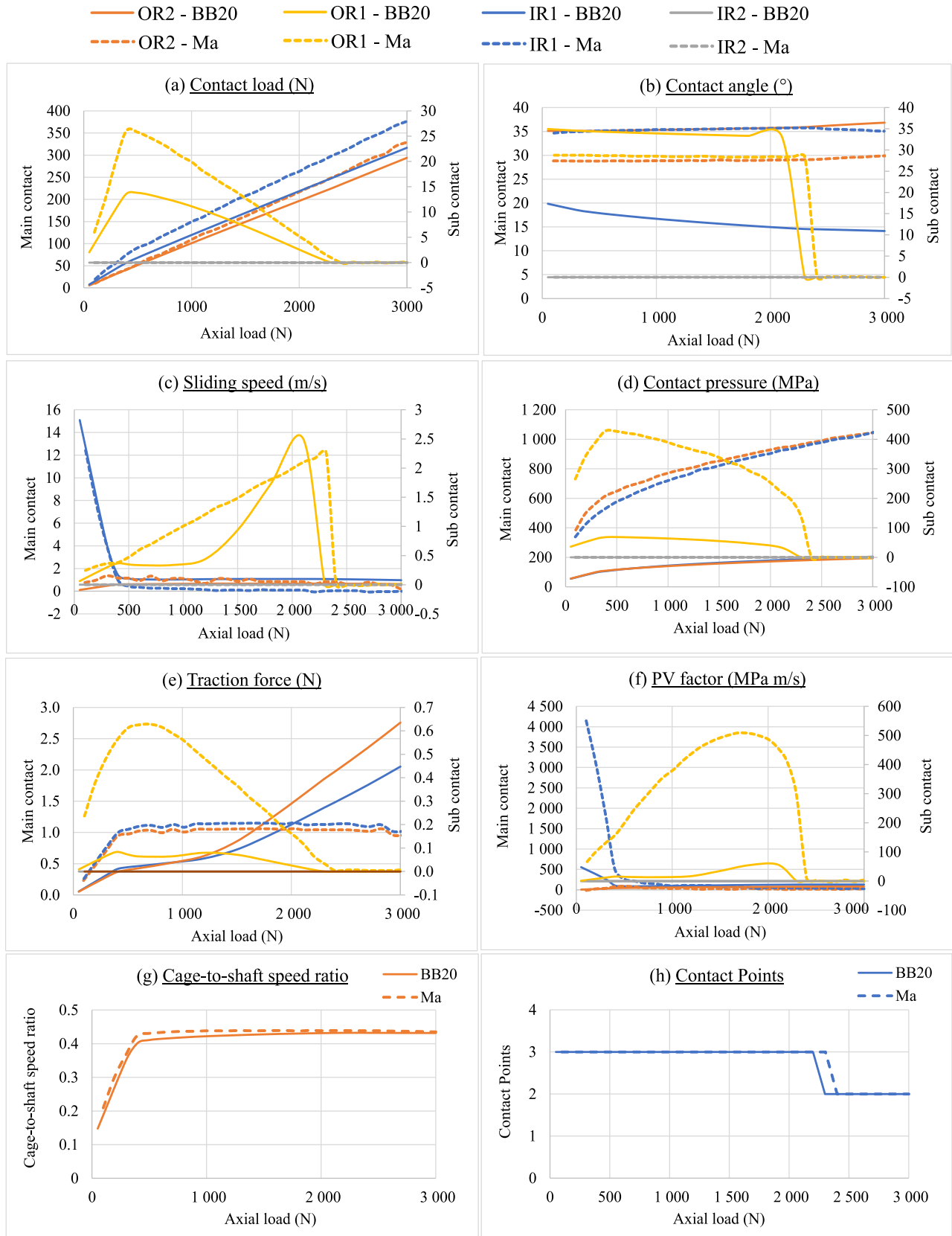


Figure 3.28 : Comparison between BB20 and Ma [174] under pure axial load

Regarding traction forces represented in Figure 3.28 (e), under small axial loads, these forces are much larger with Ma's model whereas contact loads of main contacts are comparable. Maybe, this difference is due to the fact that Ma's friction coefficient is larger than BB20's one. As well, when axial load is larger than 400N, then when sliding speeds of main contacts are equal to zero, Ma's friction forces are constant because Kragelskii's model is applied. On the contrary, Coulomb's model with constant friction coefficient is applied in BB20, then traction forces increase with contact load. Such differences show the influence of EHD traction model on ball kinematics. This confirm that this model should be improved in BB20.

Finally, BB20 and Ma's models are comparable. Few differences can be attributed to the fact that each model makes its own hypothesis. This study of ACBB with more than 2 contact points under increasing axial load shows that getting a third contact is non negligible and complicates ball kinematics. When axial load increases, bearing changes from 3 contacts with skidding, to 3 contacts without skidding, then to 2 contacts without skidding either. The third contact-point on the outer race has important sliding, then spin-to-roll ratio that generates heat and risks of burn or failure even if main contact has the largest PV value.

6.2.2 Combined loads

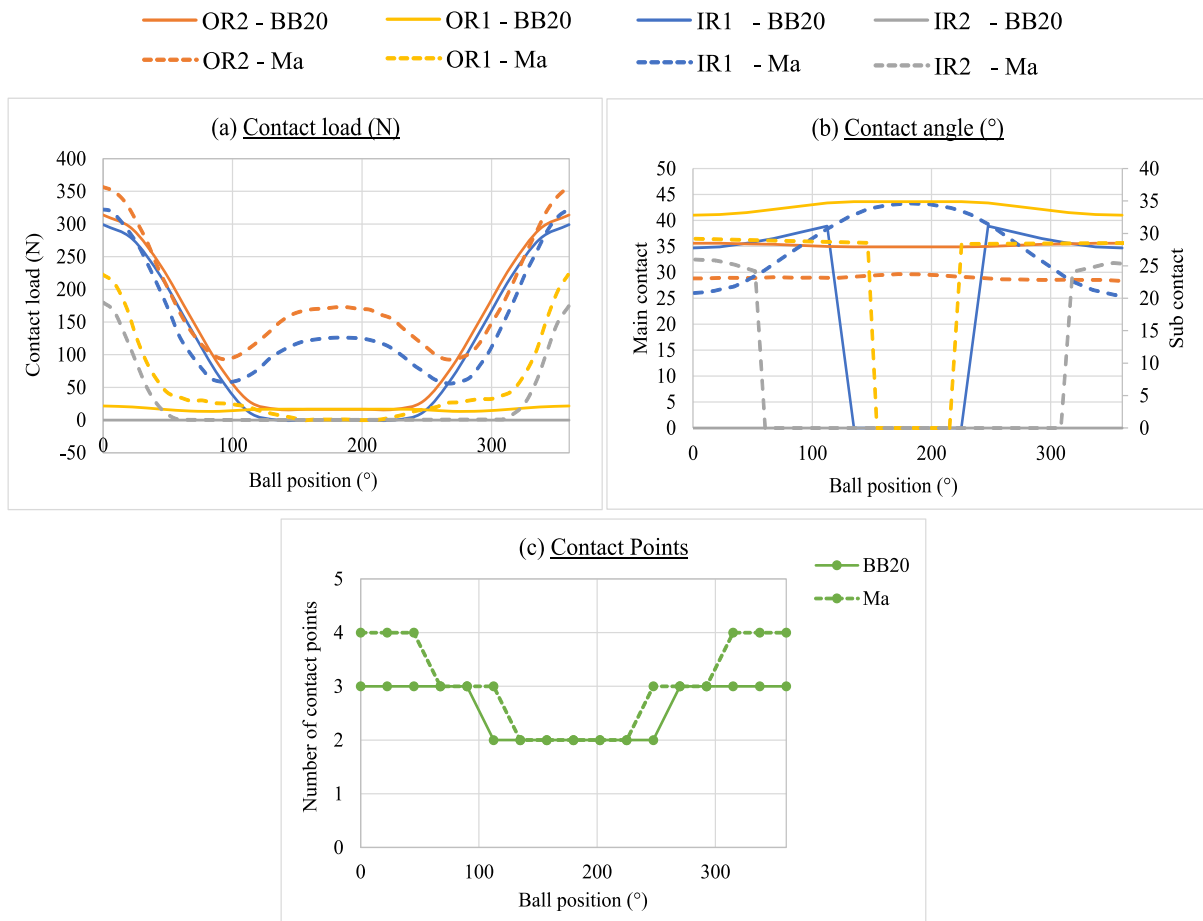


Figure 3.29 : Comparison between BB20 and Ma [174] under combined loads

Tests are still run with a speed of 5 000rpm but with combined loads $F_X = F_Y = 1\,000\text{N}$. Results obtained with BB20 and Ma's models are gathered in Figure 3.29. We can observe that with Ma's model, balls 1, 2, 3, 14, 15, 16 have 4 contact-points, balls 4, 5, 6, 11, 12, 13 have 3 contact-points (two on OR, one on IR) and balls 7 to 10 have 2 contact-points (one on each race). On the contrary, BB20 never works under 4 contact-points, many tests have been run without succeeding to get two contact-points on inner race. In the present test, balls 1 to 5 and 12 to 16 have 3 contact-points whereas balls 6 to 11 have 2 contact-points on OR, then these last balls are detached from IR.

These contact differences between both models are non negligible and probably due to the fact that BB20 is solved in quasi-dynamics and Ma's model in dynamics. We have also already noticed limits of BB20 quasi-dynamics in solving problems with axial-to-radial loads ratios greater than or equal to 1. The fact that Ma's model does not consider gyroscopic effects may also explain contact differences.

Nevertheless, we can notice in Figure 3.29 (a), that for non-detached balls, contact loads of main contacts are comparable. Sub contact loads are never comparable because of the absence of fourth contact in BB20 or the absence of ball detachment in Ma's results. Contact angles reported in Figure 3.29 (b) are also comparable in amplitudes, differences are due to contact-point differences. Finally, we have decided here to do not report further plots on sliding speeds, contact pressures, traction forces or PV factors because contact differences make kinematics too different to be compared. Such study may be interesting once BB20 will be transposed in dynamics. However, this combined load study of ACBB with up to 4 contact-points, shows again that getting more than two contact-points significantly changes ball kinematics.

7 Summary

To conclude on quasi-dynamic modelling of ACBB with rigid or flexible cage, we can summarize all cage interactions by diagram of Figure 3.30. Resolution reuse R2 quasi-static system with balls and rings. Cage interactions and corresponding equations are added to solve its equilibrium.

An extensive study has been led in order to better understand the influence on bearing behaviour of operating conditions (axial, radial load, shaft speed), bearing materials and geometry (cage guidance, pocket clearance, guiding clearance, ring truncations). Contribution of each force, like inertia, cage-race SJB, ball-to-pocket SJB, barrel-plan or ball-race interactions, has been analysed in order to understand the impact on cage center motion, ball-to-pocket positions, ball-race contacts, inner race motion and ball kinematics. It appears that motion of each element is closely related to that of each other. It was also shown that ACBB kinematics is a complex mechanism not only related to ball-race interactions but also to cage effects, to gyroscopic motion in two directions (β, β') and to additional ball-race contact-points. Besides, if modelling cage flexibility in quasi-dynamics does not influence cage center motion, it reveals non negligible pocket elastic deformations even if cage interactions are under HD regime.

We should recognize that this quasi-dynamic model still has some limits like its ability to work with radial loads larger than axial load. Ball-race EHD traction model could also be refined, cage-race dry contact and SJB misalignment could be considered. However, in terms of accuracy and computational time, this model appears to be a good compromised between quasi-statics and dynamics. In any case, its development was essential to set solid basis before modelling dynamics.

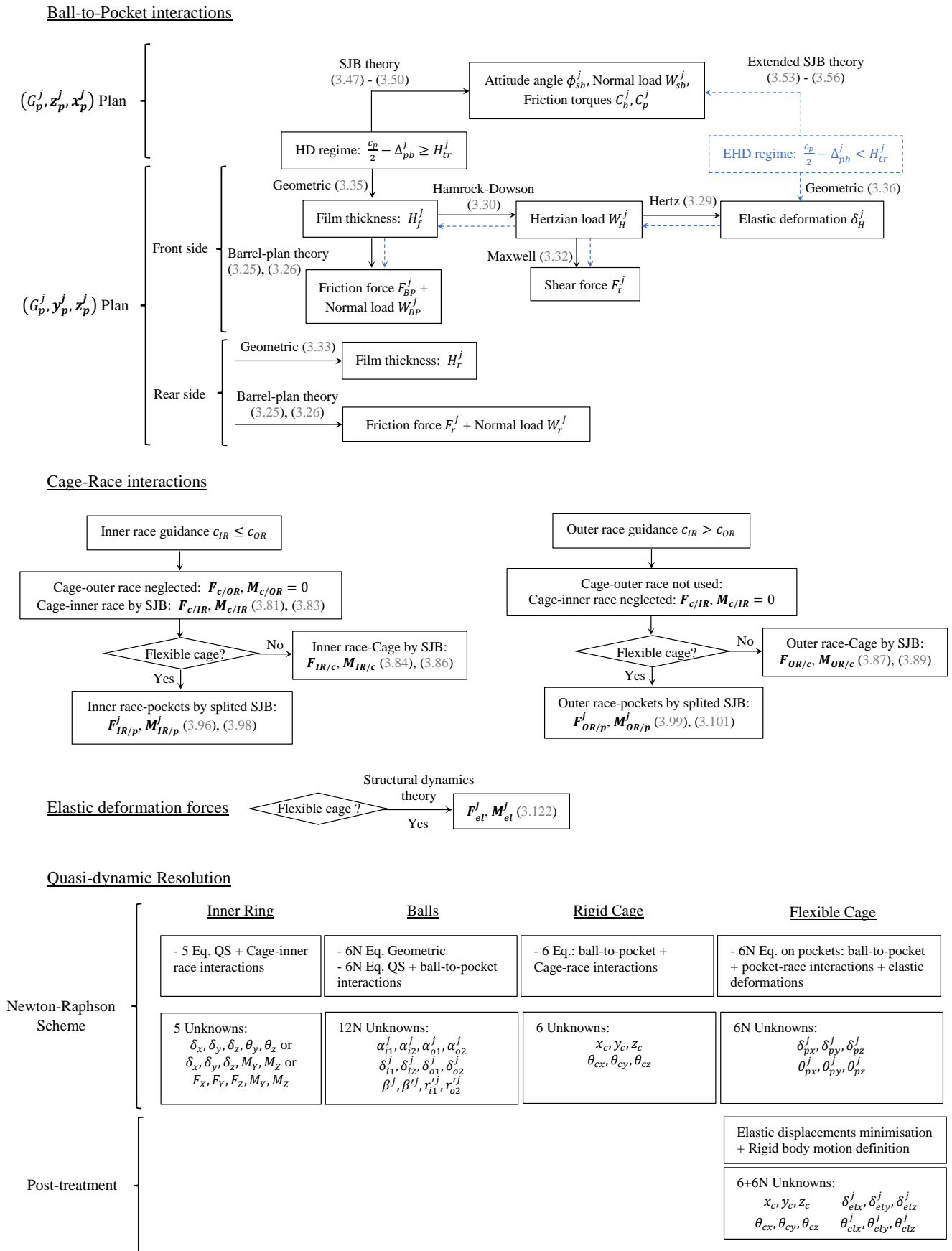


Figure 3.30 : Synthesis of cage modelling and numerical resolution

Chapter 4

Dynamic model

Contents

1	Inertia matrices	152
1.1	Inner ring	152
1.2	Balls	152
1.3	Cage	153
2	Dynamic torsors	154
2.1	Inner ring	154
2.2	Balls	154
2.3	Cage	155
3	Dynamic equations	156
3.1	Inner ring	156
3.2	Balls	156
3.3	Cage	157
4	Geometric equations	157
5	System resolution	158
5.1	Adaptive Stepsize Runge-Kutta-Fehlberg algorithm	158
5.2	System of equations and unknowns	159
6	Summary	161

1 Inertia matrices

In dynamics, masses and moments of inertia of solids (S_*) are needed. In BB20, either user directly enter their values, or it is calculated by following theory.

1.1 Inner ring

To compute its inertia matrix $\mathbf{I}(G, (S_{IR}))$, the inner ring is considered as a hollow cylinder of height w_{IR} , internal diameter d_{ei1} , external diameter d_{ei2} and mass m_{cyl} . To represent races curvature, this cylinder is cut by a half-torus of mass m_t , small-radii $r_t = f_i D$ and large-radii $R_t = 0.5d_{ei2}$. As a consequence, inner ring mass is expressed by Eq. (4.1), whereas diagonal inertia matrix is expressed by Eq. (4.2). Note that, because of small inner ring displacements δ , this matrix is supposed to be the same at bearing center G and inner ring center G_{i1} .

$$m_{IR} = m_{cyl} - m_t \text{ with } \begin{cases} m_{cyl} = \rho_{IR} \frac{\pi}{4} (d_{ei2}^2 - d_{ei1}^2) w_{IR} \\ m_t = \frac{1}{2} \rho_{IR} 2\pi^2 R_t r_t^2 \end{cases} \quad (4.1)$$

$$\mathbf{I}(G, (S_{IR})) = \begin{bmatrix} I_{IRx} & 0 & 0 \\ 0 & I_{IRy} & 0 \\ 0 & 0 & I_{IRy} \end{bmatrix}_{R_G} \text{ with } \begin{cases} I_{IRx} = \frac{m_{cyl}}{8} (d_{ei1}^2 + d_{ei2}^2) - m_t (R_t^2 + \frac{3}{4} r_t^2) \\ I_{IRy} = \frac{m_{cyl}}{12} \left[\left(\frac{3}{4} (d_{ei1}^2 + d_{ei2}^2) + w_{IR}^2 \right) \right] - \frac{m_t}{2} (R_t^2 + \frac{5}{4} r_t^2) \end{cases} \quad (4.2)$$

Inner ring dynamic behavior is directly linked to shaft behavior. To consider this contribution, another hollow cylinder of height w_s , internal diameter d_{s1} , external diameter d_{s2} , mass m_s and inertia matrix $\mathbf{I}(G, (S_{IR}))$ is added to inner ring components. Depending on user, either shaft dimensions are directly entered or shaft is considered as a full cylinder four times larger than inner ring.

$$m_s = \rho_s \frac{\pi}{4} (d_{s2}^2 - d_{s1}^2) w_s \quad (4.3)$$

$$\mathbf{I}(G, (S_s)) = \begin{bmatrix} I_{sx} & 0 & 0 \\ 0 & I_{sy} & 0 \\ 0 & 0 & I_{sy} \end{bmatrix}_{R_G} \text{ with } \begin{cases} I_{sx} = \frac{m_s}{8} (d_{s1}^2 + d_{s2}^2) \\ I_{sy} = \frac{m_s}{12} \left[\left(\frac{3}{4} (d_{s1}^2 + d_{s2}^2) + w_s^2 \right) \right] \end{cases} \quad (4.4)$$

1.2 Balls

Balls are defined as spheres of diameter D , mass m_b and diagonal inertia matrix $\mathbf{I}(B^j, (S_b^j))$ at their center.

$$m_b = \rho_b \frac{\pi}{6} D^3 \quad (4.5)$$

$$\mathbf{I}(B^j, (S_b^j)) = \begin{bmatrix} I_b & 0 & 0 \\ 0 & I_b & 0 \\ 0 & 0 & I_b \end{bmatrix}_{R_{b1}^j} \text{ with } I_b = \frac{m_b}{10} D^2 \quad (4.6)$$

1.3 Cage

To compute cage mass m_c and cage inertia matrix $\mathbf{I}(G_c, (S_c))$, we first consider that cage is a hollow cylinder of height w_c , internal diameter d_{c1} , external diameter d_{c2} , mass m_{cy} and inertia matrix $\mathbf{I}(G_c, (S_{cy}))$.

$$m_{cy} = \rho_c w_c \frac{\pi}{4} (d_{c2}^2 - d_{c1}^2) \quad (4.7)$$

$$\mathbf{I}(G_c, (S_{cy})) = \begin{bmatrix} I_{cy-x} & 0 & 0 \\ 0 & I_{cy-y} & 0 \\ 0 & 0 & I_{cy-z} \end{bmatrix}_{R_G} \quad \text{avec} \quad \begin{cases} I_{cy-x} = \frac{m_{cy}}{8} (d_{c2}^2 + d_{c1}^2) \\ I_{cy-y} = \frac{m_{cy}}{12} \left[\frac{3}{4} (d_{c1}^2 + d_{c2}^2) + w_c^2 \right] \end{cases} \quad (4.8)$$

This cage cylinder has N cylindrical holes corresponding to pockets. Such holes have a height h_c , a radii R_p , a mass m_p , an inertia matrix $\mathbf{I}(G_p^j, (S_p^j))$ at pocket center and $\mathbf{I}(G_c, (S_p^j))$ at cage center.

$$m_p = \rho_c \pi R_p^2 h_c \quad (4.9)$$

$$\mathbf{I}(G_p^j, (S_p^j)) = \begin{bmatrix} I_{px} & 0 & 0 \\ 0 & I_{py} & 0 \\ 0 & 0 & I_{pz} \end{bmatrix}_{R_p^j} \quad \text{with} \quad \begin{cases} I_{px} = \frac{m_p}{12} (3R_p^2 + h_c^2) \\ I_{py} = \frac{m_p}{2} R_p^2 \end{cases} \quad (4.10)$$

$$\mathbf{I}(G_c, (S_p^j)) = \begin{bmatrix} I_{PX}^j & 0 & 0 \\ 0 & I_{PY}^j & I_{PYZ}^j \\ 0 & I_{PYZ}^j & I_{PZ}^j \end{bmatrix}_{R_G} \quad \text{with} \quad \begin{cases} I_{PX}^j = I_{px} + m_p R_c^2 \\ I_{PY}^j = I_{py} \cos^2 \psi^j + (I_{px} + m_p R_c^2) \sin^2 \psi^j \\ I_{PYZ}^j = (I_{py} - I_{px} - m_p R_c^2) \cos \psi^j \sin \psi^j \\ I_{PZ}^j = I_{py} \sin^2 \psi^j + (I_{px} + m_p R_c^2) \cos^2 \psi^j \end{cases} \quad (4.11)$$

Then, cage mass m_c and cage inertia matrix $\mathbf{I}(G_c, (S_c))$ are computed in Eq. (4.12), (4.13) by subtracting pocket components from cage cylinder. Note that in order to work with a diagonal matrix, the extra-diagonal terms I_{cyz} are neglected if ball number N is uneven whereas they are equal to zero if N is even.

$$m_c = m_{cy} - N m_p \quad (4.12)$$

$$\mathbf{I}(G_c, (S_c)) = \begin{bmatrix} I_{cx} & 0 & 0 \\ 0 & I_{cy} & I_{cyz} \\ 0 & I_{cyz} & I_{cz} \end{bmatrix}_{R_G} \quad \text{with} \quad \begin{cases} I_{cx} = I_{cy-x} - \sum_{j=1}^N I_{PX}^j \\ I_{cy} = I_{cy-y} - \sum_{j=1}^N I_{PY}^j \\ I_{cyz} = - \sum_{j=1}^N I_{PYZ}^j = 0 \\ I_{cz} = I_{cy-z} - \sum_{j=1}^N I_{PZ}^j \end{cases} \quad (4.13)$$

2 Dynamic torsors

2.1 Inner ring

To compute the dynamic torsor of inner ring with shaft $\{D_{(S_{IR})/R_G}\}$, we consider once again small inner ring displacements δ . Especially, we suppose that inner ring displacements $\delta_x, \delta_y, \delta_z$ are small in front of accelerations $\ddot{\delta}_x, \ddot{\delta}_y, \ddot{\delta}_z, \ddot{\theta}_y, \ddot{\theta}_z$. We should specify that such hypothesis does not hold in the case of blade loss. Then, from inner ring accelerations, we directly compute the dynamic resulting $\mathbf{D}(G, (S_{IR})/R_G)$ in Eq.(4.15) and the dynamic momentum $\delta(G, (S_{IR})/R_G)$ in Eq. (4.16).

$$\{D_{(S_{IR})/R_G}\} = \left\{ \begin{array}{l} \mathbf{D}(G, (S_{IR})/R_G) \\ \delta(G, (S_{IR})/R_G) \end{array} \right\}_{R_G} \quad (4.14)$$

$$\mathbf{D}(G, (S_{IR})/R_G) = (m_{IR} + m_s) \mathbf{A}(G_{i1}, (S_{IR})/R_G) = (m_{IR} + m_s) \begin{bmatrix} \ddot{\delta}_x \\ \ddot{\delta}_y \\ \ddot{\delta}_z \end{bmatrix}_{R_G} \quad (4.15)$$

$$\delta(G, (S_{IR})/R_G) = \left[\frac{d(\mathbf{I}(G, (S_s + S_{IR})) \boldsymbol{\Omega}_{(S_{IR})/R_G})}{dt} \right]_{R_G} = \begin{bmatrix} (I_{IRx} + I_{sx}) \dot{\Omega}_I \\ (I_{IRy} + I_{sy}) \ddot{\theta}_y \\ (I_{IRy} + I_{sy}) \ddot{\theta}_z \end{bmatrix}_{R_G} \quad (4.16)$$

2.2 Balls

In dynamics, ball angular position previously defined by ψ^j becomes ψ_b^j which is a function of ψ^j the angular pocket center position and θ_m^j the ball-to-pocket relative rotation such as defined in Eq. (4.17). Then, in ball coordinate system R_{b1}^j , ball position \mathbf{GB}^j is defined by relation Eq. (4.18). Corresponding accelerations are expressed in Eq. (4.19) and dynamic resulting $\mathbf{D}(B^j, (S_b^j)/R_G)$ in Eq. (4.20).

$$\psi_b^j = \psi^j + \theta_m^j \text{ with } \psi^j = \psi_c + \frac{2\pi}{N}(j-1) \quad (4.17)$$

$$\mathbf{GB}^j = \begin{bmatrix} x_G^j \\ y_G^j \\ z_G^j \end{bmatrix} = \begin{bmatrix} \frac{q_o}{2} \lambda_o^j - GE_{o2} \sin \alpha_{o2}^j \\ \frac{d_m}{2} - (f_o - 0.5) D \cos \alpha_f + GE_{o2} \cos \alpha_{o2}^j \\ \frac{\bar{d}_m}{2} \theta_m^j \end{bmatrix}_{R_{b1}^j} \quad (4.18)$$

$$\begin{bmatrix} \ddot{x}_G^j \\ \ddot{y}_G^j \\ \ddot{z}_G^j \end{bmatrix} = \begin{bmatrix} -(\ddot{\delta}_{o2}^j - \ddot{h}_{o2}^j) \sin \alpha_{o2}^j - 2(\dot{\delta}_{o2}^j - \dot{h}_{o2}^j) \dot{\alpha}_{o2}^j \cos \alpha_{o2}^j \\ (\ddot{\delta}_{o2}^j - \ddot{h}_{o2}^j) \cos \alpha_{o2}^j - 2(\dot{\delta}_{o2}^j - \dot{h}_{o2}^j) \dot{\alpha}_{o2}^j \sin \alpha_{o2}^j \\ \frac{d_m}{2} (\dot{\omega}_m^j - \dot{\omega}_c) \end{bmatrix}_{R_{b1}^j} + \begin{bmatrix} -GE_{o2}^j \left(-(\dot{\alpha}_{o2}^j)^2 \sin \alpha_{o2}^j + \ddot{\alpha}_{o2} \cos \alpha_{o2}^j \right) \\ -GE_{o2}^j \left((\dot{\alpha}_{o2}^j)^2 \cos \alpha_{o2}^j + \ddot{\alpha}_{o2} \sin \alpha_{o2}^j \right) \\ 0 \end{bmatrix}_{R_{b1}^j} \quad (4.19)$$

$$\mathbf{D}(B^j, (S_b^j)/R_G) = m_b \mathbf{A}(B^j, (S_b^j)/R_G) = m_b \begin{bmatrix} \ddot{x}_G^j \\ \ddot{y}_G^j \\ \ddot{z}_G^j \end{bmatrix}_{R_{b1}^j} \quad (4.20)$$

Balls kinetic momentums are calculated from Eq. (4.21) to (4.23). Then, by time derivation, dynamic momentums are calculated in Eq. (4.25).

$$\boldsymbol{\sigma}(B^j, (S_b^j)/R_G) = \mathbf{I}(B^j, (S_b^j)) \boldsymbol{\Omega}_{(S_b^j)/R_G} \quad (4.21)$$

$$\boldsymbol{\Omega}_{(S_b^j)/R_G} = \begin{bmatrix} \omega_m^j \\ 0 \\ 0 \end{bmatrix}_{R_G} + \begin{bmatrix} \omega_r^j \\ 0 \\ 0 \end{bmatrix}_{R_{b3}^j} + \begin{bmatrix} 0 \\ 0 \\ \dot{\beta}^j \end{bmatrix}_{R_{b2}^j} + \begin{bmatrix} 0 \\ \dot{\beta}'^j \\ 0 \end{bmatrix}_{R_{b1}^j} \quad (4.22)$$

$$\boldsymbol{\sigma}(B^j, (S_b^j)/R_G) = I_b \begin{bmatrix} \omega_m^j + \omega_r^j \cos \beta^j \cos \beta'^j + \dot{\beta}^j \sin \beta'^j \\ \omega_r^j \sin \beta^j + \dot{\beta}'^j \\ -\omega_r^j \cos \beta^j \sin \beta'^j + \dot{\beta}^j \cos \beta'^j \end{bmatrix}_{R_{b1}^j} \quad (4.23)$$

$$\boldsymbol{\delta}(B^j, (S_b^j)/R_G) = \left[\frac{d\boldsymbol{\sigma}(B^j, (S_b^j)/R_G)}{dt} \right]_{R_{b1}^j} \quad (4.24)$$

$$\begin{aligned} \boldsymbol{\delta}(B^j, (S_b^j)/R_G) = I_b \begin{bmatrix} \dot{\omega}_m^j + \dot{\omega}_r^j \cos \beta^j \cos \beta'^j + \omega_r^j (-\dot{\beta}^j \sin \beta^j \cos \beta'^j - \beta'^j \cos \beta^j \sin \beta'^j) \\ \dot{\omega}_r^j \sin \beta^j + \omega_r^j \dot{\beta}^j \cos \beta^j \\ -\dot{\omega}_r^j \cos \beta^j \sin \beta'^j - \omega_r^j (-\dot{\beta}^j \sin \beta^j \sin \beta'^j + \beta'^j \cos \beta^j \cos \beta'^j) \end{bmatrix}_{R_{b1}^j} \\ + I_b \begin{bmatrix} \ddot{\beta}^j \sin \beta'^j + \dot{\beta}^j \beta'^j \cos \beta'^j \\ \ddot{\beta}'^j \\ \ddot{\beta}^j \cos \beta'^j - \dot{\beta}^j \beta'^j \sin \beta'^j \end{bmatrix}_{R_{b1}^j} \end{aligned} \quad (4.25)$$

2.3 Cage

In dynamics, cage self-rotation previously called θ_{cx} is included in ψ_c , itself included in ψ^j . Then, pocket removed positions are defined by relations (4.26) and (4.27).

$$\mathbf{G}_p^j \mathbf{P}^j = \begin{bmatrix} \delta_{px}^j \\ \delta_{py}^j \\ \delta_{pz}^j \end{bmatrix}_{\mathcal{R}_G} = \begin{bmatrix} x_c - R_c \cos \psi^j \theta_{cz} + R_c \sin \psi^j \theta_{cy} \\ y_c \\ z_c \end{bmatrix}_{\mathcal{R}_G} \quad (4.26)$$

$$\begin{bmatrix} \theta_{px}^j \\ \theta_{py}^j \\ \theta_{pz}^j \end{bmatrix}_{\mathcal{R}_G} = \begin{bmatrix} 0 \\ \theta_{cy} \\ \theta_{cz} \end{bmatrix}_{\mathcal{R}_G} \quad (4.27)$$

Cage dynamic torsor $\{D_{(S_c)/R_G}\}$ computation is immediate since it directly depends on accelerations of cage unknowns. This torsor is made of dynamic resulting $\mathbf{D}(G_c, (S_c)/R_G)$ expressed in Eq. (4.29) and dynamic momentum $\boldsymbol{\delta}(G_c, (S_c)/R_G)$ expressed in Eq. (4.30).

$$\{D_{(S_c)/R_G}\} = \left\{ \begin{array}{c} \mathbf{D}(G_c, (S_c)/R_G) \\ \boldsymbol{\delta}(G_c, (S_c)/R_G) \end{array} \right\}_{R_G} \quad (4.28)$$

$$\mathbf{D}(G_c, (S_c)/R_G) = m_c \mathbf{A}(G_c, (S_c)/R_G) = m_c \begin{bmatrix} \ddot{x}_c \\ \ddot{y}_c \\ \ddot{z}_c \end{bmatrix}_{R_G} \quad (4.29)$$

$$\boldsymbol{\delta}(G_c, (S_c)/R_G) = \left[\frac{d(\mathbf{I}(G_c, (S_c))\boldsymbol{\Omega}_{(S_c)/R_G})}{dt} \right]_{R_G} = \begin{bmatrix} I_{cx} \dot{\omega}_c \\ I_{cy} \ddot{\theta}_{cy} \\ I_{cz} \ddot{\theta}_{cz} \end{bmatrix}_{R_G} \quad (4.30)$$

3 Dynamic equations

Dynamic equations (4.31) to (4.47) are made of quasi-dynamic equations with the addition of acceleration component calculated in dynamic torsors. Later, dynamic forces like unbalance or ball-race, cage-race and ball-to-pocket damping should be implemented.

3.1 Inner ring

$$(m_{IR} + m_s) \ddot{\delta}_x = F_{QD/IRx} \quad (4.31)$$

$$(m_{IR} + m_s) \ddot{\delta}_y = F_{QD/IRy} \quad (4.32)$$

$$(m_{IR} + m_s) \ddot{\delta}_z = F_{QD/IRz} \quad (4.33)$$

$$(I_{IRy} + I_{sy}) \ddot{\theta}_y = M_{QD/IRy} \quad (4.34)$$

$$(I_{IRy} + I_{sy}) \ddot{\theta}_z = M_{QD/IRz} \quad (4.35)$$

3.2 Balls

$$m_b \left[-(\ddot{\delta}_{o2}^j - \ddot{h}_{o2}^j) \sin \alpha_{o2}^j - 2(\dot{\delta}_{o2}^j - \dot{h}_{o2}^j) \dot{\alpha}_{o2}^j \cos \alpha_{o2}^j - G E_{o2}^j \left(-(\dot{\alpha}_{o2}^j)^2 \sin \alpha_{o2}^j + \ddot{\alpha}_{o2} \cos \alpha_{o2}^j \right) \right] = F_{QD/bx}^j \quad (4.36)$$

$$m_b \left[(\ddot{\delta}_{o2}^j - \ddot{h}_{o2}^j) \cos \alpha_{o2}^j - 2(\dot{\delta}_{o2}^j - \dot{h}_{o2}^j) \dot{\alpha}_{o2}^j \sin \alpha_{o2}^j - G E_{o2}^j \left((\dot{\alpha}_{o2}^j)^2 \cos \alpha_{o2}^j + \ddot{\alpha}_{o2} \sin \alpha_{o2}^j \right) \right] = F_{QD/by}^j \quad (4.37)$$

$$m_b \frac{d_m}{2} (\dot{\omega}_m^j - \dot{\omega}_c) = F_{QD/bz}^j \quad (4.38)$$

$$I_b \left[\dot{\omega}_m^j + \dot{\omega}_r^j \cos \beta^j \cos \beta'^j + \omega_r^j (-\dot{\beta}^j \sin \beta^j \cos \beta'^j - \dot{\beta}'^j \cos \beta^j \sin \beta'^j) + \ddot{\beta}^j \sin \beta'^j + \dot{\beta}^j \dot{\beta}'^j \cos \beta'^j \right] = M_{QD/bx}^j \quad (4.39)$$

$$I_b \left[\dot{\omega}_r^j \sin \beta^j + \omega_r^j \dot{\beta}^j \cos \beta^j + \ddot{\beta}^j \right] = M_{QD/by}^j \quad (4.40)$$

$$I_b \left[-\dot{\omega}_r^j \cos \beta^j \sin \beta'^j - \omega_r^j (-\dot{\beta}^j \sin \beta^j \sin \beta'^j + \dot{\beta}'^j \cos \beta^j \cos \beta'^j) + \ddot{\beta}^j \cos \beta'^j - \dot{\beta}^j \dot{\beta}'^j \sin \beta'^j \right] = M_{QD/bz}^j \quad (4.41)$$

3.3 Cage

$$m_c \ddot{x}_c = F_{QD/cx} \quad (4.42)$$

$$m_c \ddot{y}_c = F_{QD/cy} \quad (4.43)$$

$$m_c \ddot{z}_c = F_{QD/cz} \quad (4.44)$$

$$I_{cx} \dot{\omega}_c = M_{QD/cx} \quad (4.45)$$

$$I_{cy} \ddot{\theta}_{cy} = M_{QD/cy} \quad (4.46)$$

$$I_{cz} \ddot{\theta}_{cz} = M_{QD/cz} \quad (4.47)$$

4 Geometric equations

To get 6 additional equations in dynamics, geometric equations are derived twice with respect to time. Then, geometric equations on outer ring becomes equations (4.48) and (4.49).

$$\begin{aligned} & \left[\ddot{\delta}_{o1}^j - \ddot{h}_{o1}^j - GE_{o1}^j \dot{\alpha}_{o1}^{j2} \right] \sin \alpha_{o1}^j + \left[2(\dot{\delta}_{o1}^j - \dot{h}_{o1}^j) \dot{\alpha}_{o1}^j + GE_{o1}^j \ddot{\alpha}_{o1}^j \right] \cos \alpha_{o1}^j + \\ & \left[\ddot{\delta}_{o2}^j - \ddot{h}_{o2}^j - GE_{o2}^j \dot{\alpha}_{o2}^{j2} \right] \sin \alpha_{o2}^j + \left[2(\dot{\delta}_{o2}^j - \dot{h}_{o2}^j) \dot{\alpha}_{o2}^j + GE_{o2}^j \ddot{\alpha}_{o2}^j \right] \cos \alpha_{o2}^j = 0 \end{aligned} \quad (4.48)$$

$$\begin{aligned} & \left[\ddot{\delta}_{o1}^j - \ddot{h}_{o1}^j - GE_{o1}^j \dot{\alpha}_{o1}^{j2} \right] \cos \alpha_{o1}^j - \left[2(\dot{\delta}_{o1}^j - \dot{h}_{o1}^j) \dot{\alpha}_{o1}^j + GE_{o1}^j \ddot{\alpha}_{o1}^j \right] \sin \alpha_{o1}^j \\ & - \left[\ddot{\delta}_{o2}^j - \ddot{h}_{o2}^j - GE_{o2}^j \dot{\alpha}_{o2}^{j2} \right] \cos \alpha_{o2}^j + \left[2(\dot{\delta}_{o2}^j - \dot{h}_{o2}^j) \dot{\alpha}_{o2}^j + GE_{o2}^j \ddot{\alpha}_{o2}^j \right] \sin \alpha_{o2}^j = 0 \end{aligned} \quad (4.49)$$

Geometric equations on inner ring becomes equations (4.50) and (4.51).

$$\begin{aligned} & \left[\ddot{\delta}_{i1}^j - \ddot{h}_{i1}^j - GE_{i1}^j \dot{\alpha}_{i1}^{j2} \right] \sin \alpha_{i1}^j + \left[2(\dot{\delta}_{i1}^j - \dot{h}_{i1}^j) \dot{\alpha}_{i1}^j + GE_{i1}^j \ddot{\alpha}_{i1}^j \right] \cos \alpha_{i1}^j + \\ & \left[\ddot{\delta}_{i2}^j - \ddot{h}_{i2}^j - GE_{i2}^j \dot{\alpha}_{i2}^{j2} \right] \sin \alpha_{i2}^j + \left[2(\dot{\delta}_{i2}^j - \dot{h}_{i2}^j) \dot{\alpha}_{i2}^j + GE_{i2}^j \ddot{\alpha}_{i2}^j \right] \cos \alpha_{i2}^j \\ & - \frac{d^2}{dt^2} \left(g_i \lambda_i^j \cos \theta_z \cos \theta_y \right) = 0 \end{aligned} \quad (4.50)$$

$$\begin{aligned} & - \left[\ddot{\delta}_{i1}^j - \ddot{h}_{i1}^j - GE_{i1}^j \dot{\alpha}_{i1}^{j2} \right] \cos \alpha_{i1}^j + \left[2(\dot{\delta}_{i1}^j - \dot{h}_{i1}^j) \dot{\alpha}_{i1}^j + GE_{i1}^j \ddot{\alpha}_{i1}^j \right] \sin \alpha_{i1}^j \\ & + \left[\ddot{\delta}_{i2}^j - \ddot{h}_{i2}^j - GE_{i2}^j \dot{\alpha}_{i2}^{j2} \right] \cos \alpha_{i2}^j - \left[2(\dot{\delta}_{i2}^j - \dot{h}_{i2}^j) \dot{\alpha}_{i2}^j + GE_{i2}^j \ddot{\alpha}_{i2}^j \right] \sin \alpha_{i2}^j \\ & - \frac{d^2}{dt^2} \left(g_i \lambda_i^j (\cos \psi_b^j \sin \theta_z - \sin \psi_b^j \sin \theta_y \cos \theta_z) \right) = 0 \end{aligned} \quad (4.51)$$

Geometric equations on inner and outer ring becomes equations (4.52) and (4.53).

$$\begin{aligned} & \left[\ddot{\delta}_{i1}^j - \ddot{h}_{i1}^j - GE_{i1}^j \dot{\alpha}_{i1}^{j2} \right] \sin \alpha_{i1}^j + \left[2(\dot{\delta}_{i1}^j - \dot{h}_{i1}^j) \dot{\alpha}_{i1}^j + GE_{i1}^j \ddot{\alpha}_{i1}^j \right] \cos \alpha_{i1}^j \\ & + \left[\ddot{\delta}_{o2}^j - \ddot{h}_{o2}^j - GE_{o2}^j \dot{\alpha}_{o2}^{j2} \right] \sin \alpha_{o2}^j + \left[2(\dot{\delta}_{o2}^j - \dot{h}_{o2}^j) \dot{\alpha}_{o2}^j + GE_{o2}^j \ddot{\alpha}_{o2}^j \right] \cos \alpha_{o2}^j = \\ & \frac{d^2}{dt^2} \left(-\delta_x + R_1 - R_1 \cos \theta_y \cos \theta_z + R_2 \cos \psi_b^j \cos \theta_y \sin \theta_z - R_2 \sin \psi_b^j \sin \theta_y \right) \end{aligned} \quad (4.52)$$

$$\begin{aligned} & - \left[\ddot{\delta}_{i1}^j - \ddot{h}_{i1}^j - GE_{i1}^j \dot{\alpha}_{i1}^{j2} \right] \cos \alpha_{i1}^j + \left[2(\dot{\delta}_{i1}^j - \dot{h}_{i1}^j) \dot{\alpha}_{i1}^j + GE_{i1}^j \ddot{\alpha}_{i1}^j \right] \sin \alpha_{i1}^j \\ & - \left[\ddot{\delta}_{o2}^j - \ddot{h}_{o2}^j - GE_{o2}^j \dot{\alpha}_{o2}^{j2} \right] \cos \alpha_{o2}^j + \left[2(\dot{\delta}_{o2}^j - \dot{h}_{o2}^j) \dot{\alpha}_{o2}^j + GE_{o2}^j \ddot{\alpha}_{o2}^j \right] \sin \alpha_{o2}^j = \\ & \frac{d^2}{dt^2} \left(R_2 + \left[-\delta_y - R_1 \sin \theta_z - R_2 \cos \psi_b^j \cos \theta_z \right] \cos \psi_b^j \right. \\ & \left. + \left[-\delta_z + R_1 \sin \theta_y \cos \theta_z - R_2 \cos \psi_b^j \sin \theta_y \sin \theta_z - R_2 \sin \psi_b^j \cos \theta_y \right] \sin \psi_b^j \right) \end{aligned} \quad (4.53)$$

Note that in these equations $\frac{d\psi_b^j}{dt} = \frac{d(\theta_m^j + \psi^j)}{dt} = \omega_m^j$ and $\frac{d^2\psi_b^j}{dt^2} = \dot{\omega}_m^j$.

5 System resolution

5.1 Adaptive Stepsize Runge-Kutta-Fehlberg algorithm

Different implicit or explicit algorithms exist to solve dynamical systems made of real-time differential equations. Depending on system characteristics, computation cost or accuracy expected, each one has its advantages and disadvantages. In dynamics, ball bearings have components with frequency differences of several orders. They are also subjected to important discontinuities due to ball-to-pocket and cage-race impacts. For these reasons, Gupta [91] stated that explicit methods were more suitable to model bearing dynamics with cage. Many authors like Walters [253], Meeks [182] or Liu [171], also developed dynamical ball bearing codes and confirmed efficiency of explicit algorithms like Runge-Kutta-Fehlberg (RKF) method. Particularity of Fehlberg method is that it proposes RK tables for higher orders than 4. It also estimates error at each step in order to adapt accurately step-size. That is why, this RKF method is implemented in BB20 with possibility to set the order between 1 and 7 depending on precision and time-computation expected.

For given initial conditions \mathbf{X}_0 on a set of vector unknowns \mathbf{X} , this method solves the differential system of equations (4.54) and gives evolution of these unknowns on discretised time interval $[t_0, t_f]$. As for that, at each new time t_{n+1} , formula (4.55) is applied to compute new unknowns x_k , k being the position in vector \mathbf{X} . In this expression, A_{ij} , B_i , C_i and D_i are scalar components of RKF tables defined in literature [69], [70].

$$\begin{cases} \dot{\mathbf{X}} = f(\mathbf{X}, t) \\ \mathbf{X} = \mathbf{X}_0 \text{ at } t = t_0 \end{cases} \quad (4.54)$$

$$\begin{cases} x_k(t_{n+1}) = x_k(t_n) + \Delta t_{n+1} \sum_{i=0}^s C_i K_i \\ Err_k(t_{n+1}) = \sum_{i=0}^s (D_i - C_i) K_i \end{cases} \quad \text{with } K_i = f\left(x_k(t_n) + \Delta t_{n+1} \sum_{j=1}^s A_{ij} K_j, t_n + B_i \Delta t_{n+1}\right) \quad (4.55)$$

To adapt time step Δt , at each time t_{n+1} , for each variable x_k , truncation error $Err_k(t_{n+1})$ is calculated by relation (4.55). For a RKF method at order m , this error is the difference between solution calculated at order $(m+1)$ and solution calculated at order m . According to Gupta [91] and as expressed in (4.56), norm of errors vector $|\mathbf{Err}(t_{n+1})|$ varies as $(m+1)^{th}$ power of previous step size Δt_n . Then, at each time step, step size Δt_{n+1} is adapted by relation (4.57), where ϵ_{R3} is error tolerance set by user. To avoid increasing or decreasing step size too much, γ factor is limited between 0.125 and 4.

$$|\mathbf{Err}(t_{n+1})| \sim (\Delta t_n)^{m+1} \quad (4.56)$$

$$\Delta t_{n+1} = \gamma \Delta t_n \quad \text{with } \gamma = 0.8 \left(\frac{\epsilon_{R3} |\mathbf{X}(t_n)|}{|\mathbf{Err}(t_{n+1})|} \right)^{1/m} \quad (4.57)$$

5.2 System of equations and unknowns

From dynamic equations expressed in sections 3 and 4, vector unknown \mathbf{X} and corresponding system of equation $\dot{\mathbf{X}} = f(\mathbf{X}, t)$ to be solved are summarised in Tables 4.1 and 4.2. To initialise unknowns \mathbf{X}_0 , solution of R2 with cage is used for lengths, rotations unknowns, cage speed ω_c , precession speeds ω_m^j and ball rotational speeds ω_R^j whereas other unknowns are set to zero.

Note that in this dynamic system, quasi-static unknowns $r_{i1}^{'j}$ and $r_{o2}^{'j}$ have been replaced by ω_m^j and ω_R^j . Then ξ_1^j and ξ_2^j are obtained by relations (4.58), (4.59) and effective rolling radius $r_{km}^{'j}$ by relations (2.80) to (2.83).

$$\xi_1^j = \frac{\omega_R^j}{\Omega_i - \omega_m^j} \quad (4.58)$$

$$\xi_2^j = \frac{\omega_R^j}{\Omega_o - \omega_m^j} \quad (4.59)$$

Besides, Gupta [91] specified the importance of nondimensionalizing equations of motion in order to correctly estimate local truncation error. As for that, length unknowns were nondimensionalized by ball radius $\frac{D}{2}$, forces by axial load F_X and time by a combination of ball mass m_b , ball radius and axial load such as defined in relation (4.60). Such strategy should be implemented in BB20 in order to work with consistent time steps comprised between 0 and 1.

$$t^* = \frac{t}{\sqrt{\frac{m_b D}{2 F_X}}} \quad (4.60)$$

At the moment, all this theory on dynamic modelling has been programmed in BB20. However, improvements still need to be made in order to get exploitable results.

Unknown	Name	Equation
δ_x	x_1	$\dot{x}_1 = x_6$
δ_y	x_2	$\dot{x}_2 = x_7$
δ_z	x_3	$\dot{x}_3 = x_8$
θ_y	x_4	$\dot{x}_4 = x_9$
θ_z	x_5	$\dot{x}_5 = x_{10}$
$\dot{\delta}_x$	x_6	$\dot{x}_6 = \ddot{\delta}_x$ from Eq. (4.31) of $F_{/IRx}$
$\dot{\delta}_y$	x_7	$\dot{x}_7 = \ddot{\delta}_y$ from Eq. (4.32) of $F_{/IRy}$
$\dot{\delta}_z$	x_8	$\dot{x}_8 = \ddot{\delta}_z$ from Eq. (4.33) of $F_{/IRz}$
$\dot{\theta}_y$	x_9	$\dot{x}_9 = \ddot{\theta}_y$ from Eq. (4.34) of $M_{/IRy}$
$\dot{\theta}_z$	x_{10}	$\dot{x}_{10} = \ddot{\theta}_z$ from Eq. (4.35) of $M_{/IRz}$
x_c	x_{11}	$\dot{x}_{11} = x_{17}$
y_c	x_{12}	$\dot{x}_{12} = x_{18}$
z_c	x_{13}	$\dot{x}_{13} = x_{19}$
ψ_c	x_{14}	$\dot{x}_{14} = x_{20}$
θ_{cy}	x_{15}	$\dot{x}_{15} = x_{21}$
θ_{cz}	x_{16}	$\dot{x}_{16} = x_{22}$
\dot{x}_c	x_{17}	$\dot{x}_{17} = \ddot{x}_c$ from Eq. (4.42) of $F_{/cx}$
\dot{y}_c	x_{18}	$\dot{x}_{18} = \ddot{y}_c$ from Eq. (4.43) of $F_{/cy}$
\dot{z}_c	x_{19}	$\dot{x}_{19} = \ddot{z}_c$ from Eq. (4.44) of $F_{/cz}$
$\dot{\psi}_c = \omega_c$	x_{20}	$\dot{x}_{20} = \ddot{\psi}_c$ from Eq. (4.45) of $M_{/cx}$
$\dot{\theta}_{cy}$	x_{21}	$\dot{x}_{21} = \ddot{\theta}_{cy}$ from Eq. (4.46) of $M_{/cy}$
$\dot{\theta}_{cz}$	x_{22}	$\dot{x}_{22} = \ddot{\theta}_{cz}$ from Eq. (4.47) of $M_{/cz}$

Table 4.1 : Inner ring and cage unknowns and equations in dynamics

Unknown	Name	Equation
ψ_b^j	x_{22+j}	$\dot{x}_{22+j} = x_{22+12N+j}$
α_{o2}^j	x_{22+N+j}	$\dot{x}_{22+N+j} = x_{22+13N+j}$
$\delta_{o2}^j - h_{o2}^j$	$x_{22+2N+j}$	$\dot{x}_{22+2N+j} = x_{22+14N+j}$
$\psi_b^j = \omega_m^j$	$x_{22+12N+j}$	$\dot{x}_{22+12N+j} = \ddot{\psi}_b^j$ from Eq. (4.38) of $F_{/bz}^j$
$\dot{\alpha}_{o2}^j$	$x_{22+13N+j}$	$\dot{x}_{22+13N+j} = \ddot{\alpha}_{o2}^j$ from Eq. (4.36), (4.37) of $F_{/bx}^j, F_{/by}^j$
$\dot{\delta}_{o2}^j - \dot{h}_{o2}^j$	$x_{22+14N+j}$	$\dot{x}_{22+14N+j} = \ddot{\delta}_{o2}^j - \ddot{h}_{o2}^j$ from Eq. (4.36), (4.37) of $F_{/bx}^j, F_{/by}^j$
α_{o1}^j	$x_{22+3N+j}$	$\dot{x}_{22+3N+j} = x_{22+15N+j}$
$\delta_{o1}^j - h_{o1}^j$	$x_{22+4N+j}$	$\dot{x}_{22+4N+j} = x_{22+16N+j}$
α_{i1}^j	$x_{22+5N+j}$	$\dot{x}_{22+5N+j} = x_{22+17N+j}$
$\delta_{i1}^j - h_{i1}^j$	$x_{22+6N+j}$	$\dot{x}_{22+6N+j} = x_{22+18N+j}$
α_{i2}^j	$x_{22+7N+j}$	$\dot{x}_{22+7N+j} = x_{22+19N+j}$
$\delta_{i2}^j - h_{i2}^j$	$x_{22+8N+j}$	$\dot{x}_{22+8N+j} = x_{22+20N+j}$
$\dot{\alpha}_{o1}^j$	$x_{22+15N+j}$	$\dot{x}_{22+15N+j} = \ddot{\alpha}_{o1}^j$ from (4.48), (4.49) of $\ddot{f}_{ORx}^j, \ddot{f}_{ORy}^j$
$\dot{\delta}_{o1}^j - \dot{h}_{o1}^j$	$x_{22+16N+j}$	$\dot{x}_{22+16N+j} = \ddot{\delta}_{o1}^j - \ddot{h}_{o1}^j$ from (4.48), (4.49) of $\ddot{f}_{ORx}^j, \ddot{f}_{ORy}^j$
$\dot{\alpha}_{i1}^j$	$x_{22+17N+j}$	$\dot{x}_{22+17N+j} = \ddot{\alpha}_{i1}^j$ from (4.52), (4.53) of $\ddot{f}_{IORx}^j, \ddot{f}_{IORy}^j$
$\dot{\delta}_{i1}^j - \dot{h}_{i1}^j$	$x_{22+18N+j}$	$\dot{x}_{22+18N+j} = \ddot{\delta}_{i1}^j - \ddot{h}_{i1}^j$ from (4.52), (4.53) of $\ddot{f}_{IORx}^j, \ddot{f}_{IORy}^j$
$\dot{\alpha}_{i2}^j$	$x_{22+19N+j}$	$\dot{x}_{22+19N+j} = \ddot{\alpha}_{i2}^j$ from (4.50), (4.51) of $\ddot{f}_{IRx}^j, \ddot{f}_{IRy}^j$
$\dot{\delta}_{i2}^j - \dot{h}_{i2}^j$	$x_{22+20N+j}$	$\dot{x}_{22+20N+j} = \ddot{\delta}_{i2}^j - \ddot{h}_{i2}^j$ from (4.50), (4.51) of $\ddot{f}_{IRx}^j, \ddot{f}_{IRy}^j$
β^j	$x_{22+9N+j}$	$\dot{x}_{22+9N+j} = x_{22+21N+j}$
θ_r^j	$x_{22+10N+j}$	$\dot{x}_{22+10N+j} = x_{22+22N+j}$
β'^j	$x_{22+11N+j}$	$\dot{x}_{22+11N+j} = x_{22+23N+j}$
$\dot{\beta}^j$	$x_{22+21N+j}$	$\dot{x}_{22+21N+j} = \ddot{\beta}^j$ from Eq. (4.39), (4.41) of $M_{/bx}^j, M_{/bz}^j$
$\dot{\theta}_r^j = \omega_r^j$	$x_{22+22N+j}$	$\dot{x}_{22+22N+j} = \ddot{\theta}_r^j$ from Eq. (4.39), (4.41) of $M_{/bx}^j, M_{/bz}^j$
$\dot{\beta}'^j$	$x_{22+23N+j}$	$\dot{x}_{22+23N+j} = \ddot{\beta}'^j$ from Eq. (4.40) of $M_{/by}^j$

Table 4.2 : Balls unknowns and equations in dynamics

6 Summary

Previous chapters have shown the necessity to transpose BB20 in dynamics. This work has been started here. As for that, balls, cage and inner race masses, inertia matrix and dynamic torsors have been defined. New dynamic system of equations and unknowns have been set. This system can be solved by a Runge-Kutta-Fehlberg algorithm that computes problem unknowns at each time-step and that adapts step size at each step. At the moment, numerical developments are still needed to get exploitable results. This should be done in a future thesis.

Conclusion

To conclude, this thesis focused on BB20, a computer code that solves quasi-static equilibrium of four contact point ball bearings. In initial model, only balls and rings are considered with lubrication, inertia, external loads on inner ring, ball-race contact and friction forces. A detailed state of the art of literature models revealed that BB20 was one of the most accurate ACBB existing model. Indeed, it considers up to 4 ball-race contact points and does not make any raceway control hypothesis to compute kinematics. Instead, all balls degrees of freedom are calculated by solving forces and torques equilibrium. Especially, both pitch and yaw angles, arising from two gyroscopic momentums, are computed. Ball-race interactions are accurately modelled by considering spinning, rolling, macro-sliding at contact and by integrating shear stress on each point of surface ellipse. In this way, detailed kinematic behaviour is calculated. However, all these considerations make numerical resolution particularly tricky to be solved.

Then, because of initial BB20 complexity and limitations, algorithm optimisation and models improvements had to be done before considering cage effects. As for that, model has been transposed in a direct coordinate system. Unknowns, coordinate systems and equations have been redefined to consider negative angles and reverse thrust load. Ball-race deformations and film thickness definition have also been reconsidered to work with a single, continuous and smooth system of equations adapted to any contact and any ring truncations. Numerical scheme, drag model, friction forces computation and system nondimensionalization have also been revised in details. It was shown that all these modifications reduce converging constraints, improve numerical continuity, system conditioning, robustness and computational time. This new model is also adapted to larger operating conditions in terms of bearing geometry, speeds or loads.

Consequently, under pure axial load or moderated radial loads, analysis of ball kinematic parameters and sliding lines on contact ellipse is in agreement with expected results. When radial load becomes larger than axial load, ball-to-inner race detachments and falls in ball-speeds are observed. Model is not adapted anymore, cage and dynamical effects should be considered. However, a solution with hypothesis on balls rotations, have been proposed to get a first overview on bearing equilibrium.

A comparative study with literature reference models has also been conducted. Similar behaviours have been observed between models, which confirms BB20 correctness. BB20 has also been validated by comparison with Safran's power loss experiments and with Kawamura's measurements of pitch angle, ball and cage rotations. Nevertheless, validation of a quasi-static model turned out to be complicated because on the one hand, each literature model makes its own hypothesis, and on the other hand, experiments are limited by ability to measure kinematic parameters.

In a second time, cage has been added into the model. As for that, cage rotational speed and ball-to-pocket ortho-radial displacements are estimated by a quasi-dynamic approach. Cage-to-guiding race interactions are modelled by short journal bearing theory. Ball-to-pocket interactions are also represented, in a given plan, by SJB theory adapted to HD or EHD regimes. In an orthogonal plan, ball-to-pocket interactions combine different effects. Indeed, barrel-plan theory models HD normal and frictions forces. EHD interactions are defined by Hertzian contact for normal loads and by dry shearing for friction forces. Numerical procedures have been developed to manage with discontinuities between these HD to EHD regimes. A strategy has also been set up to deal with important ortho-radial displacements and SJB forces that can cause singularities. Then, cage equilibrium is reached step-by-step. This involves larger computational time but ensures greater robustness.

In addition, cage can be considered as a rigid or flexible body. With rigid model, cage is defined as a single solid and 6 equations on cage center are solved. With flexible model, cage is divided into N finite elements and $6N$ equations on pockets are solved. Structural dynamics methods are used to compute 3D cage flexibility with both global and local deformations.

This quasi-dynamic model has been run with increasing axial loads. When cage is guided by the inner race, axial displacements and ball-to-pocket normal loads are larger than under outer race guidance. Under IR guidance, cage self-rotations and ball-to-pocket displacements are such that cage pulls balls whereas under OR guidance, balls are pulled by the cage. Ball kinematics have also been investigated under pure axial loads. If general results agree with literature, BB20 showed in addition the non negligible influence of axial load and shaft speed on yaw angle.

Tests have also been run with combined axial and radial loads. Because of cage-race SJB interactions, cage rotates on itself and gets positioned at 90° from radial load. And, these motions increase with radial load. As well, analysis of ball-to-pocket minimal clearance confirmed the necessity to take cage into account. Its influence on ball kinematics and ball-race contact points location have been demonstrated. It has also been shown that, under small radial load, all balls are positioned at the same place in the pocket. When radial load increases, each ball gets positioned differently until that loaded balls stand at one side of the pocket and unloaded balls at the opposite side. To better understand this behaviour, contribution of kinematic parameters and ball-to-pocket forces in each plan have been analysed. It appears that each effect is related to others by precise mechanisms.

Flexible cage has also been studied. Convergence difficulties have been observed because of quasi-dynamic limits and of simplifications on cage-race interactions. Similar cage center motions have been observed between flexible and rigid models. However, flexible cage experiences non negligible pocket elastic deformations, especially with soft materials like PEEK. Besides, rigid quasi-dynamic model has been compared with a dynamical model of four contact-point ball bearing. Similar results have been observed, which strengthens our belief in BB20 correctness. Transposition in dynamics should allow to get even closer results. Above all, this comparative study with ACBB working under 1, 2, 3 or 4 contact-points, confirmed the influence of rings truncations and pointed out that getting a third contact-point particularly complicates kinematics.

Finally, computational time analysis has shown that quasi-dynamic resolution was much longer than quasi-static, even if it cannot be longer than dynamics. Then, quasi-dynamic model is a practical tool to get a first overlook on bearing behaviour with cage. Its development was essential to introduce cage accurately, its limits have been raised and justified the necessity to transpose BB20 in dynamics. As for that, bodies inertia parameters and dynamic torsors have been defined before setting the system of equations. This system can be solved by a Runge-Kutta-Fehlberg algorithm that computes problem unknowns at each time-step. This dynamic modelling approach has been started. However, numerical developments are still needed to get correct results.

Prospects

Once the basic dynamical model solved, additional effects should be considered. For example, ball-race, cage-race and ball-to-pocket squeeze-film damping are non negligible dynamical phenomena caused by film thickness variations. Cage weight or bodies unbalance could also be added as an option. Lubrication could be improved by considering thermal effects, starvation or by improving ball-race traction model. Indeed, instead of considering a constant coefficient, Kragelskii or Maxwell-type formulations should be used. They are function of sliding speeds and lubricant characteristics, then they are more accurate. Cage-race interactions are also limited to SJB theory with coaxial bearings. To be able to represent rings misalignment, SJB solutions with misaligned axis should be considered. Cage-race dry contact should also be made possible, especially to improve numerical resolution when such contact is met over iterations.

Besides, this computer code will be used to design new cages and to validate manufacturing defects (clearances, fits, etc.). That is why, cage asymmetries should be modelled with possibility to change pockets geometry independently of one another. And, if most cages are made of cylindrical pockets, other shapes like oblong pockets exist. With such geometry, ball-to-pocket clearance is increased, then collisions are limited. It would be interesting to investigate the influence of pocket geometry on kinematics, contact forces or cage center motions. To improve cage flexible model, stiffness matrix could be imported from a finite element software, rather than being calculated analytically. In this way, different cage architectures could be considered. As well, to avoid bearing failures, surface defects like dents, bumps, spalls or debris could be added. In such a case, dynamics is essential since surface imperfections involve ball speed reduction and risks of ball-to-pocket collisions.

As well, aircraft engines bearings are submitted to important temperatures. Lubricant flow between upstream and downstream side can result in large temperature differences, then in asymmetric forces distribution. That is why, influence of such parameter could be taken into account through a thermo-mechanical model. Finally, in previous BB20 version, rings and housing deformations were considered by coupling BB20 with a finite element approach. In this new version, we did not report coordinate systems modifications to this deformable model. This could be done in order to investigate in dynamics the influence of rings deformations.

Thus, all these prospects show the huge potential offered by BB20 once the dynamic solved.

Appendix A

Review summarising Tables

Main features of each model are summarised in Tables A.1 to A.6. They are organized from the most complete to the most simplified. However, such classification is highly modular depending if we consider that a modelling criteria, as avoiding RCH, considering gyroscopic momentum or 4 contact-points, is more important than another one. As well, certain model are considered as simplified because main feature is not to model ACBB but to consider a specificity like damping, raceway defect or cage flexibility. This does not mean that the model is basic or uninteresting. Note also that if a data is not given in a table, either it is not considered in the model or information was not found.

Bearing types are defined with following notations:

- ACBB : Angular Contact Ball Bearing
- All: Any type of bearing
- ABB : Arched Ball Bearing
- BB : Ball Bearing
- CMGB : Control Moment Gyro Bearing
- CRB : Cylindrical Roller Bearing
- DGBB : Deep Groove Ball Bearing
- NRB: Needle Roller Bearing
- RB : Roller Bearing
- SB : Spindle Bearing
- TRB : Tapered Roller Bearing

Traction models can be defined by a constant friction coefficient ($=$), by a simplified Newtonian model (N), by Kragelsii's [154] (K) with coefficients extracted from literature experiments or by another model.

Film thickness is generally defined by one of the following model:

- AC : Archard and Cowking [8]
- C : Chittenden [42]
- DH : Dowson and Higginson [62]
- HD : Hamrock and Dowson [109]

Reduction factor on film thickness due to thermal effects (ϕ_T) or to starvation (ϕ_S) can be defined by those models:

- ϕ_{TC} : Cheng [41]
- ϕ_{TM} : Murch and Wilson [185]
- ϕ_{TW} : Wilson and Cheu [269]

- ϕ_{TG} : Gupta [101]
- ϕ_{SC} : Chiu [44]
- ϕ_{SHD} : Hamrock and Dowson [115]
- ϕ_{SO} : Olaru [200]

When pitch angle is calculated, following method can be used:

- ED : Equal distribution between races
- HT : Hybrid theory
- min : Contact friction minimisation
- μ : Friction coefficient is set to prevent gyroscopic slippage
- RCA : Rolling Contact Analysis
- RCH : Raceway Control Hypothesis
- $\sum \mathbf{M}$: Ball torque equilibrium

As well, 1 or 2 gyroscopic momentums can be calculated. In quasi-static, they arise from pitch and yaw angle computations.

Note that if a data is not given in a table, either it is not considered in the model or information was not found.

			Inner ring Balls Cage	EHD Film thickness	Traction model	Contact points	Pitch computation	Normal + Friction forces	Normal + Friction forces	Centrifugal forces Gyroscopic Moments Viscous drag forces
Bearing type	Authors - CODE [Ref]	Year	Degrees of freedom	Ball - Races				Ball - Pocket	Cage - Ring	Additional forces
ACBB	Yang [273]	2016	5 6 3		=	2		✓	✓	✓ 2 ✓
ACBB	Yan [272]	2015	5 6 3	✓	=	2		✓	✓	✓ 2 ✓
ACBB	Shi - READ [235]	2020	5 6 ✓	✓	[51]	2		✓	✓	✓ 2 ✓
BB	Li - READ [162]	2019	5 6 ✓	✓	✓	2		✓		✓ 2
ACBB	Cui - READ [52]	2019	5 6 ✓	HD [140]	K	2		✓		✓ 2
ACBB	Wu - READ [270]	2021	5 6 ✓	✓	[14]	2		✓		✓ 2
ACBB	Poplawski - SHABHYB [207]	1996	5 6 3	AC, ϕ_{TC} , ϕ_{SC}	✓	2	μ	✓	✓	✓ 2 ✓
MicroBB	Wen [265]	2020	5 6 3	HD	N	2		✓	✓	✓ 2 ✓
BB, CRB	Crecelius - SHABERTH [46]	1977	5 6 3	AC, ϕ_{TC} , ϕ_{SC}	✓	2	RCH	✓	✓	✓ 2 ✓
ACBB	Shoda [238]	1997	5 6 1		K [94]	2	$\Sigma \mathbf{M}$	✓	✓	✓ 2 ✓
ABB	Leblanc - BB20 [157] [158]	2007, 2008	5 6	HD	=	4	$\Sigma \mathbf{M}$			✓ 2 ✓
ACBB	Aramaki [6]	1988	6 1	HD	[142] [53]	2	$\Sigma \mathbf{M}$	✓	✓	✓ 2 ✓
ACBB	Chen - SACAB [38][39]	2012	1 5		=	2	RCA			✓ 2
ABB	Hamrock [110]	1975	3 6 0		=	3	$\Sigma \mathbf{M}$			✓ 2
BB, RB	Harris [120], Mindel [123]	1972	5 6 1	AC	N	2	$\Sigma \mathbf{M}$	✓	✓	✓ 2 ✓
BB	Servais [232]	2017	5 6		✓	2	$\Sigma \mathbf{M}$			✓ 1
BB	Bozet [27]	2016	2 6		=	2	$\Sigma \mathbf{M}$			✓ 1
ACBB	Legrand - RBL4 [159]	1997	6 6		C, ϕ_{TWS} , ϕ_{SHD}	2	$\Sigma \mathbf{M}$			✓ 1 ✓
ACBB	Tong [244] [245]	2017	5 6	HD	[16] [285]	2	ED			✓ 1 ✓
ACBB	Shi - READ [236]	2015	5 6	✓	[51]	2		✓	✓	✓ 2 ✓

Table A.1 : Quasi-static and quasi-dynamic sophisticated models

			Inner ring Balls Cage	EHD Film thickness	Traction model	Contact points	Pitch computation	Normal + Friction forces	Normal + Friction forces	Centrifugal forces Gyroscopic Moments Viscous drag forces
Bearing type	Authors - CODE [Ref]	Year	Degrees of freedom	Ball - Races			Ball - Pocket	Cage - Ring	Additional forces	
ACBB	Jones [144]	1959	3 6 0		=	2	RCH			✓ 2
SB, ACBB	Brecher [28]	2013	1 2 1		=	2	$\Sigma \mathbf{M}$	✓	✓	✓ 2
BB	Yoshida [278]	2013	5 6 1	HD	[142]	2	RCH	✓	✓	✓ 2 ✓
ACBB	Harris [119]	1971	3 6 0	AC	N	2	μ		✓	✓ 1
ACBB	Gupta [100]	2020	6 6	✓	[105]	2	min			✓ 1
ACBB	Nélias [64][186] [188] [189]	1989-1994	2 4 3	HD, ϕ_{TG}	[143][217]	2		✓	✓	✓ ✓
ABB	Joshi [147]	2015	3 6		=	4	RCH			
BB	Foord [71]	2006	3 6 0	[72]	=	2	min			✓ 1
ACBB, TRB	Houpert [128]	2002	5 6	✓	[133] [134]	2				✓ 1
ACBB	Oktaviana [199]	2018	5 2			2	ED			✓ 1
SB	Cao [34]	2004	5 6			2	RCH			✓ 1
ACBB, DGBB	Gentle [77], Boness [25]	1975	1 6	AC	[78]	2		✓		✓ 1 ✓
ACBB	Liao - Lin [166]	2006	3 4	HD	[149]	2				✓
RB	Boness [23]	1970	3	DH	[61]			✓		✓
RB	Poplawski - COBRA [206]	1972	2 3 1	DH				✓	✓	✓ ✓
RB	Rumbarger [220]	1973	1 3 1	DH, ϕ_{TC}	[179]			✓	✓	✓ 1 ✓
ACBB	Townsend [246]	1973	1 3	DH	[4]	2				✓
ABB	Hamrock, Anderson [111]	1973	1 3 0			3				✓

Table A.2 : Quasi-static and quasi-dynamic developed models

			Inner ring Balls Cage	EHD Film thickness	Traction model	Contact points	Pitch computation	Normal + Friction forces	Normal + Friction forces	Centrifugal forces Gyroscopic Moments Viscous drag forces
Bearing type	Authors - CODE [Ref]	Year	Degrees of freedom	Ball - Races			Ball - Pocket	Cage - Ring	Additional forces	
BB, RB	Mauriello [178]	1973	4 5 4	[62]	[142]	2		✓	✓	✓ 1 ✓
ABB	Ignacio Amasorrain [136]	2002	3 3			4				
BB	de Mul [56]	1989	5 2			2				✓ 1
ACBB	Antoine [5]	2006	1 2		=	2	RCH			✓ 1
ACBB	Liao - Lin [163]	2001	3 4			2				
ACBB	Liao - Lin [164]	2002	3 4			2				✓
ACBB	Liao - Lin [165]	2004	3 4			2				✓
SB, ACBB	Brecher [29]	2014	6		[205]	2	✓	✓	✓	
BB	Dominy [59]	1986	3 1		[72]	2	RCH	✓	✓	✓
ACBB	Lei [160]	2010	3 5		[7]	2	HT			✓ 1
BB	Rabréau [214]	2018	3			2	HT			✓ 1
ACBB	Zhang [283]	2020	6 5		[257]	2	HT			✓ 1
ACBB	Zhang [280]	2020	5 3		[257]	2	HT			✓ 1
ACBB	Noel [195]	2013	5 4		=	2	HT			✓ 1
ACBB	Wang [257]	2014	3 4		✓	2	HT			✓ 1
SB	Jorgensen [146]	1998	5 2			2				✓ 1
BB	Chittenden [42]	1989	0 6	C	[76][142]	2				✓
ACBB	Xu [271]	2013	1 4			2	RCH			✓ 1
ACBB	Wang [256]	2014	3 3			2	RCH			✓ 1
SB	Shin [237]	1992	3 3			2	RCH			✓ 1
SB	Jedrzejewski [141]	2010	1 2		=	2	RCH			✓ 1
ACBB	Zeng [279]	2020	3 2			2	RCH			✓ 1
ACBB	Chunjiang [45]	2015	2 2		✓	2	RCH			✓ 1

Table A.3 : Quasi-static and quasi-dynamic simplified models

			Inner ring Balls Cage	Squeeze-film damping EHD Film thickness Traction model Contact points	Normal + Friction forces Squeeze-film damping	Normal + Friction forces Squeeze-film damping	Centrifugal forces Gyroscopic Moments Viscous drag forces Cage Flexibility
Bearing type	Authors - CODE [Ref]	Year	Degrees of freedom	Ball - Races	Ball - Pocket	Cage - Ring	Additional forces
All	Gupta - BDYN,DREB,ADORE [86]-[103]	1975-2020	6 6 6	HD, ϕ_{TG} , ϕ_{SHD} K [103]	2	✓	✓ 2 ✓
All	Stacke - BEAST [240][239]	2000	6 6 6	✓ [191] [1]	2	✓ ✓	✓ 2 ✓
ACBB, DGBB	Saheta - DBM [221]	2001	6 6 6	[230]	2	✓	✓ 2
ACBB, TRB, DGBB, CRB	Ghaisas - DBM [79]	2003	6 6 6	[30][113] [108]	2	✓	✓ 2 ✓
ACBB, DGBB	Ashtekar - DBM [10][11]	2008-2010	6 6 6	[30] HD =	2	✓	✓ 2
BB	Ashtekar - DBM [9]	2012	6 6 6	[31] HD K [91]	2	✓	✓ 2 ✓ 3D
DGBB	Weinzapfel - DBM [262]	2009	6 6 5	[31] HD K [91]	2	✓	✓ 2 ✓ 2D
DGBB	Pederson - DBM [203][204]	2005	6 6 3	[31] HD [230]	2	✓	✓ 2 ✓ 2D
ABB	Yao [274]	2018	6 6 6		4	✓	✓
ABB	Ma [173][174]	2022	5 6 3	K [282]	3-4	✓	✓ ✓
ACBB	Li [161]	2020	6 6 6	K [95]	2	✓	✓ ✓ 3D
DGBB	Hahn [107]	2005	6 6 6	✓	2	✓ ✓	✓ 3D
CRB	Qian - CyBeSime [211]	2013	6 6 6	✓ [201] [175] K [184]		✓ ✓	✓ 1 ✓ 3D
ACBB	Gao [75]	2021	5 4 4	HD [117]	2	✓ ✓	✓ 1 2D
ACBB	Wen, Meng [264]	2021	5 6 6	✓ [177] [176] [265]	2	✓ ✓	✓ 2
ACBB	Wen, Meng [263]	2021	5 6 3	✓ HD [176] [265]	2	✓ ✓	✓ 2
BB	Niu [193]	2015	6 6 6	N	2	✓	✓ 2
ACBB	Liu [169]	2011	3 6 6	✓ [42][101] K [32]	2	✓ ✓	✓
ACBB	Wang [259]	2017	3 6 1	HD, ϕ_{TG} [48]	2	✓	✓ 2 ✓
BB	Wang [254]	2016	6 6 6	✓ [170] [97]	2	✓	✓ 1
BB	Nogi [196]	2017	1 6 6	✓ HD [137] [217]	2	✓	✓ 1
BB	Niu [194]	2016	6 6 6	[91] N	2	✓	✓ ✓
ACBB	Zhang [281]	2016	5 6 6	✓ K	2	✓	✓ ✓

Table A.4 : Sophisticated dynamical models

			Inner ring Balls Cage	Squeeze-film damping	EHD Film thickness	Traction model	Contact points	Normal + Friction forces Squeeze-film damping	Normal + Friction forces Squeeze-film damping	Centrifugal forces Gyroscopic Moments Viscous drag forces Cage Flexibility
Bearing type	Authors - CODE [Ref]	Year	Degrees of freedom	Ball - Races			Ball - Pocket	Cage - Ring	Additional forces	
ACBB	Liu [172]	2020	3 6 3			K [281]	2	✓	✓	✓ ✓
ACBB	Liu [171]	2020	3 6 3			=	2	✓	✓	✓ ✓
RB	Liu [167]	2021	2 3 1			[86] [79]	2	✓		✓ 2D
BB	Dong [60]	2015	6 6 6	✓	✓	[261]	2	✓	✓	✓
ACBB	Bovet [26]	2016	6 6 6		[191]	[138] [217]	2	✓	✓	✓
ACBB	Fang [68]	2018	5 6 3		HD	K [281]	2	✓	✓	✓ 1 ✓
ACBB	Han [118]	2018	3 6 3		HD	[13] [117]	2	✓	✓	✓ ✓
ACBB	Meeks - SEPDYN [181][180]	1984	2 6			[103]	2	✓ ✓	✓ ✓	✓ ✓
ACBB	Meeks - BABERDYN [182]	1996	2 6			[103]	2	✓ ✓	✓ ✓	✓ 1 ✓
ACBB	Kannel - BASDAP II [148]	1978	3		[18]	✓	2	✓ ✓	✓ ✓	✓ 1
Gyro-bearing	Walters - BASDAP [253]	1971	4 6		✓	✓	2	✓	✓	✓ 1
CMGB	Boesiger - PADRE [22]	1991	2 3			[143]	2	✓	✓	✓ ✓
RB	Houpert - CAGEDYN [129][130][131]	2010	2 3		[125]	[127]	2	✓	✓	✓ ✓ 2D
ACBB, SRB, DGBB	Prenger [210]	2003	6 6 6		[30] [113]	K	2	✓	✓	✓ 2
BB	Niu [33]	2014	6 6 0			N	2			✓ 2
BB	Ye [276][277]	2015	5 6 4			[261]	2	✓	✓	✓ ✓
BB, RB	Shao [37] [233]	2014	2 3 1		HD	K [86]	2	✓		✓
ACBB	Wang [258][260]	2015	3 6 1		HD	[48]	2	✓		✓ ✓
ACBB	Han, Chu [117]	2015	5 5 1		HD	N	2	✓		✓ 1 ✓
ACBB	Gao [74]	2020	5 4 1		HD	[50]	2	✓		✓ 1 ✓
NRB, TRB	Sakaguchi [223][224]	2006,2009	6 6		[201] [175]	K [184]		✓		✓ 1 3D
NRB	Sakaguchi [222]	2006	6 6		[31] C, ϕ_{TG}	K [184]		✓		✓ 1 2D
TRB, NRB	Sekiya [231]	2011	6 6		[201] [175]	K [184]		✓	✓	✓ 1 ✓

Table A.5 : Developed dynamical models

			Inner ring Balls Cage	Squeeze-film damping EHD Film thickness Traction model Contact points	Normal + Friction forces Squeeze-film damping Normal + Friction forces Squeeze-film damping	Centrifugal forces Gyroscopic Moments Viscous drag forces Cage Flexibility
Bearing type	Authors - CODE [Ref]	Year	Degrees of freedom	Ball - Races	Ball - Pocket Cage - Ring	Additional forces
BB	Guessasma [83]	2018	6 6	✓ [109] = 2	✓	✓ 1
ACBB	Qin [212]	2020	5 3 3	= 2	✓	✓ 1
ACBB	Qin [213]	2019	3 3 0	= 2	✓	✓ 1
ACBB	Jain, Hunt [139]	2011	3 3 1	HD [47] [49] 2	✓	✓ 1 ✓
BB, RB	Tu [247]	2012	2 3 1	K [86] 2	✓	✓
BB	Sarangi [228]	2005	2 1 0	✓ ✓ 2		✓
ACBB	Bizarre [20]	2018	5 6	✓ ✓ N 2		✓ 1
ACBB	Walford, Stone [252]	1983	2 2	✓ AC 2		
ACBB	Hagiu [106]	1996	3 2	✓ HD, ϕ_{TM} , ϕ_{SO} 2		
DGBB	Nonato [198]	2014	2	✓ ✓ 2		

Table A.6 : Simplified dynamical models

Appendix B

R2 results under pure axial load

	Test	A	B	C	D
Friction forces	F_{Xi1}^j (N)	-42.5	-3.37	-0.0002	0
	F_{Xo2}^j (N)	-149.5	-3.46	-8.845	0
	F_{Zi1}^j (N)	7.338	1.577	-0.815	-1.85
	F_{Zo2}^j (N)	0.595	-1.699	0.561	-535
	M_{Ri1}^j (N.m)	0.070	0.014	0.0078	0.0176
	M_{Ro2}^j (N.m)	0.014	-0.013	0.0056	4.83
	M_{Si1}^j (N.m)	0.052	0.051	-13E-9	-49E-9
	M_{So2}^j (N.m)	-0.028	0.051	0.0035	-0.0072
	M_{Zi1}^j (N.m)	-0.404	-0.032	-2.2E-6	0
	M_{Zo2}^j (N.m)	-1.410	-0.033	-0.084	0
Ball kinematics	V_{Xi1}^j (m/s)	-1.160	-0.00088	-0.021	0
	V_{Xo2}^j (m/s)	-1.160	-0.00088	-0.021	0
	V_{Zi1}^j (m/s)	-0.358	0.0063	72.5	3.61
	V_{Zo2}^j (m/s)	-0.605	-0.00158	-0.043	-0.031
	ω_{Si1}^j (rad/s)	-3396	-57.5	-2598	-5749
	ω_{So2}^j (rad/s)	176.2	-44.2	-62.4	3.65
	ω_{Ri1}^j (rad/s)	7677	792	3854	6838
	ω_{Ro2}^j (rad/s)	-6640	-638	-2825	-7108
Ball motion forces	M_{GY}^j (N.m)	0.106	0.000	0.001	0.000
	M_{GZ}^j (N.m)	1.813	0.032	0.083	0.000
	F_c^j (N)	1494	14	275	1729
	F_{dr}^j (N)	-7.933	-0.074	-1.460	-18.891
Bearing parameters	ω_m^j (rpm)	8022	777	3442	8628
	ω_R^j (rpm)	-71100	-6752	-30414	-76507
	β^j (°)	16.33	32.40	4.01	0.00
	β'^j (°)	0.98	0.01	0.04	0.00
	α_{i1}^j (°)	38.3	32.6	36.7	40.1
	α_{o2} (°)	19.9	32.3	3.3	0.0
	δ_{i1}^j (μm)	10.212	10.904	0.472	0.175
	δ_{o2}^j (μm)	13.805	9.125	3.146	16.936

Table B.1 : Results obtained for bearing A under pure axial load

Appendix C

Rheological parameters

1 Dynamic viscosity μ

Normal loads, friction forces and film thickness formulas presented are functions of lubricant dynamic viscosity μ . Depending on lubrication regime, viscosity can be constant or pressure and temperature dependant. In BB20, we consider W.L.F. model modified by Yasutomi [275] because it is suitable for high pressures [250]. It is based on temperature and pressure dependency on free volumes. Dynamic viscosity is expressed by relation (C.1) where $A_1, A_2, B_1, B_2, C_1, C_2$ are constants determined by curve fitting different lubricants. $F(P)$ is thermal expansion coefficient, $T_g(P)$ is glass transition temperature, T_{g0} is reference glass transition temperature and μ_g is viscosity at glass transition.

$$\log \mu(T, P) = \log \mu_g + \frac{C_1(T - T_g(P))F(P)}{C_2 + (T - T_g(P))F(P)}, \text{ with } \begin{cases} F(P) = 1 - B_1 \ln(1 + B_2 P) \\ T_g(P) = T_{g0} + A_1 \ln(1 + A_2 P) \end{cases} \quad (\text{C.1})$$

Consequently, to model lubricant in all ball-to-pocket interactions, viscosity is calculated at cage temperature T_c and at ambient pressure P_a such that $F(P_a) = 0$ and $T_g(P_a) = T_{g0}$. Note that under EHD regime, viscosity is also considered at ambient pressure because contact pressure is already taken into account in film thickness through load parameter W' . For cage-race interaction, viscosity is calculated at a temperature equal to cage-race average one, and at ambient pressure P_a because pressure is low. For ball-race interactions, viscosity is calculated at race temperature T_i or T_o , and at ambient pressure P_a .

2 Reciprocal asymptotic isoviscous pressure α^*

Reciprocal asymptotic isoviscous pressure α^* is necessary for Hamrock Dowson film thickness computation. Blok [21] expressed this parameter by relation (C.2). Integration of equation (C.1) in (C.2) gives relation (C.3) where A_{00}, A_{01}, A_{10} and A_{11} are lubricant parameters given by Nelias [187] for Mobil Jet-oil II.

$$\frac{1}{\alpha^*} = \mu(T, 0) \int_0^\infty \frac{dp}{\mu(T, p)} \quad (\text{C.2})$$

$$\alpha^* = 10^{-9} \left(\frac{A_{00}}{T} + \frac{A_{01}}{T^2} + \frac{A_{10}}{T - T_{c0}} + \frac{A_{11}}{(T - T_{c0})^2} \right) \quad (\text{C.3})$$

3 Friction coefficients

At ball-race contacts, a constant friction coefficient, set by user, is considered. At cage-race and ball-to-pocket interactions, constant coefficients equal to dynamic viscosity $\mu(T, P)$ are also considered. However, for continuity reasons, when shear force F_{sh}^j is greater than 10% of normal load W_f^j , we set F_{sh}^j equal to $0.1W_f^j$. In other words, at high pressures, shear force is replaced by a Coulomb's law with a friction coefficient of 0.1.

4 Thermal reduction factor on film thickness

Under high-speed and important sliding, energy loss due to shearing and temperature increasing occurs at contact. Since oil viscosity decreases rapidly with temperature, film thickness is reduced too. That is why, a reduction factor on film thickness ϕ_T is considered at ball-race contact. It is expressed by Gupta's [101] relation in (C.4), where L and S are dimensionless parameters that characterize, respectively, thermal load and sliding. Normal load effects are given by P_m , the maximum Hertzian pressure.

$$\phi_T = \frac{1 - 13.2 \left(\frac{P_m}{E} \right) L^{0.42}}{1 + 0.213 (1 + 2.23 S^{0.83}) L^{0.64}} \begin{cases} L = -\frac{\partial \mu}{\partial T} \frac{(U_1 + U_2)^2}{4K_f} \\ S = 2 \frac{U_1 - U_2}{U_1 + U_2} \end{cases} \quad (\text{C.4})$$

Bibliography

- [1] S. Aihara and T. Sawamoto. An experimental study of viscous rolling friction with reference to surface roughness at elasto-hydrodynamic contacts. In *Proc. 11th Leeds-Lyon Symposium, Mixed Lubrication and Lubricated Wear*, 1984.
- [2] C. W. Allen, D. P. Townsend, and E. V. Zaretsky. Elastohydrodynamic Lubrication of a Spinning Ball in a Nonconforming Groove. *Journal of Lubrication Technology*, 92(1):89–94, 1970.
- [3] C. W. Allen, D. P. Townsend, and E. V. Zaretsky. *Comparison of Conventional and Microasperity Elastohydrodynamic Lubrication of a Ball Spinning in a Nonconforming Groove*, volume Technical Report No. NASA-TP-2275. 1972.
- [4] C. W. Allen, D. P. Townsend, and E. V. Zaretsky. New generalized rheological model for lubrication of a ball spinning in a nonconforming groove. Technical report, National Aeronautics and Space Administration, 1973.
- [5] J-F. Antoine, G. Abba, and A. Molinari. A New Proposal for Explicit Angle Calculation in Angular Contact Ball Bearing. *Journal of Mechanical Design*, 128(2):468–478, 2005.
- [6] H. Aramaki, Y. Shoda, Y. Morishita, and T. Sawamoto. The Performance of Ball Bearings With Silicon Nitride Ceramic Balls in High Speed Spindles for Machine Tools. *Journal of Tribology*, 110(4):693–698, 1988.
- [7] J. F. Archard. Paper R2: Experimental Studies of Elastohydrodynamic Lubrication. *Proceedings of the Institution of Mechanical Engineers, Conference Proceedings*, 180(2):17–30, 1965.
- [8] J. F. Archard and E. W. Cowking. Paper 3: Elastohydrodynamic Lubrication at Point Contacts. *Proceedings of the Institution of Mechanical Engineers, Conference Proceedings*, 180(2):47–56, 1965.
- [9] A. Ashtekar and F. Sadeghi. A New Approach for Including Cage Flexibility in Dynamic Bearing Models by Using Combined Explicit Finite and Discrete Element Methods. *Journal of Tribology*, 134(4), 2012. 041502.
- [10] A. Ashtekar, F. Sadeghi, and L-E. Stacke. A New Approach to Modeling Surface Defects in Bearing Dynamics Simulations. *Journal of Tribology*, 130(4), 2008. 041103.

- [11] A. Ashtekar, F. Sadeghi, and L-E Stacke. Surface defects effects on bearing dynamics. *Proceedings of the Institution of Mechanical Engineers, Part J: Journal of Engineering Tribology*, 224(1):25–35, 2010.
- [12] S. Bair. An Experimental Verification of the Significance of the Reciprocal Asymptotic Isoviscous Pressure for EHD Lubricants. *Tribology Transactions - TRIBOL TRANS*, 36:153–160, 1993.
- [13] S. Bair, P. Vergne, and M. Querry. A unified shear-thinning treatment of both film thickness and traction in EHD. *Tribology Letters*, 18(2):145–152, 2005.
- [14] S. Bair and W. O. Winer. Rheological response of lubricants in EHD contacts. In *5th Leeds-Lyon Symposium on Tribology*, pages 162–169, 1978.
- [15] S. Bair and W. O. Winer. Shear Strength Measurements of Lubricants at High Pressure. *Journal of Lubrication Technology*, 101(3):251–257, 1979.
- [16] M. R. D. Bălan, V. C. Stamate, L. Houpert, and D.N. Olaru. The influence of the lubricant viscosity on the rolling friction torque. *Tribology International*, 72:1–12, 2014.
- [17] C. Barus. Isothermals, isopiestic and isometrics relative to viscosity. *American Journal of Science*, s3-45(266):87–96, 1893.
- [18] J. C. Bell and J. W. Kannel. Interpretations of the Thickness of Lubricant Films in Rolling Contact. 2. Influence of Possible Rheological Factors. *Journal of Lubrication Technology*, 93(4):485–497, 1971.
- [19] T. Beyer. *Semi-analytical modeling of damage under contact loading : Application to heterogeneous materials*. PhD thesis, INSA Lyon, 2019.
- [20] L. Bizarre, F. Nonato, and K.L. Cavalca. Formulation of five degrees of freedom ball bearing model accounting for the nonlinear stiffness and damping of elastohydrodynamic point contacts. *Mechanism and Machine Theory*, 124:179–196, 2018.
- [21] H. Blok. Inverse problem in hydrodynamic lubrication and design directives for lubricated flexible surfaces. In *Symp. Lubric. & Wear*, pages 1–151, 1963.
- [22] E. A. Boesiger, A. D. Donley, and S. Loewenthal. An Analytical and Experimental Investigation of Ball Bearing Retainer Instabilities. *Journal of Tribology*, 114(3):530–538, 1992.
- [23] R. J. Boness. The Effect of Oil Supply on Cage and Roller Motion in a Lubricated Roller Bearing. *Journal of Lubrication Technology*, 92(1):39–51, 1970.
- [24] R. J. Boness. Minimum Load Requirements for the Prevention of Skidding in High Speed Thrust Loaded Ball Bearings. *Journal of Lubrication Technology*, 103(1):35–39, 1981.
- [25] R.J. Boness and C.R. Gentle. Ball motion in thrust loaded ball bearings. *Wear*, 35(1):131–148, 1975.

-
- [26] C. Bovet and L. Zamponi. An approach for predicting the internal behaviour of ball bearings under high moment load. *Mechanism and Machine Theory*, 101:1–22, 2016.
- [27] J-L. Bozet and C. Servais. Influence of the Balls Kinematics of Axially Loaded Ball Bearings on Coulombic Frictional Dissipations. *Journal of Tribology*, 139(1), 2016. 011502.
- [28] C. Brecher, S. Bäumlér, and J. Rossaint. Calculation of Kinematics and Friction of a Spindle Bearing Using a Local EHL Friction Model. *Tribology Transactions*, 56(2):245–254, 2013.
- [29] C. Brecher, A. Hassis, and J. Rossaint. Cage Friction in High-Speed Spindle Bearings. *Tribology Transactions*, 57(1):77–85, 2014.
- [30] D. E. Brewe and B. J. Hamrock. Analysis of Starvation Effects on Hydrodynamic Lubrication in Nonconforming Contacts. *Journal of Lubrication Technology*, 104(3):410–417, 1982.
- [31] D. E. Brewe, B. J. Hamrock, and C. M. Taylor. Effect of Geometry on Hydrodynamic Film Thickness. *Journal of Lubrication Technology*, 101(2):231–237, 1979.
- [32] A. Cameron. Basic Lubrication Theory. *Ellis Horwood Ltd.*, 1981.
- [33] H. Cao, L. Niu, Z. He, and L. Yamin. Dynamic modeling and vibration response simulation for high speed rolling ball bearings with localized surface defects in raceways. *Journal of Manufacturing Science and Engineering*, 136, 2014.
- [34] Y. Cao and Y. Altintas. A General Method for the Modeling of Spindle-Bearing Systems. *Journal of Mechanical Design*, 126(6):1089–1104, 2004.
- [35] D. Changan, Z. Fuzhang, Z. Jun, and Z. Lei. Raceway control assumption and the determination of rolling element attitude angle. *Chinese Journal of Mechanical Engineering*, 37(2):58–61, 2001.
- [36] J. J. Chapman. Angular Contact Ball Bearing Dynamics, an Experimental and Theoretical Investigation. In D. Dowson, C.M. Taylor, T.H.C. Childs, and G. Dalmaz, editors, *Lubricants and Lubrication*, volume 30 of *Tribology Series*, pages 435–443. Elsevier, 1995.
- [37] J. Chen, J. Liu, Y. Shao, and C. Luo. Vibration Modeling of Lubricated Rolling Element Bearing Considering Skidding in Loaded Zone. *Journal of Failure Analysis and Prevention*, 14(6):809–817, 2014.
- [38] W. Chen, Z. Ma, L. Gao, X. Li, and J. Pan. Quasi-static analysis of thrust-loaded angular contact ball bearings part I: theoretical formulation. *Chinese Journal of Mechanical Engineering*, 25(1):71–80, 2012.
- [39] W. Chen, Z. Ma, L. Gao, X. Li, and J. Pan. Quasi-static analysis of thrust-loaded angular contact ball bearings. Part II: Results and discussion. *Chinese Journal of Mechanical Engineering*, 25(1):81–87, 2012.

- [40] H. S. Cheng. A Refined Solution to the Thermal-Elastohydrodynamic Lubrication of Rolling and Sliding Cylinders. *ASLE Transactions*, 8(4):397–410, 1965.
- [41] H. S. Cheng. Calculation of Elastohydrodynamic Film Thickness in High Speed Rolling and Sliding Contacts. Technical report, Mechanical Technology Inc Latham NY, 1967.
- [42] R. Chittenden, D. Dowson, J. Dunn, and C. Taylor. A Theoretical Analysis of the Isothermal Elastohydrodynamic Lubrication of Concentrated Contacts. I. Direction of Lubricant Entrainment Coincident with the Major Axis of the Hertzian Contact Ellipse. *Proceedings of The Royal Society A: Mathematical, Physical and Engineering Sciences*, 397:245–269, 1985.
- [43] R.J. Chittenden, D. Dowson, and C.M. Taylor. Power loss prediction in ball bearings. In D. Dowson, Cm. Taylor, M. Godet, and D. Berthe, editors, *Tribological Design of Machine Elements*, volume 14 of *Tribology Series*, pages 277–286. Elsevier, 1989.
- [44] Y. P. Chiu. An Analysis and Prediction of Lubricant Film Starvation in Rolling Contact Systems. *ASLE Transactions*, 17(1):22–35, 1974.
- [45] Z. Chunjiang, Y. Xiaokai, H. Qingxue, G. Shidong, and G. Xin. Analysis on the load characteristics and coefficient of friction of angular contact ball bearing at high speed. *Tribology International*, 87:50–56, 2015.
- [46] W. J. Crecelius and J. Pirvics. Computer program operation manual on SHABERTH. A computer program for the analysis of the steady state and transient thermal performance of shaft-bearing systems. Technical report, SKF Industries Inc King of Prussia PA Research Lab, 1976.
- [47] A. W. Crook. The lubrication of rollers II. Film thickness with relation to viscosity and speed. *Philosophical Transactions of the Royal Society of London. Series A, Mathematical and Physical Sciences*, 254(1040):223–236, 1961.
- [48] A. W. Crook. The lubrication of rollers III. A theoretical discussion of friction and the temperatures in the oil film. *Philosophical Transactions of the Royal Society of London. Series A, Mathematical and Physical Sciences*, 254(1040):237–258, 1961.
- [49] A. W. Crook. The lubrication of rollers IV. Measurements of friction and effective viscosity. *Philosophical Transactions of the Royal Society of London. Series A, Mathematical and Physical Sciences*, 255(1056):281–312, 1963.
- [50] M. M. Cross. Rheology of non-Newtonian fluids: A new flow equation for pseudo-plastic systems. *Journal of Colloid Science*, 20(5):417–437, 1965.
- [51] L. Cui. *Research on dynamic performances of high-speed rolling bearing and rotor system of aeroengine*. PhD thesis, Harbin Institute of Technology, Harbin, China, 2008.

-
- [52] L. Cui and H. Zhang. Limiting speeds of high-speed ball bearings considering prevention of skidding and overheating conditions. *Advances in Mechanical Engineering*, 11(3):1687814019835114, 2019.
- [53] G. Dalmaz. Film thickness and traction measurements in small elastohydrodynamic elliptical contacts. In *Proceedings of the 5th Leeds-Lyon Symposium on Tribology*, pages 71–80, 1978.
- [54] D. W. Dareing and K. L. Johnson. Fluid Film Damping of Rolling Contact Vibrations. *Journal of Mechanical Engineering Science*, 17(4):214–218, 1975.
- [55] A. A. Dattawadkar. Analysis of wind turbine pitch control bearings—discrete element method and finite element analysis. Master’s thesis, Purdue University, West Lafayette, IN, USA, 2011.
- [56] J. M. de Mul, J. M. Vree, and D. A. Maas. Equilibrium and Associated Load Distribution in Ball and Roller Bearings Loaded in Five Degrees of Freedom While Neglecting Friction—Part II: Application to Roller Bearings and Experimental Verification. *Journal of Tribology*, 111(1):149–155, 1989.
- [57] P. Dietl. *Damping and Stiffness Characteristics of Rolling Element Bearings - Theory and Experiment*. PhD thesis, TU Wien, 1997.
- [58] P. Dietl, J. Wensing, and G. C. van Nijen. Rolling bearing damping for dynamic analysis of multi-body systems—experimental and theoretical results. *Proceedings of the Institution of Mechanical Engineers, Part K: Journal of Multi-body Dynamics*, 214(1):33–43, 2000.
- [59] J. Dominy. The Nature of Slip in High-Speed Axially Loaded Ball Bearings. *Proceedings of the Institution of Mechanical Engineers, Part C: Journal of Mechanical Engineering Science*, 200(5):359–365, 1986.
- [60] G. Dong, Y. Liu, M. Jing, F. Wang, and H. Liu. Effect of elastohydrodynamic lubrication on the dynamic analysis of ball bearing. *Proceedings of the Institution of Mechanical Engineers, Part K: Journal of Multi-body Dynamics*, 230(2):134–146, 2016.
- [61] D. Dowson and G. R. Higginson. Theory of roller bearing lubrication and deformation. In *Proc. Lubrication and Wear Convention, Instn. Mech. Engrs., London, Paper*, volume 19, pages 216–227, 1963.
- [62] D. Dowson and G. R. Higginson. *Elasto-Hydrodynamic Lubrication—The Fundamentals of Roller and Gear Lubrication*. Pergamon Press, Oxford, Great Britain., 1966.
- [63] C. Dumartineix. *Modélisation et étude de la dynamique complexe d’un système bi-rotor aubagé couplé*. PhD thesis, Ecole Centrale Lyon, 2019.
- [64] G. Dussèrre-Telmon and D. Nélias. Roulements à billes lubrifiés: contrôle partagé de la bille entre la bague intérieure et la bague extérieure: Roulements. I. *RFM Revue française de mécanique*, (2):155–165, 1994.
-

- [65] E. P. E. P. Kingsbury. Torque variations in instrument ball bearings. *ASLE Transactions*, 8(4):435–441, 1965.
- [66] A. A. Elsharkawy and B. J. Hamrock. Subsurface Stresses in Micro-EHL Line Contacts. *Journal of Tribology*, 113(3):645–655, 1991.
- [67] A. M. Ertel et al. Hydrodynamic Lubrication based on New Principles. *Akad. Nauk SSSR Prikladnaya Matematika i Mekhanika*, 3(2):41–52, 1939.
- [68] B. Fang, J. Zhang, S. Wan, and J. Hong. Determination of Optimum Preload Considering the Skidding and Thermal Characteristic of High-Speed Angular Contact Ball Bearing. *Journal of Mechanical Design*, 140(5), 2018. 053301.
- [69] E. Fehlberg. *Classical fifth-, sixth-, seventh-, and eighth-order Runge-Kutta formulas with stepsize control*. National Aeronautics and Space Administration, 1968. Technical report No. NASA-TR-287.
- [70] E. Fehlberg. *Low-order classical Runge-Kutta formulas with stepsize control and their application to some heat transfer problems*. National aeronautics and space administration, 1969. Technical report No. NASA-TR-315.
- [71] C. A. Foord. High-speed ball bearing analysis. *Proceedings of the Institution of Mechanical Engineers, Part G: Journal of Aerospace Engineering*, 220(5):537–544, 2006.
- [72] R. A. J. Ford and C. A. Foord. The Effects of Elastohydrodynamic Traction Behavior on Cage Slip in Roller Bearings. *Journal of Lubrication Technology*, 96(3):370–375, 1974.
- [73] J. Frene, D. Nicolas, B. Degueurce, D. Berthe, and G. Godet. In *Hydrodynamic Lubrication*, volume 33 of *Tribology Series*, page iv. Elsevier, 1990.
- [74] S. Gao, S. Chatterton, L. Naldi, and P. Pennacchi. Ball bearing skidding and over-skidding in large-scale angular contact ball bearings: Nonlinear dynamic model with thermal effects and experimental results. *Mechanical Systems and Signal Processing*, 147:107120, 2021.
- [75] S. Gao, Q. Han, N. Zhou, P. Pennacchi, S. Chatterton, T. Qing, J. Zhang, and F. Chu. Experimental and theoretical approaches for determining cage motion dynamic characteristics of angular contact ball bearings considering whirling and overall skidding behaviors. *Mechanical Systems and Signal Processing*, 168:108704, 2022.
- [76] B. Gecim and W. O. Winer. Lubricant Limiting Shear Stress Effect on EHD Film Thickness. *Journal of Lubrication Technology*, 102(2):213–220, 1980.
- [77] C. R. Gentle and R. J. Boness. Prediction of Ball Motion in High-Speed Thrust-Loaded Ball Bearings. *Journal of Lubrication Technology*, 98(3):463–469, 1976.
- [78] C.R. Gentle and A. Cameron. Some granular aspects of E.H.L. traction. *Wear*, 27(1):71–81, 1974.

-
- [79] N. Ghaisas. Dynamics of Cylindrical and Tapered Roller Bearings Using the Discrete Element Method. Master's thesis, Purdue University, West Lafayette, IN, USA, 2003.
- [80] A. Gomez and Safran. LEAP-1A. <https://medialibrary.safran-group.com/Photos/media/178745>, 2017.
- [81] J. C. Gomez-Mancilla and V. Nosov. Journal bearings with misaligned axes. *Proc. Iscorma 1*, 2001.
- [82] A.N. Grubin. Fundamentals of the Hydrodynamic Theory of Lubrication of Heavily Loaded Cylindrical Surfaces. *Investigation of the Contact Machine Components*, pages 115–166, 1949.
- [83] M. Guessasma and C. Machado. Three-Dimensional DEM Modelling of Ball Bearing with Lubrication Regime Prediction. *Lubricants*, 6(2):46, 2018.
- [84] P. K. Gupta. Analysis of Cage Motion. Technical report, Mechanical Technology Inc Latham NY, 1975.
- [85] P. K. Gupta. Generalized dynamic simulation of skid in ball bearings. *Journal of Aircraft*, 12(4):260–265, 1975.
- [86] P. K. Gupta. Transient Ball Motion and Skid in Ball Bearings. *Journal of Lubrication Technology*, 97(2):261–269, 1975.
- [87] P. K. Gupta. Dynamics of Rolling-Element Bearings—Part I: Cylindrical Roller Bearing Analysis. *Journal of Lubrication Technology*, 101(3):293–302, 1979.
- [88] P. K. Gupta. Dynamics of Rolling-Element Bearings—Part II: Cylindrical Roller Bearing Results. *Journal of Lubrication Technology*, 101(3):305–311, 1979.
- [89] P. K. Gupta. Dynamics of Rolling-Element Bearings—Part III: Ball Bearing Analysis. *Journal of Lubrication Technology*, 101(3):312–318, 1979.
- [90] P. K. Gupta. Dynamics of Rolling-Element Bearings—Part IV: Ball Bearing Results. *Journal of Lubrication Technology*, 101(3):319–326, 1979.
- [91] P. K. Gupta. *Advanced Dynamics Of Rolling Elements*, volume 39. Springer, 1984.
- [92] P. K. Gupta. *Elastohydrodynamic Lubrication*, pages 76–99. Springer New York, New York, NY, 1984.
- [93] P. K. Gupta. Frictional Instabilities in Ball Bearings. *Tribology Transactions*, 31(2):258–268, 1988.
- [94] P. K. Gupta. Traction Modeling of Military Lubricants. Technical report, Pradeep K Gupta Inc, Clifton Park, NY, 1989.
- [95] P. K. Gupta. Cage unbalance and wear in ball bearings. *Wear*, 147(1):93–104, 1991.

- [96] P. K. Gupta. Dynamic loads and cage wear in high-speed rolling bearings. *Wear*, 147(1):119–134, 1991.
- [97] P. K. Gupta. Modeling of Instabilities Induced by Cage Clearances in Ball Bearings. *Tribology Transactions*, 34(1):93–99, 1991.
- [98] P. K. Gupta. On a kinematic hypothesis for angular contact ball bearings. In *ASTM Symposium on Rolling Element Bearings*, pages 22–24, 2002.
- [99] P. K. Gupta. Current Status of and Future Innovations in Rolling Bearing Modeling. *Tribology Transactions*, 54:394–403, 2011.
- [100] P. K. Gupta. Minimum Energy Hypothesis in Quasi-Static Equilibrium Solutions for Angular Contact Ball Bearings. *Tribology Transactions*, 63(6):1051–1066, 2020.
- [101] P. K. Gupta, H. Cheng, D. Zhu, N. Forster, and J. Schrand. Viscoelastic effects in MIL-L-7808-Type lubricant, Part I: Analytical formulation. *Tribology Transactions*, 35:269–274, 1992.
- [102] P. K. Gupta, J. F. Dill, J. W. Artuso, and N. H. Forster. Ball Bearing Response to Cage Unbalance. *Journal of Tribology*, 108(3):462–466, 1986.
- [103] P. K. Gupta, L. Flamand, D. Berthe, and M. Godet. On the Traction Behavior of Several Lubricants. *Journal of Lubrication Technology*, 103(1):55–64, 1981.
- [104] P. K. Gupta and H. G. Gibson. Real-Time Dynamics Modeling of Cryogenic Ball Bearings With Thermal Coupling. *Journal of Tribology*, 143(3), 2020. 031201.
- [105] P. K. Gupta, J. I. Taketa, and C. M. Price. Thermal interactions in rolling bearings. *Proceedings of the Institution of Mechanical Engineers, Part J: Journal of Engineering Tribology*, 234(8):1233–1253, 2020.
- [106] G.D. Hagi and M.D. Gafitanu. Dynamic characteristics of high speed angular contact ball bearings. *Wear*, 211(1):22–29, 1997.
- [107] K. Hahn. *Dynamik-Simulation von Wälzlagerkäfigen*. PhD thesis, Technical University of Kaiserslautern, Germany, 2005.
- [108] J. Halling. Microslip between a Rolling Element and its Track Arising from Geometric Conformity and Applied Surface Traction. *Journal of Mechanical Engineering Science*, 6(1):64–73, 1964.
- [109] B. Hamrock and D. Dowson. Minimum film thickness in elliptical contacts for different regimes of fluid-film lubrication. *Proceedings of the Society of Photo-Optical Instrumentation Engineers*, No. E-9687. 1978.
- [110] B. J. Hamrock. Ball Motion and Sliding Friction in an Arched Outer Race Ball Bearing. *Journal of Lubrication Technology*, 97(2):202–210, 1975.
- [111] B. J. Hamrock and W. J. Anderson. Analysis of an Arched Outer-Race Ball Bearing Considering Centrifugal Forces. *Journal of Lubrication Technology*, 95(3):265–271, 1973.

-
- [112] B. J. Hamrock and D. Dowson. Isothermal Elastohydrodynamic Lubrication of Point Contacts: Part I—Theoretical Formulation. *Journal of Lubrication Technology*, 98:223–228, 1975.
- [113] B. J. Hamrock and D. Dowson. Isothermal Elastohydrodynamic Lubrication of Point Contacts: Part III—Fully Flooded Results. *Journal of Lubrication Technology*, 99(2):264–275, 1976.
- [114] B. J. Hamrock and D. Dowson. Isothermal Elastohydrodynamic Lubrication of Point Contacts: Part II—Ellipticity Parameter Results. *Journal of Lubrication Technology*, 98:375–381, 1976.
- [115] B. J. Hamrock and D. Dowson. Isothermal Elastohydrodynamic Lubrication of Point Contacts: Part IV—Starvation Results. *Journal of Lubrication Technology*, 99:15–23, 1976.
- [116] B. J. Hamrock, D. Dowson, and T. E. Tallian. Ball Bearing Lubrication (The Elastohydrodynamics of Elliptical Contacts). *Journal of Lubrication Technology*, 104(2):279–281, 1982.
- [117] Q. Han and F. Chu. Nonlinear dynamic model for skidding behavior of angular contact ball bearings. *Journal of Sound and Vibration*, 354:219–235, 2015.
- [118] Q. Han, B. Wen, M. Wang, and S. Deng. Investigation of cage motions affected by its unbalance in a ball bearing. *Proceedings of the Institution of Mechanical Engineers, Part K: Journal of Multi-body Dynamics*, 232(2):169–182, 2018.
- [119] T. A. Harris. An Analytical Method to Predict Skidding in Thrust-Loaded, Angular-Contact Ball Bearings. *Journal of Lubrication Technology*, 93(1):17–23, 1971.
- [120] T. A. Harris. Ball Motion in Thrust-Loaded, Angular Contact Bearings With Coulomb Friction. *Journal of Lubrication Technology*, 93(1):32–38, 1971.
- [121] T.A. Harris and M.N. Kotzalas. *Advanced Concepts of Bearing Technology: Rolling Bearing Analysis, Fifth Edition (5th ed.)*. CRC press, 2006.
- [122] T.A. Harris and M.N. Kotzalas. *Essential Concepts of Bearing Technology (5th ed.)*. Rolling Bearing Analysis, Fifth Edition. CRC Press, 2006.
- [123] T.A Harris and M.H. Mindel. Rolling element bearing dynamics. *Wear*, 23(3):311–337, 1973.
- [124] F. Hirano. Motion of a Ball in Angular-Contact Ball Bearing. *ASLE Transactions*, 8(4):425–434, 1965.
- [125] L. Houpert. The Film Thickness in Piezoviscous-Rigid Regime; Film Thickness Lubrication Regimes Transition Criteria. *Journal of Tribology*, 106(3):375–381, 1984.
- [126] L. Houpert. Fast Numerical Calculations of EHD Sliding Traction Forces; Application to Rolling Bearings. *Journal of Tribology*, 107(2):234–239, 1985.
-

- [127] L. Houpert. New Results of Traction Force Calculations in Elastohydrodynamic Contacts. *Journal of Tribology*, 107(2):241–245, 1985.
- [128] L. Houpert. Ball Bearing and Tapered Roller Bearing Torque: Analytical, Numerical and Experimental Results. *Tribology Transactions*, 45(3):345–353, 2002.
- [129] L. Houpert. CAGEDYN: A Contribution to Roller Bearing Dynamic Calculations Part I: Basic Tribology Concepts. *Tribology Transactions*, 53(1):1–9, 2009.
- [130] L. Houpert. CAGEDYN: A Contribution to Roller Bearing Dynamic Calculations Part II: Description of the Numerical Tool and Its Outputs. *Tribology Transactions*, 53(1):10–21, 2009.
- [131] L. Houpert. CAGEDYN: A Contribution to Roller Bearing Dynamic Calculations. Part III: Experimental Validation. *Tribology Transactions*, 53(6):848–859, 2010.
- [132] L. Houpert, L. Flamand, and D. Berthe. Rheological and Thermal Effects in Lubricated E.H.D. Contacts. *Journal of Lubrication Technology*, 103(4):526–532, 1981.
- [133] L. Houpert, L. Flamand, and D. Berthe. Rheological and Thermal Effects in Lubricated E.H.D. Contacts. *Journal of Lubrication Technology*, 103(4):526–532, 1981.
- [134] L. Houpert and P. Leenders. A study of mixed lubrication in modern Deep Groove Ball Bearings. In *11th Leeds-Lyon Symp.*, Leeds, 1984.
- [135] C. H. Hsu and R. T. Lee. An Efficient Algorithm for Thermal Elastohydrodynamic Lubrication Under Rolling/Sliding Line Contacts. *Journal of Tribology*, 116(4):762–769, 1994.
- [136] J. Ignacio Amasorrain, X. Sagartzazu, and J. Damian. Load distribution in a four contact-point slewing bearing. *Mechanism and Machine Theory*, 38(6):479–496, 2003.
- [137] B. Jacod, C. H. Venner, and P. M. Lugt. A Generalized Traction Curve for EHL Contacts. *Journal of Tribology*, 123(2):248–253, 2000.
- [138] B.C. Jacod. *Friction in elasto-hydrodynamic lubrication*. PhD thesis, University of Twente, 2002.
- [139] S. Jain and H. Hunt. A dynamic model to predict the occurrence of skidding in wind-turbine bearings. In *Proc. 9th International Conference on Damage Assessment of Structures (DAMAS 2011)*, volume 305, page 012027. IOP Publishing, 2011.
- [140] J. Y. Jang, M. M. Khonsari, and S. Bair. Correction Factor Formula to Predict the Central and Minimum Film Thickness for Shear-Thinning Fluids in EHL. *Journal of Tribology*, 130(2), 2008. 024501.
- [141] J. Jedrzejewski and W. Kwasny. Modelling of angular contact ball bearings and axial displacements for high-speed spindles. *CIRP Annals-Manufacturing Technology*, 59(1):377–382, 2010.

-
- [142] K. L. Johnson and R. Cameron. Fourth Paper: Shear Behaviour of Elastohydrodynamic Oil Films at High Rolling Contact Pressures. *Proceedings of the Institution of Mechanical Engineers*, 182(1):307–330, 1967.
- [143] K. L. Johnson and Tevaarwerk J. L. Shear behaviour of elastohydrodynamic oil films. *Proceedings of the Royal Society of London. A. Mathematical and Physical Sciences*, 356(1685):215–236, 1977.
- [144] A. B. Jones. Ball Motion and Sliding Friction in Ball Bearings. *Journal of Basic Engineering*, 81(1):1–12, 1959.
- [145] A. B. Jones. The mathematical theory of rolling-element bearings. *Mechanical Design and Systems Handbook*, pages 1–13, 1964.
- [146] B. R. Jorgensen and Y. C. Shin. Dynamics of Spindle-Bearing Systems at High Speeds Including Cutting Load Effects. *Journal of Manufacturing Science and Engineering*, 120(2):387–394, 1998.
- [147] A. Joshi, B. Kachhia, H. Kikkari, M. Sridhar, and D. Nelias. Running Torque of Slow Speed Two-Point and Four-Point Contact Bearings. *Lubricants*, 3:181–196, 2015.
- [148] J. W. Kannel and S. S. Bupara. A Simplified Model of Cage Motion in Angular Contact Bearings Operating in the EHD Lubrication Regime. *Journal of Lubrication Technology*, 100(3):395–403, 1978.
- [149] J. W. Kannel and J. A. Walowit. Simplified Analysis for Traction Between Rolling-Sliding Elastohydrodynamic Contacts. *Journal of Lubrication Technology*, 93(1):39–44, 1971.
- [150] H. Kawamura and K. Touma. Motion of Unbalanced Balls in High-Speed Angular Contact Ball Bearings. *Journal of Tribology*, 112(1):105–110, 1990.
- [151] E. P. Kingsbury. Ball motion in angular contact bearings. *Wear*, 11(1):41–50, 1968.
- [152] E. P. Kingsbury and R. Walker. Motions of an Unstable Retainer in an Instrument Ball Bearing. *Journal of Tribology*, 116(2):202–208, 1994.
- [153] P. S. Kliman. High speed ball bearings - limitation and thrust requirements. *Lubrication Engineering*, 1963.
- [154] I.V. Kragelskii, M.N. Dobychin, and V.S. Kombalov. *Friction and Wear: Calculation Methods*. Pergamon Press, 1965.
- [155] S. Lacroix. *Analyse et validation expérimentale d'un modèle de roulement à billes à quatre points de contact à bagues déformables par découplage des effets locaux et structuraux*. PhD thesis, INSA Lyon, 2014.
- [156] S. Lacroix, D. Nélias, and A. Leblanc. Four-Point Contact Ball Bearing Model With Deformable Rings. *Journal of Tribology*, 135(3), 2013. 031402.
-

- [157] A. Leblanc and D. Nélias. Ball Motion and Sliding Friction in a Four-Contact-Point Ball Bearing. *Journal of Tribology*, 129(4):801–808, 2007.
- [158] A. Leblanc and D. Nélias. Analysis of Ball Bearings with 2, 3 or 4 Contact Points. *Tribology Transactions*, 51(3):372–380, 2008.
- [159] E. Legrand. Logiciel RBL4-Modélisation des Roulements à Billes à Contact Oblique. Technical report, GLCS Technical Report No. RBL4-R01, 1997.
- [160] C. Lei, Z. Rui, J. Liu, R. Feng, and J. Zhao. A New Method for Computing Contact Angle of High Speed Ball Bearing. 1:331–334, 2010.
- [161] H. Li, H. Li, Y. Liu, and H. Liu. Dynamic characteristics of ball bearing with flexible cage lintel and wear. *Engineering Failure Analysis*, 117:104956, 2020.
- [162] Z. Li, Y. Lu, C. Zhang, J. Dong, X. Zhao, and L. Wang. Traction behaviours of aviation lubricating oil and the effects on the dynamic and thermal characteristics of high-speed ball bearings. *Industrial Lubrication and Tribology*, 72(1):15–23, 2020.
- [163] N. T. Liao and J. F. Lin. A New Method for the Analysis of Deformation and Load in a Ball Bearing With Variable Contact Angle. *Journal of Mechanical Design*, 123(2):304–312, 2001.
- [164] N. T. Liao and J. F. Lin. Ball bearing skidding under radial and axial loads. *Mechanism and Machine Theory*, 37(1):91–113, 2002.
- [165] N. T. Liao and J. F. Lin. An Analysis of Misaligned Single-Row Angular-Contact Ball Bearing. *Journal of Mechanical Design*, 126(2):370–374, 2004.
- [166] N. T. Liao and J. F. Lin. Rolling-Sliding Analysis in Ball Bearing Considering Thermal Effect. *Tribology Transactions*, 49(1):1–16, 2006.
- [167] H. Liu, Z. Chen, L. Tang, and W. Zhai. Skidding dynamic performance of rolling bearing with cage flexibility under accelerating conditions. *Mechanical Systems and Signal Processing*, 150:107257, 2021.
- [168] J. Liu and Y. Shao. Overview of dynamic modelling and analysis of rolling element bearings with localized and distributed faults. *Nonlinear Dynamics*, 93(4):1765–1798, 2018.
- [169] X. Liu, S. Deng, and H. Teng. Dynamic stability analysis of cages in high-speed oil-lubricated angular contact ball bearings. *Transactions of Tianjin University*, 17(1):20–27, 2011.
- [170] X. Liu and P. Yang. On the thermal elastohydrodynamic lubrication of tilting roller pairs. *Tribology International*, 65:346–353, 2013.
- [171] Y. Liu, W. Wang, H. Liang, T. Qing, Y. Wang, and S. Zhang. Nonlinear Dynamic Behavior of Angular Contact Ball Bearings under Microgravity and Gravity. *International Journal of Mechanical Sciences*, 183:105782, 2020.

-
- [172] Y. Liu, W. Wang, T. Qing, Y. Zhang, H. Liang, and S. Zhang. The effect of lubricant temperature on dynamic behavior in angular contact ball bearings. *Mechanism and Machine Theory*, 149:103832, 2020.
- [173] S. Ma, G. He, K. Yan, W. Li, Y. Zhu, and J. Hong. Structural optimization of ball bearings with three-point contact at high-speed. *International Journal of Mechanical Sciences*, 229:107494, 2022.
- [174] S. Ma, G. He, K. Yan, W. Li, Y. Zhu, and J. Hong. A study on the dynamic contact feature of four-contact-point ball bearing. *Mechanical Systems and Signal Processing*, 174:109111, 2022.
- [175] H. M. Martin. Lubrication of gear teeth. *Engineering*, 102:119, 1916.
- [176] M. Masjedi and M. M. Khonsari. An engineering approach for rapid evaluation of traction coefficient and wear in mixed ehl. *Tribology International*, 92:184–190, 2015.
- [177] M. Masjedi and M. M. Khonsari. A study on the effect of starvation in mixed elastohydrodynamic lubrication. *Tribology International*, 85:26–36, 2015.
- [178] J. A. Mauriello, N. Lagasse, A. B. Jones, and W. Murray. Rolling element bearing retainer analysis. Technical report, AVCO LYCOMING DIV STRATFORD CT, 1973.
- [179] J. M. Mc Grew, A. Gu, H. S. Cheng, and S. F. Murray. Elastohydrodynamic lubrication: preliminary design manual. Technical report, Mechanical Technology Inc Latham NY, 1970.
- [180] C. R. Meeks. The Dynamics of Ball Separators in Ball Bearings—Part II: Results of Optimization Study. *ASLE Transactions*, 28(3):288–295, 1985.
- [181] C. R. Meeks and K. O. Ng. The Dynamics of Ball Separators in Ball Bearings—Part I: Analysis. *ASLE Transactions*, 28(3):277–287, 1985.
- [182] C. R. Meeks and L. Tran. Ball Bearing Dynamic Analysis Using Computer Methods—Part I: Analysis. *Journal of Tribology*, 118(1):52–58, 1996.
- [183] A. Mostofi. *Oil film thickness and pressure distribution in Elastohydrodynamic elliptical contacts*. PhD thesis, 1981, Imperial College, University of London, 1981.
- [184] M. Muraki and Y. Kimura. Traction Characteristics of Lubricating Oils (2nd Report). *Journal of Japan Society of Lubrication Engineers*, 28:753–760, 1983.
- [185] L. E. Murch and W. R. D. Wilson. A Thermal Elastohydrodynamic Inlet Zone Analysis. *Journal of Lubrication Technology*, 97(2):212–216, 1975.
- [186] D. Nélias. *Etude du glissement dans les roulements à billes grande vitesse de turbo-machines*. PhD thesis, INSA Lyon, 1989.
-

- [187] D. Nélías. *Contribution à l'étude des roulements. Modélisation globale des roulements et avaries superficielles dans les contacts EHD pour des surfaces réelles ou indentées*. Habilitation à diriger des recherches, INSA Lyon, 1999.
- [188] D. Nélías, P. Sainsot, and B. Bou-Saïd. Glissement dans les roulements à billes grande vitesse sous charges axiales et radiales. In *8th World Congress on The Theory of Machines and Mechanisms*, volume 5, pages 1441–1444, Prague, Czech Republic, 1991.
- [189] D. Nélías, P. Sainsot, and L. Flamand. Power Loss of Gearbox Ball Bearing Under Axial and Radial Loads. *Tribology Transactions*, 37(1):83–90, 1994.
- [190] Nélías, D. and Legrand, D. and Vergne, P. and Mondier, J.-B. Traction behavior of some lubricants used for rolling bearings in spacecraft applications: Experiments and thermal model based on primary laboratory data. *Journal of Tribology*, 124:72–81, 2002.
- [191] G. Nijenbanning, C. H. Venner, and H. Moes. Film thickness in elastohydrodynamically lubricated elliptic contacts. *Wear*, 176(2):217–229, 1994.
- [192] G. C. Nijenbanning. *On the overrolling of local imperfections in rolling bearings*. PhD thesis, University of Twente, The Netherlands, 1997.
- [193] L. Niu, H. Cao, Z. He, and Y. Li. A systematic study of ball passing frequencies based on dynamic modeling of rolling ball bearings with localized surface defects. *Journal of Sound and Vibration*, 357:207–232, 2015.
- [194] L. Niu, H. Cao, Z. He, and Y. Li. An investigation on the occurrence of stable cage whirl motions in ball bearings based on dynamic simulations. *Tribology International*, 103:12–24, 2016.
- [195] D. Noel, M. Ritou, B. Furet, and S. Le Loch. Complete Analytical Expression of the Stiffness Matrix of Angular Contact Ball Bearings. *Journal of Tribology*, 135(4):041101, 2013.
- [196] T. Nogi, K. Maniwa, and N. Matsuoka. A Dynamic Analysis of Cage Instability in Ball Bearings. *Journal of Tribology*, 140(1), 2017. 011101.
- [197] F. Nonato and K. L. Cavalca. On the non-linear dynamic behavior of elastohydrodynamic lubricated point contact. *Journal of Sound and Vibration*, 329(22):4656–4671, 2010.
- [198] F. Nonato and K. L. Cavalca. An approach for including the stiffness and damping of elastohydrodynamic point contacts in deep groove ball bearing equilibrium models. *Journal of Sound and Vibration*, 333(25):6960–6978, 2014.
- [199] V-C. Oktaviana, L. and Tong and S-W. Hong. Skidding analysis of angular contact ball bearing subjected to radial load and angular misalignment. *Journal of Mechanical Science & Technology*, 33(2), 2019.
- [200] D. Olaru and M. D. Gafitanu. Starvation in ball bearings. *Wear*, 170:219–234, 1993.

-
- [201] P. Pan and B. J. Hamrock. Simple Formulas for Performance Parameters Used in Elastohydrodynamically Lubricated Line Contacts. *Journal of Tribology*, 111(2):246–251, 1989.
- [202] R.J. Parker. *Comparison of predicted and experimental thermal performance of angular-contact ball bearings*. National aeronautics and space administration, 1984. Technical report No. NASA-TP-2275.
- [203] B. M. Pederson, F. Sadeghi, and C. Wassgren. The Effects of Cage Flexibility on Ball-to-Cage Pocket Contact Forces and Cage Instability in Deep Groove Ball Bearings. *SAE Transactions*, 115:260–271, 2006.
- [204] B.M. Pederson. The influence of cage flexibility on bearing dynamics and performance. Master’s thesis, Purdue University, West Lafayette, IN, USA, 2013.
- [205] G. Poll, D. Wang, and T. Neubauer. Wälzlager-reibmomente unter beruøcksichtigung der schmierstoff-rheologie und versorgung. *Gleit-und Wälzlagerungen:125-146*, 2011.
- [206] J. V. Poplawski. Slip and Cage Forces in a High-Speed Roller Bearing. *Journal of Lubrication Technology*, 94(2):143–150, 1972.
- [207] J. V. Poplawski, D. R. Atwell, M. J. Lubas, and V. Odessky. Predicting Steady-State Temperature, Life, Skid, and Film Thickness in a Greased Preloaded Hybrid Ball Bearing. *Journal of Engineering for Gas Turbines and Power*, 118(2):443–448, 1996.
- [208] J. V. Poplawski and Joseph A. Mauriello. *Skidding in lightly loaded high-speed ball thrust bearings*. ASME 69-LUBS-20. New York, N.Y.: ASME, 1969.
- [209] P. Prat, P. Vergne, and J. Sicre. New Results in High Pressure and Low Temperature Rheology of Liquid Lubricants for Space Applications. *Journal of Tribology*, 116(3):629–634, 1994.
- [210] N. Prenger. *Modeling the Dynamics of Rolling Element Bearings Using ADAMS*. PhD thesis, Purdue University, West Lafayette, IN, USA, 2003.
- [211] W. Qian and G. Jacobs. *Dynamic simulation of cylindrical roller bearings*. PhD thesis, RWTH Aachen, 2014.
- [212] Y. Qin, C. Li, F. Cao, and H. Chen. A fault dynamic model of high-speed angular contact ball bearings. *Mechanism and Machine Theory*, 143:103627, 2020.
- [213] Y. Qin, C. Li, X. Wu, Y. Wang, and H. Chen. Multiple-degree-of-freedom dynamic model of rolling bearing with a localized surface defect. *Mechanism and Machine Theory*, 154:104047, 2020.
- [214] C. Rabréau, J. Kekula, M. Ritou, M. Sulitka, J. Shim, S. Le Loch, and B. Furet. Influence of bearing kinematics hypotheses on ball bearing heat generation. *Procedia CIRP*, 77:622–625, 2018.
-

- [215] H. Rahnejat and R. Gohar. The Vibrations of Radial Ball Bearings. *Proceedings of the Institution of Mechanical Engineers. Part C. Mechanical engineering science*, 199, 1985.
- [216] M. Razpotnik, G. Čepon, and M. Boltežar. A smooth contact-state transition in a dynamic model of rolling-element bearings. *Journal of Sound and Vibration*, 430:196–213, 2018.
- [217] T. Ree and H. Eyring. Theory of Non-Newtonian Flow. I. Solid Plastic System. *Journal of Applied Physics*, 26(7):793–800, 1955.
- [218] T. Ree and H. Eyring. Theory of Non-Newtonian Flow. II. Solution System of High Polymers. *Journal of Applied Physics*, 26(7):800–809, 1955.
- [219] C. J. A. Roelands, W. O. Winer, and W. A. Wright. Correlational Aspects of the Viscosity-Temperature-Pressure Relationship of Lubricating Oils (Dr In dissertation at Technical University of Delft, 1966). *Journal of Lubrication Technology*, 93(1):209–210, 1971.
- [220] J. H. Rumbarger, E. G. Filetti, and D. Gubernick. Gas Turbine Engine Mainshaft Roller Bearing-System Analysis. *Journal of Lubrication Technology*, 95(4):401–416, 1973.
- [221] V. Saheta. Dynamics of rolling element bearings using discrete element method. Master’s thesis, Purdue University, West Lafayette, IN, USA, 2001.
- [222] T. Sakaguchi and K. Harada. Dynamic Analysis of Cage Behavior in a Tapered Roller Bearing. *Journal of Tribology*, 128(3):604–611, 2006.
- [223] T. Sakaguchi and K. Harada. Dynamic Analysis of Cage Stress in Tapered Roller Bearings Using Component-Mode-Synthesis Method. *Journal of Tribology*, 131(1), 2008. 011102.
- [224] T. Sakaguchi, M. Nishikawa, S. Kazama, H. Hasegawa, and M. Satou. Dynamic Analysis of Cage Stress in Needle Roller Bearings Under Planetary Motions. ASME/STLE 2007 International Joint Tribology Conference, Parts A and B:375–377, 2007.
- [225] M. Sarangi, B. C. Majumdar, and A. S. Sekhar. Stiffness and damping characteristics of lubricated ball bearings considering the surface roughness effect. part 1: Theoretical formulation. *Proceedings of the Institution of Mechanical Engineers, Part J: Journal of Engineering Tribology*, 218(6):529–538, 2004.
- [226] M. Sarangi, B. C. Majumdar, and A. S. Sekhar. Stiffness and damping characteristics of lubricated ball bearings considering the surface roughness effect. part 2: Numerical results and application. *Proceedings of the Institution of Mechanical Engineers, Part J: Journal of Engineering Tribology*, 218(6):539–548, 2004.
- [227] M. Sarangi, B. C. Majumdar, and A. S. Sekhar. On the Dynamics of Elastohydrodynamic Mixed Lubricated Ball Bearings. Part I: Formulation of Stiffness and

- Damping Coefficients. *Proceedings of the Institution of Mechanical Engineers, Part J: Journal of Engineering Tribology*, 219(6):411–421, 2005.
- [228] M. Sarangi, B. C. Majumdar, and A. S. Sekhar. On the Dynamics of Elastohydrodynamic Mixed Lubricated Ball Bearings. Part II: Non-Linear Structural Vibration. *Proceedings of the Institution of Mechanical Engineers, Part J: Journal of Engineering Tribology*, 219(6):423–433, 2005.
- [229] H. Schlichting and J. Kestin. *Boundary layer theory*, volume 121. Springer, 1961.
- [230] T. J. Schnell. Traction measurements in elastohydrodynamic contacts. Master’s thesis, Purdue University, West Lafayette, IN, USA, 1989.
- [231] M. Sekiya. Integrated Bearing Dynamic Analysis System (IBDAS) 1. 2012.
- [232] C. Servais and J.-L. Bozet. New computational method of the ball/race contacts transverse loads of high speed ball bearings without race control hypothesis. *Tribology International*, 113:206–215, 2017. 43rd Leeds - Lyon Symposium on Tribology 2016.
- [233] Y.-M Shao, W. Tu, Z. Chen, Z.-J Xie, and B.-Y Song. Investigation on skidding of rolling element bearing in loaded zone. *Journal of Harbin Institute of Technology (New Series)*, 20:34–42, 2013.
- [234] R. P. Shevchenko and P. Bolan. A visual study of ball motion in a high-speed thrust bearing. Technical report, SAE Technical Paper 570244, 1957.
- [235] X. Shi, J. Wu, B. Zhao, X. Ma, and X. Lu. Mixed thermal elastohydrodynamic lubrication analysis with dynamic performance of aero ball bearing during start-up and shut-down. *Proceedings of the Institution of Mechanical Engineers, Part J: Journal of Engineering Tribology*, 234(6):873–886, 2020.
- [236] X.-J. Shi, L.-Q. Wang, Y.-Z. Mao, and F.-Q. Qin. Coupling study on dynamics and TEHL behavior of high-speed and heavy-load angular contact ball bearing with spinning. *Tribology International*, 88:76–84, 2015.
- [237] Y. C. Shin. Bearing Nonlinearity and Stability Analysis in High Speed Machining. *Journal of Engineering for Industry*, 114(1):23–30, 1992.
- [238] Y. Shoda, S. Ijuin, H. Aramaki, H. Yui, and K. Toma. The Performance of a Hybrid Ceramic Ball Bearing Under High Speed Conditions with the Under-Race Lubrication Method. *Tribology Transactions*, 40(4):676–684, 1997.
- [239] L.-E. Stacke and D. Fritzson. Dynamic behaviour of rolling bearings: Simulations and experiments. *Proceedings of the Institution of Mechanical Engineers, Part J: Journal of Engineering Tribology*, 215(6):499–508, 2001.
- [240] L.-E. Stacke, D. Fritzson, and P. Nordling. BEAST—a rolling bearing simulation tool. *Proceedings of the Institution of Mechanical Engineers, Part K: Journal of Multi-body Dynamics*, 213(2):63–71, 1999.

- [241] R. Stribeck. Ball Bearings for Various Loads. *Transactions of the ASME*, 29:420–463, 1907.
- [242] P. Sun, W. Chen, Y. Shen, and D. Wang. Calculation method for comprehensive damping of ball bearings based on multigrid method. *Industrial Lubrication and Tribology*, 72(7):937–945, 2020.
- [243] J. L. Tevaarwerk and K. L. Johnson. The Influence of Fluid Rheology on the Performance of Traction Drives. *Journal of Lubrication Technology*, 101(3):266–273, 1979.
- [244] V-C. Tong and S-W. Hong. Improved formulation for running torque in angular contact ball bearings. *International Journal of Precision Engineering and Manufacturing*, 19(1):47–56, 2018.
- [245] V. C. Tong and S. W. Hong. Study on the running torque of angular contact ball bearings subjected to angular misalignment. *Proceedings of the Institution of Mechanical Engineers, Part J: Journal of Engineering Tribology*, 232(7):890–909, 2018.
- [246] D. P. Townsend, C. W. Allen, and E.V. Zaretsky. *Friction losses in a lubricated thrust-loaded cageless angular-contact bearing*. 1973. Technical report No. E-7284.
- [247] W. Tu, Y. Shao, and C. K. Mechefske. An analytical model to investigate skidding in rolling element bearings during acceleration. *Journal of Mechanical Science and Technology*, 26(8):2451–2458, 2012.
- [248] C. H. Venner. *Multilevel solution of the EHL line and point contact problems*. PhD thesis, University of Twente, Netherlands, 1991.
- [249] C. H. Venner and A. A. Lubrecht. Multigrid techniques: A fast and efficient method for the numerical simulation of elastohydrodynamically lubricated point contact problems. *Proceedings of the Institution of Mechanical Engineers, Part J: Journal of Engineering Tribology*, 214(1):43–62, 2000.
- [250] P. Vergne and D. Nélias. Tribological and rheological properties of a MIL-L-23699 lubricant. 1996:691–695, 1995.
- [251] J. P. Vichard. Transient effects in the lubrication of hertzian contacts. *Journal of Mechanical Engineering Science*, 13(3):173–189, 1971.
- [252] T. L. H. Walford and B. J. Stone. The Sources of Damping in Rolling Element Bearings under Oscillating Conditions. *Proceedings of the Institution of Mechanical Engineers, Part C: Journal of Mechanical Engineering Science*, 197(4):225–232, 1983.
- [253] C. T. Walters. The Dynamics of Ball Bearings. *Journal of Lubrication Technology*, 93(1):1–10, 1971.

-
- [254] F. Wang, M. Jing, H. Fan, Y. Wei, Y. Zhao, and H. Liu. Investigation on contact angle of ball bearings. *Proceedings of the Institution of Mechanical Engineers, Part K: Journal of Multi-body Dynamics*, 231(1):230–251, 2017.
- [255] L. Wang, L. Cui, D. Zheng, and L. Gu. Analysis on dynamic characteristics of aero-engine high-speed roller bearings. *Acta Aeronautica et Astronautica SINICA*, 28(6):1461, 2007.
- [256] W-Z. Wang, L. Hu, S-G. Zhang, and L-J. Kong. Modeling high-speed angular contact ball bearing under the combined radial, axial and moment loads. *Proceedings of the Institution of Mechanical Engineers, Part C: Journal of Mechanical Engineering Science*, 228(5):852–864, 2014.
- [257] W-Z. Wang, L. Hu, Z-Q. Zhang, S-G. and Zhao, and S. Ai. Modeling angular contact ball bearing without raceway control hypothesis. *Mechanism and Machine Theory*, 82:154–172, 2014.
- [258] Y. Wang, W. Wang, S. Zhang, and Z. Zhao. Investigation of skidding in angular contact ball bearings under high speed. *Tribology International*, 92:404–417, 2015.
- [259] Y. Wang, W. Wang, and Z. Zhao. Effect of race conformities in angular contact ball bearing. *Tribology International*, 104:109–120, 2016.
- [260] Y. Wang, W. Wang, and Z. Zhao. Effects of raceway surface roughness in an angular contact ball bearing. *Mechanism and Machine Theory*, 121:198–212, 2018.
- [261] Y. S. Wang, B. Y. Yang, and L. Q. Wang. Investigation into the traction coefficient in elastohydrodynamic lubrication. *Tribotest*, 11(2):113–124, 2004.
- [262] N. Weinzapfel and F. Sadeghi. A Discrete Element Approach for Modeling Cage Flexibility in Ball Bearing Dynamics Simulations. *Journal of Tribology*, 131(2), 2009.
- [263] C. Wen, X. Meng, C. Fang, J. Gu, L. Xiao, and S. Jiang. Dynamic behaviors of angular contact ball bearing with a localized surface defect considering the influence of cage and oil lubrication. *Mechanism and Machine Theory*, 162:104352, 2021.
- [264] C. Wen, X. Meng, L. Gu, J. and Xiao, S. Jiang, and H. Bi. Starved lubrication analysis of angular contact BB based on multi degree of freedom tribo-dynamic model. *Friction*, 2022.
- [265] C. Wen, X. Meng, B. Lyu, J. Gu, and L. Xiao. Influence of angular misalignment on the tribological performance of high-speed micro ball bearings considering full multibody interactions. *Proceedings of the Institution of Mechanical Engineers, Part J: Journal of Engineering Tribology*, 235(6):1168–1189, 2021.
- [266] J.A. Wensing. *On the dynamics of ball bearings*. PhD thesis, University of Twente, Netherlands, 1998.
- [267] Y. H. Wijnant. *Contact dynamics in the field of elastohydrodynamic lubrication*. PhD thesis, University of Twente, Netherlands, 2003.
-

- [268] Wikipédia. Components of jet engines. https://en.wikipedia.org/wiki/Components_of_jet_engines, 2022.
- [269] W. R. D. Wilson and S. Sheu. Effect of Inlet Shear Heating Due to Sliding on Elastohydrodynamic Film Thickness. *Journal of Lubrication Technology*, 105(2):187–188, 1983.
- [270] J. Wu, L. Wang, T. He, L. Gu, C. Zhang, and Y. Lu. Investigation on the angular contact ball bearings under low speed and heavy load with coupled mixed lubrication and quasi-dynamic analysis. *Lubrication Science*, 32(3):108–120, 2020.
- [271] T. Xu, G. Xu, Q. Zhang, C. Hua, H. Tan, S. Zhang, and A. Luo. A preload analytical method for ball bearings utilising bearing skidding criterion. *Tribology International*, 67:44–50, 2013.
- [272] K. Yan, Y. Wang, Y. Zhu, J. Hong, and Q. Zhai. Investigation on heat dissipation characteristic of ball bearing cage and inside cavity at ultra high rotation speed. *Tribology International*, 93:470–481, 2016.
- [273] Z. Yang, T. Yu, Y. Zhang, and Z. Sun. Influence of cage clearance on the heating characteristics of high-speed ball bearings. *Tribology International*, 105:125–134, 2017.
- [274] T. Yao, L. Wang, X. Liu, and Y. Huang. Multibody dynamics simulation of thin-walled four-point contact ball bearing with interactions of balls, ring raceways and crown-type cage. *Multibody System Dynamics*, 48(3):337–372, 2020.
- [275] S. Yasutomi, S. Bair, and W. O. Winer. An Application of a Free Volume Model to Lubricant Rheology I—Dependence of Viscosity on Temperature and Pressure. *Journal of Tribology*, 106(2):291–302, 1984.
- [276] Z. H. Ye and L. Q. Wang. Cage Instabilities in High-Speed Ball Bearings. 278–280:3–6, 2013.
- [277] Z. H. Ye and L. Q. Wang. Effect of external loads on cage stability of high-speed ball bearings. *Proceedings of the Institution of Mechanical Engineers, Part J: Journal of Engineering Tribology*, 229(11):1300–1318, 2015.
- [278] T. Yoshida, M. Hirota, and K. Yoshikawa. Analysis of Cage Slip in Ball Bearings Considering Non-Newtonian Behavior and Temperature Rise of Lubricating Oil. *Tribology Online*, 8:210–218, 2013.
- [279] G. Zeng, C. Zhao, X. Yu, B. Sun, Z. Xiao, Q. Bian, and B. Liu. Study on Simplified Model and Numerical Solution of High-Speed Angular Contact Ball Bearing. *Shock and Vibration*, 2020, 2020.
- [280] J-H. Zhang, B. Fang, K. Yan, and J. Hong. A novel model for high-speed angular contact ball bearing by considering variable contact angles. *Journal of Mechanical Science and Technology*, 34(2):809–816, 2020.

- [281] W. Zhang, S. Deng, G. Chen, and Y. Cui. Impact of lubricant traction coefficient on cage's dynamic characteristics in high-speed angular contact ball bearing. *Chinese Journal of Aeronautics*, 30(2):827–835, 2017.
- [282] W. Zhang, S. Deng, G. Chen, and Y. Cui. Influence of Lubricant Traction Coefficient on Cage's Nonlinear Dynamic Behavior in High-Speed Cylindrical Roller Bearing. *Journal of Tribology*, 139(6), 2017. 061502.
- [283] Y. Zhang, B. Fang, L. Kong, and Y. Li. Effect of the ring misalignment on the service characteristics of ball bearing and rotor system. *Mechanism and Machine Theory*, 151:103889, 2020.
- [284] Y-Y. Zhang, X-L. Wang, and X-L. Yan. Dynamic Behaviors of the Elastohydrodynamic Lubricated Contact for Rolling Bearings. *Journal of Tribology*, 135(2), 2012. 021501.
- [285] D. Zhu and Y-Z. Hu. A Computer Program Package for the Prediction of EHL and Mixed Lubrication Characteristics, Friction, Subsurface Stresses and Flash Temperatures Based on Measured 3-D Surface Roughness. *Tribology Transactions*, 44(3):383–390, 2001.



FOLIO ADMINISTRATIF

THESE DE L'INSA LYON, MEMBRE DE L'UNIVERSITE DE LYON

NOM : PETUYA

DATE de SOUTENANCE : 09/12/2022

Prénoms : Karine

TITRE : Angular Contact Ball Bearing modelling with flexible cage

NATURE : Doctorat

Numéro d'ordre : 2022ISAL0128

Ecole doctorale : MEGA

Spécialité : Génie Mécanique

RESUME :

Angular Contact Ball Bearings are widely used in aerospace industry because of their ability to work at high-speed and to support important loads. Depending on operating conditions, kinematic and dynamic behaviours are complex and bearing design optimisation is essential. That is why this study aims at continuing Leblanc and Nelias' quasi-static model with balls and rings. Difficulty of this model lies in the fact that up to four ball-race contact points are considered. As well, all balls degrees of freedom are calculated without making any kinematic assumption. Then, one of the purpose of this thesis is to improve computation of friction forces, EHD lubrication and kinematics at each point of contact ellipse. The model is also harmonized in order to get a single system of equations that better deals with numerical discontinuities due to contact changes. Solutions are proposed to extend operating conditions at lower speeds and higher radial loads or misalignments.

Besides, aeronautical industry is currently developing ball bearings with cages made of lighter but softer materials. Such bearings experience cage deformation and stress concentration due to ball-to-pocket impacts. These are produced during acceleration and deceleration phases or during cruise when operating with combined thrust and radial load. That is why this study aims, in a second time, at adding cage into the quasi-static model. Ball-to-pocket and cage-race interactions are considered as well as global and local cage elasticity in three dimensions. Finally, the whole system is transposed in dynamics in order to be solved over time and to consider acceleration components.

For various operating conditions, ball kinematics, ball-race interactions, cage center motion, cage local and global deformations are analysed. Model validation is done by comparison with existing models or with experimental results found in literature.

MOTS-CLÉS :

Angular Contact Ball Bearing, Modelling, Quasi-static, Dynamic, Cage, Flexible, Contact mechanics, Lubrication.

Laboratoire (s) de recherche :

Laboratoire de Mécanique des Contacts et des Structures
UMR CNRS 5259 - INSA de Lyon
18-20 rue des Sciences
69621 Villeurbanne Cedex FRANCE

Directeur de thèse: NELIAS Daniel

Président de jury : LINARES Jean-Marc

Composition du jury :

DAIDIE Alain
LEBLANC Alexandre

SADOULET-REBOUL Emeline
LEROUX Julien

DETERRE Geoffray
DUREISSEIX David

